Univerzita Karlova v Praze

Přírodovědecká fakulta

Studijní program: fyzikální chemie

Mgr. Petr Kubelík

Infračervená spektroskopie s Fourierovou transformací:
aplikace ve studiu nestabilních částic ve výbojovém a ablačním plazmatu

Fourier transform infrared spectroscopy:
application in a study of transient species in discharge and ablation plasma

Dizertační práce

Vedoucí závěrečné práce/Školitel:
Prof. RNDr. Svatopluk Civiš, CSc.

Praha, 2012

Poděkování

Rád bych poděkoval především svému školiteli Prof. RNDr. Svatopluku Civišovi, CSc. za užitečné rady a podporu při zpracovávání této práce.

Dále děkuji svým kolegům RNDr. Martinu Ferusovi za spolupráci a pomoc s experimenty, Doc. Vladislavu Chernovovi, Ph.D. a Mgr. Ekaterině Zanozině za všestrannou pomoc při zpracování výsledků. Dále pak Prof. Kentaro Kawaguchimu, Ing. Liboru Juhovi, CSc., Prof. RNDr. Patriku Španělovi, Dr. rer. nat., Mgr. Petrovi Jelínkovi a všem dalším spolupracovníkům a kolegům, kteří k práci jakkoli přispěli.

V neposlední řadě děkuji své rodině a přátelům. Především pak svým rodičům a své ženě Ažbětě za podporu a trpělivost.

V Praze 24. 5. 2012

Předmětová slova

spektroskopie, kinetika, výboj, ablace

Klíčová slova

časově rozlišená spektroskopie s Fourierovou transformací, ablace kovů, infračervená spektroskopie, kinetický model, spektroskopie výboje, nestabilní částice, chemické reakce v plazmatu

Prohlášení

Prohlašuji, že jsem závěrečnou práci zpracoval/a samostatně a že jsem uvedl/a všechny použité informační zdroje a literaturu. Tato práce ani její podstatná část nebyla předložena k získání jiného nebo stejného akademického titulu.

V Praze 24. 5. 2012

Mgr. Petr Kubelík, v. r.

Obsah

Abstrakt

Předložená dizertační práce se skládá ze dvou tématicky souvisejících částí. První z nich (obsahuje dvě publikace) se zabývá studiem chemických procesů a spektroskopií vysoce reaktivních částic vznikajících ve výbojovém plazmatu. Zahrnuje analýzu ro-vibronických spektrálních přechodů radikálu CN v infračervené oblasti a studium chemických reakcí probíhajících v pulzním výboji. Výboj zde byl využit jako nástroj pro výzkum rozkladu jednoduchých prekurzorů (BrCN, acetonitril a formamid) a následného vzniku meziproduktů a produktů reakcí v plazmatu. Získané experimentální výsledky byly interpretovány pomocí numerického modelu, který byl v souvislosti s touto prací vyvinut a použit pro simulaci kinetiky studovaných systémů.

Druhá část (zahrnuje sedm prací) je zaměřena na vysoce rozlišenou spektroskopii kovů v ablačním plazmatu. Celkem bylo studováno šest různých kovů: Au, Ag, Cu, Cs, K a Na. Hlavní motivací pro spektroskopický výzkum kovů v infračervené oblasti je získání informace o atomárních přechodech kovů, které jsou důležité zejména pro astronomickou identifikaci linií ve spektrech hvězd a jejich spektroskopické přiřazení. Každá z publikací obsahuje souhrn analyzovaných atomárních přechodů, z nichž značná část nebyla do té doby experimentálně proměřena a analyzována.

V obou částech byla pro získání spekter použita metoda časově rozlišené spektroskopie s Fourierovou transformací.

Abstract

The present dissertation consists of two thematically related parts. The first one (includes two publications) deals with the study of chemical processes and spectroscopy of highly reactive particles produced in the discharge plasma. This part includes the analysis of ro-vibronic CN radical transitions in the infrared region and the study of chemical reactions in pulsed discharges. The discharge was used as a tool for research of decomposition of simple precursors (acetonitrile, formamide and BrCN) and the subsequent formation of intermediates and reaction products in plasma. The obtained experimental results were interpreted using a numerical model developed in context of this work and used to simulate the kinetics of the studied systems.

The second part (includes seven works) is aimed at high-resolved spectroscopy of metals in the ablation plasma. A total of six different metals were studied: Au, Ag, Cu, Cs, K and Na. The main motivation for spectroscopic research on metals in the infrared region is to obtain information on atomic metals transitions, which are particularly important for astronomical identification of lines in the spectra of stars and their spectroscopic assignments. Each publication contains a summary of the analyzed atomic transitions of which a considerable portion had not been measured and analyzed.

In both parts of this thesis the Time-Resolved Fourier Transform Spectroscopy was used.

1 Úvod

Výzkum nestabilních chemických látek (jako jsou např. radikály) v prostředí plazmatu je významnou součástí moderní fyziky a chemie. Tato oblast vědy je značně rozsáhlá. To je způsobeno jak velkou různorodostí využití plazmatu, tak i širokým rozsahem fyzikálních podmínek, za kterých můžeme plazma pozorovat.

Tato práce se zaměřuje na chemické procesy a spektroskopii nestabilních molekulárních částic pozorovaných v tzv. studeném reaktivním plazmatu. Pro tento druh plazmatu je typická nižší teplota, nižší stupeň ionizace, nižší tlak a především přítomnost mnoha procesů, z nichž některé lze klasifikovat jako chemické reakce (pozorujeme rozklad a vznik chemických látek).

Chemizmus a kinetika plazmatu jsou studovány již desítky let [1–21]. Přesto jeho výzkum zůstává náročnou problematikou. I přes značné úsilí zůstává mnoho reakčních mechanismů plazmatických procesů neznámých. Velkou měrou se na této skutečnosti podílí značná komplexita studovaných procesů a v neposlední řadě také vysoká náročnost experimentálních měření. Porozumění takovýmto systémům je přitom, kromě četných praktických aplikací plazmatu, zásadní pro mnoho oblastí základního výzkumu. Příkladem může být astrochemie [22–25] nebo chemie vyšších vrstev zemské atmosféry.

Praktické využití chemických procesů probíhajících v plazmatu je rovněž velice významné. Z množství komerčně využívaných aplikací lze uvést několik příkladů: úprava povrchů materiálů a výrobků, obrábění, výroba zdrojů záření různých vlnových délek a technických parametrů, četné jsou aplikace v analytické chemii, konstrukce plynových laserů, výroba mikročipů, značný význam má i znalost reakčních mechanismů hoření souvisejících s provozem spalovacích a proudových motorů. Tento neúplný výčet aplikací dokládá význam

výzkumu v oblasti reaktivního plazmatu a excitovaných plynů.

1.1 Cíle práce.

Jak již bylo v předchozím textu naznačeno, je spektrum témat zahrnutých v této práci značně široké. Pro komplexní popis studované problematiky (nestabilních částic vznikajících v plasmě a procesů jichž se tyto částice účastní) je proto nezbytné zabývat se současně několika různými oblastmi chemie, fyziky a z pohledu praktického provedení potřebných výpočtů také informatiky. Tyto požadavky odrážejí i definované cíle této práce.

Časově rozlišená FT spektroskopie se v průběhu tohoto výzkumu osvědčila jako metoda velice vhodná pro detekci nestabilních částic vznikajících ve výbojovém plazmatu. Bylo získáno velké množství dat v podobě časově rozlišených spekter, která lze využít pro odhad chemizmu plazmatu a reakčních mechanismů, které se v plazmatu uplatňují. Interpretace takto získaných dat je však poměrně složitá. Na rozdíl od chemických systémů vyznačujících se nízkou energetickou excitací (jako například reakce v roztocích nebo plynech za laboratorní teploty), hrají v plazmatu významnou úlohu například excitace částic do různých energetických stavů. Tyto stavy je pak třeba vnímat (z hlediska chemizmu plazmatu) jako rozdílné chemické látky, protože v reakčním mechanismu mohou hrát velmi rozdílné úlohy. Další komplikací je častý výskyt termodynamické nerovnováhy. V jednom reakčním prostředí tak můžeme pozorovat různé teploty pro různé stupně volnosti molekul (např. ve výbojích za nízkých tlaků pozorujeme značné rozdíly v rotační, vibrační a excitační teplotě). Jedním z hlavních cílů proto bylo vytvořit systém (v podobě programu), který by bylo možné použít pro interpretaci a kinetické modelování experimentálně získaných dat.

Druhý cíl této práce souvisí přímo s měřením a analýzou infračervených

spekter získaných laserovou ablací kovů. Ačkoli spektroskopie kovů je studována již desítky let, v infračervené spektrální oblasti stále existují energetické přechody, jejichž vlnočty byly získány pouze teoretickým výpočtem založeným na spektrálních datech získaných ve viditelné nebo ultrafialové oblasti. Tyto spektroskopické údaje (vysoce rozlišená spektra kovů) jsou přitom významné např. pro astronomická pozorování, protože emisi záření pocházející z excitovaných kovů lze pozorovat u mnoha vesmírných objektů. Z tohoto důvodu je druhá část dizertační práce zaměřena na získání a analýzu vysoce rozlišených spekter kovů v infračervené oblasti.

2 Časově rozlišená FT spektroskopie

Časově rozlišená spektroskopie s Fourierovou transformací (FT spektoskopie) je širokospektrální technika používaná pro studium dynamiky chemických reakcí, nebo studium nestabilních částic jako jsou např. radikály. V infračervené oblasti je možné získat spektra s vysokým spektrálním rozlišením pomocí několika odlišných metod. Jedná se především o laserovou spektroskopii [26], použití difrakčních spektrometrů [27] nebo interferometrii [28]. Předložená práce je zaměřena na třetí ze jmenovaných metod — časově rozlišenou spektroskopii s Fourierovou transformací (TR-FTS — Time-Resolved Fourier Transform Spectroscopy) v infračervené spektrální oblasti.

Hlavní výhoda TR-FTS spočívá v získání spektra v široké spektrální oblasti. V porovnání např. se spektroskopií založenou na použití laseru, která se rovněž vyznačuje dobrou citlivostí analýzy a vysokým spektrálním rozlišením, je spektrální oblast proměřená během jednoho experimentu mnohonásobně širší[1]. Získáme tak mnohem detailnější informaci o procesech probíhajících

[1] V infračervené oblasti je omezení spektrálního rozsahu určeno především propustností

ve sledovaném systému neboť můžeme zároveň pozorovat časový vývoj přechodů mezi různými energetickými stavy celé řady specií.

V zásadě existují dva způsoby, jak získat časově rozlišená spektra pomocí interferometru: kontinuální skenování a skenování nekontinuální (tzv. step scan). Z metod s kontinuální posunem zrcadla interferometru je dále možné vyčlenit metody založené na velmi rychlém skenování (tzv. Rapid a Ultrarapid scan FT [29]). Používá se pro časové intervaly od 1000 s do 1 ms. Při aplikaci této metody musí být vždy splněna podmínka, že trvání studovaného procesu je výrazně delší než posun zrcadla interferometru do maximálního dráhového rozdílu. Časově rozlišené spektrum se získá z interferogramů naměřených v rychlém sledu po sobě. Omezení této metody spočívá především v nižším spektrálním rozlišení.

Poněkud odlišný způsob záznamu spektra používá metoda synchronního skenování [2] [30]. Tato metoda je vhodná pro časové intervaly od milisekund až po mikrosekundy. Aby mohla být tato metoda použita, je nezbytné, aby bylo možné studovaný proces vyvolávat opakovaně a to s dostatečně vysokou frekvencí. Příkladem může být opakované spínání výboje nebo excitace reakční směsi pomocí výbojky. Celý proces sběru dat z detektoru a opakované excitace vzorku je řízen elektronickým signálem, který vzniká v důsledku in-

optických materiálů pro záření o daných vlnových délkách. Pro změnu spektrální oblasti měření je proto nutné přenastavit instrumentaci použitou pro záznam spektra. Přesto je možné získat během jednoho měření spektrum ve spektrální oblasti široké řádově stovky až tisíce cm^{-1}. Lasery používané pro laserovou spektroskopii jsou naproti tomu proladitelné jen v rozsahu několika desítek cm^{-1} a při měření s časovým rozlišením je vlnočet laseru obvykle naladěn pouze na jedinou spektrální linii studované látky.

[2] Zde je popsána metoda a experimentální uspořádání, které bylo použito v této práci. Metoda časového rozlišení byla v naší laboratoři dodatečně implementována do spektrometru IFS 120 HR Bruker. Instrumentální vybavení jiných výrobců provozovaných v jiných laboratořích se proto mohou v některých detailech lišit.

terference laserového záření v interferometr[3]. Při měření proběhne během každé periody signálu He-Ne laseru excitace vzorku a záznam až 64 po sobě následujících hodnot proudu měřených na detektoru.

2.1 Spektroskopie doutnavého výboje

Použití doutnavého výboje je velice výhodným postupem pro studium nestabilních částic vznikajících srážkami molekul a atomů s elektrony a ionty urychlenými elektrickým polem. Spojením s časově rozlišenou spektroskopií vzniká velmi efektivní metoda vhodná pro studiu vzniku a zániku vysoce reaktivních částic. Pomocí této metody získáváme cenná experimentální data s širokým využitím.

Spektroskopie CN radikálu – předložená práce:
Civiš, S., Šedivcová Uhlíková, T., Kubelík, P., and Kawaguchi, K. (2008) *Journal of Molecular Spectroscopy* **250(1)**, 20 – 26

Časově rozlišená spektroskopie je nejčastěji využívána pro výzkum dynamických procesů, lze ji ale s výhodou použít i pro čistě spektroskopické účely. Z obr. 1, který ukazuje časově rozlišené spektrum CN radikálu, je dobře patrné, že základní rotačně-vibrační pás pozorujeme mnohem déle než ro-vibronické přechody mezi stavy $X^2\Sigma^+$ a $A^2\Pi$ (podobné efekty můžeme

[3]Interferometr je vybaven He-Ne laserem, jehož záření prochází optickou soustavou interferometru zároveň s analyzovaným zářením. Jelikož je záření laseru monochromatické, zaznamenává detektor periodická interferenční maxima a minima v závislosti na kontinuálním pohybu zrcadla interferometru. Tyto signály jsou pak elektronicky zpracovány (jsou převedeny na obdélníkové pulzy) a slouží jako vnitřní standard interferometru, podle něhož lze velice přesně určit polohu zrcadla. Tato informace je nezbytná pro provedení vysoce přesných spektroskopických měření.

pozorovat i v případě spekter různých částic[4]). Této vlastnosti časově rozlišených spekter lze využít pro zesílení signálu požadovaných linií ve spektru (jednoduše tím, že vybereme čas, kdy požadovaná linie dosahuje maxima nebo nejvýhodnějšího poměru s jinou linií, která ji překrývá nebo jinak analýzu spektra komplikuje). Další užitečnou informací, kterou lze pomocí časově rozlišené spektroskopie získat je samotný tvar časového profilu spektrální linie. Ukazuje se, že linie stejného spektrálního pásu mají i podobné časové profily intenzit. To může v některých případech velice usnadnit identifikaci neznámých linií.

Tento přístup byl využit i při analýze rotačně-vibračního spektra radikálu CN [31]. Radikál CN je částice, která vzniká velice snadno v elektrických výbojích, při hoření i jiných chemických reakcích a byl v hojné míře detegován ve vesmíru (především v mezihvězdných oblacích a molekulárních atmosférách hvězd, planet a komet [32–36]). Má proto značný význam pro astronomii, obory zabývající se mechanismy hoření a spalování a mnoho dalších oborů.

Předložená práce zabývající se analýzou spektra radikálu CN však byla motivována jinými záměry. Prvním aniontem, jehož mikrovlnné rotační spektrum bylo v laboratorních podmínkách zaznamenáno byl anion SH^- [37]. Přestože v následujících letech byla změřena rotační spektra i dalších aniontů (např. [38,39]), zůstává vysoce rozlišená spektroskopie záporně nabitých iontů náročným experimentálním problémem. Jedním z mnoha dalších aniontů s vysokým potenciálem pro využití v astronomii je anion CN^-. Proměřením jeho rotačně-vibračního spektra by bylo možné získat spektroskopické konstanty, které by poskytly přesnější predikce přechodů rotačního spek-

[4]Např. spektrální linie atomů se ve spektru objevují mnohem dříve než molekulární rotačně-vibrační přechody a také rychleji vyhasínají.

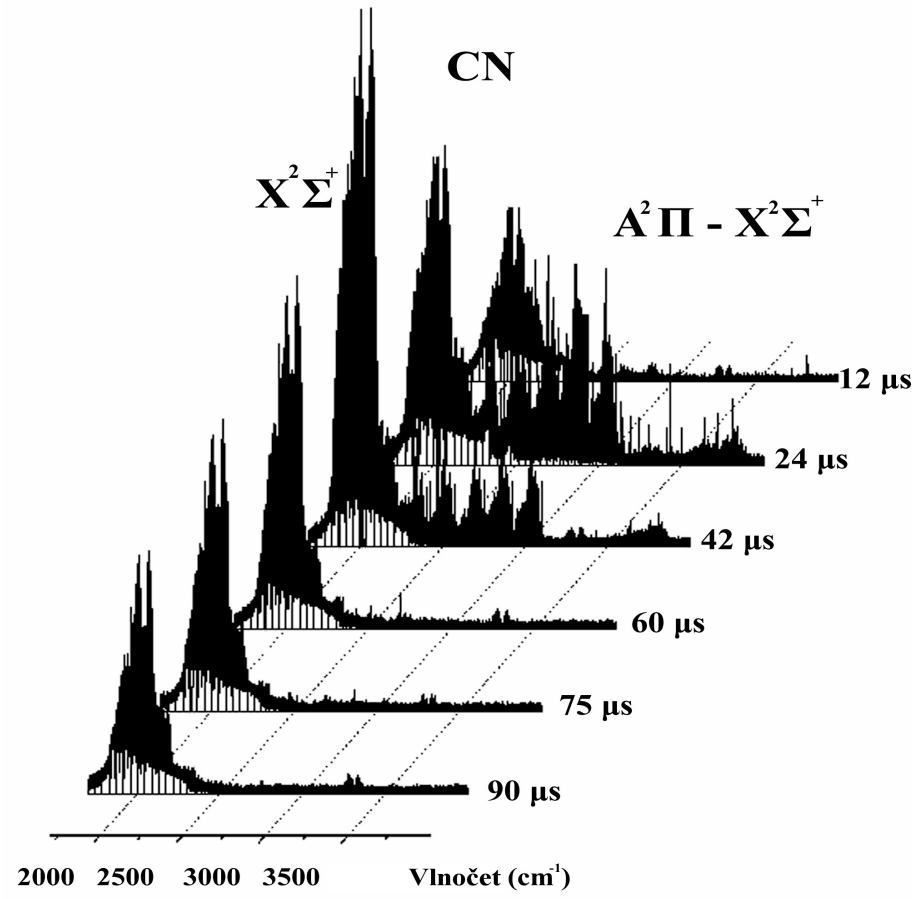

Obrázek 1: Časově rozlišené spektrum radikálu CN (převzato z [31]).

tra. Tato data pak mohou přispět k identifikaci rotačních přechodů CN^- ve vesmíru.

Rotačně-vibrační spektrum tohoto aniontu je poměrně jednoduché. Predikce polohy jeho spektrálního pásu však spadá do oblasti, kde se překrývá několik spektrálních pásů radikálu CN, což velmi znesnadňuje ne-li přímo znemožňuje hledání spektrálních linií jiné částice, jejichž přesné polohy nejsou známy. Bylo proto nutné analyzovat nejprve všechny přechody radikálu CN, které do této spektrální oblasti zasahují. Jedná se o rotačně-vibrační přechody základního elektronického stavu $X^2\Sigma^+$ (tyto přechody byly již dříve

analyzovány [40]) a ro-vibronické přechody mezi základním stavem a prvním excitovaným elektronickým stavem $A^2\Pi$ (viz. obr. 2).

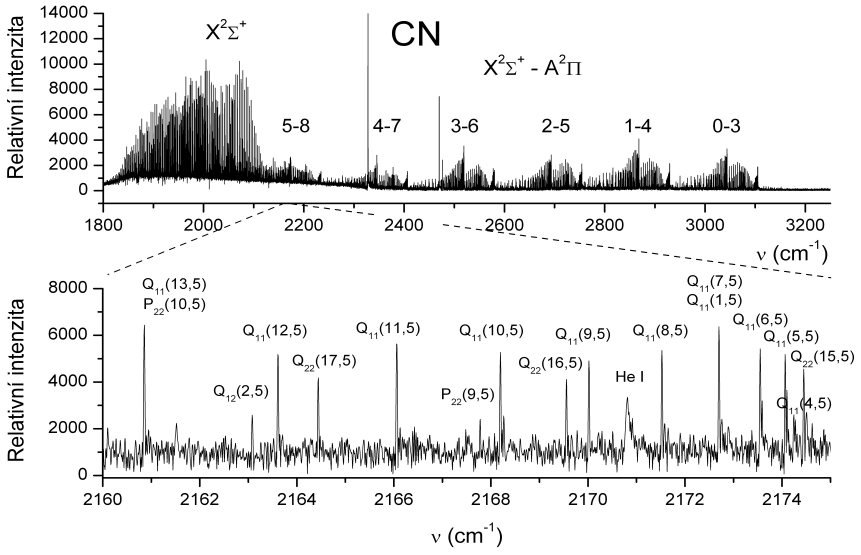

Obrázek 2: Spektrum radikálu CN (převzato z [31]).

Předložená práce [31] týkající se spektroskopie radikálu CN analyzuje právě zmíněné rovibronické přechody (konkrétně byly analyzovány přechody s $\Delta v = 3$, které spadají do oblasti přibližně 1900 – 3100 cm^{-1}). Byly publikovány také přechody pásu v = (6 – 9), jejichž vlnočty nebyly do té doby experimentálně změřeny. Přes značnou snahu se však ani po této komplexní spektroskopické analýze nepodařilo detegovat anion[5] CN^-.

Spektroskopie a kinetika výbojového plazmatu – předložená práce: Ferus, M., Kubelík, P., Kawaguchi, K., Dryahina, K., Španěl, P., and Civiš, S. (2011) *The Journal of Physical Chemistry A* **115(10)**, 1885–1899

[5]V době sepisování této práce je již vysoce rozlišené spektrum aniontu CN^- proměřeno v laboratorních podmínkách [41] a detegováno ve vesmíru [42].

Jak již bylo výše zmíněno časově rozlišená Fourierova spektroskopie je metoda umožňující studium chemických reakcí probíhajících v pulzním výboji. Tímto tématem se zabývá druhá z předložených prací [43]. Studován byl rozklad tří různých prekurzorů (acetonitril, formamid a BrCN) a následný vznik HCN a jeho nestabilního izomeru HNC. Otázka poměru koncentrací těchto dvou látek v různých oblastech vesmíru je velice zajímavá a dosud na ni neexistují jednoznačné odpovědi.

Cílem této publikace bylo získat časově rozlišná spektra meziproduktů a produktů vznikajících v reaktivním výbojovém plazmatu. Následně pak sestavit kinetický model a provést numerickou simulaci experimentálních dat.

Součástí práce proto bylo i vytvoření nástroje, který by toto numerické modelování umožnil a to nejen v případě této konkrétní studie, ale byl aplikovatelný i na jiné podobné úlohy. Popisem a podrobnějším výkladem této problematiky se zabývá kapitola 3.

2.2 Spektroskopie ablačního plazmatu

Laserová ablace je velice vhodnou metodou pro odpaření a excitaci vzorku za účelem spektroskopických měření. V této práci byla ablace aplikována ve spojení s vysoce rozlišenou spektroskopií atomů kovů. V kombinaci s časově rozlišenou spektroskopií vzniká experimentální metoda se značným potenciálem využitelným při měření spektrálních přechodů, které jsou jinak experimentu jen velmi těžko přístupné. Díky vysoko repetičnímu ArF laseru o výstupní energii kolem 10 mJ je možné studované kovy excitovat do energeticky vysoce vzbuzených stavů, jejichž přechody lze pozorovat v infračervné spektrální oblasti. Časově rozlišené měření pak poskytuje výhodu, která již byla diskutována výše v textu (možnost výběru spektra s nejvýhodnějším poměrem signálu a šumu). Tato možnost se v mnoha případech měření uka-

zuje jako klíčová pro detekci málo intenzivních přechodů.

V případě spojení časově rozlišené FT spektroskopie s laserovou ablací je však třeba vypořádat se s některými technickými komplikacemi. Jisté omezení plyne z maximální dosažitelné frekvence laserových pulzů. Tato frekvence činí 1 kHz. Minimální rychlost zrcadla interferometru je však 3 kHz. Digitální signál He-Ne laseru, který řídí činnost celého systému, se opakuje každých 333.3 μs. Zatímco laserové pulzy se mohou opakovat maximálně jednou za 1000 μs. Z tohoto poměru vyplývá, že při nastavení, které je používáno pro spektroskopii ve výboji (frekvence výbojových pulzů je zde mnohem vyšší než v případě laseru), by došlo k opoždění ablačního laserového pulzu za signálem generovaným interferometrem a měření by tedy nebylo možné vůbec provést. Řešením tohoto problému je nastavit systém tak, že pulz ablačního laseru je spuštěn pouze při každém třetím signálu He-Ne laseru interferometru. Při každém posunu zrcadla interferometru do pozice maximálního dráhového rozdílu je zaznamenána jedna třetina interferogramu. Pro získání celého interferogramu je tedy zapotřebí provést minimálně 3 posuny zrcadla. Diagram znázorňující tento proces synchronizace je uveden na obr. 3 a v publikacích [44, 45].

2.2.1 Infračervená spektroskopie kovů

Metoda jejíž základní rysy byly popsány v předchozí části textu, byla využita pro spektroskopické studie kovů. Ačkoli v ultrafialové a viditelné oblasti je k dispozici poměrně mnoho spektrálních dat (např. databáze NIST [47]), pro infračervenou oblast bylo provedeno daleko méně studií (např. [48, 49]). Značná experimentální náročnost měření vysoce rozlišených spekter kovů v infračervené oblasti spočívá především v nutnosti převést dostatečné množství kovu do plynné fáze a zajistit, aby byly atomy excitovány do vysoce

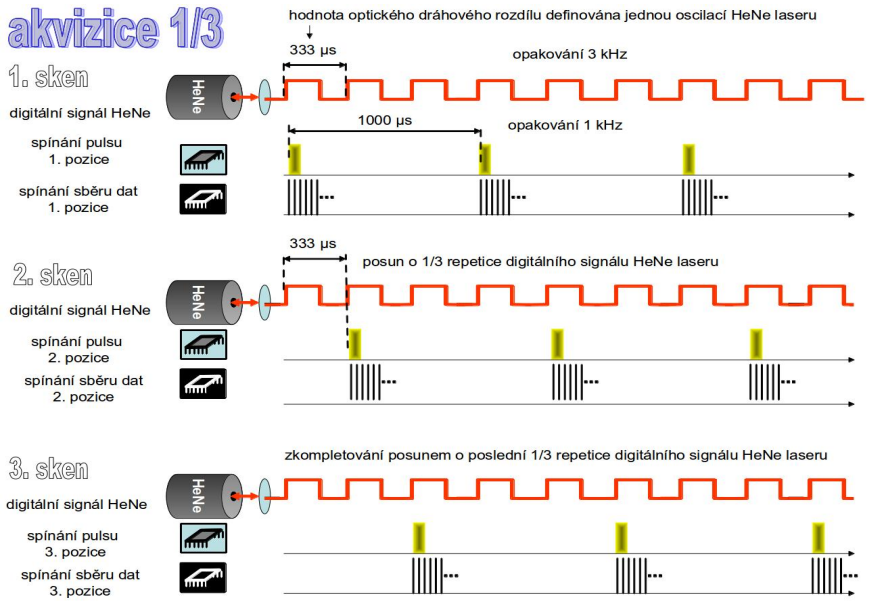

Obrázek 3: Schéma synchronizace excitace vzorku a záznamu dat v metodě časově rozlišené FT spektroskopie s kontinuálním skenováním (převzato z [46]).

vzbuzených stavů, protože právě přechody mezi vysoce excitovanými energetickými stavy spadají svými vlnočty do infračervené oblasti. Dále musí být měření prováděno přístrojem s dostatečnou citlivostí, protože zmíněné spektrální přechody jsou obvykle poměrně málo intenzivní.

FT spektroskopie ve spojení s laserovou ablací zmíněné požadavky dobře splňuje a je pro tento účel vynikající analytickou metodou. Značné zvýšení citlivosti analýzy navíc poskytuje i časové rozlišení, protože umožňuje vybrat spektrum s nejlepším poměrem signálu a šumu[6].

V průběhu několika let byla analyzována emisní spektra šesti různých kovů: Au, Ag, Cu, Cs, K a Na.

[6]Tímto způsobem lze například potlačit šum pocházející z tepelného záření analyzovaného terče bezprostředně po laserovém pulzu.

Spektroskopie zlata, stříbra a mědi – předložené práce:
Civiš, S., Matulková, I., Cihelka, J., Kubelík, P., Kawaguchi, K., and Chernov, V. E. (2010) *Physical Review A* **82**, 022502

Civiš, S., Matulková, I., Cihelka, J., Kubelík, P., Kawaguchi, K., and Chernov, V. E. (2011) *Journal of Physics B: Atomic, Molecular and Optical Physics* **44(2)**, 025002

Civiš, S., Matulková, I., Cihelka, J., Kubelík, P., Kawaguchi, K., and Chernov, V. E. (2011) *Journal of Physics B: Atomic, Molecular and Optical Physics* **44(10)**, 105002

Vysoce rozlišená spektroskopie stříbra má velký význam především z hlediska astronomických aplikací. Spektrální linie stříbra byly nalezeny např. ve spektrech hvězd [53–55]. Spektroskopické určení abundance stříbra (Ag I) v hvězdách bylo využito také pro studium procesů chemické evoluce naší galaxie [56, 57].

V práci zabývající se spektroskopií stříbra [50] bylo analyzováno spektrum v oblasti 1300 – 3600 cm^{-1}. Rozšíření a revize této práce byla provedena v publikaci [52], kde byly spolu se stříbrem analyzovány ještě zlato a měď ve spektrální oblasti 1000 – 7500 cm^{-1}.

Měď byla studována také samostatně v práci [51]. Tato studie obsahuje i vlnočty 17ti nových dosud experimentálně nezměřených spektrálních čar (v oblasti 1800 – 3800 cm^{-1}). Podobně jako stříbro je i měď prvkem, jehož spektroskopický výzkum má využití v astronomii.

Spektroskopie draslíku, sodíku a cesia – předložené práce:
Civiš, S., Ferus, M., Kubelík, P., Jelínek, P., and Chernov, V. E. (2012)

Astronomy and Astrophysics **541**, A125

S. Civiš, M. Ferus, P. Kubelík, P. Jelínek, V. E. Chernov, and E. M. Zanozina (2012) *Astronomy and Astrophysics*

Civiš, S., Kubelík, P., Jelínek, P., Chernov, V. E., and Knyazev, M. Y. (2011) *Journal of Physics B: Atomic, Molecular and Optical Physics* **44(22)**, 225006

Civiš, S., Ferus, M., Kubelík, P., Jelínek, P., Chernov, V. E., and Knyazev, M. Y. (2012) *Journal of the Optical Society of America B* **29(5)**, 1112–1118

Patrně nejstudovanějším hvězdným objektem je Slunce, jehož infračervené spektrum bylo poprvé změřeno pomocí spektrometru s Fourierovou transformací ATMOS (Atmospheric Trace Molecule Spectroscopy), který byl vynesen během misí raketoplánů Challenger, Atlantis a Discovery v letech 1985, 1992 a 1993 a dále pomocí obdobného spektrometru s názvem ACE (Atmospheric Chemistry Experient) z paluby kanadské sondy SciSat-1 vypuštěné v roce 2003. V obou spektrech se vyskytuje mnoho emisních linií atomů ve vysoce vzbuzených stavech, celá řada z nich je však chybně přiřazena nebo není přiřazena vůbec. Přitom na základě znalosti charakteristik jednotlivých linií lze získat data např. o teplotě daného prostředí, energetické distribuci vysoce vzbuzených stavů, jejich zastoupení a to i ve vertikálním profilu (pomocí matematického modelu).

Neutrální atom draslíku, jehož zastoupení ve sluneční fotosféře je asi 0.7 %, je jedním z elementů určujících metalicitu a tedy stáří a generaci hvězdy. V předkládané práci [45] bylo změřeno spektrum ablační plasmy tablety jodidu draselného s časovým a také prostorovým rozlišením ve spektrální oblasti 700 – 7000 cm^{-1}. Získaná data byla fitována a přiřazena přechodům mezi vysoce vzbuzenými excitovanými stavy, ve kterých vzbuzený

elektron přechází mezi orbitaly f, g a h. Pro každou linii byly navíc vypočteny intenzity pomocí teorie kvantového defektu (QDT, Quantum Defect Theory), která pro takto vysoce excitované stavy poskytuje i dostatečně přesné hodnoty vlnočtů. Získaná spektra byla srovnána s daty ze zmíněných satelitních měření spektrometru ACE (viz. obr 4).

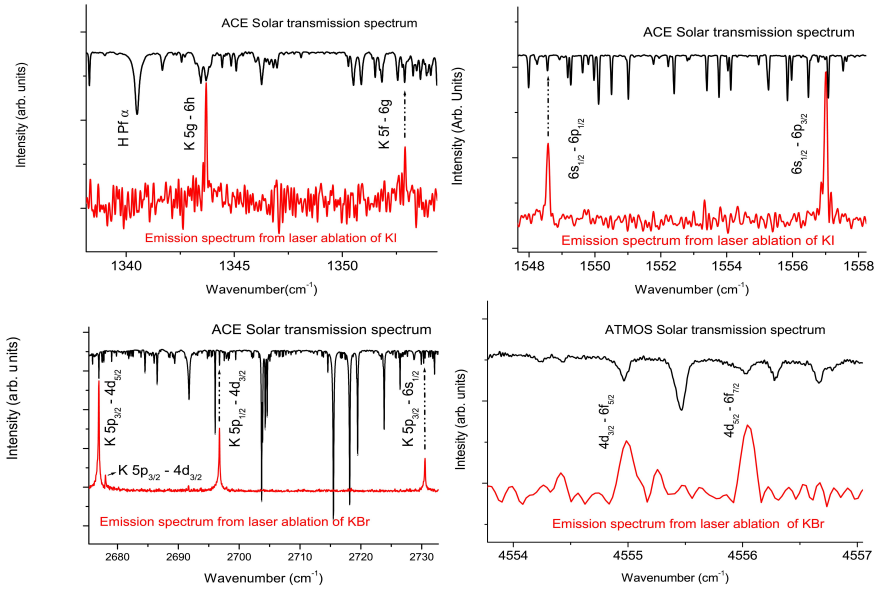

Obrázek 4: Laboratorní spektra draslíku v porovnání se solárními spektry ACE a ATMOS (převzato z [45]).

Stejně jako draslík má i sodík řadu astronomických využití. V předložené práci [58] byla provedena analýza spektra ablačního plazmatu ve spektrální oblasti přibližně 700 – 7150 cm^{-1}. Publikovány byly vlnočty 26ti spektrálních linií přičemž 20 z nich nebylo dosud v laboratorních podmínkách změřeno.

Cesium je prvkem jehož výzkum je důležitý především z hlediska moderní fyziky atomů. Tento prvek se stal předmětem řady studií, zabývajících se nejrůznějšími tématy. Jedná se např. o chování super-schlazených atomů (např. jejich vzájemné kolize), procesy formování vysoce schlazených molekul

a některé další. Velký význam cesia je i v tom, že frekvence jeho přechodů se využívají jako frekvenční standard. Spektroskopií 6h stavů cesia se zabývá práce [59]. Studované spektrální přechody spadají svými vlnočty do oblasti 1200 – 1600 cm^{-1}.

Další práce zaměřená na emisní spektra cesia v oblast 800 – 8000 cm^{-1} [44] se soustředila nejen na získání experimentálních pozic dosud nezměřených linií tohoto prvku a emisních intenzit (jako v případě K), ale také na sledování některých aspektů dynamiky ablačního plazmatu. Intenzity linií vypočtené v daném rozsahu byly použity ke stanovení teploty plazmatu a v závislosti na poloze terče ablovaného laserem byly sledována časová dynamika jednotlivých emisních linií, neboť toto nastavení je velmi důležité a při nevhodné konfiguraci nelze emisní spektra získat. Excitační teplota plazmatu byla stanovena pomocí pyrometrické přímky za použití parametrů vypočtených v této práci. Ukázalo se, že tato teplota je podle našich měření v rozsahu experimentální chyby časově i prostorově homogenní a dosahuje 2250±560 K.

3 Kinetický model reakcí v pulzním doutnavém výboji

3.1 Formulace modelu

Ačkoli výzkum výbojů není cílem této práce, byla časově rozlišená spektroskopie pulzního výboje zvolena jako nástroj pro studium kinetiky nestabilních částic (např. radikálů). Modelování kinetiky chemických reakcí v plazmatu zahrnuje mnoho různých přístupů a metod. Některé modely jsou velice komplexní a snaží se zohlednit maximum možných efektů, která

se mohou ve studovaném systému vyskytovat a tedy mít vliv na průběh a výsledek simulace [60–86]. Takovéto simulace často zohledňují prostorové rozlišení výpočtu a často také využívají různé numerické metody pro výpočet příspěvků různých fyzikálních a chemických procesů[7]. Takto komplexní systémy se však pro značnou numerickou náročnost výpočtu používají k popisu poměrně jednoduchých chemických systémů.

Přístup, který byl zvolen pro návrh vlastního nástroje pro numerické modelování chemických procesů, odráží především potřeby naší laboratoře (tj. interpretaci časově rozlišených spekter).

Původní koncepce zahrnovala pouze simulaci chemických reakcí v pozitivním sloupci doutnavého výboje. Vzhledem k tomu, že pozitivní sloupec doutnavého výboje lze považovat za homogenní byl model od počátku navržen jako prostorově nerozlišená simulace chemických procesů. Tuto aproximaci bylo možné použít díky vhodné konstrukci výbojové cely, která zaručuje, že záření pocházející z jiných oblastí výboje než je pozitivní sloupec (např. katodové záření nebo negativní sloupec) se do do spektrometru nedostane. Důraz byl kladen především na vysokou flexibilitu programu a možnost jeho pozměnění či rozšíření podle povahy modelovaného systému.

Ve výbojích mají velký význam vedle reakcí těžkých částic (molekul, atomů, iontů...) také reakce jichž se účastní volné elektrony. Protože jsou elektrony mnohonásobně lehčí než částice složené z atomů a mají nenulový náboj, jsou zároveň nejefektivnějšími přenašeči energie elektrického pole do chemických procesů. Z tohoto důvodu hrají reakce s elektrony významnou roli v reakčních mechanismech uplatňujících se ve výbojích.

[7]Někdy se využívají tzv. hybridní modely [87–90], kde např. kinetika elektronů a rychlých iontů je popisována pomocí Monte Carlo metod, zatímco kinetika neutrálních částic a pomalých iontů je řešena pomocí metod používaných pro fluidní systémy

Další specifickou vlastností výbojů jsou značné rozdíly v teplotách těžkých částic a elektronů (tyto rozdíly jsou často i několik řádů). Rychlostní konstanty jsou obvykle na teplotě závislé. Teplota však v obecném případě není explicitním parametrem výpočtu (tzn. je závislá na průběhu reakcí tvořících reakční mechanismus a tedy na reakčním mechanismu samotném). Teplota je navíc ovlivněna mnoha dalšími parametry jako jsou např. tepelné kapacity látek vyskytujících se v reakční směsi (jejíž složení se navíc v čase mění), množstvím tepla, které se uvolní při daných reakcích a v neposlední řadě také tokem tepla pryč ze systému, protože v mnoha případech nelze pozorovaný systém považovat za izolovaný. Některé programy [91] tento problém řeší tak, že v každém kroku výpočtu koncentrací vznikajících a zanikajících látek je z výše zmíněných parametrů vypočítána i teplota systému. Ačkoli má tento přístup v mnoha případech své opodstatnění, existuje možnost, jak tyto dodatečné výpočty obejít. Touto možností je právě definice rychlostních parametrů jako explicitní (předem definované) funkce času. Tento přístup je však podmíněn tím, že požadované funkce skutečně známe. Zde je nezbytné získat potřebná data přímo z experimentu. Tento problém je však ve většině případů řešitelný. Vezmeme-li v úvahu např. experimenty s výbojovým plazmatem, pro které byl program především navrhován, můžeme teplotu plasmy získat ze spektrálních dat [92, 93].

Takovýchto explicitních funkcí můžeme definovat neomezený počet. To umožňuje zahrnout do výpočtu více než jednu teplotu. V simulacích, které jsou zaměřeny na výbojové plazma může být zahrnutí několika různých teplot nezbytné[8]. Je proto důležité, aby použitý model dokázal tuto skutečnost

[8]U různých druhů plazmatu často pozorujeme (především za nižších tlaků) termodynamickou nerovnováhu. Např. rozdělení energií v jednotlivých stupních volnosti molekul vyskytujících se v plazmatu se významně liší (rotační, vibrační a excitační teplota se v takových případech liší řádově). Dalším často pozorovaným jevem je rozdíl v translační

vhodným způsobem postihnout.

Zvolen byl následující postup. Simulační program umožňuje definovat v reakčním mechanismu libovolný počet funkcí, které jsou explicitně závislé na čase (tzn. jsou předdefinované uživatelem). Tyto funkce mohou vystupovat v roli koncentrace určité částice reakčního mechanismu nebo v roli rychlostní konstanty. Použití této strategie je demonstrováno následujícím ilustrativním příkladem.

Uvažujme jednoduchý hypotetický reakční mechanismus popsaný rovnicemi:

$$\mathrm{AB} + e \;\rightarrow\; \mathrm{A} + \mathrm{B} + e \qquad k_1 \tag{1}$$

$$\mathrm{A} + \mathrm{B} + \mathrm{M} \;\rightarrow\; \mathrm{AB} + \mathrm{M} \qquad k_2 \tag{2}$$

V roli částice AB může vystupovat např. molekula HCN, e může označovat elektron. A a B by v takovém případě označovali H a CN radikál. M hraje roli jakékoli nereaktivní částice, která odnáší přebytečnou energii při vzniku částice AB (ve skutečnosti by však byl tento reakční mechanismus mnohem komplikovanější proto zůstaneme u abstraktních označení). Protože v rovnici (1) vystupuje částice e (které jsme přiřadily roli elektronu), bude rychlostní konstanta k_1 záviset na teplotě, která odpovídá energetické distribuci částic e. Konstanta k_2 však bude záviset na teplotě částic A, B a M. Použitý model umožňuje snadno definovat neomezený počet takovýchto funkcí. Abychom však tento přístup mohli použít, musíme potřebné funkce (např. teploty) znát. První možností je získat tato data z experimentálních měření (teplotu plynu lze odhadnout z rotačně-vibračního spektra a teplotu volných elektronů např. pomocí Langmuirovy sondy) nebo je lze aproximovat odhady. Např. u periodicky spínaného výboje můžeme hustotu elek-

teplotě částic o různém náboji nebo výrazně odlišné hmotnosti. V systému proto můžeme definovat rozdílné teploty neutrálních částic, iontů a elektronů.

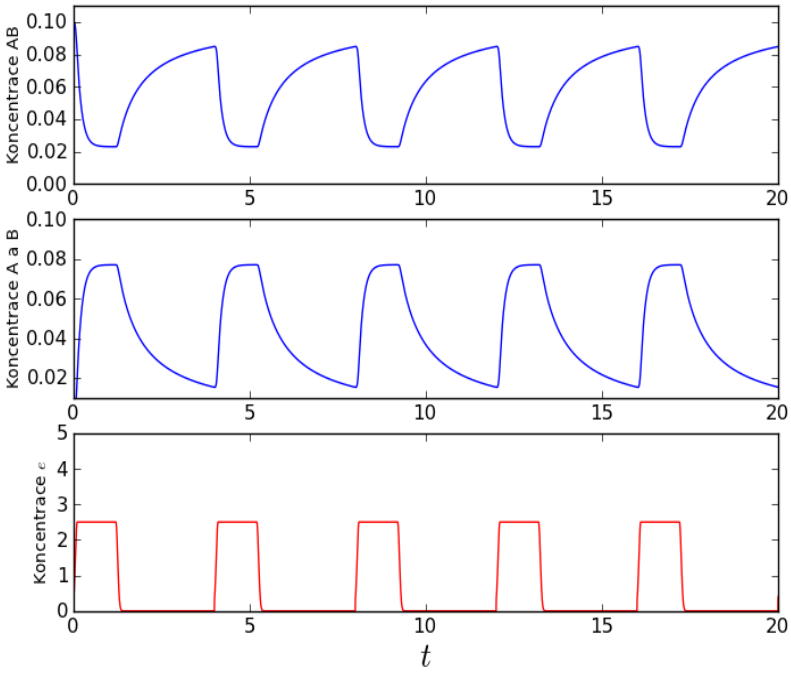

Obrázek 5: Výsledek numerického řešení demonstračního reakčního mechanismu. Koncentrace částic AB, A a B jsou vypočteny ze vstupních parametrů, koncentrace částice e je definována uživatelem a v modelu vystupuje v roli vstupních parametrů výpočtu. (Jednotky nejsou uvedeny neboť se jedná pouze o ilustrativní hodnoty.)

tronů (stejně jako jejich teplotu) v prvním přiblížení nahradit obdélníkovými pulzy. Pokud aplikujeme tento postup na reakční mechanismus popsaný rovnicemi (1) a (2), můžeme získat (v závislosti na nastavení hodnot parametrů) výsledek znázorněný na obr. 5. Koncentrace částic e je zde aproximována obdélníkovými pulzy s gaussovskými náběžnými hranami (tato funkce je mnohem vhodnější než čistě obdélníková, protože usnadňuje a urychluje průběh integrační procedury).

Podobná metoda byla aplikována i na reálné chemické systémy. Tato pro-

blematika je rozebrána v následující kapitole.

3.2 Aplikace kinetického modelu na reakce probíhající v elektrickém výboji

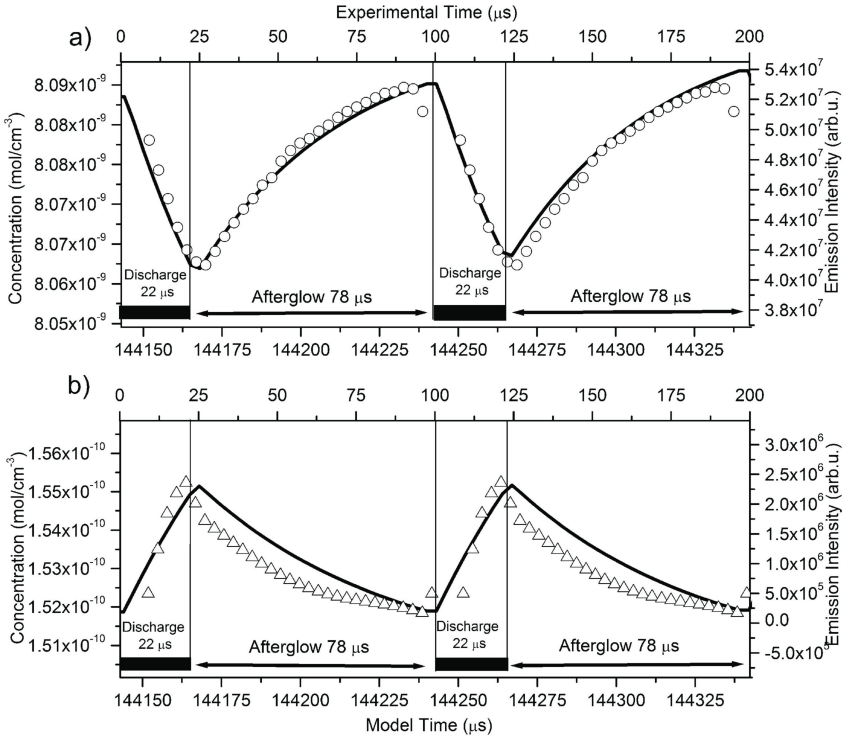

Obrázek 6: Porovnání časově rozlišeného spektra HCN (horní část obr.) a HNC (dolní část obr.) s numerickou simulací (převzato z [43]).

Metodika popsaná v kapitole 3.1 byla aplikována při interpretaci časově rozlišených spekter pulzního výboje v acetonitrilu. Spektrum vznikajících meziproduktů a produktů bylo zaznamenáno pomocí metody popsané v kapitole 2. Spektroskopicky byly detegovány: CN, HNC, HCN dále byly zaznamenány atomární spektrální přechody C, N a H. Metodou SIFT-MS (selected ion flow tube mass spectrometry) byla zjištěna i přítomnost methanu.

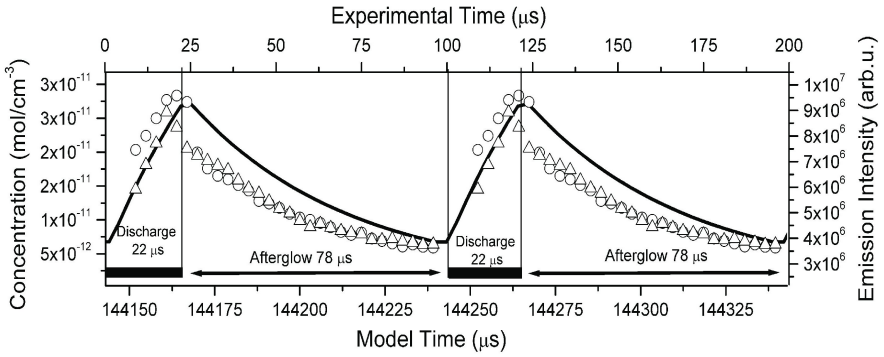

Obrázek 7: Porovnání časově rozlišeného spektra CN (rotačně-vibrační přechody základního stavu $X^2\Sigma^+$) s numerickou simulací (převzato z [43]).

Kompletní reakční mechanismus je uveden v publikaci [43]. Zahrnuté reakce lze rozdělit do dvou skupin:

- reakce s elektrony
- reakce těžkých částic

V případě reakcí těžkých částic byly jejich rychlostní konstanty považovány za přibližně konstantní (teplota plynu odhadnutá pomocí rotační teploty, získané ze spektra, se během výbojových pulzů měnila jen zanedbatelně). Pro výpočet rychlostních konstant reakcí s elektrony byl použit vztah publikovaný Morrisonem [94], ve kterém vystupuje teplota volných elektronů. Tato hodnota byla ve výpočtu fitována jako volný parametr (byla získána elektronová teplota $T_e = 1$ eV). Periodické spínání výboje bylo simulováno obdélníkovým pulzem, který ve výpočtu zastupoval hustotu volných elektronů. Jeho výška byla odhadnuta na 6×10^{11} cm^{-3}. Tato hodnota byla získána pomocí Langmuirovy sondy při stejných experimentálních podmínkách (odpovídá navíc běžně dosahovaným elektronovým hustotám v doutnavých výbojích [95, 96]).

Porovnání výsledků simulace a experimentálních dat je uvedeno na obr. 6 a 7. Ačkoli model zahrnuje poměrně mnoho aproximací je shoda s experimentem dobrá.

3.3 Popis programu *Pkin*

3.3.1 Koncepce programu a oblast jeho využití

Program *Pkin* byl vyvinut jako nástroj pro interpretaci experimentálních dat získaných pomocí časově rozlišené FT spektroskopie. Jedná se tedy o program, který na základě uživatelem definovaného reakčního mechanismu vypočte časové závislosti koncentrací jednotlivých částic v reakčním mechanismu zahrnutých. Program je určen k řešení úloh, které zahrnují následující kroky:

- zpracování vstupních souborů
- automatické sestavení soustavy diferenciálních rovnic popisujících daný systém
- numerické řešení této soustavy
- vytvoření výstupního souboru

Cílem bylo navrhnout a vytvořit program, který by byl jednoduchý, snadno ovladatelný a zároveň snadno modifikovatelný a rozšiřitelný. Zohlednit všechny zmíněné požadavky při návrhu programu je poměrně náročný úkol. Vzhledem k tomu, že program má sloužit k numerickému modelování experimentů s nejrůznějším uspořádáním (např. různé typy elektrických výbojů, termální rozklad atd.) a nastavením výchozích podmínek, byl kladen důraz především na snadnou modifikovatelnost a rozšiřitelnost programu. Způsob dosažení tohoto požadavku je podrobně diskutován v následující podkapitole.

V porovnání s jinými volně dostupnými programy, určenými k řešení kinetiky chemických reakcí[9], obsahuje program *Pkin* některé speciální funkce, jejichž vytvoření vyžadovala povaha řešených problémů.

První z těchto speciálních funkcí je možnost definovat rychlostní parametry reakcí (případně i jiných procesů jako je např. excitace nebo deexcitace) jako funkce explicitně závislé na čase. Tímto způsobem je možné do výpočtu zahrnout jakoukoli experimentálně získanou veličinu, kterou uživatel považuje za významnou pro konkrétní simulaci. Je například možné předdefinovat koncentraci některé částice na základě experimentálně získaných dat a tím značně zjednodušit použitý reakční mechanismus (tento přístup byl podrobněji popsán v kapitole 3.1).

Jak bylo uvedeno v kapitole 2, časově rozlišené FT spektroskopie vyžaduje opakovanou excitaci vzorku. Z tohoto důvodu bylo výhodné navrhnout program tak, aby uživateli umožnil snadnou definici periodicky se opakujících událostí, které do systému zasahují z vnějšího prostředí. Může se jednat například o opakované periodické spínání výboje či excitaci systému pomocí záření výbojky.

3.3.2 Implementace programu

Program *Pkin* je napsán v programovacím jazyce Python [97]. Jedná se o moderní objektově orientovaný interpretovaný programovací jazyk. Jedním z hlavních kritérií pro výběr tohoto programovacího jazyka byla jeho jednoduchost z hlediska pochopení a zvládnutí základních programovacích technik a především jeho značná oblíbenost a rozšíření v přírodovědných oborech (především chemii a biologii). Tyto dvě uvedené vlastnosti Pythonu úzce

[9] Jedním z nejkomplexnějších a pravděpodobně nejznámějších je program Cantera [91], který se v některých rysech podobá velice rozšířenému komerčnímu programu Chemkin.

souvisí s celkovou koncepcí programu *Pkin*.

Aby bylo dosaženo požadované flexibility, jsou hlavním programem nejprve načteny dva vstupní soubory, z nichž je automaticky vygenerován skript v jazyce Python, jehož spuštěním se provede výpočet. Uživatel tak má možnost upravit vygenerované skripty manuálně a tím dále zvýšit flexibilitu programu. Výhodou při tomto postupu je i skutečnost, že Python je interpretovaný jazyk (program nemusí být před spuštěním překládán do binárního kódu).

Ačkoli má uživatel možnost zasahovat přímo do zdrojového kódu programu, pro základní použití (s časově nezávislými rychlostními konstantami) není znalost programovacího jazyka nutná.

3.3.3 Instalace a použití

Vzhledem k tomu, že program je vytvořen v programovacím jazyce Python, vyznačuje se dobrou přenositelností mezi různými operačními systémy[10]. Program lze bezplatně stáhnout z internetové stránky `http://www.jh-inst.cas.cz/~ftirlab/Download/pkin.zip` jako `zip` archiv, který obsahuje všechny soubory potřebné ke spuštění programu. Po stažení a rozbalení archivu `pkin.zip` již není potřeba provádět žádnou instalaci[11]. Podrobnější popis použití programu je uveden v dodatku A.

[10]Program byl testován na operačním systému Linux, ale předpokládá se i jeho užití na systémech Microsoft Windows.

[11]Program *Pkin* využívá některé moduly, které nejsou součástí základní instalace Pythonu. Je proto nutné tyto moduly před použitím programu nainstalovat.

4 Závěr

Tato práce se zabývá chemickými procesy a spektroskopií částic k krátkou dobou života. Tyto částice (především jsme se zaměřili na radikály) často vznikají v plazmatu elektrických výbojů. Proto byl elektrický výboj ve spojení s časově rozlišenou spektroskopií s Fourierovou transformací využit jako nástroj pro studium těchto specií.

CN je jedním z radikálů, který má velký význam jak z hlediska astronomických pozorování tak i jako meziprodukt hrající klíčovou úlohu v řadě reakčních mechanismů. Proto mu byla věnována speciální pozornost. Byla provedena jeho spektroskopická analýza v oblasti 1900 – 3100 cm^{-1} (rovibronické přechody mezi stavy $X^2\Sigma^+$ a $A^2\Pi$). Radikál CN má navíc i klíčovou úlohu v plazmatických reakcí studovaných v publikaci [43].

V souvislosti s řešením chemizmu a kinetiky látek ve výbojovém plazmatu byl vyvinut program pro simulaci reakční kinetiky s jehož pomocí byla časově rozlišená spektra modelována. Tento program je použitelný např. i pro některé systémy, v nichž nedochází k ustavení úplné termodynamické rovnováhy.

Druhou oblastí studia byla časově rozlišená spektroskopie ablačního plazmatu kovů. Infračervená vysoce rozlišená spektra kovů jsou dosud v porovnání s viditelnou a UV oblastí poměrně málo známá. Mají však význam pro astronomický výzkum neboť kovy se hojně vyskytují ve vesmírných objektech (především hvězdách) a detailní znalost jejich spekter může sloužit k získávání nových informací o vesmíru.

Spojením časově rozlišené FT spektroskopie s laserovou ablací vznikla unikátní metoda vhodná pro měření i slabších spektrálních přechodů studovaných prvků. Celkem bylo studováno šest kovů: Au, Ag, Cu, Cs, K a Na. Předložené práce obsahují detailní spektroskopické analýzy těchto kovů, které v mnoha případech obsahují i dosud nepozorované spektrální přechody.

A Manuál programu *Pkin*

Pkin – nástroj pro modelování kinetiky chemických systémů

Petr Kubelík

1 Popis programu

Program Pkin je určen k numerickému výpočtu časových závislostí koncentrací částic v průběhu komplexních chemických procesů definovaných reakčním mechanismem. Reakční mechanismus je definován v jednom ze dvou vstupních souborů. Program Pkin se od podobných dostupných nástrojů liší tím, že umožňuje definovat časovou závislost vybraných částic či rychlostních konstant jako explicitní funkci času. Tento přístup umožňuje zahrnout do výpočtu experimentálně získaná data nebo jejich odhady. Příkladem může být simulace periodicky spínaného výboje pomocí hustoty volných elektronů aproximované obdélníkovým pulzem.

Program je vytvořen v programovacím jazyku Python *(www.python.org)*. Importovány jsou standardní moduly `math, re, string` (obvykle není třeba je instalovat) a moduly `numpy` *(www.numpy.org)*, `scipy` *(www.scipy.org)*, `sympy` *(www.sympy.org)* a `pyparsing` *(www.pyparsing.wikispace.com)*, které je nutno doinstalovat.

Program byl testován na operačním systému Linux (Ubuntu 9.10), numpy-1.3.0, scipy-0.7.0, sympy-0.6.4 a pyparsing-1.5.2.

2 Licence

Copyright (c) 2011, Petr Kubelík
Tento program je možné dále šířit, kopírovat a upravovat. Nakládání s moduly, které program využívá, se řídí licenčními podmínkami jejich autorů. Program je poskytován "tak jak je", bez jakékoli záruky, autor nenese žádnou odpovědnost za případné škody způsobené používáním tohoto programu.

3 Instalace

Instalaci lze v Linuxu i Microsoft Windows provést následovně:

- instalace pythonu

- instalace modulů `numpy, sympy`, `scipy` a `pyparsing`
- rozbalení souboru Pkin.zip

4 Použití programu

Po instalaci můžeme program otestovat pomocí vstupního souboru test.in. Přejdeme do adresáře, který obsahuje vstupní soubory (test.in a test.in.inp) společně se soubory programu (Pkin, ChEq.py, ChMech.py a addFunc.py). V příkazovém řádku spustíme příkaz `python Pkin -m test.in -r`. Program Pkin vygeneruje soubory dif_ode.py, jac_ode.py a main_ode.py, které jsou následně atomaticky spuštěny. Výsledek výpočtu je uložen v souboru test.in.out.

Program Pkin je možné spustit několika různými způsoby za použití různých předvoleb. Předvolba -h vypíše stručnou nápovědu, -m specifikuje vstupní soubor s popisem reakčního mechanismu , -n vygeneru druhý vstupní soubor, který je pro výpočet nezbytný. Tento soubor je nutné ručně editovat podle požadavků kladených na výpočet. Předvolba -r spustí výpočet.

Příklady spuštění programu Pkin:

- `python Pkin -h` (vypíše nápovědu)
- `python Pkin -m test.in` (v případě, že soubor test.in.inp je vygenerován a editován, vytvoří soubory dif_ode.py, jac_ode.py a main_ode.py)
- `python Pkin -m test.in -n` (vygeneruje needitovaný vstupní soubor test.in.inp (pokud tento soubor jiz existuje, bude přepsán))
- `python Pkin -m test.in -r` (v případě, že soubor test.in.inp je vygenerován a editován, vytvoří soubory dif_ode.py, jac_ode.py a main_ode.py a spustí výpočet)

5 Vstupní soubory

Pro spuštění výpočtu jsou zapotřebí dva vstupní soubory. První vstupní soubor obsahuje definici reakčního mechanismu, druhý pak dodatečné informace o mechanismu a další parametry výpočtu.

5.1 1. vstupní soubor (popis reakčního machanismu)

K programu je přiložen ukázkový vstupní soubor s reakčním mechanismem `test.in`. Modifikací tohoto souboru je možné vytvořit popis libovolného reakčního mechanismu. Při psaní vstupního souboru je však třeba dodržet určitá pravidla:

- Řádek začínající znakem # je programem považován za komentář a není dále zpracováván.
- Reakční mechanismus je popsán pomocí elementárních reakčních rovnic (např.: A + B = C + D).
- Na každém řádku může být zapsána pouze jedna rovnice.
- Každý řádek musí končit řetězcem *$ rychlostní_konstanta* kde *rychlostní_konstanta* je reálné číslo nebo funkce času definovaná v souboru addFunc.py. Tato funkce může jako parametry obsahovat i další funkce (rovněž definované v souboru addFunc.py). Čas musí v parametrech vystupovat pod proměnnou `time`. Vše, co je zapsáno za znakem *$* je přímo zkopírováno do skriptu pythonu. Proto musí být tento text zapsán podle syntaktických pravidel Pythonu. Řetězec volaní funkce musí obsahovat i název modulu (souboru (bez souborové přípony)), ze kterého je funkce importována (např. $ addFunc.k_T(350.5,1.0,2.0e-22))
- Jako separátor reaktantů a produktů může v rovnici vystupovat libovolný z následujících znaků: `=, =>, ->, -->, --->`.
- Názvem částice může být libovolný řetězec obsahující pouze písmena a číslice (musí však začínat písmenem).
- Název částice nesmí obsahovat znak "+".
- Pokud se částice v rovnici vyskytuje více než jedenkrát, lze tuto skutečnost zapsat jedním z následujících způsobů: 2 A + B..., 2*A + B... (okolo znaku '*' mohou nebo nemusí být mezery), A + A + B...

5.2 2. vstupní soubor

K programu je přiložen ukázkový vstupní soubor test.in.inp. Druhý vstupní soubor může být vygenerován programem Pkin a následně modifikován textovým editorem. Po úpravě souboru je nutné smazat první řádek s textem *after editing delete this line!* a soubor uložit.

Formát vstupního souboru:

- Hodnota `rtol` je největší povolená relativní chyba v jednom kroku integrace.
- Do bloku `initial concentrations/absolute tolerances` se doplní počáteční koncentrace částic a největší povolená absolutní chyba v jednom kroku integrace.

- Jako počáteční koncentrace částice může vystupovat reálné číslo (s desetinnou tečkou (přípustný je i semilogaritmický tvar)) nebo řetězec `!explicit`. V případě použití tohoto řetězce je počáteční hodnota koncentrace nahrazena explicitní na čase závislou funkcí definovanou v souboru addFunc.py. Řetězec volání této funkce musí být uveden na konci stejného řádku a musí začínat znakem *$*.
- Čas musí v parametrech vystupovat pod proměnnou `time`.
- Hodnota `pulse_number` udává kolikrát se bude výpočet opakovat. Při každém opakování jsou jako výchozí koncentrace částic nastaveny koncentrace získané předešlým výpočtem.
- Hodnota `step_number` udává počet bodů, v nichž se vyhodnocují koncentrace částic (v jednom dílčím výpočtu).
- Hodnota `pulse_length` udává (časovou) vzdálenost mezi body v nichž se vyhodnocují koncentrace částic.
- Hodnota `jacfl` definuje zda se jakobián použitý při řešení soustavy diferenciálních rovnic bude odhadovat numericky (jacfl = 0) nebo bude vypočten symbolicky pomocí modulu `sympy` (jacfl = 1).
- Vstupní soubory neprocházejí před zpracováním podrobnou syntaktickou kontrolou, proto je nutné dodržovat uvedený formát.

5.3 Soubor addFunc.py

V tomto souboru jsou definovány funkce, které lze použít ve vstupních souborech jako explicitní na čase závislé parametry výpočtu (např. rychlostní konstanty, koncentrace částic...). Obsah tohoto souboru může být uživatelem libovolně rozšířen o další funkce napsané v jazyce Python.

B Seznam předkládaných publikací

Publikace zahrnující kinetické modely plazmatu a časově rozlišenou FT spektroskopii:

1) Civiš, S., Šedivcová Uhlíková, T., Kubelík, P., and Kawaguchi, K. (2008) *Journal of Molecular Spectroscopy* **250(1)**, 20 – 26

2) Ferus, M., Kubelík, P., Kawaguchi, K., Dryahina, K., Španěl, P., and Civiš, S. (2011) *The Journal of Physical Chemistry A* **115(10)**, 1885–1899

Publikace zahrnující časově rozlišenou FT spektroskopii ablačního plazmatu:

3) Civiš, S., Matulková, I., Cihelka, J., Kubelík, P., Kawaguchi, K., and Chernov, V. E. (2011) *Journal of Physics B: Atomic, Molecular and Optical Physics* **44(2)**, 025002

4) Civiš, S., Matulková, I., Cihelka, J., Kubelík, P., Kawaguchi, K., and Chernov, V. E. (2010) *Physical Review A* **82**, 022502

5) Civiš, S., Matulková, I., Cihelka, J., Kubelík, P., Kawaguchi, K., and Chernov, V. E. (2011) *Journal of Physics B: Atomic, Molecular and Optical Physics* **44(10)**, 105002

6) Civiš, S., Kubelík, P., Jelínek, P., Chernov, V. E., and Knyazev, M. Y. (2011) *Journal of Physics B: Atomic, Molecular and Optical Physics* **44(22)**, 225006

7) S. Civiš, M. Ferus, P. Kubelík, P. Jelínek, V. E. Chernov, and E. M. Zanozina (2012) *Astronomy and Astrophysics*

8) Civiš, S., Ferus, M., Kubelík, P., Jelínek, P., and Chernov, V. E. (2012) *Astronomy and Astrophysics* **541**, A125

9) Civiš, S., Ferus, M., Kubelík, P., Jelínek, P., Chernov, V. E., and Knyazev, M. Y. (2012) *Journal of the Optical Society of America B* **29(5)**, 1112–1118

C Soubor předkládaných publikací

Journal of Molecular Spectroscopy 250 (2008) 20–26

Contents lists available at ScienceDirect

Journal of Molecular Spectroscopy

journal homepage: www.elsevier.com/locate/jms

Time-resolved Fourier transform emission spectroscopy of $A^2\Pi$–$X^2\Sigma^+$ infrared transition of the CN radical

S. Civiš [a,*], T. Šedivcová-Uhlíková [b], P. Kubelík [a], K. Kawaguchi [c]

[a] J. Heyrovský Institute of Physical Chemistry, Academy of Science of the Czech Republic, Dolejškova 3, 18223 Prague 8, Czech Republic
[b] Physics Department, University of Milano, Via Celoria 16-20133 Milano, Italy
[c] Department of Chemistry, Faculty of Science, Okayama University, Tsushima-naka, Okayama 700-8530, Japan

ARTICLE INFO

Article history:
Received 15 January 2008
In revised form 1 April 2008
Available online 11 April 2008

Keywords:
FT time-resolved spectroscopy
Radicals
Infrared emission spectrum
CN radical

ABSTRACT

The $A^2\Pi$–$X^2\Sigma^+\Delta v = -3$ bands of the $^{12}C^{14}N$ radical have been observed by time-resolved Fourier transform spectroscopy in the 1850–3100 cm^{-1} region with a wavenumber resolution of 0.025 cm^{-1}. The radical was produced in a pulsed positive column discharge in a cyanogene and helium mixture. Seven bands of $v = 0$–3, 1–4, 2–5, 3–6, 4–7, 5–8, and 6–9 were analyzed to give the molecular constants of each state by least-squares fitting of 801 lines. The pulsed discharge was found to be efficient for production of CN in the excited $A^2\Pi$ state. The vibrational excitation temperature was determined to be 6680 ± 835 K and 6757 ± 534 K for the $A^2\Pi$ and $X^2\Sigma^+$ states, respectively. The population of the $A^2\Pi$ was found to be 4% of that of the $X^2\Sigma^+$ state in the time after turning off the discharge.

© 2008 Elsevier Inc. All rights reserved.

1. Introduction

The CN free radical is observed in interstellar molecular clouds and the atmospheres of stars, planets and comets. It is also significant in numerous laboratory processes at high temperatures (flames, chemical reactions, discharges) where it is often formed from trace amounts of carbon and nitrogen. It is a very strong absorber/emitter of radiation and its spectra, extending from the vacuum UV far into the infrared without significant gaps, provide a very useful tool for its detection and monitoring. A vast proportion of the available spectral data arises from the $A^2\Pi$–$X^2\Sigma^+$ and $B^2\Sigma^+$–$X^2\Sigma^+$ electronic transitions [1,2] and the infrared transitions in the $X^2\Sigma^+$ ground electronic state [3,4]. In our previous paper [3], we concentrated primarily on the measuring and analysis of $^{12}C^{14}N$ vibration–rotation bands for the sequences $v = (1–0)$ through (9–8) which were observed in the spectral region 1800–2200 cm^{-1} with Fourier transform (FT) spectroscopy. From the point of view of the vibrational excitation, the most important information is obtained from vibronic data involving vibrational levels up to $v = 18$ [2]. Such high vibrational excitation corresponds to temperatures well above 45 000 K thus indicating the potential use of CN in high temperature monitoring and the possibility of experimental determination of the molecular potential energy function [3].

Cerny et al. [4] analyzed fourteen vibronic bands of the $\Delta v = 1, 0, -1, -2$ spread out in the near infrared spectral range with $v' = 0$–4 for $A^2\Pi$ electronic state. Kotlar et al. [5] carried out a pertubation analysis of data taken at the University of Berkeley, to give a deperturbed set of the constants for the $v = 0$–12 vibrational levels of the $A^2\Pi$ state. Prasad and Bernath [1] measured and analyzed the red system of CN by using a jet-cooled corona excited supersonic expansion in a spectral range of 16500–22760 cm^{-1}. They measured a total of 27 bands with $v' = 8$–21 for $A^2\Pi$ electronic state. Furio et al. [6] used the laser fluorescence excitation spectra for the measurement of the $B^2\Sigma^+$–$A^2\Pi$ ($v = 8,7$) band in the 20400 cm^{-1} spectral range and derived the constants for $v = 7$ of the $A^2\Pi$ state. Rehfuss et al. [7] used an FT spectrometer in the ultraviolet, visible and infrared region for a measurement of the CN spectrum. A total of 54 bands were observed throughout the red and infrared region from 16000 to 2500 cm^{-1}. The observed sequences include $\Delta v = +4, +3, +2, +1, 0, -1, -2$ and -3 with vibrational levels up to $v = 14$, where some sequences were not observed, due to small Franck-Condon factors and/or sensitivity of the spectrometer.

The 0–0 band of the $A^2\Pi$–$X^2\Sigma^+$ system appears at 9117 cm^{-1}. Since the vibrational frequency of CN is about 2042 and 1813 cm^{-1} in the $X^2\Sigma^+$ and $A^2\Pi$, respectively, the $\Delta v = -1, -2$ and -3 sequences occur near 7000, 5000 and 3000 cm^{-1}, respectively. In the region between 5000 and 2000 cm^{-1}, the vibronic transitions are rather unfavorable due to the Franck-Condon factors of 0.15–0.05 [1,8]. Furthermore one loses, compared with the 0–0 band, at least an additional factor of 20 due to the v^3 dependence in the Einstein A coefficient. Thus a high resolution vibronic CN spectrum with a good signal–to-noise ratio for the $\Delta v = 3$ sequence band region has not been reported until now. Only a low resolution spectrum was weakly observed by Rehfuss et al. [7].

* Corresponding author. Fax: +420 286591766.
E-mail address: civis@jh-inst.cas.cz (S. Civiš).

0022-2852/$ - see front matter © 2008 Elsevier Inc. All rights reserved.
doi:10.1016/j.jms.2008.04.002

There is still a gap for the high resolution measurement and detailed analysis of the spectral bands concerning $v = 5–6$ of the $A^2\Pi$ state. The turning point in the measurement of CN in the infrared spectral range was the introduction of time-resolved FT spectroscopy. This method makes it possible to distinguish the weak emission (or absorption) bands from strong bands appearing in the spectrum if the time-profiles are different. In the case of CN, weak vibronic bands in the 5 μm region were separated from strong long lived vibration–rotation bands. In this paper we report a spectroscopic analysis of 7 newly observed $\Delta v = -3$ sequences bands: 0–3, 1–4, 2–5, 3–6, 4–7, 5–8 and 6–9 of the $A^2\Pi–X^2\Sigma^+$ transition.

2. Experiment

The experimental arrangement and procedures were similar to those used in our previous studies of FT time-resolved measurements of molecular ions and radicals [9,10]. The parent compound $(CN)_2$ was entrained in an inert carrier gas (He) and entered in the 20 cm long positive column discharge tube with an inner diameter of 12 mm. The pulsed discharge was induced by a high voltage transistor switch HTS 81 (Behlke electronic GmbH, Frankfurt, Germany) between the stainless steel anode and grounded cathode. The plasma produced from the reaction mixture was cooled by flowing water in the outer jacket of the cell. The best conditions for the generation of CN were found to be p(He) = 3 Torr and 50 mTorr $(CN)_2$. The voltage drop across the discharge was 800 V, with a pulse width of 20 or 40 μs and 0.5 A peak-to-peak current. The scanner velocity of the FT spectrometer was set to produce a 10 kHz HeNe laser fringe frequency which was used to trigger the pulsed discharge. The recorded spectral range was 1800–4000 cm^{-1} with an optical filter, and a unapodized resolution of 0.07 or 0.025 cm^{-1}. The 32 scans were coadded so as to obtain a reasonable signal-to-noise ratio. The observed wavenumbers were calibrated using $^{12}C^{14}N$ ground state rotation-vibration lines [3] previously calibrated against the CO and CO_2 present in the spectra [11] as impurities.

3. Observed spectra and analysis

Fig. 1 shows a part of the time-resolved FT spectra of emission from a discharge in a $(CN)_2$ and He mixture, where the discharge pulse width was 20 μs. Thirty time-resolved spectra were obtained in one measurement with a time-interval of 3 μs, and 6 spectra are shown in Fig. 1. The variation in intensity of the vibrational bands in the $X^2\Sigma^+$ state is low. On the other hand, relaxation of electronic transitions is as fast as expected from a short radiative lifetime. The wavenumber resolution of Fig. 1 was 0.07 cm^{-1}, which was found to be insufficient for the analysis of the majority of the electronic transitions, because in the band-head region, the lines remained unresolved and the fit of the spectra was unsatisfactory.

In another time-resolved measurement we used a 0.025 cm^{-1} resolution with a long discharge pulse (40 μs) in order to reach

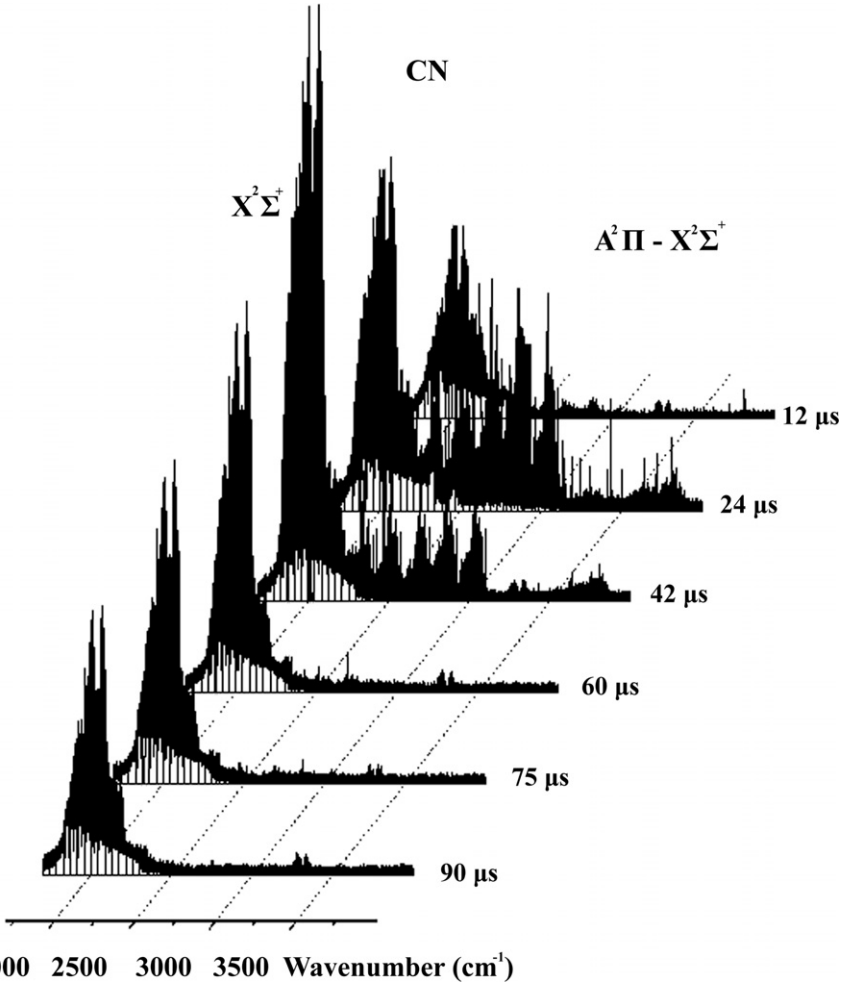

Fig. 1. The time-resolved emission FT spectrum from a pulsed discharge in a $(CN)_2$ and He mixture. The discharge pulse duration was 20 μs. The 30 time-resolved spectra were collected from $t = 0–90$ μs with a step of 3 μs. The spectra of C_2H_2 and C_2 were observed at 3300 and 3600 cm^{-1}.

the maximum excitation and to set the system into a "steady state". The data collection system was set using the offset time of 5 μs before the end of the pulse and the spectra were taken in 1 μs intervals. A series of experiments was carried out under this condition, while the basic parameters of the discharge, He pressure and discharge current were varied. A series of time-resolved FT spectra was measured in time-intervals of 1–30 μs, providing the time profile of CN relaxation from the $A^2\Pi$ state to the ground electronic state. The time-scale was short for the study of the relaxation of the vibration–rotation transitions in the ground electronic state, but is enough for observations of relaxation of atomic He, N, C lines, and the C_2 radical. From this vast complex spectra, the spectrum No. 15, as shown in Fig. 2, was chosen for the present spectroscopic analysis, which was obtained 10 μs after the end of the discharge. Although a detailed analysis of the dynamical behaviors of CN and other species will be given in a separate paper, Fig. 3 shows typical time-profiles of a vibration–rotation transition in the $X^2\Sigma^+$ state and a vibronic transition of CN, together with the

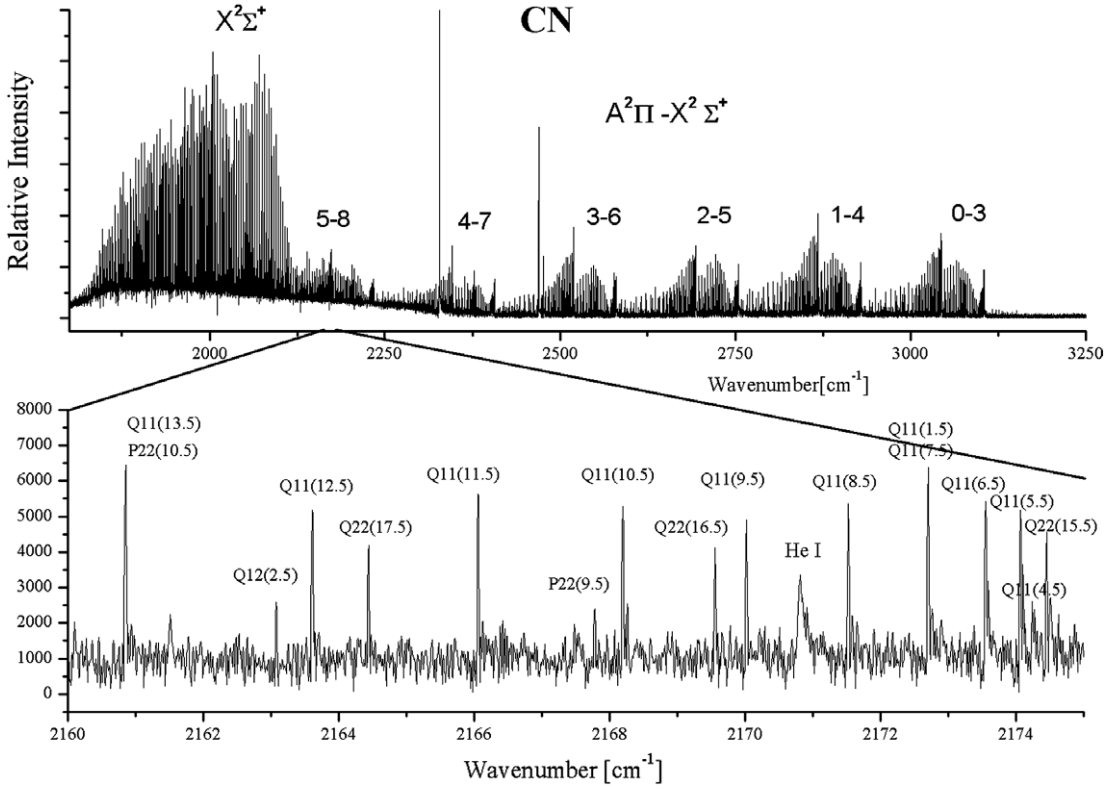

Fig. 2. The emission spectrum of the CN radical in the spectral range 3–5 μm. The overall view of the CN $A^2\Pi$- $X^2\Sigma^+ \Delta v = -3$ sequence with the 1–0 vibration–rotation band present with a band origin at 2042 cm^{-1} and the other hot bands.

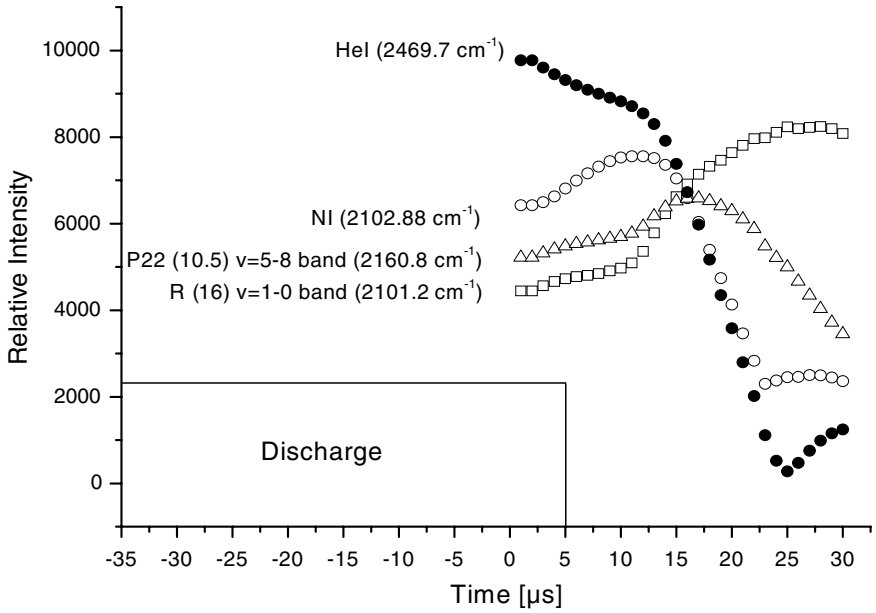

Fig. 3. Time-profiles of the He(I) atomic line, P_{22} (10.5) line of the A–X, 5–8 band and R(16) line of the 1–0 fundamental vibration–rotation band, and nitrogen atomic line. The discharge pulse was 40 μs long. The time-resolved spectra were collected after 35 μs (5 μs before the end of the discharge pulse) with a step of 1 μs.

Table 1
Observed transitions of the $A^2\Pi$ $v = 5 \rightarrow X^2\Sigma^+$ $v = 8$ and $A^2\Pi$ $v = 6 \rightarrow X^2\Sigma^+$ $v = 9$ bands of CN

Measured transitions of the $A^2\Pi \rightarrow X^2\Sigma^+$ Bands of CN											
v''	v'	Notation[a]	Obs. (cm^{-1})	Obs. − cal. (cm^{-1})	Weight	v''	v'	Notation[a]	Obs. (cm^{-1})	Obs. − cal. (cm^{-1})	Weight
8	5	$P_{11}(5.5)$	2156.743	0.001	0.1	8	5	$Q_{21}(6.5)$	2233.470	0.001	0.1
8	5	$P_{11}(6.5)$	2153.066	0.000	0.1	8	5	$Q_{21}(8.5)$	2234.173	−0.006	0.0
8	5	$P_{11}(8.5)$	2144.699	−0.003	0.1	8	5	$Q_{21}(9.5)$	2234.238	−0.006	0.0
8	5	$P_{11}(10.5)$	2135.019	−0.001	0.1	8	5	$Q_{21}(12.5)$	2233.221	0.003	0.1
8	5	$P_{11}(11.5)$	2129.692	−0.006	0.3	8	5	$Q_{21}(16.5)$	2228.846	−0.001	0.1
8	5	$P_{11}(12.5)$	2124.062	0.000	0.1	8	5	$Q_{22}(2.5)$	2219.357	0.002	0.1
8	5	$P_{11}(13.5)$	2118.117	0.002	0.1	8	5	$Q_{22}(3.5)$	2217.021	−0.001	0.1
8	5	$P_{11}(15.5)$	2105.311	0.001	0.1	8	5	$Q_{22}(4.5)$	2214.518	0.000	0.3
8	5	$P_{11}(16.5)$	2098.460	0.000	0.1	8	5	$Q_{22}(5.5)$	2211.838	0.000	0.3
8	5	$P_{11}(18.5)$	2083.883	0.001	0.1	8	5	$Q_{22}(6.5)$	2208.978	−0.001	0.3
8	5	$P_{11}(19.5)$	2076.163	0.002	0.1	8	5	$Q_{22}(7.5)$	2205.937	0.000	1.0
8	5	$P_{11}(20.5)$	2068.154	−0.001	0.1	8	5	$Q_{22}(8.5)$	2202.706	−0.002	1.0
8	5	$P_{12}(3.5)$	2149.089	0.001	0.1	8	5	$Q_{22}(9.5)$	2199.283	−0.001	1.0
8	5	$P_{12}(4.5)$	2142.623	0.012	0.3	8	5	$Q_{22}(10.5)$	2195.663	−0.001	1.0
8	5	$P_{12}(9.5)$	2105.125	−0.003	0.1	8	5	$Q_{22}(11.5)$	2191.842	0.000	1.0
8	5	$P_{21}(6.5)$	2211.801	0.002	0.1	8	5	$Q_{22}(12.5)$	2187.813	0.000	1.0
8	5	$P_{21}(12.5)$	2191.774	0.008	0.1	8	5	$Q_{22}(13.5)$	2183.577	0.003	1.0
8	5	$P_{21}(13.5)$	2187.730	−0.003	0.1	8	5	$Q_{22}(14.5)$	2179.122	0.001	0.3
8	5	$P_{22}(4.5)$	2199.558	0.004	0.1	8	5	$Q_{22}(15.5)$	2174.452	0.001	0.3
8	5	$P_{22}(5.5)$	2193.561	0.003	0.1	8	5	$Q_{22}(16.5)$	2169.561	0.002	0.3
8	5	$P_{22}(6.5)$	2187.388	0.003	0.1	8	5	$Q_{22}(17.5)$	2164.446	0.002	0.3
8	5	$P_{22}(7.5)$	2181.038	0.003	0.3	8	5	$Q_{22}(18.5)$	2159.105	0.003	0.1
8	5	$P_{22}(9.5)$	2167.783	0.004	0.1	8	5	$Q_{22}(19.5)$	2153.529	−0.003	0.3
8	5	$P_{22}(10.5)$	2160.860	−0.005	0.0	8	5	$Q_{22}(20.5)$	2147.726	−0.002	0.3
8	5	$P_{22}(11.5)$	2153.759	0.004	0.1	8	5	$Q_{22}(21.5)$	2141.692	−0.001	0.3
8	5	$P_{22}(12.5)$	2146.444	0.001	0.1	8	5	$R_{11}(1.5)$	2180.570	0.002	0.3
8	5	$P_{22}(13.5)$	2138.924	−0.001	0.1	8	5	$R_{11}(2.5)$	2184.579	−0.001	0.3
8	5	$P_{22}(14.5)$	2131.202	0.003	0.0	8	5	$R_{11}(3.5)$	2188.246	0.001	0.1
8	5	$P_{22}(15.5)$	2123.263	0.004	0.1	8	5	$R_{11}(4.5)$	2191.563	−0.001	0.3
8	5	$P_{22}(16.5)$	2115.106	0.003	0.1	8	5	$R_{11}(5.5)$	2194.545	0.001	0.3
8	5	$P_{22}(18.5)$	2098.132	0.001	0.1	8	5	$R_{11}(6.5)$	2197.184	−0.003	0.3
8	5	$P_{22}(21.5)$	2070.979	−0.002	0.1	8	5	$R_{11}(7.5)$	2199.496	−0.003	0.0
8	5	$Q_{11}(1.5)$	2172.706	0.004	0.3	8	5	$R_{11}(8.5)$	2201.482	−0.001	0.3
8	5	$Q_{11}(2.5)$	2173.555	−0.011	0.1	8	5	$R_{11}(9.5)$	2203.143	−0.002	0.3
8	5	$Q_{11}(3.5)$	2174.070	−0.009	0.1	8	5	$R_{11}(10.5)$	2204.488	−0.002	0.3
8	5	$Q_{11}(4.5)$	2174.248	0.002	0.1	8	5	$R_{11}(11.5)$	2205.521	0.000	0.3
8	5	$Q_{11}(5.5)$	2174.070	0.000	0.0	8	5	$R_{11}(12.5)$	2206.242	−0.002	0.1
8	5	$Q_{11}(6.5)$	2173.555	0.000	1.0	8	5	$R_{11}(13.5)$	2206.657	−0.002	0.1
8	5	$Q_{11}(7.5)$	2172.706	0.000	1.0	8	5	$R_{11}(14.5)$	2206.775	0.000	0.3
8	5	$Q_{11}(8.5)$	2171.529	0.001	1.0	8	5	$R_{11}(15.5)$	2206.591	0.000	0.3
8	5	$Q_{11}(9.5)$	2170.024	0.000	1.0	8	5	$R_{11}(16.5)$	2206.111	−0.001	0.1
8	5	$Q_{11}(10.5)$	2168.199	−0.002	1.0	8	5	$R_{11}(17.5)$	2205.338	−0.002	0.1
8	5	$Q_{11}(11.5)$	2166.065	0.001	1.0	8	5	$R_{11}(18.5)$	2204.273	−0.005	0.1
8	5	$Q_{11}(12.5)$	2163.616	0.001	1.0	8	5	$R_{11}(19.5)$	2202.926	−0.004	0.1
8	5	$Q_{11}(13.5)$	2160.860	0.000	1.0	8	5	$R_{11}(21.5)$	2199.376	−0.001	0.1
8	5	$Q_{11}(14.5)$	2157.804	0.001	1.0	8	5	$R_{11}(22.5)$	2197.184	0.006	0.3
8	5	$Q_{11}(15.5)$	2154.448	0.000	0.3	8	5	$R_{11}(23.5)$	2194.697	−0.001	0.1
8	5	$Q_{11}(16.5)$	2150.797	0.000	0.3	8	5	$R_{22}(3.5)$	2232.049	0.006	0.1
8	5	$Q_{11}(17.5)$	2146.852	−0.002	0.3	8	5	$R_{22}(4.5)$	2232.864	−0.002	0.1
8	5	$Q_{11}(18.5)$	2142.623	−0.001	0.3	8	5	$R_{22}(5.5)$	2233.509	0.001	0.1
8	5	$Q_{11}(19.5)$	2138.107	0.001	0.3	8	5	$R_{22}(6.5)$	2233.966	0.001	0.1
8	5	$Q_{11}(20.5)$	2133.305	0.000	0.3	8	5	$R_{22}(7.5)$	2234.238	0.007	0.0
8	5	$Q_{11}(21.5)$	2128.222	−0.001	0.3	8	5	$R_{22}(8.5)$	2234.303	0.002	0.1
8	5	$Q_{11}(22.5)$	2122.864	0.002	0.1	8	5	$R_{22}(9.5)$	2234.173	0.002	0.0
8	5	$Q_{11}(23.5)$	2117.225	0.001	0.1	8	5	$R_{22}(10.5)$	2233.840	0.003	0.3
8	5	$Q_{11}(24.5)$	2111.306	−0.004	0.1	8	5	$R_{22}(11.5)$	2233.297	0.003	0.3
8	5	$Q_{11}(25.5)$	2105.125	0.002	0.1	8	5	$R_{22}(12.5)$	2232.536	−0.001	0.0
8	5	$Q_{12}(2.5)$	2163.087	0.003	0.1	8	5	$R_{22}(13.5)$	2231.564	0.002	0.1
8	5	$Q_{12}(3.5)$	2160.106	0.001	0.1	8	5	$R_{22}(14.5)$	2230.370	0.003	0.3
8	5	$Q_{12}(4.5)$	2156.779	0.000	0.1	8	5	$R_{22}(15.5)$	2228.948	0.002	0.1
8	5	$Q_{21}(5.5)$	2232.833	0.000	0.1	8	5	$R_{22}(16.5)$	2227.297	−0.002	0.1
8	5	$R_{22}(18.5)$	2223.309	0.000	0.1	9	6	$Q_{21}(5.5)$	2061.542	−0.007	0.1
8	5	$R_{22}(22.5)$	2212.481	−0.009	0.1	9	6	$Q_{21}(6.5)$	2062.165	0.004	0.1
9	6	$P_{11}(8.5)$	1973.846	0.001	0.1	9	6	$Q_{21}(7.5)$	2062.587	−0.001	0.1
9	6	$P_{11}(9.5)$	1969.200	−0.006	0.1	9	6	$Q_{21}(9.5)$	2062.868	0.003	0.0
9	6	$P_{11}(10.5)$	1964.247	0.002	0.1	9	6	$Q_{21}(10.5)$	2062.704	−0.001	0.1
9	6	$P_{11}(11.5)$	1958.962	−0.003	0.1	9	6	$Q_{22}(4.5)$	2043.434	0.002	0.1
9	6	$P_{11}(12.5)$	1953.375	0.001	0.1	9	6	$Q_{22}(5.5)$	2040.765	−0.001	0.0
9	6	$P_{11}(13.5)$	1947.476	0.002	0.1	9	6	$Q_{22}(6.5)$	2037.913	−0.007	0.3
9	6	$P_{11}(14.5)$	1941.274	0.005	0.1	9	6	$Q_{22}(7.5)$	2034.894	0.005	0.3
9	6	$P_{11}(16.5)$	1927.962	−0.002	0.1	9	6	$Q_{22}(8.5)$	2031.666	−0.006	0.0
9	6	$P_{11}(17.5)$	1920.865	−0.006	0.1	9	6	$Q_{22}(9.5)$	2028.249	−0.011	0.1
9	6	$P_{11}(19.5)$	1905.822	0.001	0.1	9	6	$Q_{22}(10.5)$	2024.651	0.000	0.3
9	6	$P_{12}(3.5)$	1978.202	−0.006	0.1	9	6	$Q_{22}(11.5)$	2020.845	0.004	1.0

(*continued on next page*)

Table 1 (*continued*)

Measured transitions of the $A^2\Pi \rightarrow X^2\Sigma^+$ Bands of CN											
v''	v'	Notation[a]	Obs. (cm^{-1})	Obs. − cal. (cm^{-1})	Weight	v''	v'	Notation[a]	Obs. (cm^{-1})	Obs. − cal. (cm^{-1})	Weight
9	6	$P_{21}(6.5)$	2040.729	−0.001	0.1	9	6	$Q_{22}(12.5)$	2016.824	−0.002	0.1
9	6	$P_{21}(7.5)$	2037.874	−0.004	0.0	9	6	$Q_{22}(13.5)$	2012.598	−0.001	0.3
9	6	$P_{22}(3.5)$	2034.405	−0.006	0.1	9	6	$Q_{22}(14.5)$	2008.161	0.001	0.3
9	6	$P_{22}(5.5)$	2022.692	0.003	0.1	9	6	$Q_{22}(15.5)$	2003.503	0.000	0.3
9	6	$P_{22}(8.5)$	2003.776	−0.001	0.1	9	6	$Q_{22}(16.5)$	1998.624	−0.002	0.1
9	6	$P_{22}(9.5)$	1997.115	0.012	0.0	9	6	$Q_{22}(17.5)$	1993.523	−0.002	0.3
9	6	$P_{22}(10.5)$	1990.235	−0.002	0.1	9	6	$Q_{22}(19.5)$	1982.641	−0.004	0.1
9	6	$P_{22}(11.5)$	1983.173	0.000	0.1	9	6	$Q_{22}(22.5)$	1964.587	−0.003	0.1
9	6	$P_{22}(12.5)$	1975.909	0.000	0.1	9	6	$R_{11}(4.5)$	2020.243	0.004	0.1
9	6	$P_{22}(13.5)$	1968.441	0.002	0.1	9	6	$R_{11}(6.5)$	2025.793	0.002	0.1
9	6	$P_{22}(16.5)$	1944.761	−0.003	0.1	9	6	$R_{11}(7.5)$	2028.071	0.000	0.1
9	6	$P_{22}(17.5)$	1936.431	−0.008	0.0	9	6	$R_{11}(8.5)$	2030.025	0.001	0.3
9	6	$Q_{11}(2.5)$	2002.445	0.009	0.0	9	6	$R_{11}(9.5)$	2031.666	0.007	0.3
9	6	$Q_{11}(4.5)$	2003.103	−0.001	0.1	9	6	$R_{11}(11.5)$	2033.982	0.000	0.1
9	6	$Q_{11}(5.5)$	2002.931	0.006	0.0	9	6	$R_{11}(12.5)$	2034.675	−0.004	0.1
9	6	$Q_{11}(6.5)$	2002.410	0.000	0.3	9	6	$R_{11}(14.5)$	2035.156	−0.009	0.0
9	6	$Q_{11}(7.5)$	2001.561	−0.002	0.0	9	6	$R_{11}(15.5)$	2034.962	0.002	0.1
9	6	$Q_{11}(8.5)$	2000.388	0.000	0.3	9	6	$R_{11}(16.5)$	2034.459	−0.002	0.3
9	6	$Q_{11}(9.5)$	1998.893	0.002	1.0	9	6	$R_{11}(17.5)$	2033.667	−0.003	0.1
9	6	$Q_{11}(10.5)$	1997.079	0.003	0.1	9	6	$R_{11}(18.5)$	2032.593	0.002	0.1
9	6	$Q_{11}(11.5)$	1994.952	0.004	0.1	9	6	$R_{11}(21.5)$	2027.638	−0.001	0.1
9	6	$Q_{11}(12.5)$	1992.507	−0.002	1.0	9	6	$R_{12}(1.5)$	2002.445	−0.005	0.0
9	6	$Q_{11}(13.5)$	1989.766	−0.001	0.3	9	6	$R_{12}(5.5)$	2002.445	−0.001	0.0
9	6	$Q_{11}(14.5)$	1986.723	0.000	1.0	9	6	$R_{12}(7.5)$	2000.434	−0.002	0.1
9	6	$Q_{11}(15.5)$	1983.379	−0.003	1.0	9	6	$R_{12}(8.5)$	1998.940	−0.004	0.0
9	6	$Q_{11}(16.5)$	1979.748	0.000	1.0	9	6	$R_{12}(10.5)$	1995.014	0.003	0.1
9	6	$Q_{11}(17.5)$	1975.822	−0.001	0.1	9	6	$R_{22}(5.5)$	2062.200	0.002	0.3
9	6	$Q_{11}(18.5)$	1971.613	0.003	0.1	9	6	$R_{22}(6.5)$	2062.632	0.002	0.1
9	6	$Q_{11}(19.5)$	1967.118	0.006	0.1	9	6	$R_{22}(7.5)$	2062.868	−0.004	0.0
9	6	$Q_{11}(20.5)$	1962.337	0.007	0.3	9	6	$R_{22}(8.5)$	2062.920	0.002	0.0
9	6	$Q_{12}(3.5)$	1989.108	−0.002	0.3	9	6	$R_{22}(9.5)$	2062.766	0.001	0.1
9	6	$Q_{12}(4.5)$	1985.816	0.002	0.1	9	6	$R_{22}(10.5)$	2062.409	0.003	0.1
9	6	$Q_{12}(5.5)$	1982.182	0.003	0.1	9	6	$R_{22}(11.5)$	2061.837	−0.001	0.1
9	6	$Q_{12}(6.5)$	1978.202	−0.006	0.1	9	6	$R_{22}(13.5)$	2060.065	0.005	0.1
9	6	$Q_{21}(4.5)$	2060.744	−0.011	0.1						

The weights used in the fit were set according to the signal-noise ratio (SNR) as follows:
for band $v = 5–8$
SNR $\geqslant 5$ weight = 1
$5 >$ SNR $\geqslant 3$ weight = 0.3
$3 >$ SNR $\geqslant 2$ weight = 0.1
for band $v = 6–9$
SNR $\geqslant 4$ weight = 1
$4 >$ SNR $\geqslant 3$ weight = 0.3
$3 >$ SNR $\geqslant 2$ weight = 0.1
Overlapped lines and lines with SNR < 2 were weighted with 0 or removed from the fit.

[a] The transitions are labeled with the notation where P, Q and R have conventional meaning, subscripts 1 and 2 denote spin components F_1 and F_2, respectively, and the number in parentheses is J in the $X^2\Sigma^+$ state.

atomic lines. The lifetime of the $A^2\Pi$–$X^2\Sigma^+$ transition is an order of 10 μs. However, the vibrational relaxation of CN in its ground state is significantly longer; even at a time of 25 μs after the discharge, the intensity of the vibrational fundamental band is still rising. The intensity of the He atomic line (2469.7 cm^{-1}) shows a fast decay, and lines of C and N atoms also relax with a speed comparable with atomic helium.

The rotational assignments of the vibronic $A^2\Pi$–$X^2\Sigma^+$: 0–3, 1–4, 2–5, 3–6, 4–7 bands were carried out according to the transition frequency calculations using molecular constants reported by Cerny et al. [4]. The $v = 5–8$ and 6–9 bands were assigned by molecular constants from Kotlar et al. [5] who reported Dunham parameters. Relatively weak Q_{12}, Q_{21}, R_{12}, R_{21}, P_{21}, P_{12} transitions were also assigned in the spectra, where subscripts 1 and 2 denote spin components F_1 and F_2, respectively. The assigned transition frequencies are listed in Table 1 for the $v = 5–8$ and $v = 6–9$ bands and other bands are given in the Appendix, which is deposited at the Journal web site.

All the line positions have been fitted to the so-called $\mathbf{R}^2$ Hamiltonian[12] for the $A^2\Pi$ state, which was used by Cerny et al. [4] and Kotlar et al. [5]. It is noted that Prasad and Bernath [1] used $\mathbf{N}^2$ Hamiltonian, and a conversion formula [13] is necessary for comparison purposes.

In a least-squares analysis, the molecular constants for the $X^2\Sigma^+$ ground state were fixed to those obtained by Ram et al. [2], where all available data for the $X^2\Sigma^+$ state were analyzed simultaneously. The molecular constants determined in the present study are listed in Table 2. The differences between the observed and calculated frequencies using the molecular constants of Table 2 are listed in the fifth column of Table 1. The standard deviation of the fitting was 0.0009 cm^{-1}.

4. Discussion

The time-resolved experiment itself was carried out in a wide range of time-scales and with various discharge pulse lengths, thus enabling a complex study of the relaxation processes of the CN system in helium. Such a pulsed discharge gives a stronger emission for the $\Delta v = -3$ bands, compared with that of a DC discharge. In the present study we observed emission from the $v = 5$ and 6 vibrational levels of the $A^2\Pi$ state for the first time. The molecular constants for the $v = 0–4$ vibrational levels of the $A^2\Pi$ state are

Table 2
Molecular constants in the CN $A^2\Pi$ state determined in the present study, and comparison with the previous results[a]

v		B	$D \times 10^5$	A	$\gamma \times 10^2$	$p \times 10^2$	$q \times 10^3$	E[b]
0	This work	1.7073240(67)	0.6138(14)	−52.6527(11)	0.043(10)	0.7997(87)	−0.3893(47)	9117.38522(63)
	Cerny et al.[c]	1.7073145(43)	0.61497(13)	−52.65010(68)		0.8409(42)	−0.38961(52)	9117.39268(35)
	Kotlar et al.[d]	1.707265(10)	0.61323(31)	−52.6503(24)	0.718	0.842(5)	−0.3892(13)	9117.3960(58)
1	This work	1.6900552(35)	0.61586(55)	−52.58005(79)	0.0461(68)	0.7965(57)	−0.4006(23)	10905.09623(45)
	Cerny et al.	1.6900415(44)	0.61613(13)	−52.57602(98)		0.8400(34)	−0.39772(95)	10905.10365(53)
	Kotlar et al.	1.689991(13)	0.61417(35)	−52.5817(39)	0.705	0.855(14)	−0.3994(30)	10905.106(17)
2	This work	1.6727354(51)	0.61685(91)	−52.50384(86)	0.0461(81)	0.7852(65)	−0.3995(32)	12667.23408(56)
	Cerny et al.	1.6727238(49)	0.61746(18)	−52.50026(194)		0.8347(58)	−0.4084(21)	12667.24425(105)
	Kotlar et al.	1.672664(21)	0.61534(42)	−52.5131(61)	0.692	0.845(14)	−0.4070(44)	12667.245(41)
3	This work	1.6553646(70)	0.6172(12)	−52.4279(12)	0.043(10)	0.7776(98)	−0.4105(49)	14403.79203(69)
	Cerny et al.	1.6553535(100)	0.61877(66)	−52.4289(54)		0.858(25)	−0.4160(56)	14403.8029(31)
	Kotlar et al.	1.655285(35)	0.61675(53)	−52.4445(85)	0.679	0.920(49)	−0.4065(100)	14403.800(82)
4	This work	1.6379343(71)	0.6165(12)	−52.3538(14)	0.076(11)	0.763(11)	−0.4146(45)	16114.75768(78)
	Cerny et al.	1.637902(29)	0.6166(22)	−52.3705(155)		0.759(34)	−0.4112(69)	16114.7716(96)
	Kotlar et al.	1.637852(53)	0.61841(66)	−52.376(11)	0.666	0.751(55)	−0.4104(105)	16114.76(15)
5	This work	1.6204664(59)	0.6148(11)	−52.28462(94)	0.1046(94)	0.7491(74)	−0.4274(34)	17800.11813(71)
	Kotlar et al.	1.620366(75)	0.62031(81)	−52.307(14)	0.653	0.751(30)	−0.4032(47)	17800.10(25)
6	This work	1.603009(11)	0.6229(25)	−52.2461(18)	0.265(18)	0.775(14)	−0.4625(63)	19459.8615(11)
	Kotlar et al.	1.60283(10)	0.62245(99)	−52.239(17)	0.640	0.744(52)	−0.4069(93)	19459.81(40)

[a] cm^{-1} unit. Numbers in parentheses denote one standard deviation and are applied to the last digits of the constants.
[b] Measured from $v = 0$ of $X^2\Sigma^+$, where the ground state vibrational energies are taken from Ram et al. [2].
[c] Ref. [4].
[d] Ref. [5].

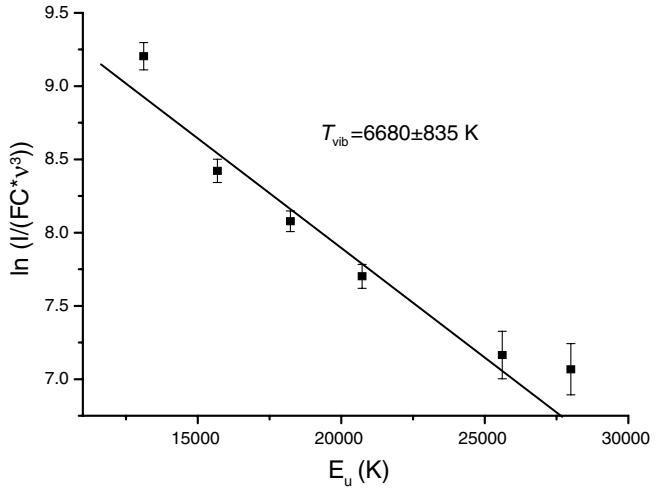

Fig. 4. The estimation of the vibrational temperature of the $A^2\Pi$ from the 6 vibronic bands. The $v = 4$–7 band was excluded from the fit due to CO_2 absorption in the same spectral region.

compared with those of Cerny et al. [4] as listed in Table 2, where in their analysis A_J instead of γ in our present analysis is used as a parameter and higher-order parameters p_J, q_J, and q_{JJ} are also included for $v = 0$–3. The presently determined γ values are different from those of Kotlar et al.[5], presumably due to a fact that they carried out deperturbed analysis including the interaction between A and X states. When we used the A_J parameters for $v = 0$–4, we obtained similar values as Cerny et al.[4]. The parameters of $v = 5$ and 6 are slightly different from those calculated from the Dunham parameters of Kotlar et al. [5]. The difference may also be due to the interaction between A and X states which is not considered in the present analysis.

The Franck-Condon factors for the $A^2\Pi$–$X^2\Sigma^+$ transitions are reported to be 0.0179, 0.0554, 0.106, 0.161, 0.211, and 0.248 for the 0–3, 1–4, 2–5, 3–6, 4–7, and 5–8 bands [1]. By considering the frequency factors in addition to the Franck-Condon factors, the observed intensity of each band was plotted against the energy value of the upper state of the transition, as shown in Fig. 4, to give a vibrational temperature of 6680 ± 835 K for the $A^2\Pi$. The value does not change significantly after 10 μs, because the vibrational relaxation is not fast. Similarly the vibrational temperature is found to be 6757 ± 534 K for the $X^2\Sigma^+$. Using the vibrational temperatures, we estimated the abundance of the $A^2\Pi$ to be 4% of that of the $X^2\Sigma^+$ in the time just after the turning off the discharge, where a vibrational transition moment of 0.052 Debye [14] and electronic band strength R_{00}^2 $(ea_0)^2 = 0.0511$ [15] were used ($e^2a_0^2 = 6.460 \times 10^{-36} cm^2 esu^2$). The abundance ratio corresponds to an effective temperature of 4100 K between the two electronic states.

Acknowledgments

This work is a part of the research programs of the Grant Agency of the Academy of Sciences of the Czech Republic (Grant No. IAA400400705) and ESF program INTROP. The present study was partially supported by a Grant-in-Aid from the Ministry of Education, Culture, Sports, Science and Technology of Japan (Grant No. 18350010).

Appendix A. Supplementary data

Supplementary data for this article are available on ScienceDirect (www.sciencedirect.com) and as part of the Ohio State University Molecular Spectroscopy Archives (http://msa.lib.ohio-state.edu/jmsa_hp.htm). Supplementary data associated with this article can be found, in the online version, at doi:10.1016/j.jms.2008.04.002.

References

[1] C.V.V. Prasad, P.F. Bernath, J. Mol. Spectrosc. 156 (1992) 327–340.
[2] R.S. Ram, S.P. Davis, L. Wallace, R. Egleman, D.R.T. Appadoo, P.F. Bernath, J. Mol. Spectrosc. 237 (2006) 225–231.
[3] V. Horká, S. Civiš, V. Špirko, K. Kawaguchi, Collect. Czech. Chem. Commun. 69 (2004) 73–89.
[4] D. Cerny, R. Bacis, G. Guelachvili, F. Roux, J. Mol. Spectrosc. 73 (1978) 154–167.
[5] A.J. Kotlar, R.W. Field, J. Steinfeld, J.A. Coxon, J. Mol. Spectrosc. 80 (1980) 86–108.
[6] N. Furio, A. Ali, P.J. Dagdigian, J. Mol. Spectrosc. 134 (1989) 199–213.
[7] B.D. Rehfuss, M.H. Suh, T.A. Miller, V. Bondybey, J. Mol. Spectrosc. 151 (1992) 437–458.
[8] C.M. Sharp, Astron. Astrophys. Suppl. Ser. 55 (1984) 33–50.

[9] S. Civiš, P. Kubát, K. Kawaguchi, Chem. Phys. Lett. 418 (2006) 448–453.
[10] Y. Hosaki, S. Civiš, K. Kawaguchi, Chem. Phys. Lett. 383 (2004) 256–260.
[11] G. Guelachvili, K.N. Rao, Handbook of Infrared Standards, Academic Press, New York, 1986.
[12] R.N. Zare, A.L. Schmeltekopf, W.J. Harrop, D.L. Albritton, J. Mol. Spectrosc. 46 (1973) 37–66.
[13] C. Amiot, J.-P. Maillard, J. Chauville, J. Mol. Spectrosc. 87 (1981) 196–218.
[14] E. Kagi, K. Kawaguchi, Molecular Structure Symposium, Tokyo, 1994.
[15] A.N. Cox (Ed.), Allen's Astrophysical Quantities, Springer, 2000, p. 90.

THE JOURNAL OF PHYSICAL CHEMISTRY A

ARTICLE

pubs.acs.org/JPCA

HNC/HCN Ratio in Acetonitrile, Formamide, and BrCN Discharge

Martin Ferus,[†,‡] Petr Kubelík,[†,‡] Kentarou Kawaguchi,[§] Kseniya Dryahina,[†] Patrik Španěl,[†] and Svatopluk Civiš*[,†]

[†]J. Heyrovský Institute of Physical Chemistry, Academy of Sciences of the Czech Republic, Dolejškova 3, 18223 Prague 8, Czech Republic

[‡]Institute of Physics, Czech Academy of Sciences, Na Slovance 2, 182 21 Prague 8, Czech Republic

[§]Faculty of Science, Okayama University, Tsushima-naka, Okayama 700-8530, Japan

ABSTRACT: Time-resolved Fourier transform (FT) spectrometry was used to study the dynamics of radical reactions forming the HCN and HNC isomers in pulsed glow discharges through vapors of BrCN, acetonitrile (CH_3CN), and formamide ($HCONH_2$). Stable gaseous products of discharge chemistry were analyzed by selected ion flow tube mass spectrometry (SIFT-MS). Ratios of concentrations of the HNC/HCN isomers obtained using known transition dipole moments of rovibrational cold bands ν_1 were found to be in the range 2.2−3%. A kinetic model was used to assess the roles the radical chemistry and ion chemistry play in the formation of these two isomers. Exclusion of the radical reactions from the model resulted in a value of the HNC/HCN ratio 2 orders of magnitude lower than the experimental results, thus confirming their dominant role. The major process responsible for the formation of the HNC isomer is the reaction of the HCN isomer with the H atoms. The rate constant determined using the kinetic model from the present data for this reaction is 1.13 (±0.2) × 10^{-13} cm^3 s^{-1}.

I. INTRODUCTION

A. HNC/HCN Ratio in Astronomically Observed Environments. HNC is a metastable isomer of hydrogen cyanide. Its origin and the mechanisms of its formation in interstellar space are still not entirely understood. The HNC isomer was first detected by radio-astronomical observations of the center of the Milky Way in the constellation of Sagittarius (dense molecular cloud Sgr B2) by Snyder and Buhl[1] in 1971. Its existence has since been proven in other environments, including cold, dense molecular clouds,[2] diffuse clouds,[3] cool carbon stars,[4] comets, and planetary atmospheres.[5]

The abundance of HNC in these various environments varies significantly. In cold molecular clouds (e.g., TMC-1, which has a temperature around 10 K), the HNC/HCN ratio[6] is around 1.55. In warmer or hot regions (e.g., OMC-1, a region of high mass star formation,[7] and hot core regions with temperatures around 200 K; a circumstellar envelope of red giant stars[8] with temperatures of 2800 K), the values range from 10^{-3} to 0.2. All of these observations reveal that temperature plays a key role in high HNC/HCN ratios.

The $HCNH^+$ ion, which has been observed by millimeter wave spectroscopy,[9] has been implicated in the formation of HNC and HCN in interstellar clouds. $HCNH^+$ ions are formed in a sequence of reactions initiated by proton donors ionized by cosmic rays, with a general formula XH^+ (e.g., H_3^+, CH^+, NH^+, H_3O^+, HCO^+) and with HCN according to the equation:[10]

$$XH^+ + HCN \rightarrow HCNH^+ + X \qquad (1)$$

or in reactions of ions with certain molecules and radicals, e.g.,

$$C^+ + NH_3 \rightarrow H_2NC^+ \text{ or } HCNH^+ \qquad (2)$$

$$N^+ + CH_3 \rightarrow HCNH^+ + H \qquad (3)$$

The H_2NC^+ isomer also can be transformed to $HCNH^+$ by the absorption of radiation:

$$H_2NC^+ + h\nu \rightarrow HCNH^+ \qquad (4)$$

Finally, the dissociative recombination of the molecular ion[11−13] $HCNH^+$

$$HCNH^+ + e^- \rightarrow HNC/HCN + H \qquad (5)$$

is considered to be the main process for the production of both HNC and HCN, with a branching ratio[14] close to 1:1, thus forming both HNC and HCN in approximately equal amounts, which explains the observational data in cold clouds.

Another possible source of HNC/HCN in interstellar clouds apart from reactions 1−5 is the neutral−neutral radical reactions.[15] According to Talbi et al.,[16] one example of such reactions is

$$C + NH_2 \rightarrow HNC + H \qquad k_{300} = 6.8 \times 10^{-11}\ cm^3\ s^{-1} \qquad (6)$$

Received: November 11, 2010
Revised: January 5, 2011
Published: February 23, 2011

ACS Publications © 2011 American Chemical Society

The authors, however, state that any considerable contribution from these reactions is disputable because of what is known of rate constants at low temperatures and the possible isomerization of HNC to HCN due to excitation by the energy released in exothermic reaction.

HNC can also be produced by photochemical processes, for example, in cometary comae, as illustrated by observations of comet Hale-Bopp.[17,18] During Hale-Bopp's approach toward the Sun, the observed HNC/HCN ratio grew from 0.02 to 0.2.

It is supposed that the exchange reaction of suprathermal hydrogen atoms between HCN and HNC plays an important role in the cometary comae. The suprathermal hydrogen atoms originate from the photoinduced decay of H-containing species[19] and both isomers are formed:

$$\mathrm{HCN} + \mathrm{H} \rightarrow \mathrm{HNC} + \mathrm{H} \quad (7)$$

$$\mathrm{HNC} + \mathrm{H} \rightarrow \mathrm{HCN} + \mathrm{H} \quad (8)$$

Sumathi and Nguyen et al.[20] and Talbi et al.[21] have given the following values for the rate constants: $k_7 = 5.6 \times 10^{-15}$ cm^3 s^{-1} for the forward reaction 7 and $k_8 = 5 \times 10^{-12}$ cm^3 s^{-1} for the reverse reaction 8. The activation barrier of reaction 7 was determined to be 17.8 kcal/mol (0.77 eV) for the forward reaction and 4.2 kcal/mol (0.18 eV) for the reverse reaction.[22] It was found that the HNC/HCN equilibrium obtained via reaction 7 is an important factor affecting the chemistry of cometary comae;[23] however, it is not the only mechanism of HNC production, and it does not always fully explain the observed HNC/HCN ratios. For this reason, it is assumed that HNC could also be directly the decay product of an unknown parent compound.

B. Laboratory Detection of HNC. In the laboratory, HNC was first observed in an argon matrix in the mid-infrared spectral range (600−4000 cm^{-1}) by Milligan and Jacox,[24] and more comprehensive measurements were obtained by Burkholder[25] or Mellau.[26] As HNC cannot be distinguished by mass from its isomer, HCN, spectroscopy is the only applicable method for the detection of this molecule, apart from collision-induced dissociative ionization measurements.[27] Deuterated isotopologues DNC and DCN have also been detected in space[28] and studied in the laboratory.[27]

In addition to the above-mentioned low-temperature mechanisms, which are typical for interstellar clouds, the simple heating[29] of HCN can be used to measure the highly resolved spectra of gaseous HNC while the spontaneous isomerization of HCN into HNC occurs. The potential energy barrier separating the two species is 50.5 kcal/mol (2.19 eV), while the energy of HNC is higher than the energy of HCN[30] by 11 kcal/mol (0.47 eV). According to the theoretical calculation of the partition function, as presented by Tennyson,[31] extremely high temperatures are necessary to reach a higher HNC/HCN ratio. The equilibrium constant of plain isomerization

$$\mathrm{HC{\equiv}N} \rightleftharpoons {}^{-}\mathrm{C{\equiv}}\overset{+}{\mathrm{H}}\mathrm{N} \quad (9)$$

under 1400 K is less than 1%. It is assumed that it is actually this thermal isomerization of HCN into HNC in reaction 9 that plays the main role in cool carbon stars, which have inner atmosphere temperatures of several thousand K.[32]

HNC/HCN can also be observed in discharges,[33,34] e.g., in the mixture of CH_4/N_2 or acetonitrile/Ar or by the reaction of translationally excited H atoms with CN containing molecules (e.g., BrCN, ClCN, ICN). These atoms have been generated by

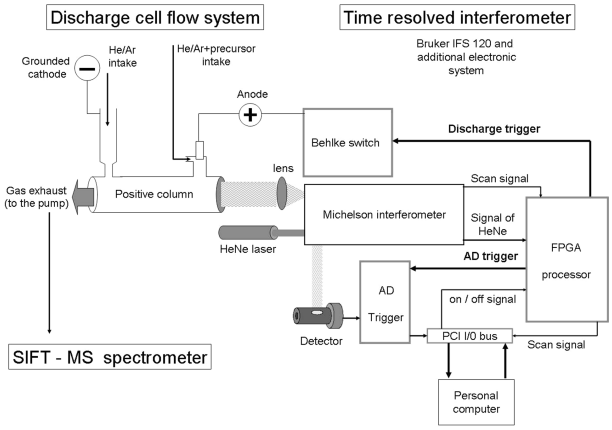

Figure 1. Schematic diagram of the experimental apparatus.

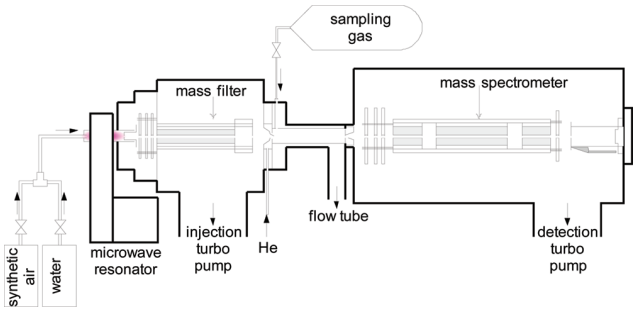

Figure 2. Schematic diagram of the SIFT-MS spectrometer.

the photolysis[35] of CH_3SH (248 nm) or directly by breaking down the parent compounds with excimer laser radiation.[36] Hydrogen reacts with the parent compound in the following way:

$$\mathrm{H} + \mathrm{BrCN} \rightarrow \mathrm{HNC} + \mathrm{Br} \quad \sigma = 1.45 \times 10^{-16}\ \mathrm{cm}^2 \quad (10)$$

$$\mathrm{H} + \mathrm{BrCN} \rightarrow \mathrm{HCN} + \mathrm{Br} \quad \sigma = 2.21 \times 10^{-17}\ \mathrm{cm}^2 \quad (11)$$

$$\mathrm{H} + \mathrm{BrCN} \rightarrow \mathrm{HBr} + \mathrm{CN} \quad \sigma = 2.89 \times 10^{-18}\ \mathrm{cm}^2 \quad (12)$$

where σ is the total reaction cross section. These reaction profiles were studied in a photolytic experiment by Macdonald,[37,38] who estimated the ratio of the total reaction cross section (0.85/0.13/0.017) and the total cross section (1.7×10^{-16} cm^2). Brupbacher et al.[88] estimated the branching ratio between (11) and (12) to be 1:1. The ratios of the reaction cross sections preferring the formation of HNC were also found. However, these ratios contradicted the thermodynamics data because, according to the theoretical prediction made by Song et al.,[39] the activation barriers of reactions 10 and 11 are 24.4 kcal/mol (1.05 eV) and 4.6 kcal/mol (0.19 eV), respectively. Therefore, the formation of HCN is favorable from an energetic point of view. Other studies have indicated that the reaction channel 10 leading to the formation of HNC is less important. For example, Arunan et al.,[40] using a flowing afterglow technique, found that the branching ratio between reactions 10 and 11 is 1:3 in favor of HCN. Arunan, however, in opposition to the theoretical assumptions,[39] determined the activation barrier of reaction 9

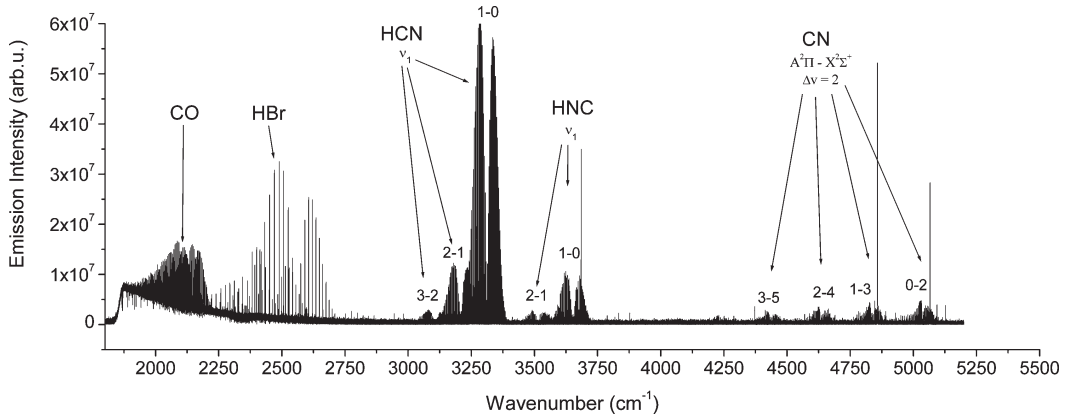

Figure 3. Emission spectrum of the BrCN + H_2 discharge (10 μs after the discharge pulse).

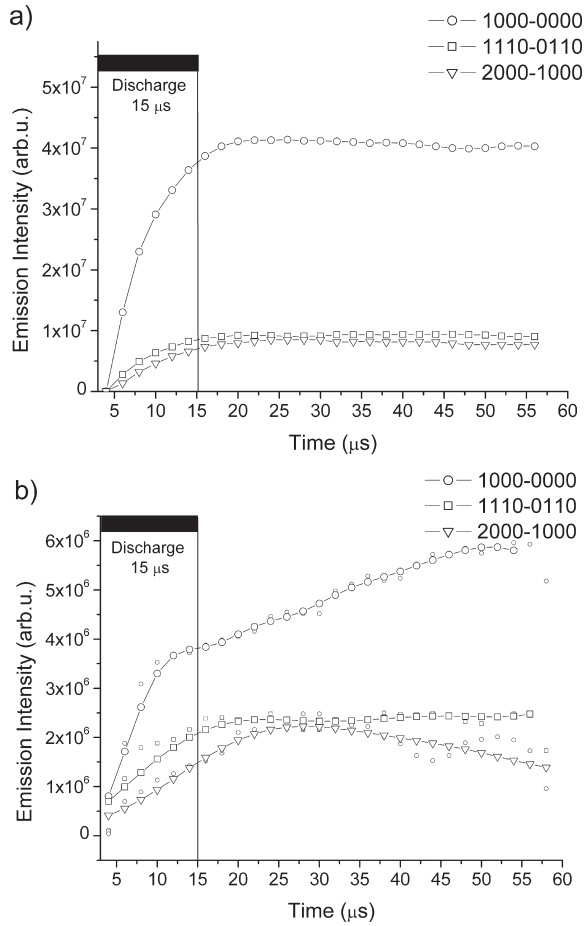

Figure 4. Time dependence of intensity profiles of HCN (a) and HNC (b) bands in the BrCN + H_2 discharge.

to be 7.8 kcal/mol (0.34 eV). The activation barrier of reaction 12 was determined[42] to be 14.1 kcal/mol (0.61 eV).

HNC has been identified as a minor product in reactions of the CN radical with hydrocarbons. Copeland et al.[41] found that the rate constants of HCN formation from hydrocarbons have values of approximately 10^{-11} cm^3 s^{-1}, but the overall emission intensity of HNC in the observed region (3425−3825 cm^{-1}) reaches only 1% of the emission intensity of HCN.

HNC has also been observed in an Ar matrix during the breakdown of formamide,[42] diazomethane,[43] and a mixture of hydrogen azide HN_3 with CO.

Precursors related to stellar and interstellar chemistry were chosen in our work. Acetonitrile was first found in space[44] in 1971 in a molecular cloud near Sgr A and Sgr B, and in 1974, it was identified in the comet Kohoutek.[45] As in the case of BrCN, acetonitrile is a simple compound, and its decay produces the CN radical. Formamide, which does not contain the CN group, was also detected[46] in Sgr A and Sgr B in 1971. In 2000, formamide was identified in comet Hale-Bopp.[47] The problematic origin of biomolecules from simple compounds is widespread,[48] and formamide is regarded as one of the possible precursors of nucleic bases.[49] The chemistry of formamide's decay is, therefore, important for understanding the mechanism of the origin of nucleic bases.

II. EXPERIMENTAL SECTION

A. Experimental Setup. The experimental setup is shown in Figure 1. A 25-cm-long positive column discharge tube with an inner diameter of 12 mm was placed in front of the interferometer window in emission configuration. The radiation was focused using a CaF_2 lens. The ac glow discharge was maintained by an HTS 81 high voltage transistor switch (Behlke electronic GmbH, Frankfurt, Germany), which was applied between the stainless steel anode and the grounded cathode. The voltage drop across the discharge was 1200 V, with a pulse width of 15 μs (BrCN) or 22 μs (CH_3CN, $HCONH_2$) and a peak-to-peak current of 0.5 A. The pressure was measured using a Baratron gauge.

An InSb detector was used at a spectral range of 1800−4000 cm^{-1} or 2000−6000 cm^{-1} with Ge interference optical filters at an unapodized resolution of 0.05 cm^{-1}. Fifty scans were averaged to obtain a reasonable signal-to-noise ratio. Synchronization of the data acquisition (AD trigger) and the discharge (discharge trigger) was provided by a FPGA processor. The system was driven by a HeNe laser interference signal (Bruker 120 IFS spectrometer) with frequencies of 5 or 10 kHz.

The stable gas phase products were analyzed using a SIFT-MS technique.

B. Continuous Scanning Time-Resolved FT Spectroscopy. Time-resolved FT spectroscopy is a wide-spectrum technique used for studying the dynamics of chemical reactions or the

Table 1. List of All Compounds Detected in the Emission Spectra (Upper Part of the Table) Using FTIR and in the Mass Spectra Using SIFT-MS (Bottom Part of the Table)[a]

	system			
compound	acetonitrile	formamide	BrCN	note
		Spectral Data, 0.6 A Peak-to-Peak Current Discharges (1.2 kV)		
HCN	2.5×10^7	1.1×10^8	1.4×10^8	max band intensity (arb units) − ν_1
HNC	3.0×10^6	1.7×10^7	2.0×10^7	max band intensity (arb units) − ν_1
HNC/HCN	2.80%	2.20%	3.00%	
CO		s		ν_1 band
CO_2		s		ν_3 band
N_2	not observed	s	not observed	electronic transition, see ref 86
CH		w		$^2\Pi^-$ ground state
NH		w		$X^3\Sigma^-$ ground state
CN	s	s	s	$X^2\Sigma$ band $\Delta\nu = 1$
CN	s	s	s	$A^2\Pi - X^2\Sigma$ band $\Delta\nu = 2$
CN	s	s	s	$A^2\Pi - X^2\Sigma$ band $\Delta\nu = 3$
C	s	s	s	atomic lines
H	s	s	s	atomic lines
N	s	s	s	atomic lines
H	s	s	s	atomic lines
		SIFT Data, 0.6 A Peak-to-Peak Current Discharges (1.2 kV)		
HNC/HCN	671	3562		
C_2H_2		147		
CH_4	56	897		
HCHO		21	not measured	signal in arb units
NO		21		
CH_3OH		9		
$(CH_3)_2CO$		7		

[a] The emission intensity of HNC/HCN is expressed in arbitrary units; in the case of other species, w means weak intensity and s means strong intensity.

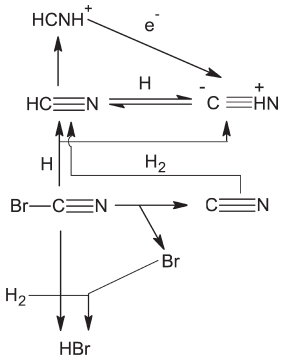

Figure 5. Scheme of the BrCN decomposition.

dynamic properties of molecules, radicals, and ions in liquid, gas, and solid states.[50] The time-resolved continuous scanning principle was the basis for the data acquisition, which was conducted using a modified Bruker IFS 120 spectrometer in our laboratory at the J. Heyrovsky Institute of Physical Chemistry, and a similarly modified spectrometer was used in Okayama, Japan. The principle of the used method has been described in detail in previous papers.[51,52]

The data acquisition system can be described as follows: The position of the traversing mirror of the Michelson interferometer was detected by reading the interference maxima of the HeNe laser emission. The input signal in a cosine function shape was digitally processed into rectangular pulses, and it became the internal standard of the interferometer. The frequency of these rectangular pulses depends on the mirror speed. In the classic measurement mode, the frequency is usually 10 kHz with a pulse duration of 100 μs. An external processor monitors the beginning of the HeNe laser digital pulse, its order, and the zero position of the mirror. During one pulse, the signal from the detector is read (30 or up to 64 readings), which is the so-called AD trigger. A discharge pulse of variable length can be arbitrarily inserted into the data acquisition process (AD trigger). This process results in 30−64 reciprocally time-shifted spectra.

C. Selected Ion Flow Tube Mass Spectrometry. Selected ion flow tube mass spectrometry (SIFT-MS; see Figure 2) is a technique that allows the quantification of trace amounts of gases and vapors present in air. SIFT-MS is based on chemical ionization using reagent ions H_3O^+, O_2^+, and NO^+. These ions do not react with the major components of air, but they selectively ionize trace amounts of other gases and vapors. Absolute quantification is achieved on the basis of a well-defined reaction time, during which chemical ionization takes place in the helium carrier gas flowing through a flow tube into which the reagent ions are injected and the sample is introduced at a known flow rate. In this study, we used SIFT-MS to analyze stable compounds produced during the decomposition of formamide and acetonitrile in a discharge pulse. Only qualitative analysis is possible under glow discharge conditions due to the highly complicated composition and possible ion

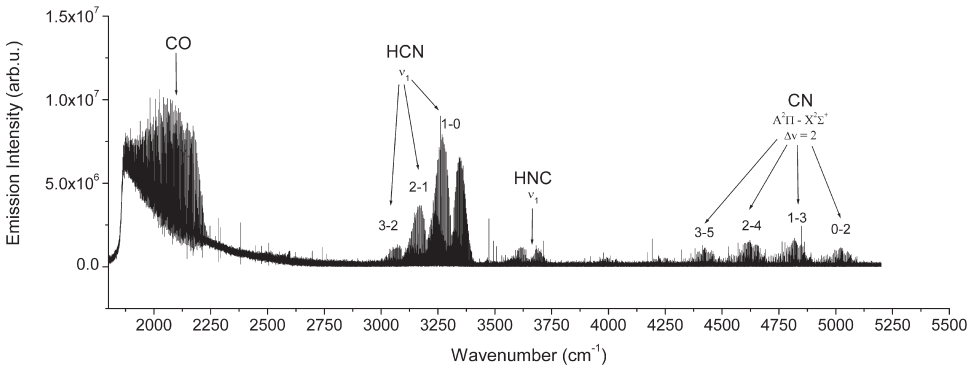

Figure 6. Emission spectrum of the acetonitrile discharge (10 μs after the discharge pulse).

chemical reactions of the products in the flow tube. SIFT-MS has been used to study trace gases in various biological systems[53] and gases produced in controlled combustion.[54]

III. RESULTS AND DISCUSSION

A. The BrCN/H_2 Discharge. The emission spectrum of the mixture of 0.5 mbar BrCN, 0.5 mbar H_2, and 2 mbar He discharge is shown in Figure 3. The HCN and HNC emission profiles (integrated intensity of the band) detected in the discharge are shown in Figure 4. The following species were detected: HBr, HCN, HNC, and CN, atomic lines of Br, C, and N, and the emission spectrum of CO (presented as an impurity). A summary of the emission bands of the identified species is given in Table 1. A summary of the other identified species, which were characteristic for the individual types of discharge, including the detection results from the SIFT-MS method for the individual systems, is also given in Table 1.

The reaction pathways of BrCN decomposition proposed on the basis of a search of the literature are shown in Figure 5. During the 15 μs discharge and 15 μs into the afterglow in the BrCN/He + H_2 mixture, collisions with electrons cause the excitation and dissociation of the hydrogen molecules into H atoms:

$$H_2 + e^- \rightarrow 2H + e^- \qquad (13)$$

as well as the direct dissociation of the BrCN precursor following the equation

$$BrCN + e^- \rightarrow CN + Br + e^- \qquad (14)$$

The process of Penning ionization[55,56] occurring in discharges in carrier gases with high ionization energies also produces energetic electrons in reactions involving metastable atoms with molecules M. The energy of such Penning electron is between the ionization energy of the collision partner and the energy of the excited rare gas atom (e.g., He ≈ 20 eV):

$$He^* + M \rightarrow He + M^+ + e^- \qquad (15)$$

The energetic electrons contribute to the dissociation of the precursor molecules. The dissociation energy of the Br−CN bond is 3.69 eV. In the case of the collision with atomic hydrogen, and analogous to the photolytic experiment, some contributions from reactions 10−12 can be taken into account in addition to the mechanism of direct dissociation via (13) and (14).

The emissions of the atomic species of H, Br, and He reach their maxima at the time of the termination of the discharge (15 μs), and they are followed by the emission maximum of the $A^2\Pi-X^2\Sigma$ CN band.

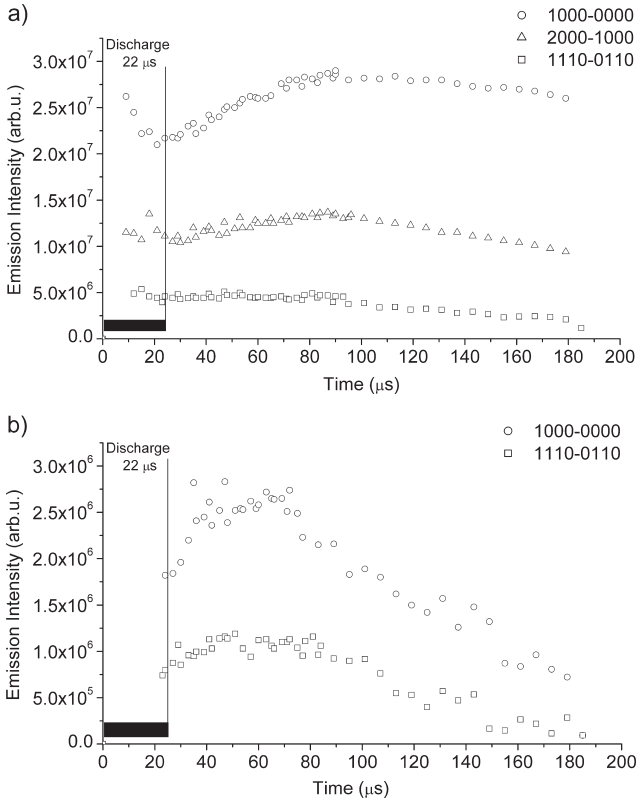

Figure 7. Time dependence of intensity profiles of HCN (a) and HNC (b) bands in the CH_3CN discharge.

The maximum emission of HNC ν_1 − GS (GS = ground state) is reached within 40−50 μs, but the excited $2\nu_1 - \nu_1$ band reaches its maximum immediately after the discharge pulse. The HCN maximum occurs around 25 μs.

The reverse decay of hydrogen cyanide into the CN radical[57] and molecular hydrogen is a reaction with a low rate constant:

$$H + HCN \rightarrow H_2 + CN \quad k_{500} = 1.07 \times 10^{-20}\ cm^3\ s^{-1} \qquad (16)$$

The produced CN radical can react with the precursor molecule according to the equation[58]

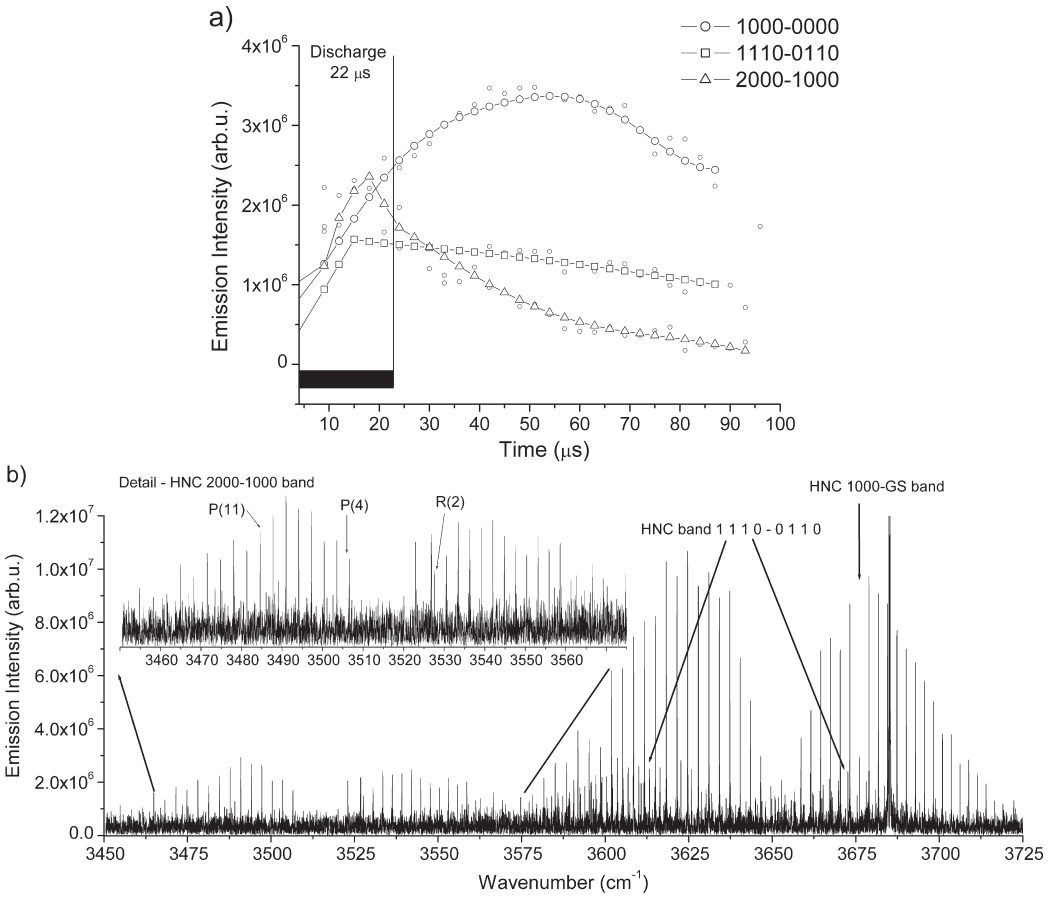

Figure 8. Time dependence of intensity profiles of HNC (a) bands in the $CH_3CN + H_2$ together with details of the $2\nu_1 - \nu_1$ band 10 μs after the discharge pulse (b).

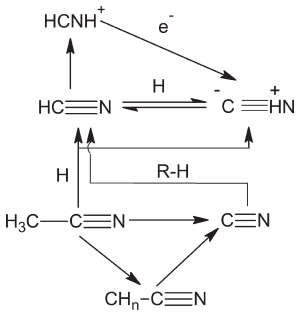

Figure 9. Scheme of the CH_3CN decomposition.

$$CN + BrCN \rightarrow (CN)_2 + Br \qquad k_{500} = 2.1 \times 10^{-15}\ cm^3\ s^{-1} \tag{17}$$

However, $(CN)_2$ was detected neither in the discharge nor in its products. Due also to the low rate constant when compared to the H + CN reaction and the fast dissociation of BrCN, this reaction can be neglected. We assume that the equilibrium is also affected by reactions of HCN and HNC with the hydrogen radical according to eqs 7 and 8.

B. The CH_3CN Discharge. HCN and HNC as well as CN, H, N, and C radicals were identified in the emission spectra of a discharge in 0.5 mbar acetonitrile and 2.5 mbar He/Ar. In some cases 0.5−1.5 mbar of H_2 have been used. Using the SIFT-MS method, HCN and methane were found to be the most abundant in the discharge products. The emission spectrum is shown in Figure 6. The time progression of the HNC and HCN formation is shown in Figure 7. The addition of 0.5 mbar hydrogen led to an increase in the emission intensity of both HNC and HCN, while a clearly visible HNC $2\nu_1 - \nu_1$ band was also found. The time progression in comparison to the other HNC and HCN transitions is shown in Figure 8. A summary of the identified species and their emission bands is given in Table 1.

The reaction diagram of acetonitrile decomposition, drawn on the basis of a search of the literature, is shown in Figure 9. During 22 μs of the discharge and 15 μs into its afterglow, acetonitrile is dissociated by a collision with a fast electron, and species H and C as well as the CN radical are produced. The CN emission spectrum was observed at 25 μs, i.e., 3 μs after the discharge termination, as it was the case in the BrCN/He + H_2 discharge. The acetonitrile dissociation process is described by the following equation:

$$CH_3CN + e^- \rightarrow CN + \text{other products} + e^- \qquad \sigma_{(8\,eV)} = 1 \times 10^{-20}\ cm^2 \tag{18}$$

The reaction cross section given with eq 18 is valid for acetonitrile dissociation in an electron beam resulting in CN^- and CH_3, as stated by Märk et al.[59] The dissociation of only a single hydrogen from the molecule producing CH_2CN has a reaction cross section of $\sigma_{(3.5\,eV)} = 4 \times 10^{-19}\ cm^2$. Märk et al. found that the ratios of

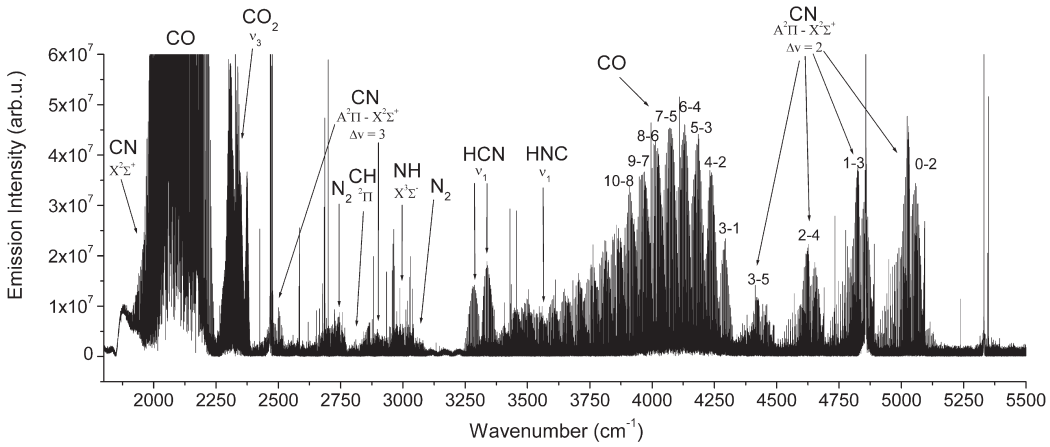

Figure 10. Emission spectrum of the formamide discharge (10 μs after the discharge pulse).

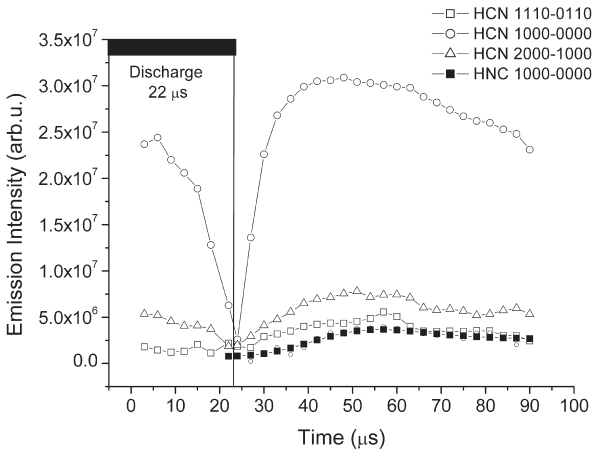

Figure 11. Time dependence of intensity profiles of HCN and HNC bands in the formamide discharge.

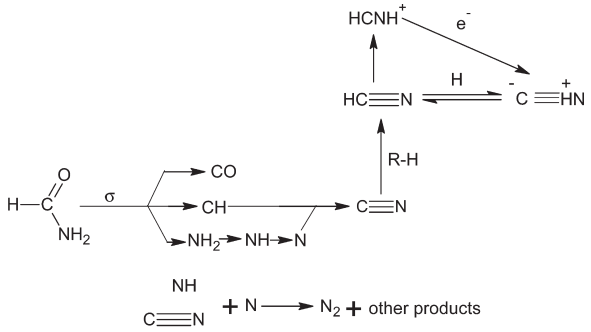

Figure 12. Scheme of the formamide decomposition.

reaction cross sections for the products are 2000:35:7:50 for CH_2CN^-, $CHCN^-$, CCN^-, and CN^-, respectively. With regard to these conclusions, it can be assumed that reaction 18 is composed of the following partial dissociation reactions:

$$CH_nCN \rightarrow CH_{n-1}CN + H \qquad (19)$$

while the last step is the split into atomic carbon and the CN radical

$$CCN \rightarrow C + CN \qquad (20)$$

The CH_3, CH_2, and CH radicals are, therefore, produced in smaller concentrations than CN. Neither the CH_3, CH_2, and CH nor the C−CN species were detected in the emission spectra. This fact, explained in the conclusion of our paper, deals with the decomposition of methane in a glow discharge.

The emission lines of CH, C_2, and molecular hydrogen were detected in the observed spectra. It was found that the CH radical is produced by the dehydrogenation of the parent compound, that is, in the same way as we expected in the case of the elimination of CN from CH_3CN. This process is generally described by the equation

$$CH_n \rightarrow CH_{n-1} + H \qquad (21)$$

We found that only the CH radical was present in a detectable concentration. We therefore assume that the mechanism is the same as in the case of CH_3CN and the CN radical. The results of the SIFT-MS method of measuring the product composition also showed that the main reaction product is HCN (about 80 %) and not hydrocarbons.

Analogous to the case of BrCN and reaction 12, we could assume that CN is also produced in the reaction of hydrogen radicals with the parent compound according to the equation[60]

$$CH_3CN + H \rightarrow CH_4 + CN \qquad k_{550} = 1.09 \times 10^{-14}\ cm^3\ s^{-1} \qquad (22)$$

Note that reactions similar to 10 and 11 leading to the formation of HNC/HCN + CH_3 are possible, but no accurate information regarding their rates is available.

C. The $HCONH_2$ Discharge. The discharge in formamide is chemically different from the discharges in compounds like BrCN and CH_3CN, which contain the CN group. In the case of formamide dissociation, the CN radical is a product of subsequent reactions. The study of formamide decomposition is, therefore, important as a reference experiment. For this reason, the formamide dissociation is mentioned in the presented article, although its exact mechanism, and a comparison with the dissociation by UV ArF laser, will be described in detail in a separate work.[61]

The following species were identified in the emission spectra of the discharge in formamide (Figure 10): molecular nitrogen, CO, CO_2; CN, CH, and NH radicals, HNC, HCN, and the atomic lines of C, N, O, and H. The HNC and HCN emission progression is shown in Figure 11. Among the species identified in the discharge products by the SIFT-MS method were HCN, acetylene, methane, formaldehyde, nitrous oxide, and methanol. Some species, such as carbon monoxide or dinitrogen oxide,

could not be detected due to their low reactivity with the ions used in the SIFT-MS method. Spectral analysis is an important counterpart of this type of mass detection.

The reaction mechanism of the formamide decomposition composed on the basis of a search of the available literature is summarized in Figure 12. The major primary dissociation channel is known to be[62]

$$HCONH_2 + e^- \rightarrow HCO + NH_2 + e^- \qquad (23)$$

This reaction was studied at 193 nm in an Ar matrix by Fourier transform IR spectroscopy,[44] and HCO was identified as the main product. In the discharge, the mentioned dissociation by the collision with a fast electron takes place again during the 22 μs discharge period and in the afterglow. The HCO radical is dissociated (the dissociation energy is 0.68 eV), producing CO, which is a stable product (dissociation energy 11.14 eV).

The species with general formula NH_n (n = 1, 2, 3) are dehydrogenated in the glow discharge

$$NH_n + e^- \rightarrow NH_{n-1} + H + e^- \qquad (24)$$

and subsequently, CN is formed in the reaction of CH with atomic nitrogen:[63]

$$HC + N \rightarrow CN + H \qquad k_{500} = 1.58 \times 10^{-10}\ cm^3\ s^{-1} \qquad (25)$$

The reaction of the reverse formation of NH has a significantly lower rate constant than in the CN formation:[64]

$$CH + N \rightarrow NH + C \qquad k_{500} = 1.58 \times 10^{-12}\ cm^3\ s^{-1} \qquad (26)$$

Molecular nitrogen N_2 was detected exclusively in the spectra of formamide; it was not detected in the experiments with acetonitrile or BrCN. We assume that, in this system, N_2 is produced in the reaction of atomic nitrogen with NH and CN according to the following equations:[65,66]

$$NH + N \rightarrow N_2 + H \qquad k_{500} = 2.49 \times 10^{-11}\ cm^3\ s^{-1} \qquad (27)$$

$$CN + N \rightarrow N_2 + C \qquad k_{500} = 1.12 \times 10^{-11}\ cm^3\ s^{-1} \qquad (28)$$

The absence of molecular nitrogen in the acetonitrile and BrCN spectra can be explained by the large dissociation energy of the CN radical (6.11 eV), so that CN, instead of dissociation, more probably enters a reaction, producing stable HNC/HCN. In contrast, the formamide molecule is dissociated into NH_2 and NH, i.e., species with lower dissociation energies (3.29 and 3.27 eV, respectively). NH_2 and NH subsequently break down and produce reactive atomic nitrogen. This atomic nitrogen reacts with these radicals in reverse according to eqs 25, 27, and 28, producing molecular nitrogen or CN.

The CN radical in the formamide/Ar discharge subsequently reacts with molecules containing hydrogen (HCO, NH_n), e.g.,

$$HCO + CN \rightarrow HCN + CO \qquad (29)$$

producing hydrogen cyanide as the product of this discharge.

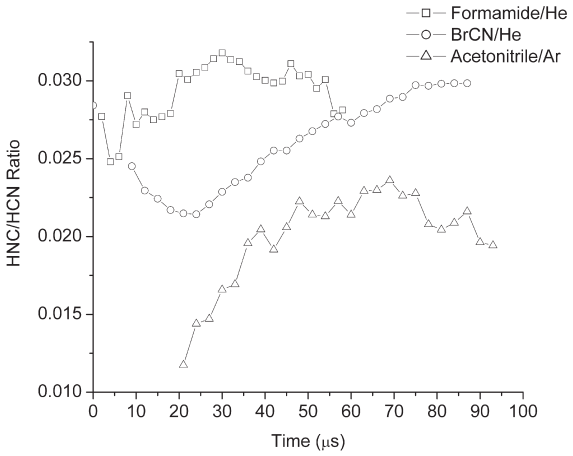

Figure 13. Time dependence of HNC/HCN ratios in formamide, BrCN, and acetonitrile.

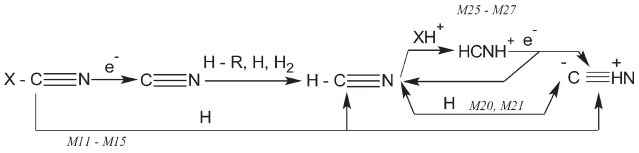

Figure 14. Proposed scheme of the HNC formation in the glow discharge. M is related to the chemical equation in the model. The precursor (general formula X−CN) is dissociated to the CN radical. The second possibility is a reaction with the atomic hydrogen. The CN radical reacts with hydrogen containing species (R−H) or hydrogen, and HNC/HCN is formed. HCN reacts with H to HNC or it is protonated to $HCNH^+$, which forms HNC by the dissociation recombination with the electron.

D. Determining the Ratios of HNC/HCN and the Mechanism of HNC Formation. Knowledge of the transition moment or the band strength of a particular molecule provides information on its quantitative abundance. The transition dipole moment of the HCN band ν_1 is 0.083 D, and the transition dipole moment of the HNC band[67] ν_1 is 0.156 D. According to Tennyson et al.,[68] the equation for the intensity of the band using common SI units can be written as

$$S_{ji} = \frac{2\pi^2 N_A \nu_{ji}}{3hc\varepsilon_0}\left[1 - \exp\left(\frac{-hc\nu_{ji}}{kT}\right)\right] \cdot |\langle j|\mu|i\rangle|^2 \qquad (30)$$

where N_A is Avogadro's number, ν_{ji} is the frequency of the transition, h is the Planck constant, c is the speed of light, ε_0 is the permittivity of the vacuum, $|\langle j|\mu|i\rangle|$ is the transition dipole moment, and T is the thermodynamic temperature. The factor in square brackets in eq 30 is the population difference between the two vibrational states i and j. This factor gives rise to induced emission and is very close to unity for the temperature typical for the glow discharge (approximately 500−600 K). After substitution and conversion of the dipole moment to the Debye units (1 D = 3.336 × 10^{-30} Cm) and the wavenumber to cm^{-1}, this equation can be enumerated as follows:

$$S_{ji} = 2.5066379 \cdot 10^5 \cdot \nu_{ji} \cdot |\langle j|\mu|i\rangle|^2 \qquad (31)$$

The intensity of the HCN band ν_1 calculated from eq 31 is S_{HCN} = 5.78 × 10^6 cm/mol, which conforms to the data from the literature. The intensity of S_{HNC} = 2.27 × 10^7 cm/mol was

Table 2. Reactions Used in the Model of HNC/HCN Chemistry

reaction type	no.	reaction	threshold energy (eV)	remark
electron impact dissociation	M0	$BrCN + e^- \rightarrow Br + CN + e^-$	3.30	predicted using eq 37
	M1	$CH_3CN + e^- \rightarrow CH_3 + CN + e^-$	5.30	
	M2	$CH_3CN + e^- \rightarrow H + CH_2CN + e^-$	3.12	
	M3	$CH_2CN + e^- \rightarrow CHCN + H + e^-$	3.12	
	M4	$CHCN + e^- \rightarrow CCN + H + e^-$	3.12	
	M5	$CCN + e^- \rightarrow C + CN + e^-$	6.29	
	M6	$HCN + e^- \rightarrow H + CN + e^-$	5.41	
	M7	$HNC + e^- \rightarrow H + CN + e^-$	4.92	
	M8	$H_2 + e^- \rightarrow H + H + e^-$	4.17	
	M9	$D_2 + e^- \rightarrow D + D + e^-$	4.55	

reaction type	no.	reaction	rate constant ($cm^3 \cdot s^{-1}$)	remark
HCN channels	M10	$H_2 + CN \rightarrow HCN + H$	5.38×10^{-13}	ref 87
	M11	$BrCN + H \rightarrow Br + HCN$	1.02×10^{-12}	estimated using ref 88
	M14	$CH_3CN + H \rightarrow HCN + CH_3$	1.36×10^{-14}	ref 62
	M16	$CN + CH_3CN \rightarrow HCN + CH_2CN$	3.01×10^{-12}	estimated using ref 89
	M17	$CN + CH_2CN \rightarrow HCN + CHCN$	1.00×10^{-13}	
	M18	$CN + CHCN \rightarrow HCN + CCN$	1.00×10^{-13}	
	M19	$CN + HBr \rightarrow HCN + Br$	3.74×10^{-12}	ref 78
	M20	$HNC + H \rightarrow HCN + H$	5.00×10^{-12}	refs 21 and 22
	M22	$M + CN + H \rightarrow HCN + M$	7.19×10^{-31}	ref 90
	M48	$CH_4 + CN \rightarrow CH_3 + HCN$	4.17×10^{-12}	ref 91
	M49	$CH_3 + CN \rightarrow CH_2 + HCN$	4.17×10^{-12}	estimated using ref 91
	M50	$CH_2 + CN \rightarrow CH + HCN$	4.17×10^{-12}	
	M51	$CH + CN \rightarrow C + HCN$	4.17×10^{-12}	
	M56	$CCN + H \rightarrow CH + HCN$	1.36×10^{-14}	estimated using ref 87
HNC channels	M12	$BrCN + H \rightarrow Br + HNC$	3.33×10^{-13}	refs 42 and 88
	M21	$HCN + H \rightarrow HNC\ (v' = 2) + H$	9.28×10^{-14}	fitted using refs 20−22
	D1	$HNC\ (v' = 2) + M = HNC\ (v'' = 1) + M^*$	1.15×10^{-11}	fitted
	D2	$HNC\ (v' = 1) + M = HNC\ (GS) + M^*$	2.2×10^{-12}	fitted
	M15	$CH_3CN + H \rightarrow HNC + CH_3$	4.53×10^{-15}	estimated using refs 42 and 88
	M23	$M + CN + H \rightarrow HNC + M$	7.19×10^{-32}	ref 92
ionic chemistry	M24	$HCN + MH^+ \rightarrow HCNH^+ + M$	7.41×10^{-09}	ref 81
	M25	$HCNH^+ + e^- \rightarrow HNC + H$	1.18×10^{-07}	
	M26	$HCNH^+ + e^- \rightarrow HCN + H$	1.18×10^{-07}	
	M27	$HCNH^+ + e^- \rightarrow CN + H + H$	1.13×10^{-07}	
other reactions	M53	$CH_3CN + H \rightarrow CH_4 + CN$	1.36×10^{-14}	ref 62
	M54	$CH_2CN + H \rightarrow CH_3 + CN$	1.09×10^{-14}	estimated using ref 62
	M55	$CHCN + H \rightarrow CH_2 + CN$	1.09×10^{-14}	estimated using ref 62
	M57	$CH_2CN + H \rightarrow CH_3CN$	1.60×10^{-10}	estimated using ref 62
	M58	$CHCN + H \rightarrow CH_2CN$	1.60×10^{-10}	estimated using ref 62
	M59	$CCN + H \rightarrow CHCN$	1.60×10^{-10}	estimated using ref 62
	M61	$Br + H_2 \rightarrow HBr + H$	1.20×10^{-18}	ref 93
	M52	$M + CH_3 + H \rightarrow CH_4 + M$	2.13×10^{-29}	ref 94
	M13	$BrCN + H \rightarrow HBr + CN$	1.02×10^{-12}	estimated using refs 39, 40, and 87

found[69] for the same band of HNC. The HCN absorption band ν_1 is, therefore, about 4 times weaker than the band of HNC. Equation 30 can be expressed using a formalism based on the Einstein coefficient A_{ji} instead of the transition dipole moment

$$A_{ij} = \frac{16\pi^3 {\nu_0}^3}{3\varepsilon_0 h} \cdot |\langle j|\mu|i\rangle|^2 \qquad (32)$$

and we obtain the equation

$$S_{ji} = \frac{A_{ij} \cdot N_A}{8\pi c {\nu_{ji}}^2}\left[1 - \exp\left(\frac{-hc\nu_0}{kT}\right)\right] \qquad (33)$$

For the observed HNC band ν_1, the Einstein coefficient of A_{ij} = 370 s^{-1} can be calculated from the dipole moment. The obtained value of the Einstein coeffcient of HCN was[69] 77.2 s^{-1}. The

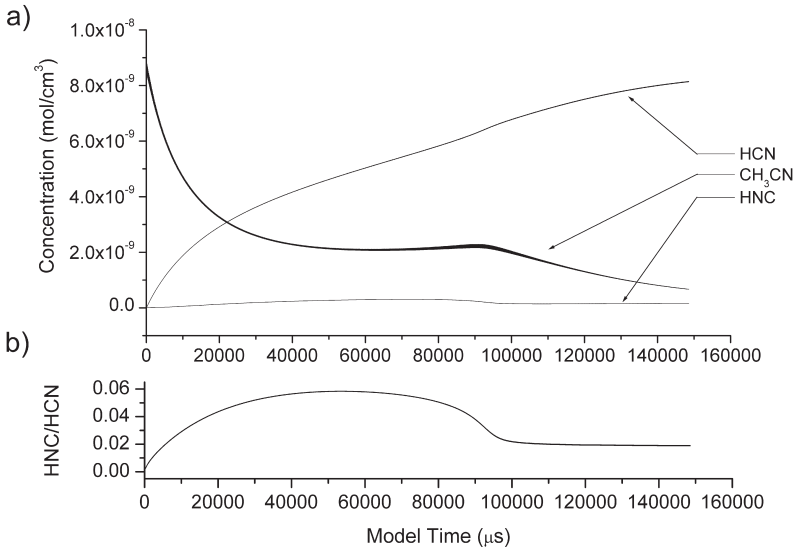

Figure 15. Concentration of HCN, HNC, and the precursor molecule estimated using the model (a). HNC/HCN ratio predicted by the model (b). After 1000 pulses, an equilibrium concentration of about 2% HNC/HCN is reached.

emission spectrum of HNC is stronger in comparison with the spectra of HCN; therefore, it can be easily detected despite relatively lower concentrations.

If we consider the reverse absorption of the emitted radiation to be negligible, the calculated Einstein coefficients of the spontaneous emission of the ν_1 cold band transitions for HNC and HCN can be used to correct the HNC emission spectrum strength and calculate the HNC/HCN ratio in the afterglow of the studied systems. The rotational temperature of the discharge at 550 K determined by the Boltzmann plot showed that, during the afterglow, the system was in thermal equilibrium.

The intensity of spontaneous emission is directly proportional to the population of the excited state of the particular species. Therefore, with regard to the detector response to an emission quantum with the energy of $h\nu_0$, the quantitative ratio in thermal equilibrium can be written in the following way:

$$\frac{[\mathrm{HNC}]}{[\mathrm{HCN}]} \approx \frac{I(\mathrm{HNC})}{I(\mathrm{HCN})} \cdot \frac{A_{ij}(\mathrm{HCN}) \cdot \nu_0(\mathrm{HCN})}{A_{ij}(\mathrm{HNC}) \cdot \nu_0(\mathrm{HNC})} \approx \frac{I(\mathrm{HNC})}{I(\mathrm{HCN})} \cdot \frac{1}{5.26} \quad (34)$$

where I is the emission intensity of the band, A_{ij} is the Einstein coefficient of spontaneous emission, and ν_0 is the band origin in wavenumber of the observed bands.

To obtain the band intensity, 56 lines in the HCN and HNC spectra were assigned and integrated in a C++ program. The intensity was subsequently corrected using the Einstein A_{ij} coefficient, and the HNC/HCN ratio was determined.

The time-resolved development of the HNC/HCN ratio in the afterglow of the studied systems is shown in Figure 13. The highest ratio, HNC/HCN ≈ 3.0%, was found in the discharge in the mixture of formamide and He. In the discharge in BrCN/He, the ratio was found to be HNC/HCN ≈ 2.8%, and in the acetonitrile/Ar system, the ratio was found to be HNC/HCN ≈ 2.2%. Although the individual systems had different precursors, the HNC/HCN ratios were always close to 3%. We assume this result indicates that the mechanisms of HNC/HCN production are similar, regardless of the discharge type. This ratio is unlikely to result from thermal chemical equilibrium via reaction, because the HNC abundance calculated for the temperature of 550 K, typical for a glow discharge, is only[33] 6×10^{-4} %.

Comparing the reaction mechanisms found on the basis of a search of the literature, we found that numerous reactions take place in all systems. The simplified pathway of HNC/HCN formation is shown in Figure 14. It is a key objective of the kinetic model of the processes occurring in the experimentally studied gas discharges that will be discussed in the following section to identify the dominant reaction channels with respect to the formation of HNC.

E. Kinetic Model of HNC/HCN Hydrogen Chemistry. A kinetic model of the BrCN and acetonitrile HNC/HCN discharge and afterglow was designed on the basis of the reactions listed in Table 2 to provide a description of the radical and hydrogen chemistry and to explain the observed emission time profiles and HNC/HCN ratio. The model focuses on the radical chemistry because no ions were directly observed.

The key features of the model are summarized in the following points:

- The numerical model was implemented in the Python 2.6.4 programming language. The decrease of calculation speed caused by the interpreted nature of Python was partially compensated by using modules Numpy[70] and Scipy[71] for the acceleration of numerical algorithms.
- The model was constructed without spatial dimensions as a so-called zero-dimensional model describing only the time evolution of the concentrations. This type of model is appropriate for data originating from the homogeneous region of the positive column of a glow discharge.
- A set of ordinary differential equations constructed according to the postulated reaction scheme (Table 2) was numerically solved by the Scipy module using the ODEPACK library.[72] The time dependencies of the concentrations of the individual species were obtained for the given initial conditions.
- The activity of the discharge was simulated by a rectangular pulse of electron number density of 22 and 15 μs duration in accordance with the experiment. The typical values of electron densities in a glow discharge are[73,74] between 10^9

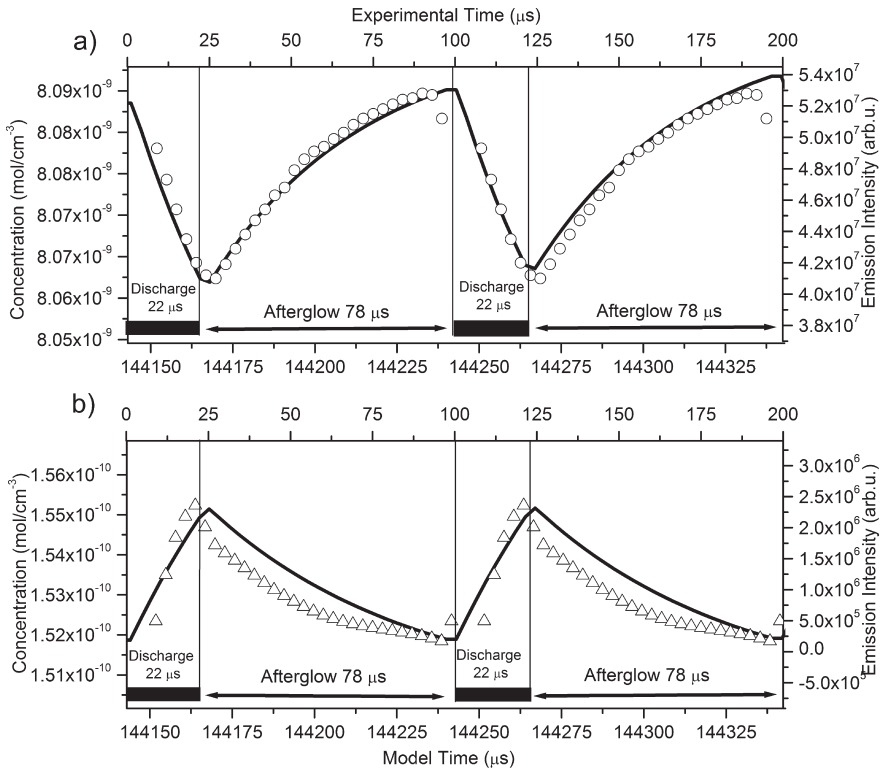

Figure 16. Comparison of the HCN concentration profile predicted by the acetonitrile discharge model (solid line) with the emission profile (circles) of the $\nu_1 - GS$ band (a). Comparison of the HNC concentration profile predicted by the acetonitrile discharge model (solid line) with the emission profile (triangles) of the $2\nu_1 - \nu_1$ band (b).

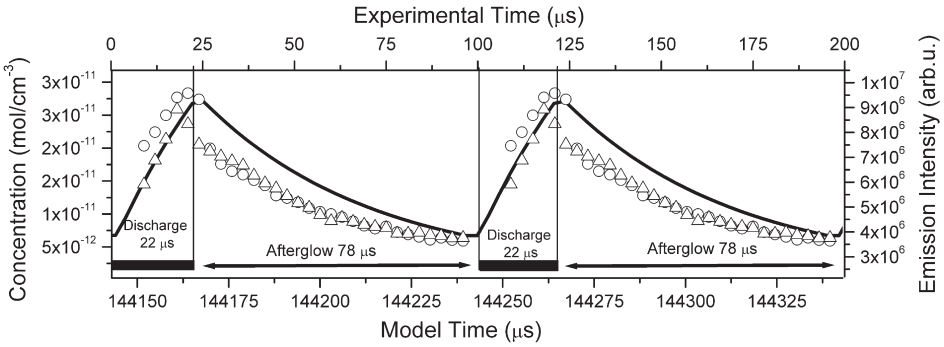

Figure 17. Comparison of the CN concentration profile in the acetonitrile discharge model (solid line) with the CN emission profile of the ground state $X^2\Sigma^+$ (triangles: 2 − 1, circles: 1 − GS bands).

and 10^{11} particles/cm^3. We used a value of 6×10^{11} cm^{-3} obtained by a Langmuir probe measurement in the actual experimental discharge. The electron temperature not obtained by measurement was estimated as 1 eV and was treated as a free parameter for the fitting of the experimental results by the model.

- The concentration of MH^+ ions in reaction M24 was forced to be proportional to the electron number density and was thus represented by a rectangular pulse.
- The number densities of the precursor molecules and the hydrogen molecules were fixed at 6.58×10^{15} cm^{-3}, as calculated from their partial pressures of 50 Pa and temperature 550 K.
- The electron temperature and the rate constant M21 were treated as free parameters for fitting the model results to the experimental values of the HNC/HCN ratios (2.2% for CH_3CN and 3% for $BrCN + H_2$) using the Nelder−Mead simplex algorithm.[75]
- The accumulation of reaction products from the previous discharge pulses (illustrated in Figure 7) was accounted for by modeling a sequence of 3000 pulses in each run (2−4 h of CPU time) while accounting for the loss of the products by convection in a flow of the buffer gas into the pump. The concentrations during the last pulse were used for the fitting.

Rate Constants. The rate constants of reactions involved in the hydrogen chemistry of HNC/HCN were adopted from the NIST[76] database and original literature (citations listed in Table 2). The temperature dependence of the rate constants

was estimated using the Arrhenius plot of the experimental data according to the equation:

$$\ln k = K(1000/T) + Q \quad (35)$$

where the slope is $K = -E_A/R$ (R is the universal gas constant, and E_A is the activation energy), and the constant term Q represents the temperature-independent logarithm of preexponential factor A. From the Boltzmann plot of the HCN lines, the rotational temperature of the discharge was estimated to be 550 K. The values of the rate constants given in Table 2 for reactions M10−M61 were calculated using eq 35 where possible.

The main mechanism of the dissociation of the molecules in the glow discharge is the collisions with free electrons generated by electron ionization and by Penning ionization (15). The second-order dissociation reaction can be generally written as

$$X - CN + e^- \rightarrow X + CN + e^- \quad (36)$$

The rate constant of electron dissociation was calculated according to the formulation used by Morrison et al.[77,78] as

$$k(T_e) = \pi\left(\frac{e}{4\pi\varepsilon_0 E_A}\right)^2 \cdot \left(\frac{8eT_e}{\pi m_e}\right)^{1/2} \cdot \left(1 + \frac{2T_e}{E_A}\right) \exp(-E_A/T_e) \quad (37)$$

Here, e and m_e are the electronic charge and mass, ε_0 is the permittivity of the vacuum (all in SI units), E_A is the activation energy for dissociation in eV, and T_e is the electron temperature expressed in eV (11600 K = 1 eV). Thus, the rate constants for reactions M0−M9 were calculated from the E_a values given in Table 2 using eq 37.

As the rate constants for the formation of HNC are not accurately known, they were treated as free model parameters, and they were fitted so that the resulting HNC/HCN ratios were within a range of 2.2−3%. The following constraints were used for the rate constants:

- The ratio of the rate constants M11/M12 and M14/M15 was fixed at 3:1 on the basis of work by Arunan.[42]
- The initial value of the rate constant for reaction M21 was taken as $k_{M21} = 5.6 \times 10^{-15}$ cm^3 s^{-1} according to theory by Sumathi et al.[21] The final value resulting from the fitting in the present model and the importance of reaction M21 will be discussed below.
- The rate constant for the formation of $HCNH^+$ by the protonation of HCN (M24) was taken as the rate constant of the reaction[79] of H_3^+, which has the quickest reaction among all the potential proton donors. The concentration of proton donors MH^+ was fixed as 1/10 of the electron number density.
- The dissociative recombination[80] reactions M25−M27 were assumed to produce HNC and HCN in equal amounts.

Results of Modeling, Reaction Channels Important for HNC Production. As discussed in the previous sections, collisions of HCN molecules with molecules and atoms in the ground internal energy states at the 550 K discharge temperature represent a negligible contribution to the HCN → HNC isomerization. Also, the energies of the lowest excited states of Ar ($^2P^\circ_{3/2}$ = 11.55 eV) and He (^3S = 19.81 eV) do not overlap with the energy barrier for the isomerization of 2.19 eV. Thus, the collisions of excited He or Ar atoms with HCN are likely to lead to Penning ionization (the ionization energy of HCN is 13.61 eV) or to the dissociation of HCN to the H atom and the CN radical (dissociation energy E_{dis} = 4.8 eV).

The numerical kinetic model confirmed that the reaction products are accumulated in the discharge cell during a sequence of pulses and that the molecules remaining from the previous pulses significantly affect the experimentally obtained emission spectra (see Figure 15). Especially important for the present study is the accumulation of HCN after several thousands of pulses (several tenths of a second after the beginning of the experimental sequence). Due to the substantial initial concentration of HCN at the onset of the pulse, the equilibrium between the HNC/HCN isomers is established by the conversions of HCN to HNC and back in reactions with hydrogen atoms H (eqs 7 and 8 in the Introduction, designated as M20 and M21 in the model) or by the protonation of HCN producing $HNCH^+$, followed by its dissociative recombination with electrons producing HNC/HCN (eq 5, designated as M25 − M27). The experimental time profiles of HNC and HCN emissions are compared with the modeled profiles in Figure 16. A similar comparison for the CN radical is shown in Figure 17. Other species mentioned in the model have significantly lower concentration than CN, HCN, and HNC except HBr and H. However, their emission profiles are in agreement with the model. The main question now is which mechanism is more important for the formation of HNC molecules in the glow discharges: is it the ion chemistry or the radical chemistry?

The simplest ions that can form in a discharge in mixtures containing hydrogen are H_2^+ and H_3^+. However, H_2^+ reactions with the CN radical[81] and HCN molecules

$$CN + H_2^+ \rightarrow HNC^+ + H \quad (39)$$

$$HCN + H_2^+ \rightarrow HCN^+ + H_2 \quad (40)$$

do not produce the $HCNH^+$ ion or the HNC isomer. However, the H_3^+ ions that are so important in interstellar chemistry do react with HCN by proton transfer to produce $HCNH^+$ according to eq 1, as mentioned in the Introduction (designated M24 in the model).

The method of continuous scanning time-resolved Fourier transform spectroscopy has been used in the 1800−4000 cm^{-1} spectral region to observe the formation of the H_3^+ ion in a hydrogen discharge.[82] To generate high concentrations of this ion, a high pressure of molecular hydrogen is required at several tens of mbar, much greater than the pressure used in the present study. It is noteworthy that, in the present experiments, molecular hydrogen, a precursor of H_3^+ that is easily detected in this spectral region,[83] was not detected. There was also no evidence for the presence of the $HCNH^+$ ions.

Ion molecule reactions are generally rapid and can thus play an important role even when the ion concentrations are below the detection limit of the spectroscopy methods. Thus, it is necessary to use the results of modeling to assess their contribution to the formation of HNC. If the neutral radical reaction channels leading to HNC formation (reactions M12, M15, M21, and M23) are excluded from the model, the resulting HNC/HCN ratio is only 0.07% and, notably, it does not depend on the MH^+ concentration, because the reverse conversion of HNC back to HCN (reaction M20) involves the H atoms produced both by the dissociative recombination of $HCNH^+$ and the dissociation of H_2. Reaction M20 thus significantly controls the HNC/HCN ratio. When the neutral reactions M12, M15, M21, and M23 are enabled, the modeled ratio of HNC/HCN rises to 2.2−3%, indicating that these reactions represent the main route to the

formation of HNC in the positive column of the glow discharge. The value of the HNC/HCN ratio is in accordance with the model result of equilibrium in reactions M20 and M21.

Recently, Amano et al.[84] studied the negative column of a glow discharge in a mixture of CH_4/N_2 at liquid nitrogen temperature, and they observed a 33% HNC/HCN ratio. This result, which is much higher than our observations in the positive columns, was attributed to dissociative recombination (eq5, M25 and M26). Extended negative glow discharge is a good source of positive ions, including the $HCNH^+$ that was actually observed. At liquid nitrogen temperature and at low pressures of 10^{-3} mbar, the neutral radical processes (including reactions M20 and M21) are insignificant due to the low collisional frequencies and lower reaction rate constants, and the ion chemistry dominates. However, in the positive column at 550 K and 1 mbar in this study, the neutral radical chemistry played the major role, and this is also supported by our model.

The fitting of the chemistry models in the BrCN and CH_3CN discharges to the experimental data provided rate constants for reaction M21 of 1.33×10^{-13} and 9.3×10^{-14} cm^3 s^{-1}, respectively. This difference demonstrates the accuracy of our results. The previous values reported in the literature ranged from 5.6×10^{-15} cm^3 s^{-1}, obtained by theoretical calculation,[21] to 7×10^{-11} cm^3 s^{-1}, obtained by the modeling of cometary chemistry,[20] and no direct experimental data are available in the current literature. Our results are thus closer to the lower theoretical value by Sumathi.[21] However, it must be kept in mind that the conditions of our experiments are given by the plasma environment of the glow discharge at a temperature of 550 K, an electron temperature of 1 eV, and a number density of electrons of 6×10^{10} cm^{-3}.

Emission and Concentration Profiles. The model results for the time profiles of the species concentrations in the discharge correspond to the observed experimental data qualitatively, but not quantitatively (as shown in Figures 16 and 17). The modeled change of concentration during one pulse was relatively small, while the change of the emission intensity recorded by the detector was comparatively large. This mismatch can be explained by the excitation of the radiating species in the active discharge and by their subsequent collisional relaxation (quenching). The details of these processes can be illustrated by the HNC and HCN emission profiles:

The ground state of HCN in collisions with excited hydrogen atoms H* produces HNC ($v' = 2$, observed band $2\nu_1 - \nu_1$):

$$HCN + H^* \rightarrow HNC\ (v' = 2) + H \quad k_{M21} = 9.28 \times 10^{-14}\ cm^3\ s^{-1} \qquad (41)$$

Then, HNC ($v' = 2$) is quenched in collisions with a molecule M to $v'' = 1$ (observed band $\nu_1 - GS$) and is further quenched to the ground vibrational state (GS).

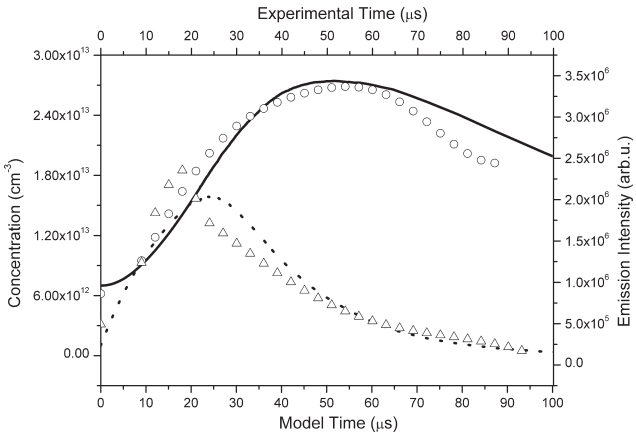

Figure 18. Comparison of the acetonitrile discharge model of HNC excited $v' = 2$ formation (dashed line) followed by the collisional deexcitation to the $v'' = 1$ state (solid line) and to the GS with the experimental profiles of these bands (circles, $\nu_1 - GS$ band; triangles, $2\nu_1 - \nu_1$ band).

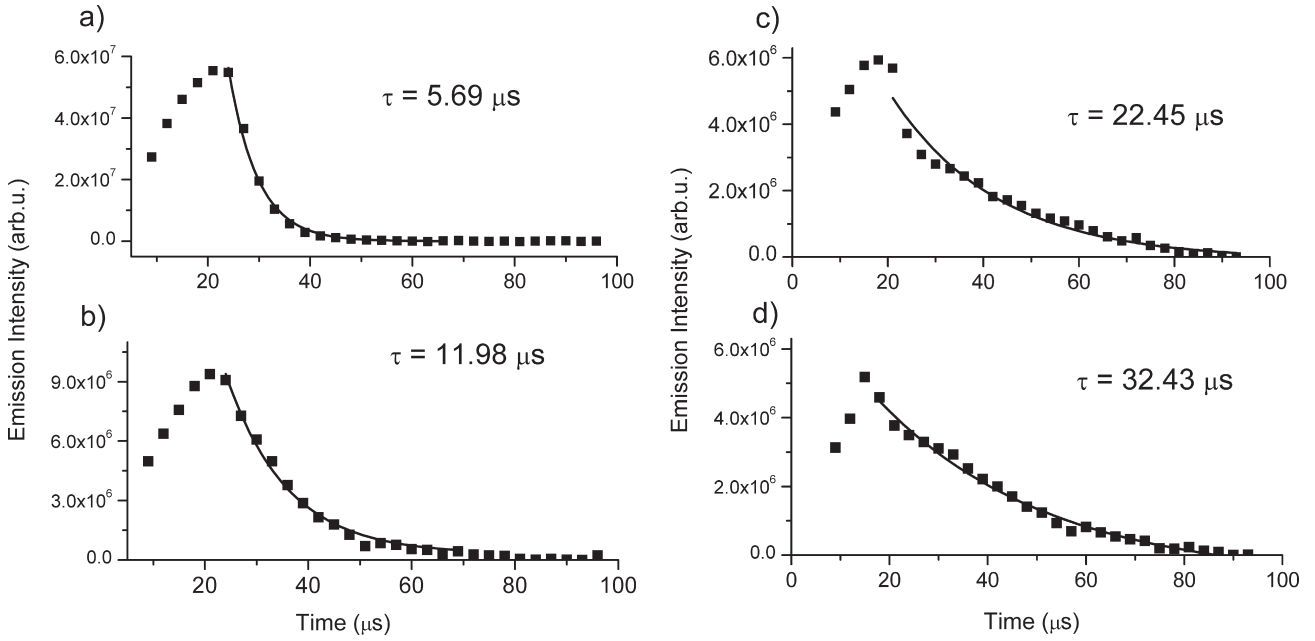

Figure 19. Emission profiles of the CN $X^2\Sigma^+$ 2 − 1 (a) and 1 − GS (b) bands in the case of $CH_3CN + H_2$ discharge compared with the profiles of the same bands in the case of CH_3CN discharge without extra added molecular hydrogen (c, d).

$$\mathrm{HNC}(v' = 2) + \mathrm{M} \rightarrow \mathrm{HNC}\ (v'' = 1) + \mathrm{M}^*$$
$$k_{2-1} = 1.15 \times 10^{-11}\ \mathrm{cm}^3\ \mathrm{s}^{-1} \quad (42)$$

$$\mathrm{HNC}(v' = 1) + \mathrm{M} \rightarrow \mathrm{HNC}\ (\mathrm{GS}) + \mathrm{M}^*$$
$$k_{1-\mathrm{GS}} = 2.2 \times 10^{-12}\ \mathrm{cm}^3\ \mathrm{s}^{-1} \quad (43)$$

The results of the kinetic model of this sequence involving the same number of collision partners and molecules HCN and HNC (4.85×10^{15} cm^{-3}) are shown in Figure 18. The agreement of the presented emission profiles with the experimental results indicates that quenching significantly influences the time profiles of the emission intensities. The actual rate of quenching is strongly influenced by the nature of the colliding species and by the differences in the excitation levels of the exciting species and the energy acceptor. The rate constants for quenching by rare gas atoms are known to be slow. For example, the relaxation rates of highly excited states[85] of NCNO are in the order of 10^{-14} cm^3 s^{-1} for collisions with He and Ar atoms, but for collisions with molecular gas N_2, the quenching rate constant is 10^{-10} cm^3 s^{-1}. This value is close to a typical collisional rate constant. Spontaneous emission lifetimes are comparatively long and do not strongly influence the observed time profiles. For HNC, the spontaneous emission lifetime is 2702.7 μs, while the observed exponential time constant of decay in the discharge is only 115.2 μs. The effect of collisions on the experimental lifetime τ_{exp} of the CN emission lines is also demonstrated experimentally with the addition of H_2. In the acetonitrile/Ar discharge without the added hydrogen, the lifetime of the emission line R(8) in the ground state $X^2\Sigma^+$, 2 − 1, was τ_{exp} = 22.45 μs (not truly exponential, see Figure 19); in the case of the R(8) line in the ground state $X^2\Sigma^+$, 1 − GS, it was τ_{exp} = 32.43 μs. After the addition of 0.5 mbar of hydrogen to the discharge, these lifetimes shortened to τ_{exp} = 5.69 μs and τ_{exp} = 11.98 μs, respectively.

IV. CONCLUSIONS

Time-resolved Fourier transform emission spectroscopy was used to study the formation of HNC and HCN. On the basis of the strength of the HCN and HNC bands, the HNC/HCN ratios were studied in the glow discharge in three different mixtures: acetonitrile/Ar, BrCN/H_2/He, and formamide/He. The aim of the work was to determine whether the HNC/HCN ratio depends on the type of precursor used. In all three mixtures, HNC/HCN experimental ratios between 2 and 3% were found. The final products of the discharges in the acetonitrile/He and the formamide were detected using the SIFT-MS method. The main decay products in both acetonitrile and formamide were HCN, methane, and acetylene.

Kinetic modeling was conducted to identify the reaction channels responsible for the formation of HNC in the given concentration ratio to the HCN present in the gas mixture. A numerical kinetic model was constructed that contained 61 reactions covering both ion chemistry and neutral radical chemistry. The results of fitting the model predictions to the experimental data revealed the following:

- The products of the discharge chemistry are accumulated in the cell in a sequence of pulses.
- The ratio of HNC/HCN was 2 orders of magnitude smaller than the experimental results when the radical chemistry was excluded and only the ion chemistry was enabled. The full model, including the radical chemistry, reproduced the experimental results.
- HNC is formed primarily by the reaction of HCN with the H atoms (equations M21 and M20), and the rate constant for reaction M21 was determined to be in the range 9.3 × 10^{-14} to 1.33 × 10^{-13} cm^3 s^{-1}.
- The time profiles of emission intensities are influenced by the collisional quenching of the vibrationally excited states in addition to the concentration profiles of the chemical compounds produced by the discharge chemistry. The value of HNC/HCN ratio can therefore be influenced by collisions, and rate constant M21 must be accepted like an effective value.

AUTHOR INFORMATION

Corresponding Author

*E-mail: civis@jh-inst.cas.cz. Phone: +420-286 591 766.

ACKNOWLEDGMENT

This work is part of the research programs funded by the Grant Agency of the Academy of Sciences of the Czech Republic (Grant Nos. IAA400400705 and IAAX00100903) and by the Grant Agency of the Czech Republic (Grant Nos. P208/10/2302 and 202/09/0800).

REFERENCES

(1) Snyder, L. E.; Buhl, D. *Bull. Am. Astron. Soc.* **1971**, *3*, 388.
(2) Goldsmith, P. F.; Langer, W. D.; Ellder, J.; Irvine, W.; Kollberg, E. *Astrophys. J.* **1981**, *249*, 524.
(3) Liszt, H.; Lucas, R. *Astron. Astrophys.* **2001**, *370*, 576.
(4) Nyman, L., A.; Olofsson, H.; Johansson, L. E. B.; Carstrom, U.; Wolstencroft, R. *Astron. Astrophys.* **1993**, *1*, 377.
(5) Lellouch, E.; Romani, P. N.; Rosenqvist, J. *Icarus* **1994**, *108*, 112.
(6) Irvine, W. M.; Schloerg, F. P. *Astrophys. J.* **1984**, *282*, 516.
(7) Schilke, P.; Walmsley, M. C.; Pineau des Forests, G.; Rouell, E.; Flower, D. R.; Guilloteau, S. *Astron. Astrophys.* **1992**, *256*, 595.
(8) Ziurys, L. M.; Tenenbaum, E. D.; Pulliam, R. L.; Woolf, N. J.; Milam, S. N. *Astrophys. J.* **2009**, *695*, 1604.
(9) Schilke, P.; Walmsley, C. M.; Millar, T. J.; Henkel, C *Astron. Astrophys.* **1991**, *247*, 487.
(10) Brown, R. D.; Burden, F. R.; Cuno, A. *Astrophys. J.* **1989**, *347*, 855.
(11) Watson, W. D. *Rev. Mod. Phys.* **1976**, *48*, 513.
(12) Turner, B. E.; Pirogov, L.; Minh, Y. C. *Astrophys. J.* **1997**, *483*, 235.
(13) Allen, T. L.; Goddard, J. D.; Shaefer, H. F. *J. Chem. Phys.* **1980**, *73* (7), 3255.
(14) Talbi, D.; Ellinger, Y. *Chem. Phys. Lett.* **1998**, *288*, 155.
(15) Graedel, T. E.; Langer, W. D.; Frerking, M. A. *Astrophys. J.* **1982**, *48*, 321.
(16) Herbst, E.; Terzieva, R.; Talbi, D. *Mon. Not. R. Astron. Soc.* **2000**, *311*, 869.
(17) Kawaguchi, K.; Hirota, T.; Yamamoto, S.; Sakamoto, A.; Ukuta, N. *Astrophys. J.* **1999**, *520*, 895.
(18) Irvine, W. M.; Dickens, J. E.; Loverll, A. J.; Schloerb, P. F.; Senay, M.; Bergin, E. A.; Jewitt, D.; Matthews, E. *Faraday Discuss.* **1998**, *109*, 475.
(19) Rodgers, S. D.; Charnley, S. B. *Astrophys. J.* **1998**, *501*, L227.
(20) Sumathi, R.; Nguyen, M. T. *J. Phys. Chem. A* **1998**, *102*, 8013.
(21) Talbi, D.; Ellinger, Y; Herbst, E *Astron. Astrophys.* **1996**, *314*, 688.
(22) Talbi, D.; Ellinger, Y. *Chem. Phys. Lett.* **1996**, *263*, 385.

(23) Rodgers, S. D.; Charnley, S. B. *Mon. Not. R. Astron. Soc.* **2005**, *356*, 1542.
(24) Milligan, D. E.; Jacox, M. E. *J. Chem. Phys.* **1963**, *3* (39), 712.
(25) Burkholder, J. B.; Sinha, A.; Hamer, P. H.; Howard, C. J. *J. Mol. Spectrosc.* **1987**, *126*, 72.
(26) Maki, A. G.; Mellau, G. Ch. *J. Mol. Spectrosc.* **2001**, *206*, 47.
(27) Burgers, P. C.; Holmes, J. L.; Mommers, A. A.; Terlouw, J. K. *Chem. Phys. Lett.* **1983**, *1*, 1.
(28) Snell, R. L.; Wootten, H. A. *Astrophys. J.* **1977**, *216*, L111.
(29) Maki, A. G.; Sams, R. L. *J. Chem. Phys.* **1981**, *75*, 4178.
(30) Kumeda, Y.; Minami, Y.; Takano, K.; Taketsugu, T.; Hirano, T. *THEOCHEM* **1999**, *458*, 285.
(31) Barber, R. J.; Harris, G. J.; Tennyson, J. *J. Chem. Phys.* **2002**, *24* (117), 11239.
(32) Harris, G. J.; Pavlenko, Y. V.; Jones, H. R. A.; Tennyson, J. *Mon. Not. R. Astron. Soc.* **2003**, *344*, 1107.
(33) Nezu, M.; Amano, T.; Kawaguchi, K. *J. Mol. Spectrosc.* **1998**, *192*, 41.
(34) Kawaguchi, K.; Fujimoto, J. Time-resolved Fourier transform infrared emission spectra of HNC/HCN. 62nd OSU International Symposium on Molecular Spectroscopy, Columbus, OH, 2007.
(35) He, G.; Macdonald, R. G. *Chem. Phys. Lett.* **1999**, *301*, 175.
(36) Northrup, F. J.; Bethardy, G. A.; Macdonald, R. G. *J. Mol. Spectrosc.* **1997**, *186*, 349.
(37) Decker, B. K.; He, G.; Tokue, I.; Macdonald, R. G. *J. Phys. Chem. A* **2001**, *105*, 5759.
(38) He, G.; Tokue, I.; Macdonald, R. G. *J. Chem. Phys.* **2000**, *112*, 6689.
(39) Song, Y; Sushan, D. *J. Mol. Struct.* **1996**, *362*, 387.
(40) Arunan, E.; Manke, G.; Setser, D. W. *Chem. Phys. Lett.* **1993**, *1*, 81.
(41) Copeland, L. R.; Mohammad, F.; Zahedi, M.; Volman, D. H. *J. Chem. Phys.* **1992**, *96*, 5817.
(42) Lundell, J.; Krajewska, M.; Räsänen, M. *J. Phys. Chem. A* **1998**, *102*, 6643.
(43) Moore, M. H.; Hudson, R. L. *Icarus* **2003**, *161*, 486.
(44) Solomon, P. M.; Jefferts, K. B.; Penzias, A. A.; Wilson, R. W. *Astrophys. J.* **1971**, *168*, L107.
(45) Ulick, B. L.; Conklin, E. K. *Nature* **1974**, *248*, 121.
(46) Rubin, R. H.; Swenson, G. W., Jr.; Solomon, R. C.; Flygare, H. L. *Astrophys. J.* **1971**, *169*, L39–L44.
(47) Bockelée-Morvan, D.; Lis, D. C.; Wink, J. E.; Despois, D.; Crovisier, J.; Bachiller, R.; Benford, D. J.; Biver, N.; Colom, P.; Davies, J. K.; Gérard, E.; Germain, B.; Houde, M.; Mehringer, D.; Moreno, R.; Paubert, G.; Phillips, T. G.; Rauer, H. *Astron. Astrophys.* **2000**, *353*, 1101–1114.
(48) Civis, S.; Juha, L.; Babankova, D. *Chem. Phys. Lett.* **2004**, *386*, 169.
(49) Saladino, R.; Crestini, C.; Ciciriello, F.; Costanzo, G.; Di Mauro, E. *Chem. Biodiversity* **2007**, *4*, 694.
(50) Tokaryk, D. W.; Civis, S. *J. Chem. Phys.* **1995**, *10*, 3928.
(51) Results will be published.
(52) Kawaguchi, K.; Hama, Y.; Nishida, S. *J. Mol. Spectrosc.* **2005**, *232*, 1.
(53) Smith, D.; Spanel, P. *Mass Spectrom. Rev.* **2005**, *24*, 661–700.
(54) Sovova, K.; Ferus, M.; Matulkova, I.; Spanel, P.; Dryahina, K.; Dvorak, O.; Civis, S. *Mol. Phys.* **2008**, *106*, 1205–1214.
(55) Tokue, I.; Sakai, Y.; Yamasaki, K. *J. Chem. Phys.* **1997**, *106* (11), 4491.
(56) Yencha, A. J. *Electron spectroscopy: theory, techniques and applications*; Bundle, C. R., Baker, A. D., Eds.; Academic: London, 1984; Vol. 5.
(57) Baulch, D. L.; Duxbury, J.; Grant, S. J.; Montague, D. C. *J. Phys. Chem. Ref. Data* **1981**, *10*, 1.
(58) Haruhiko, I.; Kawamura, Y. *J. Non-Cryst. Solids* **2008**, *354*, 3267.
(59) Sailer, W.; Pelc, A.; Limao-Vieira, P.; Mason, N. J.; Limtrakul, J.; Scheier, P.; Probst, M.; Märk, T. D. *Chem. Phys. Lett.* **2003**, *381*, 216.
(60) Jamieson, J. V. S.; Brown, G. R.; Tanner, J. S. *Can. J. Chem.* **1970**, *48*, 3619.
(61) Results will be published.
(62) Liu, D.; Fang, W.; Fu, X. *Chem. Phys. Lett.* **2000**, *318*, 291.
(63) Brownsword, R.A..; Gatenby, S.D.; Herbert, L.B.; Smith, I.W. M.; Stewart, D.W.A.; Symonds, A. C. *J. Chem. Soc., Faraday Trans.* **1996**, *92*, 723.
(64) Mayer, S.W.; Schieler, L. *J. Chem. Phys.* **1966**, *45*, 385.
(65) Caridade, P. J. S. B.; Rodrigues, S. P. J.; Sousa, F.; Varandas, A. J. C. *J. Phys. Chem. A* **2009**, *109*, 2356.
(66) Atakan, B.; Kocis, D.; Wolfrum, J.; Nelson, P. *Symp. Int. Combust. Proc.* **1992**, *24*, 691.
(67) Nezu, M.; Amano, T.; Kawaguchi, K. *J. Mol. Spectrosc.* **1999**, *198*, 186.
(68) Harris, G. J.; Polynsky, O. L.; Tennyson, J. *Spectrochim. Acta, Part A* **2002**, *58*, 673.
(69) Botschwina, P. *Chem. Phys.* **1983**, *81*, 73.
(70) URL: http://numpy.org/, downloaded Oct 25, 2010.
(71) URL: http://scipy.org/, downloaded Oct 25, 2010.
(72) URL: http://people.sc.fsu.edu/~jburkardt/f77_src/odepack/odepack.html, downloaded Oct 25, 2010.
(73) Winchester, M.; Payling, R. *Spectrochim. Acta, Part B* **2004**, *59*, 607.
(74) Corbella, C.; Polo, M. C.; Oncins, G.; Pascual, E.; Andújar, J. L.; Bertran, E. *Thin Solid Films* **2005**, *482*, 172.
(75) Scientific Tools for Python, SciPy, <http://scipy.org/>.
(76) NIST Chemical Kinetics Database: Standard Reference Database 17, Version 7.0 Web Version, Release 1.4.3, Data Version 2009.01 <http://kinetics.nist.gov/kinetics/index.jsp>, dowloaded Oct 25, 2010.
(77) Morrison, N. A.; William, C.; Milne, W. I. *J. Appl. Phys.* **2003**, *11*, 7031.
(78) Lieberman, M. A.; Lichtenberg, A. J. *Principles of Plasma Discharges and Materials Processing*, 1st ed.; Wiley: New York, 1994; p 79.
(79) Mackay, G. I.; Betowski, L. D.; Payzant, J. D.; Shiff, H. I.; Bohme, D. K. *J. Phys. Chem.* **1976**, *80*, 29919.
(80) Semaniak, J.; Minaev, B. F.; Derkatch, A. M.; Hellberg, F.; Neau, A.; Rosén, S.; Thomas, R.; Larsen, M; Danaid, H.; Paál, A.; Ugglas, M. *Astrophys. J. Suppl.* **2001**, *135*, 275.
(81) The UMIST database for Astrochemistry, <http://www.udfa.net/>.
(82) Civiš, S.; Kubát, P.; Nishida, S.; Kawaguchi, K. *Chem. Phys. Lett.* **2005**, *418*, 448.
(83) Dabrowski, I.; Herzber,g, G. *Acta Phys. Hung.* **1984**, *55*, 219.
(84) Amano, T.; Zelinger, Z.; Hirao, T.; Takano, J.; Toyoda, R. *J. Mol. Spectrosc.* **2008**, *251*, 252.
(85) Wright, S. M. A.; Sims, I. R.; Smith, I. W. M. *Phys. Chem. Chem. Phys.* **2001**, *3*, 2203.
(86) Saum, K. A.; Benesch, W. M. *Appl. Opt.* **1970**, *9*, 195.
(87) Sun, Q; Yang, D. L; Wang, N. S; Bowman, J. M; Lin, M. C. *J. Chem. Phys.* **1990**, *93*, 4730.
(88) Brupbacher, J. M; Esneault, C. P; Kern, R. D. *J. Phys. Chem.* **1977**, *81*, 1128.
(89) Yang, D. L.; Yu, T.; Lin, M. C.; Melius, C. F. *Chem. Phys.* **1993**, *177*, 271.
(90) Tsang, W. *Chem. Kinet. Data* **1992**, *21*, 753.
(91) Baulch, D. L.; Cobos, C. J.; Cox, R. A.; Frank, P.; Hayman, G.; Just, Th.; Kerr, J. A.; Murrells, T.; Pilling, M. J.; Troe, J.; Walker, R. W.; Warnatz, J. *J. Phys. Chem. Ref. Data* **1994**, *23*, 847.
(92) Tsang, W *Chem. Kinet. Data* **1992**, *21*, 753.
(93) Seakins, P. W.; Pilling, M. J. *J. Phys. Chem.* **1991**, *95*, 9878.
(94) Golden, D. M. *Int. J. Chem. Kinet.* **2008**, *40*, 310.

Home Search Collections Journals About Contact us My IOPscience

Time-resolved FTIR emission spectroscopy of Cu in the 1800–3800 cm^{-1} region: transitions involving f and g states and oscillator strengths

This article has been downloaded from IOPscience. Please scroll down to see the full text article.

2011 J. Phys. B: At. Mol. Opt. Phys. 44 025002

(http://iopscience.iop.org/0953-4075/44/2/025002)

View the table of contents for this issue, or go to the journal homepage for more

Download details:
IP Address: 132.70.34.115
The article was downloaded on 12/01/2011 at 18:47

Please note that terms and conditions apply.

J. Phys. B: At. Mol. Opt. Phys. **44** (2011) 025002 (7pp) doi:10.1088/0953-4075/44/2/025002

Time-resolved FTIR emission spectroscopy of Cu in the 1800–3800 cm^{-1} region: transitions involving f and g states and oscillator strengths

S Civiš[1], I Matulková[1], J Cihelka[1], P Kubelík[1], K Kawaguchi[2] and V E Chernov[3]

[1] J Heyrovský Institute of Physical Chemistry, v.v.i., Academy of Sciences of the Czech Republic, Dolejškova 3, 18223 Prague 8, Czech Republic
[2] Faculty of Science, Okayama University, Tsushima-naka, Okayama 700-8530, Japan
[3] Voronezh State University, 394693 Voronezh, Russia

E-mail: civis@jh-inst.cas.cz

Received 26 October 2010, in final form 18 November 2010
Published 12 January 2011
Online at stacks.iop.org/JPhysB/44/025002

Abstract
Time-resolved Fourier-transform spectroscopy was applied to the study of the emission spectra of Cu vapours in a vacuum (10^{-2} Torr) produced in ablation of a Cu metal target by a high-repetition rate (1.0 kHz) pulsed nanosecond ArF laser ($\lambda = 193$ nm, output energy of 15 mJ). The time-resolved infrared emission spectrum of Cu was recorded in the 1800–3800 cm^{-1} spectral region with a resolution of 0.017 cm^{-1}. The time profiles of the measured lines have maxima at 18–20 μs after a laser shot and display non-exponential decay with a decay time of 5–15 μs. This study reports 17 lines (uncertainty 0.0003–0.018 cm^{-1}) of Cu I not previously observed. This results in seven newly-found levels and revised energy values for 11 known levels (uncertainty 0.01–0.03 cm^{-1}). We also calculate transition probabilities and oscillator strengths for several transitions involving the reported Cu levels.

(Some figures in this article are in colour only in the electronic version)

1. Introduction

The great advantages of Fourier-transform infrared spectroscopy (FTIR), such as its constant high resolution and energy throughput, have made the IR spectral region more accessible for laboratory spectral measurements (Nilsson 2009). The infrared range is becoming more and more important in astronomical research, for instance in studies of dust-obscured objects and interstellar clouds, cool objects such as discs, planets and the extended atmospheres of evolved stars, including objects at cosmological distances from the Earth (Kerber *et al* 2009). Nevertheless, the powerful capacities of IR astronomy (e.g. ESO's CRyogenic Infra-Red Echelle Spectrograph, CRIRES) cannot be fully utilized without detailed spectroscopical information, first of all, on atomic line wavelengths and oscillator strengths in the IR region (Biémont 1994, Grevesse and Noels 1994, Pickering 1999, Jorissen 2004, Johansson 2005). A general drawback of the IR spectral region is the much lower number of atomic and ionic lines available (as compared to the visible and ultraviolet range) (Ryde 2010), so reporting new IR atomic lines is important.

Cu is the element (together with Zn) immediately following the iron peak, and its abundance is important in studies of scenarios of the chemical evolution of the Galaxy implied by different nucleosynthesis models (Sneden *et al* 1991, Matteucci *et al* 1993, Prochaska *et al* 2000, Cunha *et al* 2002, Mishenina *et al* 2002, Simmerer *et al* 2003, Bihain *et al* 2004, Ecuvillon *et al* 2004, Sobeck *et al* 2008). Copper abundance can be analysed from the IR spectra of cool stars (Ryde 2009, Wahlgren *et al* 2009), metal-poor stars (Cowan *et al* 2002, Honda *et al* 2007) and substellar objects (Jones *et al* 2005).

 © 2011 IOP Publishing Ltd Printed in the UK & the USA

It should be noted that the studies of copper abundances in stars and the interstellar medium were performed mostly with optical 510.554, 521.820 and 578.212 nm (Sneden *et al* 1991, Mishenina *et al* 2002, Cunha *et al* 2002, Simmerer *et al* 2003, Ecuvillon *et al* 2004, Prochaska *et al* 2000) or ultraviolet 327.395 nm (Bihain *et al* 2004, Sobeck *et al* 2008) and 324.754 nm (Sobeck *et al* 2008) Cu I lines. To our knowledge, no infrared lines of Cu I were involved in the abundance analysis except the 809.263 nm line used in the study of stellar abundances in the thick disc of the Galaxy (Prochaska *et al* 2000). Nor have we encountered literature data about Cu I lines with wavelengths above 2 μm, and this work is intended to supply information about Cu I infrared lines and transition moments in the 2.7–5.5 μm range. This work continues the previous studies on Au I (Civiš *et al* 2010a) and Ag I (Civiš *et al* 2010b).

Atomic copper has been attracting the great interest of spectroscopists for many decades since its spectrum gives one of the best examples of the majority of peculiarities in atomic spectra due to a number of series perturbations observed below the first ionization threshold. Analysis of the main features of the Cu I spectrum began in the 1920s, and the first critical and exhaustive study of Cu I lines and levels was reported by Shenstone (1948). He published the spectrum from 150.4 to 1822.9 nm (5484–66485 cm^{-1}) including both his own measurements and the previous results of other authors.

The simplest Cu I term structure originates from the closed $3d^{10}$ core yielding $3d^{10}nl_j$ states with a total angular momentum $J = j = l \pm \frac{1}{2}$. Other terms arise due to excitation of a 3d electron into an $n'l'$ state. The core-excited $3d^9nln'l'$ Cu I states were studied both by numerical *ab initio* calculations (Martin and Sugar 1969, Carlsson 1988) and by VUV photoabsorption (Tondello 1973, Longmire *et al* 1980, Baig *et al* 1992); for a more detailed review see Baig *et al* (1997). The most comprehensive reports of the closed-core $3d^{10}nl_j$ states of Cu were made by Longmire *et al* (1980) (for *n*s states up to $n = 41$ and *n*p states up to $n = 57$) and by MacAdam *et al* (2009) (for s, p, d, f and g states for $n = 23$–28).

The aim of this work is the study of the Cu I spectrum in the infrared domain using FTIR spectroscopy of laser-ablated Cu plasma. The lines in this domain are due to transitions between the levels with $n = 4$–7; the energies of some levels (for the f and g states) have not been previously reported. To identify the transitions involving these and other low-Rydberg Cu levels, we use the information on the relative intensity of the transitions obtained here by the calculation of dipole transition matrix elements (or transition dipole moments) using the Fues model potential (FMP) approach (Civiš *et al* 2010b). The comparison tables presented in section 3.1 show a reasonable agreement between our calculations and the experimental and theoretical results for oscillator strengths. The dipole transition matrix elements calculated in section 3.1 are used in section 3.2 for classification of the observed lines resulting in revised values for some terms of Cu I.

2. Method

The experimental setup has already been described in detail in our previous papers (Civiš *et al* 2010a, Kawaguchi *et al* 2008). The time-resolution FTIR spectra were measured using the modified Bruker IFS 120 HR spectrometer in the J. Heyrovský Institute in Prague. The modification of the apparatus for the time-resolution scan of emission data was previously developed in Okayama University. The Bruker high resolution interferometer is calibrated against the internally stabilized HeNe laser with a precision around 0.001 cm^{-1}.

The Bruker system was equipped with an analogue–digital converter (ADC 4322: Analogic, USA), which was connected to a PC containing a programmable control processor of a field programmable gate array—FPGA, (ACEX 1K: Altera, USA) set up at a frequency of 33 MHz, and digital input board PCI (2172C: Interface, Japan). The data collection process and synchronization with the laser were controlled by the FPGA processor programmed by QUARTUS II 7.1, Altera. The software programs for data acquisition and fast FT transformation and displaying of the data were written in C $^{++}$ language.

Time-resolved FTIR spectroscopy was applied for observations of the emission arising after the irradiation of metals with a pulsed nanosecond ArF ($\lambda = 193$ nm) laser. A high repetition rate ArF laser ExciStar S-Industrial V2.0 1000 (193 nm, laser pulse width 12 ns, frequency 1 kHz) with 15 mJ output power was focused on a rotating and linearly traversing copper target inside a vacuum chamber (average pressure 10^{-2} Torr). The infrared emission (axial distance from the target 10 mm) was focused into the spectrometer using a CaF_2 (100 mm) lens. The emission was observed in the 1800–3800 cm^{-1} spectral region with a time profile showing maximum emission intensity at 18–20 μs after the laser shot.

For data sampling, we used the so-called 1/3 sampling, where the scanner rate was set to produce a 3 kHz HeNe laser interference signal, the ArF laser oscillation was triggered, and 60 sets of time-resolved data were recorded with a preset time interval of 1 μs. Three scans were needed for a complete interferogram, and only five scans were coadded to improve the signal-to-noise ratio (SNR). The spectral resolution in such a procedure was about 0.1 cm^{-1}. We also performed measurements with only one scan but with higher resolution of about 0.017 cm^{-1} but worse SNR. The acquired spectra were post-zerofilled (zero filling 2, trapezoid apodization function) using the Bruker OPUS software and subsequently corrected by subtracting the blackbody background spectrum. The wavenumbers, line widths and their intensities were then obtained using the OPUS internal peak picking procedure.

The Fues model potential method for the calculation of dipole matrix elements was outlined in the previous paper (Civiš *et al* 2010b). For Cu I, the radial quantum number n_r (which is equal to the number of nodes of the radial wavefunction) was assumed as

$$n_r = \begin{cases} n-4 & \text{for} \quad \text{s, p, d states} \quad (n \geqslant 4); \\ n-l-1 & \text{for} \quad l \geqslant 3 \quad \text{states} \quad (n \geqslant l+1). \end{cases} \tag{1}$$

Table 1. Comparison of FMP-calculated oscillator strengths for transitions between some $3d^{10}nl_j$ states of Cu I with the values from other sources.

Transition	FMP (this work)	Other values
$4s_{\frac{1}{2}}$–$4p_{\frac{1}{2}}$	0.223	0.221 75[a]; 0.215(6)[b]; 0.2631[c]; 0.214[d]; 0.224[e]; 0.215[f]; 0.220(15)[g]; 0.22[h]; 0.2230[i]; 0.323(4)[j]; 0.153[k]; 0.16(4)[l]; 0.0158[m]
$4s_{\frac{1}{2}}$–$4p_{\frac{3}{2}}$	0.449	0.447 56[a]; 0.439(12)[b]; 0.5296[c]; 0.432[d]; 0.453[e]; 0.434[f]; 0.432(28)[g]; 0.43(2)[n]; 0.4460[i]; 0.66[j]; 0.322[k]; 0.31(3)[l]; 0.0316[m]
$4p_{\frac{1}{2}}$–$5s_{\frac{1}{2}}$	0.171	0.151[e]; 0.1690[i]
$4p_{\frac{3}{2}}$–$5s_{\frac{1}{2}}$	0.172	0.153[e]; 0.1730[i]
$4p_{\frac{1}{2}}$–$6s_{\frac{1}{2}}$	0.0134	0.0136[e]; 0.009 09[i]; 0.0148[m]
$4p_{\frac{3}{2}}$–$6s_{\frac{1}{2}}$	0.0131	0.0136[e]; 0.0131[i]; 0.0157[m]
$4p_{\frac{3}{2}}$–$6d_{\frac{5}{2}}$	0.0465	0.044 41[c]; 0.003 78[m]
$4p_{\frac{1}{2}}$–$7s_{\frac{1}{2}}$	0.004 19	0.004 064[c]; 0.007 23[m]
$4p_{\frac{1}{2}}$–$8s_{\frac{1}{2}}$	0.001 91	0.001 899[c]; 0.002 45[m]
$4p_{\frac{1}{2}}$–$9s_{\frac{1}{2}}$	0.001 05	0.001 053[c]; 0.000 251[m]
$4p_{\frac{3}{2}}$–$9s_{\frac{1}{2}}$	0.001 02	0.001 027[c]; 0.000 56[m]
$4p_{\frac{1}{2}}$–$4d_{\frac{3}{2}}$	0.592	0.511 06[a]; 0.551[d]; 0.546[e]; 0.4880[i]
$4p_{\frac{3}{2}}$–$4d_{\frac{5}{2}}$	0.538	0.467 27[a]; 0.503[d]; 0.499[e]; 0.4650[i]
$4p_{\frac{3}{2}}$–$4d_{\frac{3}{2}}$	0.0598	0.052 01[a]; 0.056[d]; 0.0555[e]; 0.0614[i]
$4p_{\frac{1}{2}}$–$5d_{\frac{3}{2}}$	0.131	0.1238[c]; 0.117[e]; 0.0932[i]
$4p_{\frac{3}{2}}$–$5d_{\frac{5}{2}}$	0.118	0.1114[c]; 0.107[e]; 0.0791[i]
$4p_{\frac{3}{2}}$–$5d_{\frac{3}{2}}$	0.0131	0.012 36[c]; 0.0119[e]

[a] Solution of one-electron Schrödinger equation with Hartree–Slater potential corrected by core polarization and spin–orbital interaction (Curtis and Theodosiou 1989).
[b] Laser-induced fluorescence from sputtered metal vapours (Hannaford and Lowe 1983).
[c] Numerical Coulomb-like approximation (Lindgård *et al* 1980).
[d] Relativistic Hartree–Fock calculation with account for core polarization effects (Migdałek and Baylis 1978).
[e] Relativistic Hartree–Fock calculation with model potential accounting for exchange and core polarization (Migdałek 1978).
[f] Relativistic Hartree–Fock calculation with model potential and core polarization (Migdałek and Baylis 1979).
[g] Calculation using the level-crossing measurement of lifetimes and configuration coupling coefficient deduced by fitting other experimental measurements of lifetimes and relative oscillator strengths (Siefart *et al* 1974).
[h] Atomic absorption measurements on flames (Lvov 1970).
[i] Critical survey of experimentally-determined oscillator strengths (Corliss 1970).
[j] Rozhdestvenskii's hook method (Slavenas 1966).
[k] Curves of growth in absorption measurement (Moise 1966).
[l] Atomic-beam absorption (Bell *et al* 1958).
[m] Arc emission measurements (Allen and Asaad 1957).
[n] Atomic-beam absorption (Bell and Tubbs 1970).

3. Results and discussion

3.1. Calculation of the dipole transition matrix elements

It is generally considered that the choice of a Coulomb approximation monoconfigurational approach (such as the FMP approach used here) is justified for transitions involving high-energy unperturbed Rydberg states; the transitions appearing mostly in the IR region are considered here. This approach however is reasonable for the calculation of transitions also involving low-excited and even ground states. The comparison of FMP calculations with experimental and theoretical results (including *ab initio* calculations) for transitions in Ag was presented in the previous paper (Civiš *et al* 2010b). It was shown that the agreement of FMP calculations with the experiment and with the results of other calculations is satisfactory for the majority of transitions. For few transitions, there were some discrepancies. However, the results of other theoretical calculations for these transitions differ from each other by some orders of magnitude and some are close to our results. On the other hand, the FMP calculations themselves are not our main aim in this work; we use them in analysing the relative intensities of the observed IR transitions only. To show that FMP calculations of dipole transition matrix elements are adequate for such a purpose we compare some FMP-calculated Cu oscillator strengths with the experimental and theoretical data available in the literature.

The results of such a comparison with the experiment and with other calculations are presented in table 1. The overall agreement of our calculations with other results can be considered to be reasonable. There are some large discrepancies between our data and the values from the half-century old sources given by Allen and Asaad (1957) for 4p–*n*s

Table 2. FMP-calculated transition dipole moments (oscillator strengths f_{ik}, transition probabilities A_{ki}) between the Cu I states observed in this work. The energies of all levels are taken from this measurement except those for 4f and 7s levels taken from Shenstone (1948). The air wavelengths λ are calculated using these energy values.

Transition	Lower level (cm^{-1})	Upper level (cm^{-1})	ν (cm^{-1})	λ (nm)	f_{ik}	A_{ki} (s^{-1})
$5f_{\frac{7}{2}}$–$6g_{\frac{9}{2}}$	57 911.09	59 266.676	1355.586	7374.87	1.14	1.12×10^{6}
$5f_{\frac{5}{2}}$–$6g_{\frac{7}{2}}$	57 905.041	59 267.202	1362.161	7339.28	1.17	1.08×10^{6}
$5f_{\frac{7}{2}}$–$6g_{\frac{7}{2}}$	57 911.09	59 267.202	1356.112	7372.01	3.26×10^{-2}	3.99×10^{4}
$6p_{\frac{3}{2}}$–$7s_{\frac{1}{2}}$	54 784.081	56 671.387	1887.306	5297.11	4.26×10^{-1}	2.02×10^{6}
					3.606×10^{-1}[a]	1.714×10^{6}[a]
$6s_{\frac{1}{2}}$–$6p_{\frac{3}{2}}$	52 848.752	54 784.081	1935.329	5165.67	1.02	1.28×10^{6}
					1.126×10^{-1}[a]	1.406×10^{6}[a]
$5f_{\frac{7}{2}}$–$7g_{\frac{9}{2}}$	57 911.09	60 074.98	2163.890	4620.05	2.23×10^{-1}	5.58×10^{5}
$5f_{\frac{7}{2}}$–$7g_{\frac{7}{2}}$	57 911.09	60 076.159	2165.069	4617.53	6.40×10^{-3}	2.00×10^{4}
$5f_{\frac{5}{2}}$–$7g_{\frac{7}{2}}$	57 905.041	60 076.159	2171.118	4604.67	2.31×10^{-1}	5.46×10^{5}
$6d_{\frac{5}{2}}$–$7f_{\frac{7}{2}}$	57 895.084	60 071.51	2176.426	4593.44	1.86×10^{-1}	4.41×10^{5}
$6s_{\frac{1}{2}}$–$6p_{\frac{1}{2}}$	52 848.752	55 027.763	2179.011	4587.99	5.34×10^{-1}	1.69×10^{6}
$4f_{\frac{5}{2}}$–$5g_{\frac{7}{2}}$	55 429.8	57 924.61	2494.810	4007.23	1.34	4.19×10^{6}
$4f_{\frac{7}{2}}$–$5g_{\frac{9}{2}}$	55 426.3	57 924.075	2497.775	4002.47	1.31	4.35×10^{6}
$4f_{\frac{7}{2}}$–$5g_{\frac{7}{2}}$	55 426.3	57 924.61	2498.310	4001.61	3.73×10^{-2}	1.55×10^{5}
$5d_{\frac{5}{2}}$–$5f_{\frac{5}{2}}$	55 390.569	57 905.041	2514.472	3975.89	4.16×10^{-2}	1.76×10^{5}
					4.140×10^{-2}[a]	1.745×10^{5}[a]
$5d_{\frac{3}{2}}$–$5f_{\frac{5}{2}}$	55 387.621	57 905.041	2517.420	3971.24	8.73×10^{-1}	2.46×10^{6}
					8.667×10^{-1}[a]	2.443×10^{6}[a]
$5d_{\frac{5}{2}}$–$5f_{\frac{7}{2}}$	55 390.569	57 911.09	2520.521	3966.35	8.28×10^{-1}	2.63×10^{6}
					8.235×10^{-1}[a]	2.611×10^{6}[a]
$6p_{\frac{1}{2}}$–$6d_{\frac{3}{2}}$	55 027.763	57 893.028	2865.265	3489.13	3.80×10^{-1}	1.04×10^{6}
					3.532×10^{-1}[a]	9.672×10^{5}[a]
$6p_{\frac{3}{2}}$–$6d_{\frac{3}{2}}$	54 784.081	57 893.028	3108.947	3215.65	2.59×10^{-2}	1.67×10^{5}
					2.247×10^{-2}[a]	1.448×10^{5}[a]
$5p_{\frac{1}{2}}$–$6s_{\frac{1}{2}}$	49 383.263	52 848.752	3465.489	2884.81	3.27×10^{-1}	2.62×10^{6}
					2.871×10^{-1}[a]	2.299×10^{6}[a]
$5p_{\frac{3}{2}}$–$6s_{\frac{1}{2}}$	49 382.949	52 848.752	3465.803	2884.55	3.27×10^{-1}	5.25×10^{6}
					2.870×10^{-1}[a]	4.599×10^{6}[a]
$4f_{\frac{5}{2}}$–$6g_{\frac{7}{2}}$	55429.8	59267.202	3837.402	2605.22	1.85×10^{-1}	1.37×10^{6}
$4f_{\frac{7}{2}}$–$6g_{\frac{9}{2}}$	55426.3	59266.676	3840.376	2603.20	1.80×10^{-1}	1.42×10^{6}
$4f_{\frac{7}{2}}$–$6g_{\frac{7}{2}}$	55426.3	59267.202	3840.902	2602.84	5.16×10^{-3}	5.08×10^{4}
$4f_{\frac{5}{2}}$–$7g_{\frac{7}{2}}$	55429.8	60076.159	4646.359	2151.64	5.96×10^{-2}	6.43×10^{5}
$4f_{\frac{7}{2}}$–$7g_{\frac{9}{2}}$	55426.3	60074.98	4648.68	2150.56	5.77×10^{-2}	6.66×10^{5}
$4f_{\frac{7}{2}}$–$7g_{\frac{7}{2}}$	55426.3	60076.159	4649.859	2150.02	1.66×10^{-3}	2.40×10^{4}

[a] Numerical Coulomb-like approximation (Lindgård *et al* 1980).

transitions with $n = 7, 8, 9$. In such cases, table 1 contains the corresponding oscillator strength values calculated in the Coulomb-like approximation (Lindgård *et al* 1980). We did not present here a full comparison with Lindgård *et al* (1980) because of the large data reported in it. However, since the Coulomb-like approximation used by Lindgård *et al* (1980) is in essence similar to FMP, the majority of the results of Lindgård *et al* (1980) coincide with the FMP values with a discrepancy of not more than 20%. We demonstrate this in table 2 for the transitions involving the Cu I states observed in our experiment. All the uncertainties in the tables below are given in round brackets after the corresponding values and should be treated as their rightmost significant digits, e.g. 123.4(56) means 123.4 ± 5.6.

The further analysis of the observed Cu lines given in the next section is based on the FMP calculation of the line strengths S for transitions between the $3d^{10}nl_j$ states which can be easily obtained from oscillator strengths f or transition probabilities A presented in table 2. When available, the corresponding results of Lindgård *et al* (1980) were presented for comparison; the other values have not been reported previously. Table 2 can serve as a supplement to the tables of Lindgård *et al* (1980) and to the review by Fu *et al* (1995).

3.2. Lines observed

Figure 1 shows parts of the observed IR emission spectra of Cu I at 20 μs after the laser shot, when the emission intensity is maximal for almost all of the observed lines. The list of the IR lines observed for Cu I is presented in table 3. Their full widths at half-maxima (FWHM) are calculated from fitting to the Lorentzian shape (Civiš *et al* 2010a, Civiš *et al* 2010b).

Table 3. Experimental Cu I lines and their identification. The decay time, T, was calculated by exponential fitting of the measured time profiles of the corresponding lines.

Wavenumber (cm^{-1})	Intensity (arb. units)	SNR	FWHM (cm^{-1})	Decay time (μs)	Identification
1887.307(6)	1.30×10^4	17	0.083(16)	12.1(44)[b]	$6p_{\frac{3}{2}}$–$7s_{\frac{1}{2}}$
1935.313(2)	6.58×10^4	63	0.106(5)	5.88(221)[b]	$6s_{\frac{1}{2}}$–$6p_{\frac{3}{2}}$
2163.890(16)	3.42×10^2	6.2	0.104(46)	16.2(41)[a]	$5f_{\frac{7}{2}}$–$7g_{\frac{9}{2}}$
2171.118(18)	1.64×10^2	4.6	0.074(55)	9.50(266)[a]	$5f_{\frac{5}{2}}$–$7g_{\frac{7}{2}}$
2176.426(16)	2.16×10^2	5.6	0.077(43)	12.8(34)[b]	$6d_{\frac{5}{2}}$–$7f_{\frac{7}{2}}$
2179.011(3)	7.68×10^4	58	0.065(10)	9.06(479)[a]	$6s_{\frac{1}{2}}$–$6p_{\frac{1}{2}}$
2494.8098(3)	2.98×10^5	63	0.038(1)	11.7(42)[b]	$4f_{\frac{5}{2}}$–$5g_{\frac{7}{2}}$
2497.7750(3)	3.77×10^5	121	0.041(1)	11.3(36)[b]	$4f_{\frac{7}{2}}$–$5g_{\frac{9}{2}}$
2513.814(4)	4.65×10^3	8.4	0.048(13)	11.5(41)[b]	$5d_{\frac{5}{2}}$–$5f_{\frac{5}{2}}$
2517.4511(3)	1.03×10^5	78	0.051(1)	15.0(57)[b]	$5d_{\frac{3}{2}}$–$5f_{\frac{5}{2}}$
2521.0550(3)	1.58×10^5	129	0.049(1)	14.9(57)[b]	$5d_{\frac{5}{2}}$–$5f_{\frac{7}{2}}$
2865.233(2)	2.32×10^4	37	0.062(5)	7.93(167)[b]	$6p_{\frac{1}{2}}$–$6d_{\frac{3}{2}}$
3110.955(4)	2.06×10^4	27	0.087(11)	8.53(214)[b]	$6p_{\frac{3}{2}}$–$6d_{\frac{5}{2}}$
3465.481(4)	8.46×10^4	10	0.089(13)	5.06(87)[b]	$5p_{\frac{1}{2}}$–$6s_{\frac{1}{2}}$
3465.8044(7)	1.70×10^5	23	0.048(2)	5.25(90)[b]	$5p_{\frac{3}{2}}$–$6s_{\frac{1}{2}}$
3837.402(12)	7.49×10^3	9.5	0.193(36)	8.51(209)[a]	$4f_{\frac{5}{2}}$–$6g_{\frac{7}{2}}$
3840.376(15)	9.64×10^3	11	0.235(47)	14.7(190)[a]	$4f_{\frac{7}{2}}$–$6g_{\frac{9}{2}}$

[a] Time profile demonstrates significant deviation from the exponential decay.

[b] The decay curve has essentially non-exponential form with a plateau or secondary maxima; τ value is absent or roughly approximate.

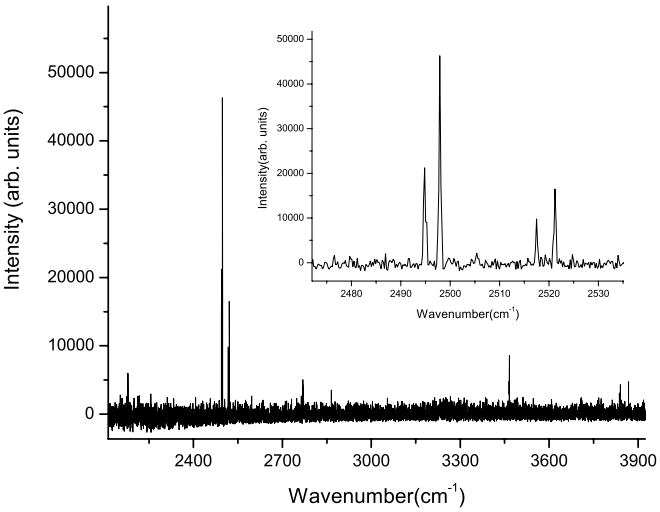

Figure 1. Observed emission IR spectrum of Cu I with a detailed structure of the most prominent lines around 2480–2530 cm^{-1}. Both the inset and the main spectrum correspond to the resolution of 0.017 cm^{-1}.

As in the previous papers (Civiš *et al* 2010a, Civiš *et al* 2010b) we have measured the emission spectrum at a different delay time, from 0 to 60 μs after the laser shot. This allows us to record the time profiles of the observed Cu lines, i.e. their emission intensities $I(t)$ as functions of the delay time, t. Such information can be helpful for diagnostics of the electronic state populations of neutral atoms in plumes formed by pulsed laser ablation (Furusawa *et al* 2004); however, there are few reports of investigations on such population dynamics (Rossa *et al* 2009). The temporal dynamics of several lines is shown in figure 2. While the temporal decay of some lines can be fitted, at least roughly, by an exponential function

$$I(t) = I_{\text{background}} + I_0 \exp\left(-\frac{t - t_0}{T}\right), \qquad (2)$$

several lines display essentially non-exponential behaviour including some 'plateaux' or even secondary maxima at 35–50 μs after the laser shot. Their decay time, T, values are therefore estimated in table 3 in a rough approximation; it is seen from this table that for essentially non-exponential decays the uncertainty ΔT is of the same order of magnitude as T itself. Note that this temporal decay is due to a complex combination of the collisional cascade repopulation of the emitting levels (Civiš *et al* 2010a) and the transfer processes in ablation products (Kawaguchi *et al* 2008). The decay times T given in table 3 are not related to the radiative lifetimes of Cu $3d^{10}nl$ levels which are at least two orders shorter (typical orders are $\sim 10^1$–10^3 ns (Fu *et al* 1995)).

After the assignment we refined the energy values for some levels involved with the classified transitions; the revised values of these energies are presented in table 4. This procedure was similar to that used in the previous paper (Civiš *et al* 2010b), but unfortunately there is no high precision data on these levels, so the overall uncertainty of the refined level energy values is roughly that achieved in the old measurements (0.01–0.03 cm^{-1} by Shenstone (1948) and 0.07 cm^{-1} by Longmire *et al* (1980)). Nevertheless, the difference between the energy value obtained in this work for $5f_{\frac{7}{2}}$ level and that reported long ago (Shenstone 1948) is about 2.5 cm^{-1} and lies beyond the uncertainty limits. Due to the better resolution of our measurements, the values listed in table 4 can be considered to be more accurate.

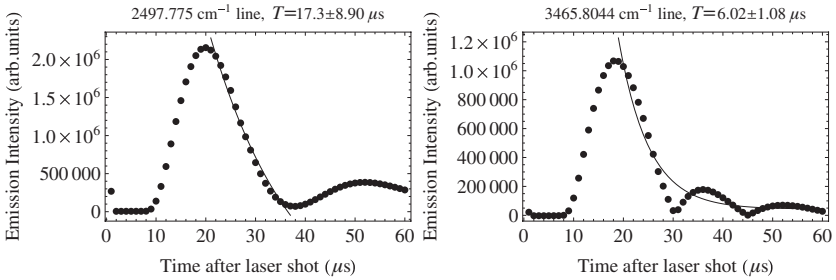

Figure 2. The time profiles of some observed Cu I lines (dots) and their fit with exponential decay (solid curves).

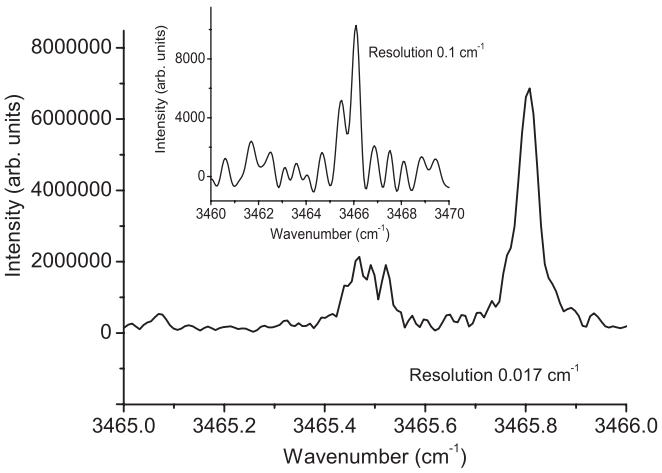

Figure 3. The $5p_{\frac{1}{2},\frac{3}{2}}$–$6s_{\frac{1}{2}}$ doublet lines of Cu I in two different resolutions. The $5p_{\frac{1}{2}}$–$6s_{\frac{1}{2}}$ component (with centre of gravity at 3465.481 cm^{-1}) is split due to the hyperfine structure.

Table 4. Revised values of some levels of Cu I.

Term	Energy (cm^{-1})	Other sources
$3d^{10}5p_{\frac{1}{2}}$	49 383.263(23)	49 383.26[a]
$3d^{10}5p_{\frac{3}{2}}$	49 382.949(14)	49 382.95[a]
$3d^{10}5d_{\frac{3}{2}}$	55 387.621(11)	55 387.668[a]
$3d^{10}5d_{\frac{5}{2}}$	55 390.569(9)	55 391.292[a]
$3d^{10}5f_{\frac{5}{2}}$	57 905.041(14)	57 905.2[a], 57 905.23[b]
$3d^{10}5f_{\frac{7}{2}}$	57 911.090(12)	57 908.7[a]
$3d^{10}5g_{\frac{7}{2}}$	57 924.610(30)	This work
$3d^{10}5g_{\frac{9}{2}}$	57 924.075(30)	This work
$3d^{10}6s_{\frac{1}{2}}$	52 848.752(9)	52 848.749[a]
$3d^{10}6p_{\frac{1}{2}}$	55 027.763(26)	55 027.74[a], 55 027.713[b]
$3d^{10}6p_{\frac{3}{2}}$	54 784.081(21)	54 784.06[a], 54 784.073[b]
$3d^{10}6d_{\frac{3}{2}}$	57 893.028(24)	57 893.05[a]
$3d^{10}6d_{\frac{5}{2}}$	57 895.084(24)	57 895.1[a]
$3d^{10}6g_{\frac{7}{2}}$	59 267.202(33)	This work
$3d^{10}6g_{\frac{9}{2}}$	59 266.676(34)	This work
$3d^{10}7f_{\frac{7}{2}}$	60 071.510(30)	This work
$3d^{10}7g_{\frac{7}{2}}$	60 076.159(23)	This work
$3d^{10}7g_{\frac{9}{2}}$	60 074.980(20)	This work

[a] Shenstone (1948).
[b] Longmire *et al* (1980).

It is interesting to note that the fine-structure 5p doublet (fine-structure splitting is about 0.3 cm^{-1}) is well resolved in our experiment, unlike the previous measurements (Shenstone 1948, Longmire *et al* 1980) where only a single blended line was observed. The ratio of the $5p_{\frac{3}{2}}$–$6s_{\frac{1}{2}}$ and $5p_{\frac{1}{2}}$–$6s_{\frac{1}{2}}$ transition intensities is close to the theoretical nonrelativistic value 2:1. This doublet is shown in figure 3 in different resolutions, the $5p_{\frac{1}{2}}$–$6s_{\frac{1}{2}}$ component demonstrates hyperfine splitting.

4. Conclusion

This work continues the series of studies of emission IR spectra of metal vapours formed in ablation by a pulsed laser radiation (Civiš *et al* 2010a, Civiš *et al* 2010b) where TR FTIR spectroscopy is applied to observations of the emission arising after the irradiation of a copper target with a pulsed laser. The knowledge of Cu spectra is extended by reporting 18 lines not previously observed. All are classified as due to transitions between low-excited states: $3d^{10}ns$ with $n = 6, 7$, $3d^{10}np$ ($n = 5, 6$), $3d^{10}nd$ ($n = 5, 6$), $3d^{10}nf$ ($n = 4, 5, 7$) and $3d^{10}ng$ ($n = 5, 6, 7$).

The line classification is performed using relative line strengths expressed in terms of transition dipole matrix elements calculated with the help of the Fues model potential; these calculations show agreement with the experimental and calculated data available in the literature. In addition to these data we calculate the transition probabilities and oscillator strengths for transitions between the reported $3d^{10}nl_j$ states of Cu I.

This study reports revised values for energies of eleven known and of seven previously not reported $3d^{10}nl$ levels of neutral Cu with $n = 4$–7 and $l = 5$–7. The newly-found 5g, 6g and 7g ^{2}G terms are inverted. We also record time profiles of the observed lines as functions of the delay time (0–60 μs) after the laser shot with maxima of emission intensity at 18–20 μs after the shot. Some lines display single-exponential temporal decay, while the decay of other lines is essentially non-exponential and demonstrates some 'plateaux' (or even secondary maxima) at 40–50 μs after the laser shot. The approximate decay time for different lines varies in the 5–15 μs range.

Acknowledgments

This work was financially supported by the Grant Agency of the Academy of Sciences of the Czech Republic (grants numbers IAA400400705 and KAN 100500652).

References

Allen C W and Asaad A S 1957 *Mon. Not. R. Astron. Soc.* **117** 36–49

Baig M A, Hanif M, Bhatti S A and Hormes J 1997 *J. Phys. B: At. Mol. Opt. Phys.* **30** 5381–99 (http://stacks.iop.org/0953-4075/30/i=23/a=007)

Baig M A, Rashid A, Hanif M, Dussa W, Ahmad I and Hormes J 1992 *Phys. Rev.* A **45** 2108–11

Bell G D, Davis M H, King R B and Routly P M 1958 *Astrophys. J.* **127** 775–96

Bell G D and Tubbs E F 1970 *Astrophys. J.* **159** 1093–100

Biémont E 1994 Infrared solar physics *154th Symp. of Int. Astronomical Union* (*IAU Symposia* vol 154) ed D M Rabin, J T Jefferies and C Lindsey pp 501–10 (1st Int. Meeting devoted to Infrared Physics, Tucson, AZ, 2–6 March 1992) http://adsabs.harvard.edu/abs/1994IAUS..154..501B

Bihain G, Israelian G, Rebolo R, Bonifaci P and Molaro P 2004 *Astron. Astrophys.* **423** 777–86

Carlsson J 1988 *Phys. Rev.* A **38** 1702–10

Civiš S, Matulková I, Cihelka J, Kawaguchi K, Chernov V E and Buslov E Y 2010a *Phys. Rev.* A **81** 012510

Civiš S, Matulková I, Cihelka J, Kubelík P, Kawaguchi K and Chernov V E 2010b *Phys. Rev.* A **82** 022502

Corliss C H 1970 *J. Res. Natl Bur. Stand.* A **74** 781–90

Cowan J J *et al* 2002 *Astrophys. J.* **572** 861–79

Cunha K, Smith V V, Suntzeff N B, Norris J E, Da Costa G S and Plez B 2002 *Astron. J.* **124** 379–88 (http://stacks.iop.org/1538-3881/124/i=1/a=379)

Curtis L J and Theodosiou C E 1989 *Phys. Rev.* A **39** 605–15

Ecuvillon A, Israelian G, Santos N C, Mayor M, Villar V and Bihain G 2004 *Astron. Astrophys.* **426** 619–30

Fu K, Jogwich M, Knebel M and Wiesemann K 1995 *At. Data Nucl. Data Tables* **61** 1–30

Furusawa H, Sakka T and Ogata Y H 2004 *J. Appl. Phys.* **96** 975–82 (http://link.aip.org/link/?JAP/96/975/1)

Grevesse N and Noels A 1994 *25th Conf. of the European-Group-for-Atomic-Spectroscopy (EGAS) (Caen, France, 13–16 July 1993), Phys. Scr.* T **51** 47–50 http://stacks.iop.org/1402-4896/T51/47

Hannaford P and Lowe R M 1983 *Opt. Eng.* **22** 532–44

Honda S, Aoki W, Ishimaru Y and Wanajo S 2007 *Astrophys. J.* **666** 1189–97 (http://iopscience.iop.org/0004-637X/666/2/1189)

Johansson S 2005 *High Resolution Infrared Spectroscopy in Astronomy: Proc. ESO Astrophysics Symposia (Garching, Germany, 18–21 Nov. 2003)* ed H U Kaufl, R Siebenmorgen and A Moorwood (Berlin: Springer) pp 62–67 (http://www.springerlink.com/content/yg313t42u72643j6/)

Jones H R A *et al* 2005 *Ultralow-Mass Star Formation and Evolution Workshop (La Palma, SPAIN, 28 June–1 July 2005), Astron. Nachr.* **326** 920–4

Jorissen A 2004 *Phys. Scr.* T **112** 73–86

Kawaguchi K, Sanechika N, Nishimura Y, Fujimori R, Oka T N, Hirahara Y, Jaman A and Civiš S 2008 *Chem. Phys. Lett.* **463** 38–41

Kerber F, Nave G, Sansonetti C J and Bristow P 2009 *Phys. Scr.* T **134** 014007

Lindgård A, Curtis L J, Martinson I and Nielsen S E 1980 *Phys. Scr.* **21** 47–62

Longmire M S, Brown C M and Ginter M L 1980 *J. Opt. Soc. Am.* **70** 423–9

Lvov B V 1970 *Opt. Spectrosk.* **28** 8–12

MacAdam K B, Dyubko S F, Efremov V A, Gerasimov V G and Kutsenko A S 2009 *J. Phys. B: At. Mol. Opt. Phys.* **42** 165009

Martin W C and Sugar J 1969 *J. Opt. Soc. Am.* **59** 1266–80

Matteucci F, Raiteri C M, Busson M, Gallino R and Gratton R 1993 *Astron. Astrophys.* **272** 421–9 http://adsabs.harvard.edu/abs/l993A%26A..272..421M

Migdałek J 1978 *J. Quant. Spectrosc. Radiat. Transfer* **20** 81–7

Migdałek J and Baylis W E 1978 *J. Phys. B: At. Mol. Phys.* **11** L497–501

Migdałek J and Baylis W E 1979 *J. Phys. B: At. Mol. Phys.* **12** 1113 (http://stacks.iop.org/0022-3700/12/i=7/a=014)

Mishenina T V, Kovtyukh V V, Soubiran C, Travaglio C and Busso M 2002 *Astron. Astrophys.* **396** 189–201

Moise N L 1966 *Astrophys. J.* **144** 774–81

Nilsson H 2009 *9th Int. Conf. on Atomic Spectroscopy and Oscillator Strengths for Astrophysical and Laboratory Plasma (Lund, Sweden, 7–10 Aug. 2007), Phys. Scr.* T **134** 014009 (http://iopscience.iop.org/1402-4896/2009/T134/014009)

Pickering J C 1999 *6th Int. Colloquium on Atomic Spectra and Oscillator Strengths (ASOS 6) (Victoria, Canada, 9–13 Aug. 1998), Phys. Scr.* T **83** 27–34 http://stacks.iop.org/1402-4896/T83/27

Prochaska J X, Naumov S O, Carney B W, McWilliam A and Wolfe A M 2000 *Astron. J.* **120** 2513–49

Rossa M, Rinaldi C A and Ferrero J C 2009 *J. Appl. Phys.* **105** 063306 (http://ieeexplore.ieee.org/xpl/freeabs_all.jsp?arnumber=5133154)

Ryde N 2009 *9th Int. Conf. on Atomic Spectroscopy and Oscillator Strengths for Astrophysical and Laboratory Plasma (Lund, Sweden, 7–10 Aug. 2007), Phys. Scr.* T **134** 014001 (http://iopscience.iop.org/1402-4896/2009/T134/014001)

Ryde N 2010 *Astron. Nachr.* **331** 433–48

Shenstone A G 1948 *Phil. Trans. R. Soc.* A **241** 297–322

Siefart E, Ney J, Bucka H and Bolouri H 1974 *J. Phys. B: At. Mol. Phys.* **7** 1279–83 (http://stacks.iop.org/0022-3700/7/i=11/a=014)

Simmerer J, Sneden C, Ivans I I, Kraft R P, Shetrone M D and Smith V V 2003 *Astron. J.* **125** 2018–28 (http://stacks.iop.org/1538-3881/125/i=4/a=2018)

Slavenas I Y Y 1966 *Opt. Spectrosk.* **20** 485–7

Sneden C, Gratton R G and Crocker D A 1991 *Astron. Astrophys.* **246** 354–67 http://adsabs.harvard.edu/abs/1991A%26A...246..354S

Sobeck J S, Primas F, Sneden C and Ivans I I 2008 *First Stars III: Int. Conf. (Santa Fe, NM, July 2007)* (*AIP Conf. Proc.* vol 990) ed B W O'Shea, A Heger and T Abel (Los Alamos National Lab.; New Mexico Consortium Institute Advance Study; Kavli Institute Particle Astrophysics & Cosmology; Joint Institute Nucl. Astrophysics; American Institute Physics, Melville, NY, USA) pp 187–91 (http://link.aip.org/link/?APC/990/187/1)

Tondello G 1973 *J. Opt. Soc. Am.* **63** 346–52

Wahlgren G M, Carpenter K G and Norris R P 2009 *Cool Stars, Stellar Systems and the Sun: 15th Cambridge Workshop (Scotland, July 2008) (AIP Conference Proceedings* vol 1094) ed E Stempels (Royal Astronomical Society; Scottish Universities Physics Alliance; European Space Agency; NASA Astrobiology Institute; America Institute Physics, Melville, NY) pp 892–5 (http://link.aip.org/link/?APC/1094/892/1)

Time-resolved Fourier-transform infrared emission spectroscopy of Ag in the (1300–3600)-cm^{-1} region: Transitions involving f and g states and oscillator strengths

S. Civiš,* I. Matulková, J. Cihelka, and P. Kubelik
J. Heyrovský Institute of Physical Chemistry, Academy of Sciences of the Czech Republic, Dolejškova 3, CZ-18223 Prague 8, Czech Republic

K. Kawaguchi
Faculty of Science, Okayama University, Tsushima-naka, Okayama 700-8530, Japan

V. E. Chernov
Voronezh State University, 394693 Voronezh, Russia
(Received 30 May 2010; published 3 August 2010)

We report on a study of the emission spectra of Ag vapor in a vacuum (10^{-2} Torr) formed in ablation of an Ag metal target by a high-repetition rate (1.0 kHz) pulsed nanosecond ArF laser ($\lambda = 193$ nm, output energy of 15 mJ). The time-resolved infrared emission spectrum of Ag was recorded in the 1300- to 3600-cm^{-1} spectral region using the Fourier transform infrared spectroscopy technique with a resolution of 0.02 cm^{-1}. The time profiles of the measured lines have maxima at 5–6 μs after a laser shot and display nonexponential decay with a decay time of 3–7 μs. The lines reported here are given with an uncertainty of 0.0005–0.016 cm^{-1}. The line classification is performed using relative line strengths expressed in terms of transition dipole matrix elements calculated with the help of the Fues model potential; these calculations show agreement with the large experimental and calculated data sets available in the literature. In addition to these data we also calculate transition probabilities and line and oscillator strengths for a number of transitions in the 1300- to 5000-cm^{-1} range between $(4d^{10})nl_j$ states of Ag.

DOI: 10.1103/PhysRevA.82.022502 PACS number(s): 32.30.Bv, 52.38.Mf, 07.57.Ty, 31.15.B−

I. INTRODUCTION

Silver has been observed in stellar spectra for several decades. The solar abundance of AgI has been evaluated based on measurements of the 3280.7 Å and 3382.9 Å lines [1]. The neutral silver 3382.9 Å line was detected in the spectra of stars of Se [2] and Ap type (e.g., the 4210.94 Å and 4668.48 Å lines in the Cr-Eu-Sr subgroup star [3] and the 5209.1 Å and 5465.5 Å lines in a Przybylski's star [4]). The AgI abundances obtained from 3382.9 Å and 3280.7 Å line measurements in metal-poor halo stars [5,6] were employed to study the processes of the chemical evolution of the Galaxy. For the correct interpretation of high-resolution astrophysical spectra, improved accuracy is required for atomic-level energies and transition probabilities (or oscillator strengths) data [7,8], including the infrared (IR) spectral region [9]. Infrared astronomy is very promising in studies of dust-obscured objects and interstellar clouds, cool objects such as brown dwarfs, and objects at cosmological distances from Earth [10].

Although the spectra of Ag have been studied for some decades [11–27], only a few lines in the IR region have been reported since a century ago: the two lines 2502.4 and 2506.3 cm^{-1} [11] and seven lines in the 5438–13004 cm^{-1} range [12]. One of the present work's aims is to supply information on Ag spectra in the 1300- to 3600-cm^{-1} range. This article continues our study of the IR spectra of metals started in Ref. [28].

The terms of the neutral Ag atom can be classified according to the $4d$ core state. The simplest level structure originates from the closed $4d^{10}$ core yielding $(4d^{10})nl_j$ states with a total angular momentum $J = j = l \pm \frac{1}{2}$ [13,16,19,25,26]. Other terms arise due to excitation of a $4d$ electron into a $n'l'$ state yielding $4d^9 5sn's$ [13,15,16,22,24,25], $4d^9 5sn'p$ [16–23,25,27], $4d^9 5sn'd$ [16,18,22], and $4d^9 5sn'f$ [20,23,27] states. These states are treated in terms of LS coupling with parentage schemes $4d^9(^3D_{J_{\rm II}})5s(^{1,3}D_{1,2,3})n'l'[^{2S+1}L_J]$ (Refs. [13,15,16,18–20,22,24,25]) or $5s5p(^{1,3}P_{J_{\rm I}})4d^{10}[^{2S+1}L_J]$ (Refs. [17,21]) as well as jj coupling $[(5s5p)_{J_{\rm I}}(4d^{10})_{J_{\rm II}}]_J$ (Ref. [17]) or the J_cK coupling scheme $4d^9 5s(^{1,3}D_{1,2,3})n'l'[K]_J$ (with $l' = 1,3$ [23,27]). The level diagrams of Ag can be found in Refs. [20,24,25].

One of the first comprehensive lists of Ag lines and term values was published by Shenstone [16]. Together with the results of his own measurements in the 40000- to 1250 Å (2500- to 80,000 cm^{-1}) range using an arc and hollow cathode lamp, Shenstone reported some lines observed previously by other researchers [11–14]. In the same year Rasmussen [15] reported values of some new levels, including the $4d^9 5s^2[^2D_{\frac{3}{2},\frac{5}{2}}]$ metastable doublet. More than 30 years later these data were extended by Johannsen and Linke's measurements of the Ag arc spectrum in the 1100 to 9800 Å range yielding values for some core-excited $4d^9 5sn'l'$ levels with $l' = 0,1,2$. The core-excited $4d^9 n'l'$ states were studied both by numerical *ab initio* calculations [17] and by VUV photoabsorption [19–23,27]; for $n' \geqslant 5$ or $l' \geqslant 2$ these levels correspond to autoionizing states lying above the first ionization threshold of Ag.

The most comprehensive reports of the closed-core $(4d^{10})nl_j$ states of Ag were made by Brown and Ginter [19] for np states up to $n = 71$ and by MacAdam *et al.* [26]

*Corresponding author: e-mail: civis@jh-inst.cas.cz

 ©2010 The American Physical Society

for s, p, and d states for $n = 28 - 39$. The most accurate values of $(4d^{10})nl_j$ level energies for $n \leqslant 10$ (as well as $4d^9 5s^2 2D_{\frac{3}{2},\frac{5}{2}}$ and $4d^9 5s(^3D_3)[^4P_{\frac{3}{2}\frac{5}{2}}]$ level energies) were presented by Pickering and Zilio [25] and therefore we use their level energies as "reference" values in the identification of the IR lines measured in this work (see subsection IV B below).

However, due to the great number of Rydberg levels populated in the conditions of a laser ablated plasma, the above information on Ag levels is not always sufficient for correct classification of the observed IR emission lines. While the $(4d^{10})nl$ level energies for $l \leqslant 2$ can be obtained by interpolation of the above cited data sources, such interpolation is impossible for f and g levels (i.e., $l = 3,4$) since their energies are known for only one or two n values ($n = 4,5$ for f states and $n = 5$ for the g state without fine structure) obtained 70 years ago [16]. To identify the transitions involving these and other low-Rydberg Ag levels, we use the information on the relative intensity of the transitions between Ag $(4d^{10})nl$ levels. Such information is obtained here by the calculation of dipole transition matrix elements (or transition dipole moments) using the Fues model potential (FMP) approach (see Sec. III).

The transition dipole moments for the Ag atom have been studied for some decades both theoretically and experimentally, and in the literature they are most frequently reported as oscillator strengths. Direct experimentally measured data on oscillator strengths in Ag, to our knowledge, are available mostly for the resonance doublet, i.e., for the $5s_{\frac{1}{2}} - 5p_{\frac{1}{2},\frac{3}{2}}$ transitions. The oscillator strengths for these transitions were obtained by Hinnov and Kohn [29] from the measured density dependence of the intensity of the atomic lines emitted by an acetylene-air flame; this dependence is determined by the cross section of the collisional interaction between the emitting atoms with foreign molecules (optical cross section). Some years later, the oscillator strengths for the Ag resonance doublet were measured: by Penkin and Slavenas [30] using the anomalous dispersion curves (Rozhdestvenskii hook method); by Lawrence, Link, and King [31] using the atomic-beam technique; by Moise [32] using curves of growth in the furnace absorption tube along with vapor-pressure data; by Levin and Budick [33] using level-crossing spectroscopy (Hanle effect); by Klose [34] using delayed coincidence with excitation of the $5p_{\frac{3}{2}}$ level by a tunable dye laser; by Selter and Kunze [35] with direct observation of the exponential decay of the $5p_{\frac{3}{2}}$ level excited by a pulsed dye laser; by Hannaford and Lowe [36] using laser-induced fluorescence on an uncollimated atomic beam; and by Soltanolkotabi and Gupta [37] using level-crossing spectroscopy (Hanle effect).

The most accurate measurement of the oscillator strengths for the Ag resonance doublet was performed by Carlsson, Jonsson, and Sturesson [38] using time-resolved laser spectroscopy with delayed coincidence technique. A review of experimental methods for the determination of oscillator strengths of resonance atomic lines was presented by Doidge [39]. A critical compilation of oscillator strengths for 2249 spectral lines arising from the ground states of atoms and ions for astronomy needs is given in Ref. [40].

The experimental data on f values for the transition between excited states are scarce. The oscillator strengths for the second doublet $5s_{\frac{1}{2}} - 6p_{\frac{1}{2},\frac{3}{2}}$ were measured by Slavenas [41] using the Rozhdestvenskii hook method. The radiative lifetimes of the $(4d^{10})nd_{\frac{3}{2},\frac{5}{2}}$ and $(4d^{10})ns_{\frac{1}{2}}$ levels (and some core-excited states) of Ag were measured by Plekhotkina [42] using delayed coincidence with electron-beam excitation for n up to 8. Zhankui *et al.* [43] measured the lifetimes of the $(4d^{10})nd_{\frac{3}{2}}$ and $(4d^{10})ns_{\frac{1}{2}}$ states with n up to 10 by direct recording of time-resolved fluorescence decay curves with selective stepwise excitation using two pulsed dye lasers. Bengtsson *et al.* measured the lifetimes of the $(4d^{10})6p_{\frac{1}{2},\frac{3}{2}}$ [44] and $(4d^{10})7p_{\frac{1}{2},\frac{3}{2}}$ [45] states using both level-crossing and time-resolved spectroscopy methods.

One of the first theoretical calculations of oscillator strengths in the Ag isoelectronic series was performed by Cheng and Kim [46] using the multiconfiguration Hartree-Fock method (RHF) and by Migdałek and Baylis [47–50] using single-configuration RHF combined with relativistic model potential (RMP) methods. The latter methods were based on local approximations for the valence electron's exchange interaction [50] (these approximations will be denoted by roman numerals in the further comparison with present work calculations). Moreover, these authors also considered the core-polarization (CP) effects by the mean of one-electron dipole potential of the core due to its static polarizability. The influence of this potential on the oscillator strengths both *via* the valence electron wave functions and via the dipole transition operator was studied separately [48]. The above dipole potential was regularized at small distances using an effective core radius r_0 which was set equal to the mean radius of the outermost core orbital or the value was adjusted to match experimental energy levels; these cases are denoted as (A) and (B) correspondingly in the further comparison with the results of Migdałek and Baylis.

The effect of the induced dipole moment of the core (due to its dynamic polarizability) on the oscillator strengths was studied by Chichkov and Shevelko [51] using a Coulomb-like approximation for radial matrix elements for the dipole transition of the valence electron. A variant of the Coulomb-like approximation, the quantum-defect orbital (QDO) method, was used by Martín, Almaraz, and Lavin [52,53] for the calculation of oscillator strengths for Ag isoelectronic series with an account for relativistic (RQDO) and CP effects. As will be shown below, the Coulomb-like approximation [including the Fues model potential (FMP) exploited in this work] gives good results for the Ag oscillator strengths. For the majority of the transition studied, the Coulomb-like approximation gives results close to those of *ab initio* calculations.

One of recent *ab initio* studies of oscillator strengths for the Ag isoelectronic series was performed by Migdałek and Garmulewicz [54] using single-configuration Dirac-Fock (DF) with an account for exchange by local model potentials (denoted as DX with a roman numeral enumerating their types). Safronova, Savukov, and Johnson [55] performed calculations of oscillator strengths, transition probabilities, level energies, and lifetimes in Ag isoelectronic series using third-order relativistic many-body perturbation theory

TABLE I. Oscillator strengths ($f \times 100$) and wavelengths for $5s \rightarrow 5p$ transitions in Ag. CP means an account for core polarization, (P) and (T) means CP account in the potential and in transition matrix element; I–IV denote different variants for local exchange potential; (A) and (B) denote different variants of effective core radius choice (see text for more details).

	$5s_{\frac{1}{2}} \rightarrow 5p_{\frac{1}{2}}$		$5s_{\frac{1}{2}} \rightarrow 5p_{\frac{3}{2}}$	
Method	λ (Å)	$f \times 100$	λ (Å)	$f \times 100$
Optical cross section [29]	3383.	22.	3281.	39.
Rozhdestvenskii hook [30]		24.7(4)		50.6(4)
Atomic beam [31]	3382.89	21.5(22)	3280.68	45.0(45)
Absorption tube [32]	3383.	19.6(15)	3280.	45.9(34)
Hanle effect [33][a]				43.7(41)
Delayed coincidence [34][a]				49.7(50)
Laser-ind. fluoresc. [35]			3280.7	44.(2)
Laser-ind. fluoresc. [36][a]		25.3(11)		51.3(16)
Hanle effect [37][a]		22.7(7)		50.9(14)
Del. coincidence [38][a]		23.2(1)		47.6(2)
From compil. tables [40]	3283.836	21.0	3281.627	45.2
RHF [46]	4126.	32.9	4025.	66.6
RHF [47]		40.3		82.2
RHF + CP [47]		19.8		41.3
RMPI [48]	3383.86	32.9	3281.5	67.2
RMPI + CP(A) [48]	3383.86	21.5	3281.5	44.6
RHF + CP(P) [49]		34.0		69.5
RHF + CP(PT) [49]		21.4		44.5
RMPII [50]		34.4		70.2
RMPII + CP(A) [50]		20.8		43.4
RMPI + CP(B) [50]		19.6		41.0
RMPII + CP(A) [50]		22.1		46.0
RMPII + CP(B) [50]		21.3		44.4
QDO [53]		22.713		45.425
RQDO [53]		22.402		45.714
RQDO + CP [53]		19.400		39.674
DXI + CP [54]		21.4		44.5
DXIII + CP [54]		23.5		48.6
DXIV + CP [54]		23.7		48.9
DF + CP [54]		22.2		46.2
RMBPT [55]	3562.14	24.97	3454.71	51.34
MCHF + BP [56]	4157.67	37.204	4073.05	36.3846
FMP (this work)	3383.85	27.9	3281.626	57.2

[a]The f values are extracted from the reported lifetimes according to the Eqs. (2) and (3) using FMP-calculated ratios.

(RMBPT). Özdemir, Karaçoban, and Ürer [56] calculated oscillator strengths and transition probabilities in neutral Ag using the multiconfiguration Hartree-Fock method with Breit-Pauli relativistic correction (MCHF + BP).

In the present work oscillator and line strengths are calculated using the FMP approach briefly sketched in Sec. III. The comparison tables presented in subsection IV A show reasonable agreement of our calculations with the above experimental and numerical results. The line strengths calculated for the transitions in the 1300- to 5000-cm^{-1} range are used in subsection IV B for classification of the observed lines resulting in revised values for some terms of neutral Ag. The experimental setup has already been published in detail in our previous articles [28,57] and therefore the following section gives a brief description only. All the uncertainties are given in round brackets after the corresponding values and should be treated as their rightmost significant digits, e.g., 112.8(72) means 112.8 ± 7.2.

II. EXPERIMENTAL

Time-resolved Fourier-transform infrared (FTIR) spectroscopy was applied for observations of the emission arising after the irradiation of metals with a pulsed nanosecond ArF ($\lambda = 193$ nm) laser at fluences between 2 and 20 J/cm^2. A high-repetition-rate ArF laser ExciStar S-Industrial V2.0 1000 (193 nm, laser pulse width 12 ns, frequency 1 kHz) with 15-mJ output power was focused on a rotating and linearly traversing silver target inside a vacuum chamber (average pressure 10^{-2} Torr).

The time-resolution FTIR spectra were measured using the Bruker IFS 120 HR spectrometer (modified for the

TABLE II. Oscillator strengths ($f \times 100$) for $5p \rightarrow ns$ transitions in Ag. For description of the methods see Table I and text.

Method	$5p \rightarrow 6s$		$5p \rightarrow 7s$		$5p \rightarrow 8s$		$5p \rightarrow 9s$		$5p \rightarrow 10s$	
$J_l \rightarrow J_u$	$\frac{1}{2} \rightarrow \frac{1}{2}$	$\frac{3}{2} \rightarrow \frac{1}{2}$	$\frac{1}{2} \rightarrow \frac{1}{2}$	$\frac{3}{2} \rightarrow \frac{1}{2}$	$\frac{1}{2} \rightarrow \frac{1}{2}$	$\frac{3}{2} \rightarrow \frac{1}{2}$	$\frac{1}{2} \rightarrow \frac{1}{2}$	$\frac{3}{2} \rightarrow \frac{1}{2}$	$\frac{1}{2} \rightarrow \frac{1}{2}$	$\frac{3}{2} \rightarrow \frac{1}{2}$
Delayed coincidence [42][a]			1.69(13)	1.58(18)	0.338(32)	0.311(29)				
Laser-ind. fluoresc. [43][a]	14.5(19)	14.9(20)	1.32(12)	1.23(12)	0.480(50)	0.441(45)	0.224(19)	0.205(17)	0.120(8)	0.109(7)
RMPI [48]	14.5	15.4	1.50	1.46						
RMPI + CP(A) [48]	15.7	16.6	1.58	1.53						
RHF [50]	21.6	22.4	1.68	1.59	0.535	0.501	0.248	0.231		
RMPI [50]	14.5	15.4	1.50	1.46	0.504	0.488	0.239	0.230		
RMPII [50]	15.2	16.2	1.60	1.57	0.532	0.513	0.251	0.240		
RHF + CP [50]	15.8	16.7	1.68	1.61	0.574	0.542	0.273	0.257		
RMPI + CP(A) [50]	16.0	16.8	1.69	1.62	0.573	0.540	0.273	0.255		
RMPI + CP(B) [50]	16.1	16.9	1.72	1.65	0.589	0.552	0.282	0.262		
RMPII + CP(A) [50]	15.9	16.8	1.65	1.58	0.557	0.528	0.264	0.249		
RMPII + CP(B) [50]	15.7	16.6	1.66	1.58	0.557	0.524	0.264	0.248		
DXI + CP [54]	16.1	17.0								
DXIII + CP [54]	15.4	16.5								
DXIV + CP [54]	17.0	17.7								
DF + CP [54]	16.1	17.0								
MCHF + BP [56]	0.763	1.05	0.443	0.904						
FMP (this work)	16.6	17.1	1.49	1.38	0.480	0.441	0.222	0.203	0.123	0.112

[a]The f values are extracted from the reported lifetimes according to the Eqs. (2) and (3) using FMP-calculated ratios.

TABLE III. Oscillator strengths ($f \times 10^4$) for $5s \rightarrow np$ transitions in Ag. For description of the methods see Table I and text.

Method	$5s \rightarrow 6p$		$5s \rightarrow 7p$		$5s \rightarrow 8p$		$5s \rightarrow 9p$		$5s \rightarrow 10p$	
$J_l \rightarrow J_u$	$\frac{1}{2} \rightarrow \frac{1}{2}$	$\frac{1}{2} \rightarrow \frac{3}{2}$	$\frac{1}{2} \rightarrow \frac{1}{2}$	$\frac{1}{2} \rightarrow \frac{3}{2}$	$\frac{1}{2} \rightarrow \frac{1}{2}$	$\frac{1}{2} \rightarrow \frac{3}{2}$	$\frac{1}{2} \rightarrow \frac{1}{2}$	$\frac{1}{2} \rightarrow \frac{3}{2}$	$\frac{1}{2} \rightarrow \frac{1}{2}$	$\frac{1}{2} \rightarrow \frac{3}{2}$
Hook [41]	11.(2)	45.(8)								
Laser-ind. fluoresc. [44,45][a]	45.1(29)	112.8(72)	13.5(12)	30.9(24)						
MCHF [44][a]	110.	258.8								
From compil. tables [40]	9.64	39.5								
RHF [50]	110.	289.	23.4	67.2	8.82	26.6	4.34	13.4		
RMPI [50]	57.3	167.	10.6	35.4	3.75	13.4	1.77	6.62		
RMPII [50]	66.1	188.	13.6	43.3	5.10	17.1	2.50	8.65		
RHF + CP [50]	5.91	32.9	0.00965	2.24	0.0808	0.279	0.118	0.0419		
RMPI + CP(A) [50]	4.34	27.5	0.0344	1.24	0.247	0.0578	0.258	0.00033		
RMPI + CP(B) [50]	1.35	16.3	0.652	0.847	0.898	0.0129	0.726	0.28		
RMPII + CP(A) [50]	8.22	40.3	0.112	3.48	0.0153	0.613	0.0498	0.156		
RMPII + CP(B) [50]	3.93	27.0	0.0599	1.18	0.291	0.0485	0.293	0.00118		
MP + BP [51]	3.6	23.	0.48	0.051	1.1	0.31	1.0	0.53		
QDO [53]	128.9	257.7	37.0	74.0	16.0	32.1	8.5	16.9	5.1	10.2
RQDO [53]	117.0	269.9	33.2	77.9	14.3	33.9	7.6	17.9	4.5	10.9
RQDO + CP [53]	86.5	203.5	23.2	56.0	9.8	23.8	5.1	12.4	3.0	7.5
MCHF + BP [56]	0.7605	75.95								
FMP (this work)	111.	265.	28.4	70.1	11.7	29.2	6.0	15.0	3.51	9.07

[a]The f values are extracted from the reported lifetimes according to Eqs. (2) and (3) using FMP-calculated ratios.

TABLE IV. Oscillator strengths ($f \times 100$) for $5p \rightarrow nd$ transitions in Ag. For description of the methods see Table I and text.

Method	$5p \rightarrow 5d$			$5p \rightarrow 6d$			$5p \rightarrow 7d$			$5s \rightarrow 8d$			$5p \rightarrow 9d$		
$J_l \rightarrow J_u$	$\frac{1}{2} \rightarrow \frac{3}{2}$	$\frac{3}{2} \rightarrow \frac{3}{2}$	$\frac{3}{2} \rightarrow \frac{5}{2}$	$\frac{1}{2} \rightarrow \frac{3}{2}$	$\frac{3}{2} \rightarrow \frac{3}{2}$	$\frac{3}{2} \rightarrow \frac{5}{2}$	$\frac{1}{2} \rightarrow \frac{3}{2}$	$\frac{3}{2} \rightarrow \frac{3}{2}$	$\frac{3}{2} \rightarrow \frac{5}{2}$	$\frac{1}{2} \rightarrow \frac{3}{2}$	$\frac{3}{2} \rightarrow \frac{3}{2}$	$\frac{3}{2} \rightarrow \frac{5}{2}$	$\frac{1}{2} \rightarrow \frac{3}{2}$	$\frac{3}{2} \rightarrow \frac{3}{2}$	$\frac{3}{2} \rightarrow \frac{5}{2}$
Delayed coincidence [42][a]	53.1(3.3)	5.52(3)		11.3(12)	1.12(12)		4.18(38)	0.407(37)	3.97(28)						
Laser-ind. fluoresc. [43] [a]	62.3(170)	6.48(177)		13.1(20)	1.30(20)		4.22(41)	0.411(40)		2.17(16)	0.210(16)		1.20(9)	0.115(8)	
RHF [46]	71.1		66.9												
RHF [47]	88.2	9.1	22.0												
RHF + CP [47]	56.2	6.0	53.2												
RMPI [48]	60.2	6.35	56.9	13.3	1.33	11.9									
RMPI + CP [48]	55.8	5.92	53.0	11.4	1.16	10.4									
RHF [49]	88.2	9.15	82.0												
RHF + CP(P) [49]	61.8	6.53	58.5												
RHF + CP(PT) [49]	56.5	5.99	53.6												
RHF [50]	88.2	9.15	82.0	15.5	1.52	13.7	5.72	0.550	4.97	2.81	0.267	2.42	1.61	0.152	1.38
RMPI [50]	60.2	6.35	56.9	13.3	1.33	12.0	5.21	0.509	4.60	2.63	0.254	2.30	1.52	0.146	1.33
RMPII [50]	61.3	6.49	5.79	13.1	0.131	11.8	5.06	0.498	4.48	2.54	0.247	2.23	1.47	0.142	1.29
RHF + CP [50]	56.4	5.98	53.6	11.5	1.16	10.4	4.4	0.435	3.94	2.21	0.215	1.95	1.28	0.123	1.12
RMPI + CP(A) [50]	55.9	5.93	53.1	11.4	0.114	10.3	4.33	0.425	3.84	2.15	0.209	1.89	1.24	0.120	1.08
RMPI + CP(B) [50]	55.2	5.86	52.4	11.2	1.12	10.1	4.24	0.417	3.77	2.10	0.205	1.85	1.21	0.117	1.06
RMPII + CP(A) [50]	56.3	5.97	53.5	11.4	1.12	10.3	4.35	0.428	3.87	2.16	0.211	1.91	1.25	0.121	1.09
RMPII + CP(B) [50]	55.0	5.86	52.4	11.2	1.12	10.1	4.25	0.418	3.77	2.11	0.206	1.86	1.21	0.117	1.07
QDO [52]	61.19	6.12	55.08	13.13	1.31	11.81	5.16	0.52	4.65	2.62	0.26	2.35	1.52	0.15	1.37
RQDO [52]	59.69	6.20	55.75	13.18	1.31	11.78	5.23	0.51	4.61	2.66	0.26	2.33	1.56	0.15	1.36
RQDO + CP [52]	54.60	5.69	51.16	11.47	1.14	10.28	4.44	0.43	3.92	2.23	0.22	1.95	1.29	0.12	1.13
DXI + CP [54]	56.4	6.1	54.2												
DXIII + CP [54]	50.4	5.5	49.1												
DXIV + CP [54]	66.3	6.9	62.0												
DF + CP [54]	58.3	5.6	55.5												
RMBPT [55]	57.73	6.13	54.91												
MCHF + BP [56]	1.97077	0.385625	2.3042	1.0736	0.210415	1.2734									
FMP (this work)	59.7	6.20	55.8	13.2	1.31	11.8	5.23	0.510	4.61	2.66	0.257	2.33	1.56	0.150	1.36

[a]The f values are extracted from the reported lifetimes according to the Eqs. (2) and (3) using FMP-calculated ratios.

TABLE V. Comparison of oscillator strengths ($f \times 100$) in Ag calculated using quantum-defect orbitals (Ref. [53] for $6s \rightarrow np$ transitions and Ref. [52] for $5p \rightarrow 10d$ transitions; see also the Tables I and IV) with the present FMP calculation and the laser-induced measurement of the radiative lifetimes of $6s_{\frac{1}{2}}$ [44] and $7s_{\frac{1}{2}}$ [45] levels (the f values are extracted by Eqs. (2) and (3) using FMP-calculated ratios).

Transition	QDO	RQDO	RQDO + CP	Expt.	FMP (this work)
$6s_{\frac{1}{2}} \rightarrow 6p_{\frac{1}{2}}$	39.480	39.234	38.572	16.0(10)	39.3
$6s_{\frac{1}{2}} \rightarrow 6p_{\frac{3}{2}}$	78.960	79.156	77.865	33.8(22)	79.2
$6s_{\frac{1}{2}} \rightarrow 7p_{\frac{1}{2}}$	1.737	1.545	1.448	73.2(64)	1.54
$6s_{\frac{1}{2}} \rightarrow 7p_{\frac{3}{2}}$	3.474	3.671	3.465	1.62(13)	3.67
$6s_{\frac{1}{2}} \rightarrow 8p_{\frac{1}{2}}$	0.450	0.389	0.355		0.390
$6s_{\frac{1}{2}} \rightarrow 8p_{\frac{3}{2}}$	0.900	0.963	0.886		0.964
$6s_{\frac{1}{2}} \rightarrow 9p_{\frac{1}{2}}$	0.188	0.162	0.144		0.161
$6s_{\frac{1}{2}} \rightarrow 9p_{\frac{3}{2}}$	0.376	0.403	0.365		0.403
$6s_{\frac{1}{2}} \rightarrow 10p_{\frac{1}{2}}$	0.100	0.084	0.074		0.084
$6s_{\frac{1}{2}} \rightarrow 10p_{\frac{3}{2}}$	0.201	0.218	0.196		0.218
$5p_{\frac{1}{2}} \rightarrow 10d_{\frac{1}{2}}$	0.97	0.99	0.82		0.994
$5p_{\frac{3}{2}} \rightarrow 10d_{\frac{3}{2}}$	0.10	0.10	0.08		0.0954
$5p_{\frac{3}{2}} \rightarrow 10d_{\frac{5}{2}}$	0.88	0.87	0.71		0.866

time-resolution scan of emission data) in a spectral range of 1800–6000 cm^{-1} using a CaF_2 beam splitter and InSb detector. In the 1200- 1800-cm^{-1} spectral range a mercury-cadmium-telluride (MCT) detector was used. The infrared emission (axial distance from the target 10 mm) was focused into the spectrometer using a CaF_2 lens.

For data sampling, we used so-called 1/3 sampling [28], where the scanner velocity was set to produce a 3-kHz He-Ne laser interference signal, and the ArF laser oscillation was triggered at one-third of the He-Ne frequency. Measurements were carried out with a resolution of 0.02 cm^{-1} and three scans were needed to complete the interferogram. Three to thirty scans were usually coadded to obtain a reasonable signal-to-noise ratio (SNR). The infrared emission was observed in the 1800- to 3600-cm^{-1} (with MID IR interference filter) spectral region with a time profile showing maximum emission intensity in 5–6 μs after a laser shot. The acquired spectra and accumulated line profiles were postzero filled by a factor of 4 and analyzed using using a commercial software routine (Bruker OPUS version 3.1) [58]. Subsequently, the spectra were corrected by subtracting the blackbody background spectrum.

III. TRANSITION DIPOLE MOMENTS: THE FUES MODEL POTENTIAL CALCULATION

Under thermal equilibrium conditions, the intensity of a spectral line due to radiative transition from the upper state $|k\rangle$ to the lower state $|i\rangle$ is proportional to the transition probability $A_{k\rightarrow i}$ [59]:

$$I_{k\rightarrow i} \sim g_k A_{k\rightarrow i} \omega_{ik} \mathrm{e}^{-E_k/T}, \tag{1}$$

where E_k and g_k are the upper level's excitation energy and degeneracy factor, respectively, $\omega_{ik} = E_k - E_i$ is the transition frequency and T is the temperature. In the majority of experimental works the transition probability, $A_{k\rightarrow i}$, is determined by measurements of the upper level's lifetime, τ_k:

$$\tau_k = \sum_l A^{-1}_{k\rightarrow i}. \tag{2}$$

If the probabilities of transitions other than the $|k\rangle \rightarrow |i\rangle$ transition are not significant then $\tau_k = A^{-1}_{k\rightarrow i}$. This is the case for the Ag resonance doublet, i.e., for $|k\rangle = |5p_{\frac{1}{2},\frac{3}{2}}\rangle$. The probabilities $A_{k\rightarrow i}$ for the electric dipole $|k\rangle \rightarrow |i\rangle$ transition can be expressed in terms of oscillator strengths [39]:

$$\begin{aligned} f_{i\rightarrow k} &= \frac{m_\mathrm{e} c^2}{2\alpha\hbar\omega^2_{ik}} \frac{g_k}{g_i} A_{k\rightarrow i} = \frac{m_\mathrm{e} c \lambda^2_{ik}}{8\pi^2 e^2} \frac{g_k}{g_i} A_{k\rightarrow i} \\ &\simeq 1.50 \times 10^{-16} \lambda^2_{ik} \frac{g_k}{g_i} A_{k\rightarrow i}. \end{aligned} \tag{3}$$

Here m_e and e are the electron mass and charge, c is the light velocity, $\alpha = \frac{e^2}{\hbar c} \simeq 1/137.036$ is the fine-structure constant, $\hbar$ is the Planck constant, and λ_{ik} is the transition wavelength. If the hyperfine structure is not taken into account, the degeneracy factor $g_s = 2J_s + 1$ is determined by the total angular momentum, J_s ($s = i,k$). The last numerical expression (3) assumes $A_{k\rightarrow i}$ to be measured in s^{-1} and λ_{ik} in Ångströms.

In our analysis of the relative line intensities it is convenient to use the line strengths

$$S_{i\rightarrow k} = \frac{3\hbar e^2 g_i}{2m_\mathrm{e}\omega_{ik}} f_{i\rightarrow k} \tag{4}$$

since, according to Eq. (1), the line intensity is proportional to the S value.

The above f, A, and S values can be expressed in terms of a dipole transition matrix element (so-called transition dipole moment). The wave function of an atomic state with one

TABLE VI. Comparison of oscillator strengths ($f \times 100$) for transitions from np states in Ag ($n = 5 - 10$) with the data extracted from the experimental lifetimes ns and nd levels [42,43] with the help of Eqs. (2) and (3) using FMP-calculated ratios).

Transition	[42]	[43]	FMP (this work)	Transition	[42]	[43]	FMP (this work)
$6p_{\frac{1}{2}} \rightarrow 7s_{\frac{1}{2}}$	36.3(28)	28.6(27)	32.2	$8p_{\frac{1}{2}} \rightarrow 9s_{\frac{1}{2}}$		61.2(52)	60.7
$6p_{\frac{3}{2}} \rightarrow 7s_{\frac{1}{2}}$	37.2(29)	29.1(28)	32.7	$8p_{\frac{3}{2}} \rightarrow 9s_{\frac{1}{2}}$		62.9(53)	61.6
$6p_{\frac{1}{2}} \rightarrow 8s_{\frac{1}{2}}$	1.64(15)	2.33(24)	2.33	$8p_{\frac{1}{2}} \rightarrow 10s_{\frac{1}{2}}$		3.86(26)	3.96
$6p_{\frac{3}{2}} \rightarrow 8s_{\frac{1}{2}}$	1.50(14)	2.12(22)	2.12	$8p_{\frac{3}{2}} \rightarrow 10s_{\frac{1}{2}}$		3.48(23)	3.57
$6p_{\frac{1}{2}} \rightarrow 9s_{\frac{1}{2}}$		0.731(62)	0.726	$8p_{\frac{1}{2}} \rightarrow 7d_{\frac{3}{2}}$	15.1(14)	15.3(15)	18.9
$6p_{\frac{3}{2}} \rightarrow 9s_{\frac{1}{2}}$		0.654(55)	0.649	$8p_{\frac{3}{2}} \rightarrow 7d_{\frac{3}{2}}$	0.748(68)	0.755(74)	0.936
$6p_{\frac{1}{2}} \rightarrow 10s_{\frac{1}{2}}$		0.328(22)	0.336	$8p_{\frac{3}{2}} \rightarrow 7d_{\frac{5}{2}}$	8.32(59)		9.68
$6p_{\frac{3}{2}} \rightarrow 10s_{\frac{1}{2}}$		0.291(19)	0.299	$8p_{\frac{1}{2}} \rightarrow 8d_{\frac{3}{2}}$		40.5(31)	49.6
$6p_{\frac{1}{2}} \rightarrow 5d_{\frac{3}{2}}$	8.10(50)	9.50(259)	9.10	$8p_{\frac{3}{2}} \rightarrow 8d_{\frac{3}{2}}$		4.54(35)	5.56
$6p_{\frac{3}{2}} \rightarrow 5d_{\frac{3}{2}}$	0.438(27)	0.514(140)	0.492	$8p_{\frac{1}{2}} \rightarrow 9d_{\frac{3}{2}}$		10.6(8)	13.8
$6p_{\frac{1}{2}} \rightarrow 6d_{\frac{3}{2}}$	43.5(48)	50.5(78)	50.8	$8p_{\frac{3}{2}} \rightarrow 9d_{\frac{3}{2}}$		1.13(8)	1.47
$6p_{\frac{3}{2}} \rightarrow 6d_{\frac{3}{2}}$	4.70(51)	5.46(84)	5.49	$9p_{\frac{1}{2}} \rightarrow 10s_{\frac{1}{2}}$		72.7(48)	74.6
$6p_{\frac{1}{2}} \rightarrow 7d_{\frac{3}{2}}$	10.4(9)	10.5(10)	13.0	$9p_{\frac{3}{2}} \rightarrow 10s_{\frac{1}{2}}$		73.7(49)	75.6
$6p_{\frac{3}{2}} \rightarrow 7d_{\frac{3}{2}}$	1.07(10)	1.08(11)	1.34	$9p_{\frac{1}{2}} \rightarrow 8d_{\frac{3}{2}}$		19.3(15)	23.6
$6p_{\frac{3}{2}} \rightarrow 7d_{\frac{5}{2}}$	10.4(7)		12.0	$9p_{\frac{3}{2}} \rightarrow 8d_{\frac{3}{2}}$		0.983(76)	1.20
$6p_{\frac{1}{2}} \rightarrow 8d_{\frac{3}{2}}$		4.51(35)	5.53	$9p_{\frac{1}{2}} \rightarrow 9d_{\frac{3}{2}}$		39.2(30)	50.9
$6p_{\frac{3}{2}} \rightarrow 8d_{\frac{3}{2}}$		0.456(35)	5.59	$9p_{\frac{3}{2}} \rightarrow 9d_{\frac{3}{2}}$		4.42(34)	5.74
$6p_{\frac{1}{2}} \rightarrow 9d_{\frac{3}{2}}$		2.26(17)	2.93	$10p_{\frac{1}{2}} \rightarrow 9d_{\frac{3}{2}}$		21.8(17)	28.4
$6p_{\frac{3}{2}} \rightarrow 9d_{\frac{3}{2}}$		0.226(17)	0.294	$10p_{\frac{3}{2}} \rightarrow 9d_{\frac{3}{2}}$		0.976(74)	1.27
$7p_{\frac{1}{2}} \rightarrow 8s_{\frac{1}{2}}$	32.9(31)	46.7(48)	46.7	$4f_{\frac{5}{2}} \rightarrow 7d_{\frac{3}{2}}$	0.643(58)	0.649(64)	0.804
$7p_{\frac{3}{2}} \rightarrow 8s_{\frac{1}{2}}$	33.4(31)	47.4(48)	47.4	$4f_{\frac{5}{2}} \rightarrow 7d_{\frac{5}{2}}$	0.0475(33)		0.0553
$7p_{\frac{1}{2}} \rightarrow 9s_{\frac{1}{2}}$		3.17(27)	3.15	$4f_{\frac{7}{2}} \rightarrow 7d_{\frac{5}{2}}$	0.713(51)		0.830
$7p_{\frac{3}{2}} \rightarrow 9s_{\frac{1}{2}}$		2.87(24)	2.85	$4f_{\frac{5}{2}} \rightarrow 8d_{\frac{3}{2}}$		0.116(9)	0.142
$7p_{\frac{1}{2}} \rightarrow 10s_{\frac{1}{2}}$		0.942(62)	0.966	$4f_{\frac{5}{2}} \rightarrow 9d_{\frac{3}{2}}$		0.0385(29)	0.0501
$7p_{\frac{3}{2}} \rightarrow 10s_{\frac{1}{2}}$		0.835(55)	0.856	$5f_{\frac{5}{2}} \rightarrow 7d_{\frac{3}{2}}$	0.723(66)	0.730(72)	0.904
$7p_{\frac{1}{2}} \rightarrow 6d_{\frac{3}{2}}$	12.1(13)	14.1(22)	14.2	$5f_{\frac{5}{2}} \rightarrow 7d_{\frac{5}{2}}$	0.0934(66)		0.109
$7p_{\frac{3}{2}} \rightarrow 6d_{\frac{3}{2}}$	0.611(67)	0.709(109)	0.714	$5f_{\frac{7}{2}} \rightarrow 7d_{\frac{5}{2}}$	1.40(10)		1.63
$7p_{\frac{1}{2}} \rightarrow 7d_{\frac{3}{2}}$	39.3(3.6)	39.7(39)	49.2	$5f_{\frac{5}{2}} \rightarrow 8d_{\frac{3}{2}}$		1.66(13)	2.03
$7p_{\frac{3}{2}} \rightarrow 7d_{\frac{3}{2}}$	4.34(0.39)	4.39(43)	5.43	$5f_{\frac{5}{2}} \rightarrow 9d_{\frac{3}{2}}$		0.297(22)	0.386
$7p_{\frac{3}{2}} \rightarrow 7d_{\frac{5}{2}}$	41.6(29)		48.3	$6f_{\frac{5}{2}} \rightarrow 9d_{\frac{3}{2}}$		3.11(23)	4.04
$7p_{\frac{1}{2}} \rightarrow 8d_{\frac{3}{2}}$		10.9(9)	13.4				
$7p_{\frac{3}{2}} \rightarrow 8d_{\frac{3}{2}}$		1.15(9)	1.40				
$7p_{\frac{1}{2}} \rightarrow 9d_{\frac{3}{2}}$		4.52(34)	5.88				
$7p_{\frac{3}{2}} \rightarrow 9d_{\frac{3}{2}}$		0.466(35)	0.606				

electron over a closed core [such as the $(4d^{10})nl_j$ states in Ag] can be written as a Clebsch-Gordan sum

$$\langle r|nljm\rangle = R_{nlj}(r)\sum_{\mu\sigma}\left\langle l\mu\frac{1}{2}\sigma\middle|jm\right\rangle Y_{l\mu}(\hat{r})\chi_{\frac{1}{2}\sigma}. \qquad (5)$$

Then we have [59]:

$$\begin{aligned} A_{k\to i} &= \frac{8\alpha}{3c^2}\frac{\omega_{ik}^3}{2j_k+1}Q_{ki}l_{\max}|\mathcal{D}_{ki}|^2 \\ f_{i\to k} &= \frac{4m_e}{3\hbar}\frac{\omega_{ik}}{2j_i+1}Q_{ki}l_{\max}|\mathcal{D}_{ki}|^2 \\ S_{i\to k} &= 2e^2Q_{ki}l_{\max}|\mathcal{D}_{ki}|^2, \quad l_{\max} = \max\{l_k,l_i\}, \end{aligned} \qquad (6)$$

where the angular matrix element is expressed in terms of $6j$ symbols:

$$Q_{ik} = \frac{1}{2}(2j_i+1)(2j_k+1)\begin{Bmatrix} l_i & j_i & \frac{1}{2} \\ j_k & l_k & 1 \end{Bmatrix}^2.$$

We calculate the radial dipole matrix elements

$$\mathcal{D}_{ik} = \int_0^\infty drr^3R_{n_il_ij_i}(r)R_{n_kl_kj_k}(r) \qquad (7)$$

using the Fues model potential (FMP) [60,61]. This method has proved its efficiency for the calculation of atomic and molecular matrix elements of single [62] and higher [63] orders. The FMP approach is close to single-channel quantum defect theory which is also a simple and quantitatively

TABLE VII. Comparison of oscillator strengths involving nf and ng states calculated using different methods.

Transition	RHF [46]	RMBPT [55]	MCHF + BP [56]	FMP (this work)
$5d_{\frac{3}{2}} \rightarrow 4f_{\frac{5}{2}}$	1.073	1.0118		1.0094
$5d_{\frac{5}{2}} \rightarrow 4f_{\frac{5}{2}}$		0.0484		0.0481
$5d_{\frac{5}{2}} \rightarrow 4f_{\frac{7}{2}}$	1.015	0.9678		0.9622
$5d_{\frac{3}{2}} \rightarrow 5f_{\frac{5}{2}}$	0.150			0.1580
$5d_{\frac{5}{2}} \rightarrow 5f_{\frac{5}{2}}$				0.0075
$5d_{\frac{5}{2}} \rightarrow 5f_{\frac{7}{2}}$	0.141			0.1498
$4f_{\frac{5}{2}} \rightarrow 5g_{\frac{7}{2}}$	1.346	1.3800	1.1910	1.3438
$4f_{\frac{7}{2}} \rightarrow 5g_{\frac{7}{2}}$		0.0383	0.0441	0.0373
$4f_{\frac{7}{2}} \rightarrow 5g_{\frac{9}{2}}$	1.308	1.3405	1.2351	1.3065
$5f_{\frac{5}{2}} \rightarrow 5g_{\frac{7}{2}}$	0.003		0.2956	0.0174
$5f_{\frac{7}{2}} \rightarrow 5g_{\frac{7}{2}}$			0.0109	0.00048
$5f_{\frac{7}{2}} \rightarrow 5g_{\frac{9}{2}}$	0.002		0.3066	0.0169

adequate method for the calculation of first- [62] and second-order [64] matrix elements in atoms and molecules.

The radial wave function of the valence nl_j electron in FMP has a Coulomb-like form and can be expressed in terms of Whittaker functions, Gaussian hypergeometric functions or Laguerre polynomials [65]:

$$R_{nlj}(r) = \frac{2Z^{3/2}}{n^{*2}} \frac{N}{\Gamma(2l^*+2)} \frac{1}{x} M_{n^*,l^*+\frac{1}{2}}(x) = \frac{2Z^{3/2}}{n^{*2}} \frac{N x^{l^*} \mathrm{e}^{-x/2}}{\Gamma(2l^*+2)} {}_1F_1(-n_r, 2l^*+2; x) = \frac{2Z^{3/2}}{n^{*2}} \frac{1}{N} x^{l^*} \mathrm{e}^{-x/2} L_{n_r}^{2l^*+1}(x); \quad (8)$$

$$N = \sqrt{\frac{\Gamma(n_r + 2l^* + 2)}{n_r!}}, \qquad x = \frac{2Zr}{n^*},$$

where $\Gamma(\cdot)$ is the Γ function. The effective principal quantum number n^* is connected to the energy level $E(nl_j)$ and quantum defect μ_{lj} via the Rydberg formula:

$$E(nl_j) = V_{\mathrm{ion}} - \frac{Z^2 \mathcal{R}_{\mathrm{Ag}}}{n^{*2}} = V_{\mathrm{ion}} - \frac{Z^2 \mathcal{R}_{\mathrm{Ag}}}{(n - \mu_{lj})^2}, \quad (9)$$

TABLE VIII. FMP-calculated transition dipole moments (line strengths $S_{i\rightarrow k}$, oscillator strengths $f_{i\rightarrow k}$, transition probabilities $A_{k\rightarrow i}$) between $(4d^{10})n_i f$ and $(4d^{10})n_k g$ states of Ag atom in the 1300- to 4000-cm^{-1} range. The Ritz wave numbers ν and vacuum wavelengths λ are calculated using the energy-level values from the cited references.

Transition $i \leftarrow k$	Lower level (cm^{-1})	Upper level (cm^{-1})	ν (cm^{-1})	λ (nm)	S_{ik} (a. u.)	f_{ik}	A_{ki} (s^{-1})
$4f_{\frac{5}{2}} \leftarrow 5g_{\frac{7}{2}}$	54204.73 [16]	56711.1 [16]	2506.370	3989.83	1.06×10^3	1.34	4.32×10^7
$4f_{\frac{7}{2}} \leftarrow 5g_{\frac{7}{2}}$	54204.73 [16]	56711.1 [16]	2506.370	3989.83	3.92×10^1	3.73×10^{-2}	1.60×10^6
$4f_{\frac{7}{2}} \leftarrow 5g_{\frac{9}{2}}$	54204.73 [16]	56711.1 [16]	2506.370	3989.83	1.37×10^3	1.31	7.01×10^7
$4f_{\frac{5}{2}} \leftarrow 6g_{\frac{7}{2}}$	54204.73 [16]	58054.723 [66]	3849.993	2597.41	9.57×10^1	1.87×10^{-1}	1.42×10^7
$4f_{\frac{7}{2}} \leftarrow 6g_{\frac{7}{2}}$	54204.73 [16]	58054.723 [66]	3849.993	2597.41	3.54	5.18×10^{-3}	5.25×10^5
$4f_{\frac{7}{2}} \leftarrow 6g_{\frac{9}{2}}$	54204.73 [16]	58054.723 [66]	3849.993	2597.41	1.24×10^2	1.81×10^{-1}	2.30×10^7
$5f_{\frac{5}{2}} \leftarrow 6g_{\frac{7}{2}}$	56691.275 [66]	58054.723 [66]	1363.448	7334.35	1.69×10^3	1.17	1.11×10^7
$5f_{\frac{7}{2}} \leftarrow 6g_{\frac{7}{2}}$	56691.397 [66]	58054.723 [66]	1363.326	7335.00	6.26×10^1	3.24×10^{-2}	4.11×10^5
$5f_{\frac{7}{2}} \leftarrow 6g_{\frac{9}{2}}$	56691.397 [66]	58054.723 [66]	1363.326	7335.00	2.19×10^3	1.13	1.80×10^7
$5f_{\frac{5}{2}} \leftarrow 7g_{\frac{7}{2}}$	56691.275 [66]	58864.694 [16][a]	2173.419	4601.05	2.10×10^2	2.32×10^{-1}	5.60×10^6
$5f_{\frac{7}{2}} \leftarrow 7g_{\frac{7}{2}}$	56691.397 [66]	58864.694 [16][a]	2173.297	4601.30	7.79	6.43×10^{-3}	2.07×10^5
$5f_{\frac{7}{2}} \leftarrow 7g_{\frac{9}{2}}$	56691.397 [66]	58864.694 [16,66][a]	2173.297	4601.30	2.73×10^2	2.25×10^{-1}	9.08×10^6
$5f_{\frac{5}{2}} \leftarrow 8g_{\frac{7}{2}}$	56691.275 [66]	59390.301 [16][a]	2699.026	3705.04	6.33×10^1	8.65×10^{-2}	3.23×10^6
$5f_{\frac{7}{2}} \leftarrow 8g_{\frac{7}{2}}$	56691.397 [66]	59390.301 [16][a]	2698.904	3705.21	2.35	2.40×10^{-3}	1.20×10^5
$5f_{\frac{7}{2}} \leftarrow 8g_{\frac{9}{2}}$	56691.397 [66]	59390.301 [16,66][a]	2698.904	3705.21	8.21×10^1	8.41×10^{-2}	5.23×10^6
$6f_{\frac{5}{2}} \leftarrow 8g_{\frac{7}{2}}$	58045.481 [66]	59390.301 [16][a]	1344.820	7435.94	3.61×10^2	2.46×10^{-1}	2.28×10^6
$6f_{\frac{7}{2}} \leftarrow 8g_{\frac{7}{2}}$	58040.839 [16,66][a]	59390.301 [16][a]	1349.462	7410.36	1.33×10^1	6.83×10^{-3}	8.49×10^4
$6f_{\frac{7}{2}} \leftarrow 8g_{\frac{9}{2}}$	58040.839 [16,66][a]	59390.301 [16,66][a]	1349.462	7410.36	4.66×10^2	2.39×10^{-1}	3.72×10^6

[a]Obtained by extrapolation from the cited data.

TABLE IX. FMP-calculated transition dipole moments (line strengths $S_{i\to k}$, oscillator strengths $f_{i\to k}$, transition probabilities $A_{k\to i}$) between $(4d^{10})n_i g$ and $(4d^{10})n_k f$ states of Ag atom in the 1300- to 4000-cm^{-1} range. The Ritz wave numbers ν and vacuum wavelengths λ are calculated using the energy-level values from the cited references.

Transition $i \leftarrow k$	Lower level (cm^{-1})	Upper level (cm^{-1})	ν (cm^{-1})	λ (nm)	S_{ik} (a. u.)	f_{ik}	A_{ki} (s^{-1})
$5g_{\frac{7}{2}} \leftarrow 6f_{\frac{5}{2}}$	56711.1 [16]	58045.481 [66]	1334.381	7494.11	1.56×10^{1}	7.90×10^{-3}	7.21×10^{4}
$5g_{\frac{7}{2}} \leftarrow 6f_{\frac{7}{2}}$	56711.1 [16]	58040.839 [16,66][a]	1329.739	7520.27	6.10×10^{-1}	3.08×10^{-4}	3.72×10^{3}
$5g_{\frac{9}{2}} \leftarrow 6f_{\frac{7}{2}}$	56711.1 [16]	58040.839 [16,66][a]	1329.739	7520.27	2.13×10^{1}	8.62×10^{-3}	1.30×10^{5}
$5g_{\frac{7}{2}} \leftarrow 7f_{\frac{5}{2}}$	56711.1 [16]	58854.51 [66]	2143.410	4665.46	1.63	1.33×10^{-3}	3.13×10^{4}
$5g_{\frac{7}{2}} \leftarrow 7f_{\frac{7}{2}}$	56711.1 [16]	58854.765 [66]	2143.665	4664.91	6.03×10^{-2}	4.91×10^{-5}	1.54×10^{3}
$5g_{\frac{9}{2}} \leftarrow 7f_{\frac{7}{2}}$	56711.1 [16]	58854.765 [66]	2143.665	4664.91	2.11	1.37×10^{-3}	5.39×10^{4}
$5g_{\frac{7}{2}} \leftarrow 8f_{\frac{5}{2}}$	56711.1 [16]	59384.182 [16,66][a]	2673.082	3741.00	4.27×10^{-1}	4.33×10^{-4}	1.59×10^{4}
$5g_{\frac{7}{2}} \leftarrow 8f_{\frac{7}{2}}$	56711.1 [16]	59383.409 [16,66][a]	2672.309	3742.08	1.61×10^{-2}	1.63×10^{-5}	7.96×10^{2}
$5g_{\frac{9}{2}} \leftarrow 8f_{\frac{7}{2}}$	56711.1 [16]	59383.409 [16,66][a]	2672.309	3742.08	5.63×10^{-1}	4.57×10^{-4}	2.79×10^{4}
$6g_{\frac{7}{2}} \leftarrow 8f_{\frac{5}{2}}$	58054.723 [66]	59384.182 [16,66][a]	1329.459	7521.85	7.52	3.80×10^{-3}	3.44×10^{4}
$6g_{\frac{7}{2}} \leftarrow 8f_{\frac{7}{2}}$	58054.723 [66]	59383.409 [16,66][a]	1328.686	7526.23	2.83×10^{-1}	1.43×10^{-4}	1.72×10^{3}
$6g_{\frac{9}{2}} \leftarrow 8f_{\frac{7}{2}}$	58054.723 [66]	59383.409 [16,66][a]	1328.686	7526.23	9.91	4.00×10^{-3}	6.03×10^{4}

[a]Obtained by extrapolation from the cited data.

where $V_{\text{ion}} = 61106.45$ cm^{-1} [26] stands for the ionization potential of the Ag atom whose $(4d^{10})$ core's charge is $Z = 1$; $\mathcal{R}_{\text{Ag}} = 109736.758$ cm^{-1} [27] is the mass-corrected Rydberg constant for Ag. The noninteger parameter l^* accounts for the non-Coulombic potential of the core and is connected to the principal quantum number in the following way:

$$n^* = n_r + l^* + 1. \tag{10}$$

The integer radial quantum number n_r is equal to the number of nodes of the radial wave function $R(r)$; for the Ag atom this number was determined as

$$n_r = \begin{cases} \max\{1, n-5\} & \text{for} \quad s \text{ states } (n \geqslant 5); \\ n-5 & \text{for} \quad p,d \text{ states } (n \geqslant 5); \\ n-l-1 & \text{for} \quad l \geqslant 3 \text{ states } (n \geqslant l+1). \end{cases} \tag{11}$$

TABLE X. FMP-calculated transition dipole moments (line strengths $S_{i\to k}$, oscillator strengths $f_{i\to k}$, transition probabilities $A_{k\to i}$) between $(4d^{10})n_i d$ and $(4d^{10})n_k f$ states of Ag atom in the 1300- to 4000-cm^{-1} range. The Ritz wave numbers ν and vacuum wavelengths λ are calculated using the energy-level values from the cited references.

Transition $i \leftarrow k$	Lower level (cm^{-1})	Upper level (cm^{-1})	ν (cm^{-1})	λ (nm)	S_{ik} (a. u.)	f_{ik}	A_{ki} (s^{-1})
$6d_{\frac{3}{2}} \leftarrow 5f_{\frac{5}{2}}$	54203.119 [66]	56691.275 [66]	2488.156	4019.04	4.70×10^{2}	8.88×10^{-1}	1.41×10^{7}
$6d_{\frac{5}{2}} \leftarrow 5f_{\frac{5}{2}}$	54213.564 [66]	56691.275 [66]	2477.711	4035.98	3.39×10^{1}	4.25×10^{-2}	1.00×10^{6}
$6d_{\frac{5}{2}} \leftarrow 5f_{\frac{7}{2}}$	54213.564 [66]	56691.397 [66]	2477.833	4035.78	6.78×10^{2}	8.50×10^{-1}	2.67×10^{7}
$6d_{\frac{3}{2}} \leftarrow 6f_{\frac{5}{2}}$	54203.119 [66]	58045.481 [66]	3842.362	2602.57	6.36×10^{1}	1.85×10^{-1}	7.01×10^{6}
$6d_{\frac{5}{2}} \leftarrow 6f_{\frac{5}{2}}$	54213.564 [66]	58045.481 [66]	3831.917	2609.66	4.55	8.82×10^{-3}	4.97×10^{5}
$6d_{\frac{5}{2}} \leftarrow 6f_{\frac{7}{2}}$	54213.564 [66]	58040.839 [16,66][a]	3827.275	2612.83	9.07×10^{1}	1.76×10^{-1}	1.32×10^{7}
$7d_{\frac{3}{2}} \leftarrow 6f_{\frac{5}{2}}$	56699.911 [66]	58045.481 [66]	1345.570	7431.79	8.29×10^{2}	8.47×10^{-1}	3.93×10^{6}
$7d_{\frac{5}{2}} \leftarrow 6f_{\frac{5}{2}}$	56705.435 [66]	58045.481 [66]	1340.046	7462.43	6.00×10^{1}	4.07×10^{-2}	2.81×10^{5}
$7d_{\frac{5}{2}} \leftarrow 6f_{\frac{7}{2}}$	56705.435 [66]	58040.839 [16,66][a]	1335.404	7488.37	1.22×10^{3}	8.24×10^{-1}	7.52×10^{6}
$7d_{\frac{3}{2}} \leftarrow 7f_{\frac{5}{2}}$	56699.911 [66]	58854.51 [66]	2154.599	4641.23	1.20×10^{2}	1.96×10^{-1}	2.34×10^{6}
$7d_{\frac{5}{2}} \leftarrow 7f_{\frac{5}{2}}$	56705.435 [66]	58854.51 [66]	2149.075	4653.16	8.61	9.36×10^{-3}	1.66×10^{5}
$7d_{\frac{5}{2}} \leftarrow 7f_{\frac{7}{2}}$	56705.435 [66]	58854.765 [66]	2149.330	4652.61	1.72×10^{2}	1.87×10^{-1}	4.43×10^{6}
$7d_{\frac{3}{2}} \leftarrow 8f_{\frac{5}{2}}$	56699.911 [66]	59384.182 [16,66][a]	2684.271	3725.41	3.93×10^{1}	8.01×10^{-2}	1.48×10^{6}
$7d_{\frac{5}{2}} \leftarrow 8f_{\frac{5}{2}}$	56705.435 [66]	59384.182 [16,66][a]	2678.747	3733.09	2.81	3.81×10^{-3}	1.05×10^{5}
$7d_{\frac{5}{2}} \leftarrow 8f_{\frac{7}{2}}$	56705.435 [66]	59383.409 [16,66][a]	2677.974	3734.17	5.61×10^{1}	7.60×10^{-2}	2.79×10^{6}
$8d_{\frac{3}{2}} \leftarrow 8f_{\frac{5}{2}}$	58049.973 [25]	59384.182 [16,66][a]	1334.209	7495.08	2.02×10^{2}	2.05×10^{-1}	9.34×10^{5}
$8d_{\frac{5}{2}} \leftarrow 8f_{\frac{5}{2}}$	58053.404 [25]	59384.182 [16,66][a]	1330.778	7514.40	1.45×10^{1}	9.80×10^{-3}	6.66×10^{4}
$8d_{\frac{5}{2}} \leftarrow 8f_{\frac{7}{2}}$	58053.404 [25]	59383.409 [16,66][a]	1330.005	7518.77	2.91×10^{2}	1.96×10^{-1}	1.78×10^{6}

[a]Obtained by extrapolation from the cited data.

TABLE XI. FMP-calculated transition dipole moments (line strengths $S_{i\to k}$, oscillator strengths $f_{i\to k}$, transition probabilities $A_{k\to i}$) between $(4d^{10})n_i f$ and $(4d^{10})n_k d$ states of Ag atom in 1300- to 4000-cm^{-1} range. The Ritz wave numbers ν and vacuum wavelengths λ are calculated using the energy-level values from the cited references.

Transition $i \leftarrow k$	Lower level (cm^{-1})	Upper level (cm^{-1})	ν (cm^{-1})	λ (nm)	S_{ik} (a. u.)	f_{ik}	A_{ki} (s^{-1})
$4f_{\frac{5}{2}} \leftarrow 7d_{\frac{3}{2}}$	54204.73 [16]	56699.911 [66]	2495.181	4007.73	6.36	8.04×10^{-3}	1.28×10^{5}
$4f_{\frac{5}{2}} \leftarrow 7d_{\frac{5}{2}}$	54204.73 [16]	56705.435 [66]	2500.705	3998.87	4.37×10^{-1}	5.53×10^{-4}	1.33×10^{4}
$4f_{\frac{7}{2}} \leftarrow 7d_{\frac{5}{2}}$	54204.73 [16]	56705.435 [66]	2500.705	3998.87	8.74	8.30×10^{-3}	2.66×10^{5}
$4f_{\frac{5}{2}} \leftarrow 8d_{\frac{3}{2}}$	54204.73 [16]	58049.973 [25]	3845.243	2600.62	7.28×10^{-1}	1.42×10^{-3}	5.37×10^{4}
$4f_{\frac{5}{2}} \leftarrow 8d_{\frac{5}{2}}$	54204.73 [16]	58053.404 [25]	3848.674	2598.30	5.01×10^{-2}	9.77×10^{-5}	5.56×10^{3}
$4f_{\frac{7}{2}} \leftarrow 8d_{\frac{5}{2}}$	54204.73 [16]	58053.404 [25]	3848.674	2598.30	1.00	1.47×10^{-3}	1.11×10^{5}
$5f_{\frac{5}{2}} \leftarrow 8d_{\frac{3}{2}}$	56691.275 [66]	58049.973 [25]	1358.698	7359.99	2.95×10^{1}	2.03×10^{-2}	9.59×10^{4}
$5f_{\frac{5}{2}} \leftarrow 8d_{\frac{5}{2}}$	56691.275 [66]	58053.404 [25]	1362.129	7341.45	2.02	1.40×10^{-3}	9.95×10^{3}
$5f_{\frac{7}{2}} \leftarrow 8d_{\frac{5}{2}}$	56691.397 [66]	58053.404 [25]	1362.007	7342.11	4.05×10^{1}	2.09×10^{-2}	1.99×10^{5}
$5f_{\frac{5}{2}} \leftarrow 9d_{\frac{3}{2}}$	56691.275 [66]	58862.463 [25]	2171.188	4605.77	3.51	3.86×10^{-3}	4.66×10^{4}
$5f_{\frac{5}{2}} \leftarrow 9d_{\frac{5}{2}}$	56691.275 [66]	58864.614 [25]	2173.339	4601.21	2.42×10^{-1}	2.67×10^{-4}	4.84×10^{3}
$5f_{\frac{7}{2}} \leftarrow 9d_{\frac{5}{2}}$	56691.397 [66]	58864.614 [25]	2173.217	4601.47	4.85	4.00×10^{-3}	9.68×10^{4}
$5f_{\frac{5}{2}} \leftarrow 10d_{\frac{3}{2}}$	56691.275 [66]	59388.97 [19]	2697.695	3706.87	1.04	1.42×10^{-3}	2.65×10^{4}
$5f_{\frac{5}{2}} \leftarrow 10d_{\frac{5}{2}}$	56691.275 [66]	59390.587 [25]	2699.312	3704.65	7.16×10^{-2}	9.78×10^{-5}	2.74×10^{3}
$5f_{\frac{7}{2}} \leftarrow 10d_{\frac{5}{2}}$	56691.397 [66]	59390.587 [25]	2699.190	3704.82	1.43	1.47×10^{-3}	5.48×10^{4}
$6f_{\frac{5}{2}} \leftarrow 10d_{\frac{3}{2}}$	58045.481 [66]	59388.97 [19]	1343.489	7443.31	1.07×10^{1}	7.29×10^{-3}	3.37×10^{4}
$6f_{\frac{5}{2}} \leftarrow 10d_{\frac{5}{2}}$	58045.481 [66]	59390.587 [25]	1345.106	7434.36	7.38×10^{-1}	5.03×10^{-4}	3.49×10^{3}
$6f_{\frac{7}{2}} \leftarrow 10d_{\frac{5}{2}}$	58040.839 [16,66][a]	59390.587 [25]	1349.748	7408.79	1.41×10^{1}	7.23×10^{-3}	6.74×10^{4}

[a]Obtained by extrapolation from the cited data.

IV. RESULTS AND DISCUSSION

A. Oscillator and line strengths calculation

Before using the FMP-calculated line strengths for analyzing the relative intensities of the observed IR transitions we demonstrate that the accuracy of FMP is adequate for such a task. Since oscillator strengths are more commonly available in literature than the line strengths or radial dipole transition matrix elements, our comparison with the data reported in the literature will involve the f values.

TABLE XII. FMP-calculated transition dipole moments (line strengths $S_{i\to k}$, oscillator strengths $f_{i\to k}$, transition probabilities $A_{k\to i}$) between $(4d^{10})n_i p$ and $(4d^{10})n_k d$ states of Ag atom in the 1300- to 4000-cm^{-1} range. The Ritz wave numbers ν and vacuum wavelengths λ are calculated using the energy-level values from the cited references.

Transition $i \leftarrow k$	Lower level (cm^{-1})	Upper level (cm^{-1})	ν (cm^{-1})	λ (nm)	S_{ik} (a. u.)	f_{ik}	A_{ki} (s^{-1})
$7p_{\frac{1}{2}} \leftarrow 7d_{\frac{3}{2}}$	54041.087 [66]	56699.911 [66]	2658.824	3761.06	1.22×10^{2}	4.92×10^{-1}	2.97×10^{6}
$7p_{\frac{3}{2}} \leftarrow 7d_{\frac{3}{2}}$	54121.059 [66]	56699.911 [66]	2578.852	3877.69	2.78×10^{1}	5.43×10^{-2}	6.17×10^{5}
$7p_{\frac{3}{2}} \leftarrow 7d_{\frac{5}{2}}$	54121.059 [66]	56705.435 [66]	2584.376	3869.41	2.46×10^{2}	4.83×10^{-1}	8.27×10^{6}
$7p_{\frac{3}{2}} \leftarrow 8d_{\frac{3}{2}}$	54121.059 [66]	58049.973 [25]	3928.914	2545.23	4.71	1.40×10^{-2}	3.70×10^{5}
$7p_{\frac{3}{2}} \leftarrow 8d_{\frac{5}{2}}$	54121.059 [66]	58053.404 [25]	3932.345	2543.01	4.21×10^{1}	1.26×10^{-1}	4.98×10^{6}
$8p_{\frac{1}{2}} \leftarrow 8d_{\frac{3}{2}}$	56620.876 [66]	58049.973 [25]	1429.097	6997.43	2.29×10^{2}	4.96×10^{-1}	8.65×10^{5}
$8p_{\frac{3}{2}} \leftarrow 8d_{\frac{3}{2}}$	56660.556 [66]	58049.973 [25]	1389.417	7197.26	5.27×10^{1}	5.56×10^{-2}	1.83×10^{5}
$8p_{\frac{3}{2}} \leftarrow 8d_{\frac{5}{2}}$	56660.556 [66]	58053.404 [25]	1392.848	7179.53	4.66×10^{2}	4.93×10^{-1}	2.45×10^{6}
$8p_{\frac{1}{2}} \leftarrow 9d_{\frac{3}{2}}$	56620.876 [66]	58862.463 [25]	2241.587	4461.13	4.05×10^{1}	1.38×10^{-1}	5.92×10^{5}
$8p_{\frac{3}{2}} \leftarrow 9d_{\frac{3}{2}}$	56660.556 [66]	58862.463 [25]	2201.907	4541.52	8.80	1.47×10^{-2}	1.22×10^{5}
$8p_{\frac{3}{2}} \leftarrow 9d_{\frac{5}{2}}$	56660.556 [66]	58864.614 [25]	2204.058	4537.09	7.85×10^{1}	1.31×10^{-1}	1.63×10^{6}
$8p_{\frac{1}{2}} \leftarrow 10d_{\frac{3}{2}}$	56620.876 [66]	59388.97 [19]	2768.094	3612.59	1.47×10^{1}	6.18×10^{-2}	4.04×10^{5}
$8p_{\frac{3}{2}} \leftarrow 10d_{\frac{3}{2}}$	56660.556 [66]	59388.97 [19]	2728.414	3665.13	3.12	6.46×10^{-3}	8.21×10^{4}
$8p_{\frac{3}{2}} \leftarrow 10d_{\frac{5}{2}}$	56660.556 [66]	59390.587 [25]	2730.031	3662.96	2.79×10^{1}	5.79×10^{-2}	1.10×10^{6}
$9p_{\frac{1}{2}} \leftarrow 10d_{\frac{3}{2}}$	58005.05 [19]	59388.97 [19]	1383.920	7225.85	6.81×10^{1}	1.43×10^{-1}	2.34×10^{5}
$9p_{\frac{3}{2}} \leftarrow 10d_{\frac{3}{2}}$	58027.0 [19]	59388.97 [19]	1361.970	7342.31	1.49×10^{1}	1.54×10^{-2}	4.88×10^{4}
$9p_{\frac{3}{2}} \leftarrow 10d_{\frac{5}{2}}$	58027.0 [19]	59390.587 [25]	1363.587	7333.60	1.32×10^{2}	1.37×10^{-1}	6.53×10^{5}

TABLE XIII. FMP-calculated transition dipole moments (line strengths $S_{i\to k}$, oscillator strengths $f_{i\to k}$, transition probabilities $A_{k\to i}$) between $(4d^{10})n_i d$ and $(4d^{10})n_k p$ states of Ag atom in the 1300- to 4000-cm^{-1} range. The Ritz wave numbers ν and vacuum wavelengths λ are calculated using the energy-level values from the cited references.

Transition $i \leftarrow k$	Lower level (cm^{-1})	Upper level (cm^{-1})	ν (cm^{-1})	λ (nm)	S_{ik} (a. u.)	f_{ik}	A_{ki} (s^{-1})
$6d_{\frac{3}{2}} \leftarrow 8p_{\frac{1}{2}}$	54203.119 [66]	56620.876 [66]	2417.757	4136.06	1.86×10^{1}	3.42×10^{-2}	1.71×10^{5}
$6d_{\frac{3}{2}} \leftarrow 8p_{\frac{3}{2}}$	54203.119 [66]	56660.556 [66]	2457.437	4069.28	3.01	5.61×10^{-3}	5.78×10^{4}
$6d_{\frac{5}{2}} \leftarrow 8p_{\frac{3}{2}}$	54213.564 [66]	56660.556 [66]	2446.992	4086.65	2.79×10^{1}	3.46×10^{-2}	5.31×10^{5}
$6d_{\frac{3}{2}} \leftarrow 9p_{\frac{1}{2}}$	54203.119 [66]	58005.05 [19]	3801.931	2630.24	2.31	6.67×10^{-3}	8.23×10^{4}
$6d_{\frac{3}{2}} \leftarrow 9p_{\frac{3}{2}}$	54203.119 [66]	58027.0 [19]	3823.881	2615.14	3.91×10^{-1}	1.13×10^{-3}	2.83×10^{4}
$6d_{\frac{5}{2}} \leftarrow 9p_{\frac{3}{2}}$	54213.564 [66]	58027.0 [19]	3813.436	2622.31	3.61	6.96×10^{-3}	2.59×10^{5}
$7d_{\frac{3}{2}} \leftarrow 9p_{\frac{1}{2}}$	56699.911 [66]	58005.05 [19]	1305.139	7662.02	5.91×10^{1}	5.85×10^{-2}	8.51×10^{4}
$7d_{\frac{3}{2}} \leftarrow 9p_{\frac{3}{2}}$	56699.911 [66]	58027.0 [19]	1327.089	7535.29	9.68	9.76×10^{-3}	2.93×10^{4}
$7d_{\frac{5}{2}} \leftarrow 9p_{\frac{3}{2}}$	56705.435 [66]	58027.0 [19]	1321.565	7566.79	8.99×10^{1}	6.02×10^{-2}	2.69×10^{5}
$7d_{\frac{3}{2}} \leftarrow 10p_{\frac{1}{2}}$	56699.911 [66]	58834.25 [19]	2134.339	4685.29	7.25	1.18×10^{-2}	4.57×10^{4}
$7d_{\frac{3}{2}} \leftarrow 10p_{\frac{3}{2}}$	56699.911 [66]	58849.83 [67]	2149.919	4651.34	1.21	1.98×10^{-3}	1.56×10^{4}
$7d_{\frac{5}{2}} \leftarrow 10p_{\frac{3}{2}}$	56705.435 [66]	58849.83 [67]	2144.395	4663.32	1.12×10^{1}	1.21×10^{-2}	1.43×10^{5}

While the theoretical publications report f values, the majority of the experimental studies deal with measurements of transition probabilities or lifetimes. However, f values can be extracted from the reported lifetimes according to the Eqs. (2) and (3) if the ratios between the pairs of oscillator strengths $f_{i\to k}$ (transition probabilities $A_{k\to i}$) are known, e.g., from theoretical calculations. In our comparison we used the FMP method to calculate the theoretical ratios between the transition probabilities.

The results of such comparison with the experiment and with other calculations are presented in Tables I, II, III, IV, V, VI, and VII. The overall agreement of our calculations with other results can be considered to be reasonable with the exception of the $ns \to n'p$ transitions with $n' > 5$. However, the results of other theoretical calculations for these transitions (see Table III) differs by some orders of magnitude and some are close to our results. The f values extracted from the experimental lifetimes of the $6s_{\frac{1}{2}}$ [44] and $7s_{\frac{1}{2}}$ [45] levels differ both from the f values measured by the Rozhdestvenskii hook method [41] and from our theoretical values used for the calculation of the ratios of transition probability to extract the f values. This fact suggests that the use of FMP for extracting f values from the experimental lifetimes does not alone guarantee that the extracted f values will be close to those calculated using FMP. However, this is the case for transitions between higher-excited states; see Tables II, IV, and VI. In particular, for $5p \to 5d$ transitions the f values extracted according to FMP theoretical ratios demonstrate an agreement with the FMP-calculated f values which are not worse than the f values extracted using other theoretical ratios (see Table 2 in Ref. [54]).

For the further analysis of the observed Ag lines given in the next section we made an FMP calculation of the line strengths S for transitions between the $(4d^{10})nl_j$ states in the 1300- to 5000-cm^{-1} range. These results are presented in Tables VIII, IX, X, XI, XII, XIII, XIV, and XV. We consider the data presented in the tables in this section to be the most comprehensive compilation of f values for neutral Ag.

B. Lines observed

Some parts of the observed IR emission spectra of the Ag atom are presented in Fig. 1 at 11 μs after the laser shot, when the time profile of the emission intensity is maximum for all

TABLE XIV. FMP-calculated transition dipole moments (line strengths $S_{i\to k}$, oscillator strengths $f_{i\to k}$, transition probabilities $A_{k\to i}$) between $(4d^{10})n_i s$ and $(4d^{10})n_k p$ states of Ag atom in the 1300- to 4000 cm^{-1} range. The Ritz wave numbers ν and vacuum wavelengths λ are calculated using the energy-level values from the cited references.

Transition $i \leftarrow k$	Lower level (cm^{-1})	Upper level (cm^{-1})	ν (cm^{-1})	λ (nm)	S_{ik} (a. u.)	f_{ik}	A_{ki} (s^{-1})
$7s_{\frac{1}{2}} \leftarrow 7p_{\frac{1}{2}}$	51886.954 [66]	54041.087 [66]	2154.133	4642.24	1.66×10^{2}	5.43×10^{-1}	1.08×10^{6}
$7s_{\frac{1}{2}} \leftarrow 7p_{\frac{3}{2}}$	51886.954 [66]	54121.059 [66]	2234.105	4476.07	3.21×10^{2}	1.09	4.64×10^{6}
$8s_{\frac{1}{2}} \leftarrow 9p_{\frac{1}{2}}$	55581.246 [66]	58005.05 [19]	2423.804	4125.75	7.78	2.87×10^{-2}	7.19×10^{4}
$8s_{\frac{1}{2}} \leftarrow 9p_{\frac{3}{2}}$	55581.246 [66]	58027.0 [19]	2445.754	4088.72	1.80×10^{1}	6.69×10^{-2}	3.42×10^{5}
$8s_{\frac{1}{2}} \leftarrow 10p_{\frac{1}{2}}$	55581.246 [66]	58834.25 [19]	3253.004	3074.08	1.47	7.27×10^{-3}	3.29×10^{4}
$8s_{\frac{1}{2}} \leftarrow 10p_{\frac{3}{2}}$	55581.246 [66]	58849.83 [67]	3268.584	3059.43	3.66	1.82×10^{-2}	1.66×10^{5}
$9s_{\frac{1}{2}} \leftarrow 10p_{\frac{1}{2}}$	57425.078 [25]	58834.25 [19]	1409.172	7096.37	1.65×10^{1}	3.54×10^{-2}	3.00×10^{4}
$9s_{\frac{1}{2}} \leftarrow 10p_{\frac{3}{2}}$	57425.078 [25]	58849.83 [67]	1424.752	7018.77	3.87×10^{1}	8.37×10^{-2}	1.45×10^{5}

TABLE XV. FMP-calculated transition dipole moments (line strengths $S_{i\to k}$, oscillator strengths $f_{i\to k}$, transition probabilities $A_{k\to i}$) between $(4d^{10})n_i p$ and $(4d^{10})n_k s$ states of Ag atom inthe 1300- to 4000-cm^{-1} range. The Ritz wave numbers ν and vacuum wavelengths λ are calculated using the energy-level values from the cited references.

Transition $i \leftarrow k$	Lower level (cm^{-1})	Upper level (cm^{-1})	ν (cm^{-1})	λ (nm)	S_{ik} (a. u.)	f_{ik}	A_{ki} (s^{-1})
$6p_{\frac{1}{2}} \leftarrow 7s_{\frac{1}{2}}$	48297.402 [25,66]	51886.954 [66]	3589.552	2785.86	5.90×10^{1}	3.22×10^{-1}	1.77×10^{6}
$6p_{\frac{3}{2}} \leftarrow 7s_{\frac{1}{2}}$	48500.804 [66]	51886.954 [66]	3386.150	2953.21	1.27×10^{2}	3.27×10^{-1}	3.21×10^{6}
$7p_{\frac{1}{2}} \leftarrow 8s_{\frac{1}{2}}$	54041.087 [66]	55581.246 [66]	1540.159	6492.84	1.99×10^{2}	4.67×10^{-1}	4.72×10^{5}
$7p_{\frac{3}{2}} \leftarrow 8s_{\frac{1}{2}}$	54121.059 [66]	55581.246 [66]	1460.187	6848.44	4.27×10^{2}	4.74×10^{-1}	8.62×10^{5}
$7p_{\frac{1}{2}} \leftarrow 9s_{\frac{1}{2}}$	54041.087 [66]	57425.078 [25]	3383.991	2955.09	6.13	3.15×10^{-2}	1.54×10^{5}
$7p_{\frac{3}{2}} \leftarrow 9s_{\frac{1}{2}}$	54121.059 [66]	57425.078 [25]	3304.019	3026.62	1.14×10^{1}	2.85×10^{-2}	2.66×10^{5}
$8p_{\frac{1}{2}} \leftarrow 10s_{\frac{1}{2}}$	56620.876 [66]	58478.047 [25]	1857.171	5384.53	1.40×10^{1}	3.96×10^{-2}	5.82×10^{4}
$8p_{\frac{3}{2}} \leftarrow 10s_{\frac{1}{2}}$	56660.556 [66]	58478.047 [25]	1817.491	5502.09	2.59×10^{1}	3.57×10^{-2}	1.01×10^{5}

the observed lines. The most prominent IR lines observed for Ag are listed in Table XVI. Their full widths at half-maxima (FWHM) are calculated from fitting to a Voigt profile, but under our conditions this profile does not differ much from the Lorentzian shape (see Ref. [28]).

We measured the emission spectrum at a different delay time, from 0 to 30 μs, after the laser shot. This allows us to measure the time profiles of the observed Ag lines. Some such profiles are shown in Fig. 2. The temporal decay of some lines is well described by exponential fitting, while some lines display nonexponential (including some "plateaux" at 20–25 μs after the laser shot) and even nonmonotonic behavior. Therefore their decay time, τ, values are estimated in Table XVI in a rough approximation; so, for essentially nonexponential decays, the standard deviation $\Delta\tau$ is of order of τ.

It should be noted that the decay times $\tau \simeq 1 - 10\,\mu$s given in Table XVI are not related to the radiative lifetimes of Ag atom levels which are at least two orders shorter [43–45]. The temporal dynamics shown in Fig. 2 is due to a complex combination of the collisional cascade repopulation of the emitting levels [28] and the transfer processes in ablation products [57].

For classification of the observed lines, we checked all the transitions in the 1300- to 3600-cm^{-1} range allowed by the electric dipole rules. In the cases of transitions with close wave numbers we chose those with greater line strengths defined by the Eq. (4). Although, due to self-absorption and nonequilibrium population dynamics in the plasma plume, the observed line intensities can display some deviations from the equilibrium values described by Eq. (1), the qualitative picture of the relative intensities of different lines should be adequately described by S values. These values for the transitions between the $(4d^{10})nl_j$-core states with $n \leqslant 10$ in the 1300 to 5000-cm^{-1} range are given in Tables VIII, IX, X, XI, XII, XIII, XIV, and XV.

After classification we can refine the energy values for some levels involved in the classified transitions. However, the standard algorithms of such refinement (i.e., least-squares fitting used in Ref. [25]) are not appropriate for our case since the number of the measured lines is less than the number of the levels involved into the transitions. To obtain the best estimates for the level energy values E_i, we performed a minimization of a sum of deviations not only between $E_i - E_j$ and the measured wave numbers but included also the deviations between some E_i and the "reference" values for these levels taken from Refs. [19,25]. The weights in the sum of squared deviations were proportional to inverse uncertainties of the corresponding wave numbers or "reference" energies. The revised energy values E_i of some Ag terms are presented in Table XVII. For the levels with $n \leqslant 6$ our values coincides with the reference values within the uncertainty intervals, but it is not the case for $n > 6$. However, we consider our values preferable since they are extracted from spectra recorded with 0.02-cm^{-1} resolution while the reference values were obtained from spectra with resolution of 0.035–0.045 cm^{-1} [25] and 0.06 cm^{-1} [19].

According to Table VIII there should be two strong lines near 2506 cm^{-1} corresponding to $4f_{\frac{5}{2}} \leftarrow 5g_{\frac{7}{2}}$ and $4f_{\frac{7}{2}} \leftarrow 5g_{\frac{9}{2}}$ transitions. The presence of only one peak in the recorded spectra can be explained by coincidence of two corresponding lines within their width. Indeed, the measured fine splitting of f states is of order of this width, 0.122 cm^{-1} for the $5f$ state and 0.245 cm^{-1} for $7f$ state, and the fine splitting for g states should be of the same order or even less. Note that we did not observed the 2502.37 cm^{-1} line reported a century ago by Paschen [11]. To obtain reliable values of the fine-splitting component of f levels one should consider transitions from these states to nd states with larger fine splitting; see Table X.

Some of these transitions lie in the 1330- to 1350-cm^{-1} range but we observed only one line near 1345 cm^{-1} while,

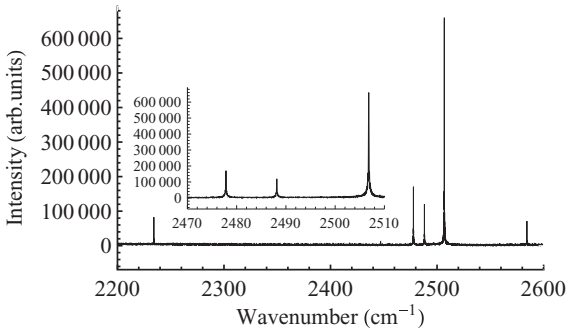

FIG. 1. A section of the the observed IR emission spectra of Ag.

TABLE XVI. Experimental Ag lines and their identification. The decay time, τ, was calculated by exponential fitting of the measured time profiles of the corresponding lines.

Wave number (cm^{-1})	Intensity (arb. units)	SNR	FWHM (cm^{-1})	Decay time (μs)	Identification
1345.570(6)	14889	14.	0.125(55)	4.17(104)[b]	$(4d^{10})7d_{\frac{3}{2}} \leftarrow (4d^{10})6f_{\frac{5}{2}}$
1363.326(14)	3910	4.3	0.146(150)	5.90(609)[b]	$(4d^{10})5f \leftarrow (4d^{10})6g$
1460.115(6)	4530	5.6	0.111(035)	3.34(170)[b]	$(4d^{10})7p_{\frac{3}{2}} \leftarrow (4d^{10})8s_{\frac{1}{2}}$
2149.320(2)	6956	2.4	0.025(19)	7.17(206)[b]	$(4d^{10})7d_{\frac{5}{2}} \leftarrow (4d^{10})7f_{\frac{7}{2}}$
2153.988(4)	32525	9.4	0.031(21)	3.07(15)	$(4d^{10})7s_{\frac{1}{2}} \leftarrow (4d^{10})7p_{\frac{1}{2}}$
2154.599(2)	5958	2.2	0.029(11)	12.8(78)[b]	$(4d^{10})7d_{\frac{3}{2}} \leftarrow (4d^{10})7f_{\frac{5}{2}}$
2234.168(1)	74835	13.	0.035(6)	3.63(34)	$(4d^{10})7s_{\frac{1}{2}} \leftarrow (4d^{10})7p_{\frac{3}{2}}$
2417.757(2)	4880	5.9	0.030(14)	5.03(214)[b]	$(4d^{10})6d_{\frac{3}{2}} \leftarrow (4d^{10})8p_{\frac{1}{2}}$
2447.045(2)	5463	6.6	0.026(24)	4.88(81)[b]	$(4d^{10})6d_{\frac{5}{2}} \leftarrow (4d^{10})8p_{\frac{3}{2}}$
2477.833(1)	113278	10.	0.044(4)	4.27(29)	$(4d^{10})6d_{\frac{5}{2}} \leftarrow (4d^{10})5f_{\frac{7}{2}}$
2488.1560(9)	78947	7.0	0.048(4)	4.20(35)[a]	$(4d^{10})6d_{\frac{3}{2}} \leftarrow (4d^{10})5f_{\frac{5}{2}}$
2506.8196(5)	460526	41.	0.056(2)	3.87(20)	$(4d^{10})4f \leftarrow (4d^{10})5g$
2579.210(3)	5252	6.2	0.036(21)	5.14(202)[b]	$(4d^{10})7p_{\frac{3}{2}} \leftarrow (4d^{10})7d_{\frac{3}{2}}$
2584.3387(6)	48450	31.	0.041(3)	4.20(37)[b]	$(4d^{10})7p_{\frac{3}{2}} \leftarrow (4d^{10})7d_{\frac{5}{2}}$
2658.7911(9)	22693	14.	0.038(5)	4.15(39)[a]	$(4d^{10})7p_{\frac{1}{2}} \leftarrow (4d^{10})7d_{\frac{3}{2}}$
3386.152(1)	98370	9.2	0.059(6)	3.35(28)	$(4d^{10})6p_{\frac{3}{2}} \leftarrow (4d^{10})7s_{\frac{1}{2}}$
3589.552(5)	13825	15.	0.065(4)	3.15(11)[a]	$(4d^{10})6p_{\frac{1}{2}} \leftarrow (4d^{10})7s_{\frac{1}{2}}$

[a]Time profile demonstrates significant deviation from the exponential decay.
[b]The decay curve has essentially nonexponential form with a plateau or a second maximum; the τ value is roughly approximate.

according to Table X, there should be two lines separated by approximately 5–10 cm^{-1}. Another unexplained feature is that, according to Table VIII, the 1363-cm^{-1} line corresponding to the $5f \leftarrow 6g$ transition should have greater intensity than the 1345-cm^{-1} line, but this is not supported by our observation. It can be due to the fact that, in our laser-ablated plasma the $6f$ and $6g$ states are less populated. It should also be noted that our spectra in the 1200- to 1800-cm^{-1} range was recorded using a MCT detector and demonstrate high level of noise. Since our data are insufficient to resolve the fine structure components of the $5f \leftarrow 6g$ transition, the value 58054.723 cm^{-1}, which is given in the Table XVII for the $6g$ state without specifying

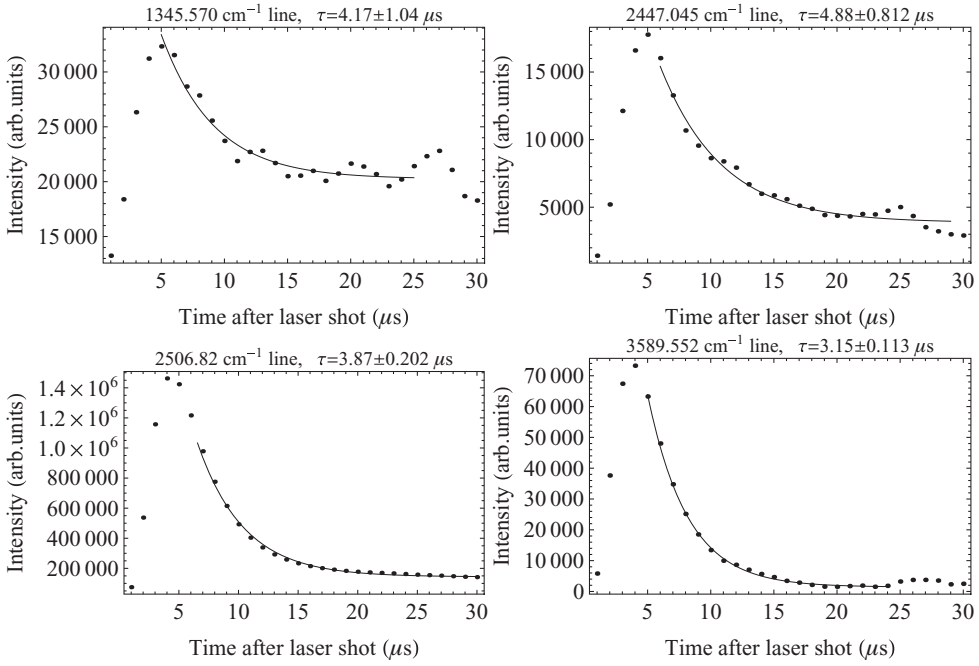

FIG. 2. The time profiles of some observed lines (dots) and their fit with exponential decay (solid curves).

TABLE XVII. Revised values of some levels of Ag I.

Term	Energy (cm^{-1})	Other sources
$(4d^{10})5f_{\frac{5}{2}}$	56691.275(2)	56691.4 [16], 56692.5 [55]
$(4d^{10})5f_{\frac{7}{2}}$	56691.397(4)	56691.4 [16], 56694.4 [55]
$(4d^{10})6p_{\frac{1}{2}}$	48297.402(2)	48297.402(3) [25]
$(4d^{10})6p_{\frac{3}{2}}$	48500.804(1)	48500.804(2) [25]
$(4d^{10})6d_{\frac{3}{2}}$	54203.119(2)	54203.119(2) [25]
$(4d^{10})6d_{\frac{5}{2}}$	54213.564(3)	54213.570(3) [25]
$(4d^{10})6f_{\frac{5}{2}}$	58045.481(7)	This work
$(4d^{10})6g$	58054.723(16)	This work
$(4d^{10})7s_{\frac{1}{2}}$	51886.954(1)	51886.971(2) [25]
$(4d^{10})7p_{\frac{1}{2}}$	54041.087(2)	54040.99(6) [19]
$(4d^{10})7p_{\frac{3}{2}}$	54121.059(2)	54121.129(5) [25]
$(4d^{10})8s_{\frac{1}{2}}$	55581.246(3)	55581.258(3) [25]
$(4d^{10})8p_{\frac{1}{2}}$	56620.876(3)	56620.72(6) [19]
$(4d^{10})8p_{\frac{3}{2}}$	56660.596(6)	56660.559(17) [25]
$(4d^{10})7d_{\frac{3}{2}}$	56699.911(2)	56699.768(3) [25]
$(4d^{10})7d_{\frac{5}{2}}$	56705.435(2)	56705.498(3) [25]
$(4d^{10})7f_{\frac{5}{2}}$	58854.510(3)	This work
$(4d^{10})7f_{\frac{7}{2}}$	58854.755(3)	This work

the j value, appears in Tables VIII and IX for both $(4d^{10})6g_{\frac{5}{2},\frac{7}{2}}$ sublevels.

V. CONCLUSION

This work continues the series of studies of emission IR spectra of metal vapors formed in ablation by pulsed laser radiation [28]. The TR FTIR spectroscopy was applied to observations of the emission arising after the irradiation of a silver target with a pulsed laser. This study extends the knowledge of the Ag spectra by reporting 12 lines not previously observed. We classify most of them as due to transitions between low Rydberg $(4d^{10})ns$, p, d, f, and g states with n between 5 and 8. The classification of the lines is performed by accounting for line strengths calculated by the Fues model potential. This method was shown to be appropriate for Ag by extensive comparison of the present calculations with the available experimental and theoretical results. These results are further extended for transitions in the observed range; the tables of oscillator strengths presented in this work are the most comprehensive report of the dipole transition matrix element between $(4d^{10})nl_j$ states of the neutral Ag atom. Revised values are given for energies of the $(4d^{10})ns_{\frac{1}{2}}$ $(n=7,8)$, $(4d^{10})np_{\frac{1}{2},\frac{3}{2}}$ $(n=6,7,8)$, $(4d^{10})nd_{\frac{3}{2},\frac{5}{2}}$ $(n=6,7)$, and $(4d^{10})5f_{\frac{5}{2},\frac{7}{2}}$ states. The presented energy values for $(4d^{10})6f_{\frac{5}{2}}$, $(4d^{10})7f_{\frac{5}{2},\frac{7}{2}}$, and $(4d^{10})6g$ states have not been reported previously. We also recorded time profiles of the observed lines as a function of the delay time, from 0 to 30 μs, after the laser shot with maxima of emission intensity at 5–6 μs after the shot. The temporal decay of some lines is well described by a single-exponential function, while some lines display nonexponential (including some "plateaux" or secondary maxima at 20–25 μs after the laser shot). The approximate decay time for different lines varies in the 3- to 12-μs range.

ACKNOWLEDGMENTS

This work was financially supported by the Grant Agency of the Academy of Sciences of the Czech Republic (Grants No. IAA400400705 and KAN 100500652).

[1] J. E. Ross and L. H. Aller, Sol. Phys. **25**, 30 (1972).
[2] P. W. Merrill, Astrophys. J. **105**, 360 (1947).
[3] M. Jaschek and E. Brandi, Astron. Astrophys. **20**, 233 (1972).
[4] C. R. Cowley, T. Ryabchikova, F. Kupka, D. J. Bord, G. Mathys, and W. P. Bidelman, Mon. Not. R. Astron. Soc. **317**, 299 (2000).
[5] J. A. Johnson and M. Bolte, Astrophys. J. **579**, 616 (2002) [http://arxiv.org/abs/arXiv:astro-ph/0208375].
[6] J. J. Cowan, C. Sneden, S. Burles, I. I. Ivans, T. C. Beers, J. W. Truran, J. E. Lawler, F. Primas, G. M. Fuller, B. Pfeiffer, and K. Kratz, Astrophys. J. **572**, 861 (2002) [http://arxiv.org/abs/arXiv:astro-ph/0202429].
[7] N. Grevesse and A. Noels, Phys. Scripta **51**, 47 (1994).
[8] J. C. Pickering, Phys. Scripta **83**, 27 (1999).
[9] A. Jorissen, Phys. Scripta **112**, 73 (2004).
[10] F. Kerber, G. Nave, C. J. Sansonetti, and P. Bristow, Phys. Scripta **134**, 014007 (2009).
[11] F. Paschen, Ann. Phys. (Leipzig) **338**, 717 (1910).
[12] H. M. Randall, Astrophys. J. **34**, 1 (1911).
[13] H. A. Blair, Phys. Rev. A **36**, 1531 (1930).
[14] C. W. Hetzler, R. W. Boreman, and K. Burns, Phys. Rev. **48**, 656 (1935).
[15] E. Rasmussen, Phys. Rev. **57**, 243 (1940).
[16] A. G. Shenstone, Phys. Rev. **57**, 894 (1940).
[17] W. C. Martin and J. Sugar, J. Opt. Soc. Am. **59**, 1266 (1969).
[18] H.-U. Johannsen and R. Lincke, Z. Phys. A **272**, 147 (1975).
[19] C. M. Brown and M. L. Ginter, J. Opt. Soc. Am. **67**, 1323 (1977).
[20] A. M. Cantù, E. Jannitti, M. Mazzoni, M. Pettini, and G. Tondello, Phys. Scripta **19**, 283 (1979).
[21] J. P. Connerade, M. A. Baig, M. W. D. Mansfield, and E. Radtke, Proc. R. Soc. London A **361**, 379 (1978); J. P. Connerade and M. A. Baig, *ibid.* **365**, 253 (1979).
[22] S. Baier, M. Martins, B. R. Muller, M. Schulze, and P. Zimmermann, J. Phys. B **23**, 3095 (1990).
[23] M. Aslam Baig, A. Rashid, M. Hanif, W. Dussa, I. Ahmad, and J. Hormes, Phys. Rev. A **45**, 2108 (1992).
[24] S. Guérandel, T. Badr, M. Plimmer, P. Juncar, and M. Himbert, Eur. Phys. J. D **10**, 33 (2000); T. Badr, S. Guérandel, M. D. Plimmer, P. Juncar, and M. E. Himbert, *ibid.* **14**, 39 (2001).
[25] J. C. Pickering and V. Zilio, Eur. Phys. J. D **13**, 181 (2001).
[26] K. B. MacAdam, S. F. Dyubko, V. A. Efremov, V. G. Gerasimov, and M. P. Perepechay, J. Phys. B **42**, 085003 (2009).
[27] M. A. Baig, Phys. Rev. A **79**, 012509 (2009).

[28] S. Civiš, I. Matulková, J. Cihelka, K. Kawaguchi, V. E. Chernov, and E. Y. Buslov, Phys. Rev. A **81**, 012510 (2010).
[29] E. Hinnov and H. Kohn, J. Opt. Soc. Am. **47**, 156 (1957).
[30] N. P. Penkin and I.-Y. Y. Slavenas, Opt. Spectrosk. **15**, 9 (1963) [Opt. Spectrosc. (USSR) **15**, 3 (1963)].
[31] G. M. Lawrence, J. K. Link, and R. B. King, Astrophys. J. **141**, 293 (1965).
[32] N. L. Moise, Astrophys. J. **144**, 774 (1966).
[33] L. A. Levin and B. Budick, Bull. Am. Phys. Soc. **11**, 455 (1966).
[34] J. Z. Klose, Astrophys. J. **198**, 229 (1975).
[35] K. P. Selter and H. Kunze, Astrophys. J. **221**, 713 (1978).
[36] P. Hannaford and R. M. Lowe, Opt. Eng. **22**, 532 (1983).
[37] M. Soltanolkotabi and R. Gupta, Phys. Lett. A **96**, 399 (1983); Soltanolkotabi and R. M., Gupta, Physica B&C **123**, 386 (1984).
[38] J. Carlsson, P. Jönsson, and L. Sturesson, Z. Phys. D **16**, 87 (1990).
[39] P. S. Doidge, Spectrochim. Acta, Part B **50**, 209 (1995).
[40] D. A. Verner, P. D. Barthel, and D. Tytler, Astron. Astrophys. Suppl. Ser. **108**, 287 (1994).
[41] I.-Y. Y. Slavenas, Opt. Spectrosk. **20**, 485 (1966) [Opt. Spectrosc. (USSR) **20**, 264 (1966)].
[42] G. L. Plekhotkina, Opt. Spectrosk. **51**, 194 (1981) [Opt. Spectrosc. (USSR) **51**, 106 (1981)].
[43] J. Zhankui, P. Jönsson, J. Larsson, and S. Svanberg, Z. Phys. D **17**, 1 (1990).
[44] J. Bengtsson, J. Larsson, and S. Svanberg, Phys. Rev. A **42**, 5457 (1990).
[45] G. J. Bengtsson, P. Jönsson, J. Larsson, and S. Svanberg, ZPD **22**, 437 (1991).
[46] K.-T. Cheng and Y.-K. Kim, J. Opt. Soc. Am. **69**, 125 (1979).
[47] J. Migdałek and W. E. Baylis, J. Phys. B **11**, L497 (1978).
[48] J. Migdałek, J. Quant. Spectrosc. Ra. **20**, 81 (1978).
[49] J. Migdałek and W. E. Baylis, J. Quant. Spectrosc. Ra. **22**, 113 (1979).
[50] J. Migdałek and W. E. Baylis, Can. J. Phys. **57**, 1708 (1979).
[51] B. N. Chichkov and V. P. Shevelko, Phys. Scr. **23**, 1055 (1981).
[52] C. Lavin, M. A. Almaraz, and I. Martín, Z. Phys. D **34**, 143 (1995).
[53] I. Martín, M. A. Almaraz, and C. Lavin, Z. Phys. D **35**, 239 (1995).
[54] J. Migdałek and M. Garmulewicz, J. Phys. B **33**, 1735 (2000).
[55] U. I. Safronova, I. M. Savukov, M. S. Safronova, and W. R. Johnson, Phys. Rev. A **68**, 062505 (2003).
[56] L. Özdemir, B. Karaçoban, and G. Ürer, Indian J. Phys. **81**, 705 (2007).
[57] K. Kawaguchi, N. Sanechika, Y. Nishimura, R. Fujimori, T. N. Oka, Y. Hirahara, A. Jaman, and S. Civiš, Chem. Phys. Lett. **463**, 38 (2008).
[58] OPUS, "Opus spectroscopy software" [http://www.brukeroptics.com/opus.html].
[59] I. I. Sobelman, *Atomic Spectra and Radiative Transitions*, Springer Series in Chemical Physics, Vol. 1 (Springer–Verlag, Berlin, 1979).
[60] G. Simons, J. Chem. Phys. **60**, 645 (1974).
[61] I. Martin and G. Simons, J. Chem. Phys. **62**, 4799 (1975).
[62] P. G. Alcheev, V. E. Chernov, and B. A. Zon, J. Mol. Spectrosc. **211**, 71 (2002).
[63] N. L. Manakov, V. D. Ovsiannikov, and L. P. Rapoport, Phys. Rep. **141**, 320 (1986).
[64] V. E. Chernov, D. L. Dorofeev, I. Y. Kretinin, and B. A. Zon, Phys. Rev. A **71**, 022505 (2005); E. V. Akindinova, V. E. Chernov, I. Y. Kretinin, and B. A. Zon, *ibid.* **79**, 032506 (2009).
[65] I. S. Gradshteyn and I. M. Ryzhik, *Table of Integrals, Series, and Products*, 7th ed. (Academic Press, Orlando, FL, 2007).
[66] Table XVII, (2010), present work, Table XVII.
[67] NSU, "Electronic structure of atoms project" (2007), [http://i-portal.nsu.ru/lemma.dll?db=GROTRIAN&int=ENGLISH_VIEW&class=CMAINVIEW&templ=MAIN].

J. Phys. B: At. Mol. Opt. Phys. **44** (2011) 105002 (10pp) doi:10.1088/0953-4075/44/10/105002

Low-excited f-, g- and h-states in Au, Ag and Cu observed by Fourier-transform infrared spectroscopy in the 1000–7500 cm^{-1} region

S Civiš[1], I Matulková[1], J Cihelka[1], P Kubelík[1], K Kawaguchi[2] and V E Chernov[3]

[1] J. Heyrovský Institute of Physical Chemistry, Academy of Sciences of the Czech Republic, Dolejškova 3, 18223 Prague 8, Czech Republic
[2] Faculty of Science, Okayama University, Tsushima-naka, Okayama 700-8530, Japan
[3] Voronezh State University, 394693 Voronezh, Russia

E-mail: civis@jh-inst.cas.cz

Received 8 March 2011, in final form 27 March 2011
Published 27 April 2011
Online at stacks.iop.org/JPhysB/44/105002

Abstract
The infrared emission spectra of Au, Ag and Cu resulting from the laser ablation of metal targets in a vacuum were recorded using time-resolved Fourier-transform spectroscopy in the 1200–1600, 1900–3600, 4100–5000 and 5200–7500 cm^{-1} ranges with a resolution of 0.017 cm^{-1}. The majority of the observed lines correspond to transitions between low-excited Rydberg $(N\mathrm{d}^{10})nl_j$ states of Cu ($N = 3$), Ag ($N = 4$) and Au ($N = 5$) with a principal quantum number $n = 4, \ldots, 10$; the most prominent lines being due to transitions between the states with high orbital momenta $l = 3, \ldots, 5$. This study reports 32 new lines of Au, 12 of Ag and 20 of Cu (with uncertainties of 0.0003–0.03 cm^{-1}). From the lines observed here and in our previous works, we extract revised energy values for 85 energy levels (uncertainty 0.01–0.03 cm^{-1}) of which eight levels of Au, three of Ag and four of Cu are reported for the first time. These newly reported levels have high orbital momentum $l = 3, 4, 5$.

1. Introduction

The atomic states with high angular momentum are of interest for various problems of atomic physics. Since Fano's formulation of the fundamental principles of large angular momentum transfer in electron–atom scattering (Fano 1974), the high-l states have been shown to play an important role in understanding the correlation effects in processes such as the excitation and decay of autoionizing states (Napier *et al* 2008, Themelis 2010). Atomic Rydberg states with a high orbital momentum are non-penetrating states, i.e. the Rydberg electron in such states moves far away from the atomic core. Therefore, these high-l states have very small quantum defects determined by long-range interaction with the atomic core (Lundeen 2005). These interactions are described by simple analytical expressions that allow us to extract the characteristics of the atomic core ion as polarizabilities, multipole momenta from precise microwave (Hanni *et al* 2008) or optical (Keele *et al* 2010) measurements of high-l states (for the use of high-l spectroscopy for the measurement of some relativistic interaction constants, see Lundeen (2005)). Note that the theoretical calculations of these values depend crucially on very precise atomic wavefunction behaviour in the vicinity of the nucleus, and therefore the above measurements can also be considered as a test of the atomic *ab initio* calculations.

The above-mentioned measurements (Hanni *et al* 2008, Keele *et al* 2010) were performed for Rydberg multiplets corresponding to the principal quantum numbers $n = 9, \ldots, 10$ by observing transitions from these levels to states with $n' = 20, \ldots, 21$ or $n' = 30, \ldots, 31$. At the same time, information about low-lying states with $l \geqslant 4$ is rather scarce. For instance, no g-levels are reported for Au; only 5g levels are listed for Ag and Cu (the high Rydberg ng levels of Cu with $n = 23, \ldots, 28$ were studied using microwave spectroscopy

 © 2011 IOP Publishing Ltd Printed in the UK & the USA

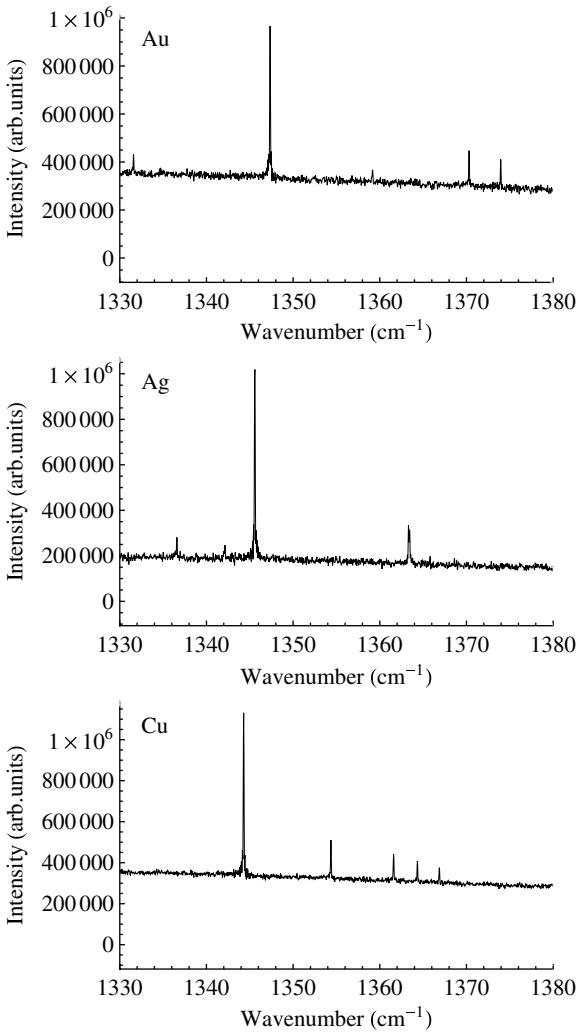

Figure 1. Emission spectra of Cu, Ag and Au in the 1330–1380 cm^{-1} range. The most prominent line (near 1345–1348 cm^{-1}) for all metals corresponds to the 5g–6h transition.

(MacAdam *et al* 2009)). No h-states have been reported for the above atoms. This paper attempts to fill this gap; this is a continuation of our study of the IR spectra of metals started in previous works (Civiš *et al* 2010a, 2010b, 2011).

We show that g- and h-states with $n = 5, \ldots, 7$ play a key role in the interpretation of the infrared spectra of Au, Ag and Cu arising in pulsed laser ablation of the metal targets in a vacuum. Some emission lines in the 2000–4000 cm^{-1} range were previously reported by us (Civiš *et al* 2010a, 2010b) with incorrect identification; after having performed the present measurements to cover the 1200–1600, 4100–5000 and 5200–7500 cm^{-1} ranges, we are able to discover the 5g-state for the gold and the 6h-states for all three metals considered. The energies of n'g- and n''h-states can easily be predicted roughly using the Rydberg formula and then refined using the measured line wavenumbers. These states allow us to give consistent classification for all lines observed in the four IR ranges mentioned.

Table 1. Radial quantum number n_r for $(N\mathrm{d}^{10})nl_j$ states of Cu ($N = 3$), Ag ($N = 4$) and Au ($N = 5$) used in the Fues model potential calculation of dipole matrix elements in this work.

	$l = 0$	$l = 1$	$l = 2$	$l = 3$	$l \geqslant 4$
Cu	$n-4$	$n-4$	$n-4$	$n-l-1$	$n-l-1$
Ag	$n-5$	$n-5$	$n-5$	$n-l-1$	$n-l-1$
Au	$n-6$	$n-6$	$n-5$	$n-5$	$n-l-1$

2. Methods

In this paper we report the IR emission spectra of Au, Ag and Cu atoms recorded using time-resolved Fourier-transform spectroscopy of the metal vapours produced during the ablation of the metal targets by a high-repetition rate (1.0 kHz) pulsed nanosecond ArF laser ($\lambda = 193$ nm, output energy of 15 mJ) in a vacuum (10^{-2} Torr). The experimental setup has already been described in detail in our previous papers (Civiš *et al* 2010a, Kawaguchi *et al* 2008). As compared to our previous studies of the spectra of these atoms (Civiš *et al* 2010a, 2010b, 2011), this work records their Fourier-transform infrared (FTIR) spectra in four spectral ranges (1200–1600, 1900–3600, 4100–5000 and 5200–7500 cm^{-1}). In the 1200–1600 cm^{-1} range we used a high-sensitivity mercury cadmium telluride (MCT) detector that allowed us to record the spectra with a reasonable signal-to-noise ratio (SNR) as compared to the previous work (Civiš *et al* 2010b). For the measurements in the 1900–3600, 4100–5000 and 5200–7500 cm^{-1} ranges, an InSb detector was used. Parts of the measured spectra are shown in figure 1.

For data sampling we used the so-called 1/3 sampling where the scanner rate was set to produce a 3 kHz He–Ne laser interference signal, the ArF laser oscillation was triggered, and 30 sets of time-resolved data were recorded with a preset time interval of 1 μs. Three scans were needed for a complete interferogram, and only five scans were co-added to improve the SNR. The spectral resolution in such a procedure was about 0.1 cm^{-1}. We also performed measurements with only one scan but with a higher resolution of about 0.017 cm^{-1} and worse SNR. The acquired spectra were post-zero-filled (zero filling 2, trapezoid apodization function) using Bruker OPUS software and subsequently corrected by subtracting the blackbody background spectrum. The wavenumbers, line widths and their intensities (as well as the uncertainties for these quantities) were then obtained using a fitting to, e.g., the Gaussian line shape. For some lines we resolved their hyperfine structure. In such cases we reported each hyperfine multiplet as a single Gaussian line whose position $\bar{p}$, full width at half maximum (FWHM) $\bar{w}$ and intensity $\bar{A}$ can be obtained using the averaging procedure:

$$\bar{A} = \sum A_i; \qquad \Delta\bar{A} = \left[\sum (\Delta A_i)^2\right]^{\frac{1}{2}} \quad \bar{p} = \frac{1}{\bar{A}} \sum p_i A_i;$$

$$\Delta\bar{p} = \frac{1}{\bar{A}} \left[\sum (A_i \Delta p_i)^2 + \sum (p_i - \bar{p})^2 (\Delta A_i)^2\right]^{\frac{1}{2}}$$

$$\bar{w} = \frac{1}{\bar{A}} \sum A_i \left[w_i^2 + (\bar{p} - p_i)^2\right] = -\bar{p}^2 + \frac{1}{\bar{A}} \sum A_i \left(w_i^2 + p_i^2\right)$$

Table 2. Au I lines and their identification. Each of the four spectral ranges (1200–1600, 1900–3600, 4100–5000 and 5200–7500 cm^{-1}) has its own scale of arbitrary units for the emission intensity.

Wavenumber (cm^{-1})	Intensity (arbitrary units)	SNR	FWHM (cm^{-1})	Identification
1289.364(8)	1.08×10^4	11.1	0.068(20)	$9s_{\frac{1}{2}}$–$9p_{\frac{3}{2}}$
1331.582(9)	1.10×10^4	7.33	0.086(28)	$8d_{\frac{5}{2}}$–$7f_{\frac{7}{2}}$
1347.3390(7)	1.00×10^5	30.7	0.023(2)	5g –6h
1370.302(3)	2.18×10^4	18.1	0.028(9)	$8d_{\frac{3}{2}}$–$7f_{\frac{5}{2}}$
1373.952(5)	1.53×10^4	13.8	0.023(14)	$6f_{\frac{5}{2}}$–$6g_{\frac{7}{2}}$
2156.521(11)	1.80×10^4	4.43	0.065(39)	5g –7h
2174.019(3)	1.77×10^4	6.48	0.033(11)	$\left[\left(5d^9_{\frac{3}{2}}6s\right)_2 6p_{\frac{3}{2}}\right]_{\frac{1}{2}}$–$8s_{\frac{1}{2}}$
2178.742(2)	1.61×10^4	14.5	0.019(4)	$7d_{\frac{3}{2}}$–$9p_{\frac{1}{2}}$
2180.650(12)	1.82×10^4	5.93	0.081(41)	$6f_{\frac{7}{2}}$–$7g_{\frac{9}{2}}$
2184.294(13)	1.06×10^4	4.67	0.067(42)	$6f_{\frac{5}{2}}$–$7g_{\frac{7}{2}}$
2193.0300(5)	1.26×10^5	62.7	0.031(1)	$8s_{\frac{1}{2}}$–$8p_{\frac{1}{2}}$
2459.403(3)	1.29×10^4	10.3	0.028(8)	$7d_{\frac{5}{2}}$–$9p_{\frac{3}{2}}$
2471.304(2)	1.70×10^4	13.9	0.028(6)	$7d_{\frac{5}{2}}$–$6f_{\frac{5}{2}}$
2474.9613(4)	6.07×10^5	82.6	0.046(1)	$7d_{\frac{5}{2}}$–$6f_{\frac{7}{2}}$
2484.120(2)	1.40×10^4	12.8	0.029(7)	$8p_{\frac{3}{2}}$–$8d_{\frac{3}{2}}$
2512.2183(3)	4.11×10^5	91.3	0.044(1)	$7d_{\frac{3}{2}}$–$6f_{\frac{5}{2}}$
2518.4851(2)	1.49×10^6	265.	0.037(1)	$5f_{\frac{7}{2}}$–$5g_{\frac{9}{2}}$
2520.6809(5)	2.08×10^5	60.0	0.044(2)	$8p_{\frac{3}{2}}$–$8d_{\frac{5}{2}}$
2522.6828(3)	1.13×10^6	131.	0.035(1)	$5f_{\frac{5}{2}}$–$5g_{\frac{7}{2}}$
2744.3848(3)	3.47×10^5	150.	0.040(1)	$8s_{\frac{1}{2}}$–$8p_{\frac{3}{2}}$
3035.474(1)	5.49×10^4	27.6	0.044(3)	$8p_{\frac{1}{2}}$–$8d_{\frac{3}{2}}$
3179.051(2)	2.11×10^4	11.5	0.025(6)	$\left[\left(5d^9_{\frac{3}{2}}6s\right)_1 6p_{\frac{3}{2}}\right]_{\frac{1}{2}}$–$8s_{\frac{1}{2}}$
3187.8097(9)	4.13×10^4	17.2	0.032(3)	$\left[\left(5d^9_{\frac{3}{2}}6s\right)_2 6p_{\frac{1}{2}}\right]_{\frac{3}{2}}$–$6d_{\frac{5}{2}}$
4463.816(21)	9.76×10^4	8.47	0.283(66)	$\left[\left(5d^9_{\frac{3}{2}}6s\right)_2 6p_{\frac{3}{2}}\right]_{\frac{3}{2}}$–$7d_{\frac{3}{2}}$
4504.725(9)	1.09×10^6	7.34	0.282(34)	$\left[\left(5d^9_{\frac{3}{2}}6s\right)_2 6p_{\frac{3}{2}}\right]_{\frac{3}{2}}$–$7d_{\frac{5}{2}}$
4644.939(13)	6.48×10^4	7.11	0.120(40)	$7d_{\frac{5}{2}}$–$8f_{\frac{7}{2}}$
4672.724(10)	9.40×10^4	12.7	0.141(30)	$5f_{\frac{7}{2}}$–$7g_{\frac{9}{2}}$
4676.968(11)	3.51×10^4	7.55	0.087(36)	$5f_{\frac{5}{2}}$–$7g_{\frac{7}{2}}$
4688.344(12)	5.17×10^4	8.94	0.115(38)	$7d_{\frac{3}{2}}$–$8f_{\frac{5}{2}}$
4709.816(3)	4.62×10^5	23.2	0.124(10)	$7p_{\frac{1}{2}}$–$8s_{\frac{1}{2}}$
4900.786(8)	8.96×10^4	15.4	0.131(24)	$\left[\left(5d^9_{\frac{3}{2}}6s\right)_2 6p_{\frac{3}{2}}\right]_{\frac{1}{2}}$–$7d_{\frac{3}{2}}$
4984.048(5)	1.20×10^5	18.3	0.116(15)	$6d_{\frac{3}{2}}$–$8p_{\frac{1}{2}}$
5227.367(10)	2.63×10^4	8.82	0.082(30)	$8s_{\frac{1}{2}}$–$9p_{\frac{3}{2}}$
5454.902(3)	3.18×10^4	9.45	0.029(7)	$6d_{\frac{5}{2}}$–$5f_{\frac{5}{2}}$
5459.1214(5)	1.06×10^6	22.3	0.039(2)	$6d_{\frac{5}{2}}$–$5f_{\frac{7}{2}}$
5537.3925(4)	6.70×10^5	35.3	0.038(1)	$6d_{\frac{3}{2}}$–$5f_{\frac{5}{2}}$
5547.842(8)	2.20×10^4	5.89	0.087(22)	$7s_{\frac{1}{2}}$–$7p_{\frac{1}{2}}$
5896.366(9)	3.95×10^4	10.7	0.118(24)	$\left[\left(5d^9_{\frac{3}{2}}6s\right)_2 6p_{\frac{1}{2}}\right]_{\frac{3}{2}}$–$8s_{\frac{1}{2}}$
5905.855(6)	2.86×10^4	20.1	0.078(33)	$\left[\left(5d^9_{\frac{3}{2}}6s\right)_1 6p_{\frac{3}{2}}\right]_{\frac{3}{2}}$–$7d_{\frac{3}{2}}$
7118.816(14)	2.17×10^4	5.55	0.061(41)	$\left[\left(5d^9_{\frac{3}{2}}6s\right)_1 6p_{\frac{3}{2}}\right]_{\frac{3}{2}}$–$9s_{\frac{1}{2}}$
7436.611(6)	2.70×10^4	10.6	0.102(18)	$7p_{\frac{1}{2}}$–$7d_{\frac{3}{2}}$

$$\Delta\bar{w} = \frac{1}{2\bar{w}}\left[\sum\left(\frac{\partial\bar{w}^2}{\partial w_i}\Delta w_i\right)^2 + \sum\left(\frac{\partial\bar{w}^2}{\partial p_i}\Delta p_i\right)^2 + \sum\left(\frac{\partial\bar{w}^2}{\partial A_i}\Delta A_i\right)^2\right]^{\frac{1}{2}} \qquad \frac{\partial\bar{w}^2}{\partial w_i} = \frac{2A_i w_i}{\bar{A}}; \qquad \frac{\partial\bar{w}^2}{\partial p_i} = \frac{2A_i(p_i-\bar{p})}{\bar{A}}; \qquad \frac{\partial\bar{w}^2}{\partial A_i} = \frac{(p_i-\bar{p})^2 + w_i^2 - \bar{w}^2}{\bar{A}}. \tag{1}$$

Table 3. FMP-calculated transition dipole moments (line strengths S_{ik}, oscillator strengths f_{ik}, transition probabilities A_{ki}) between the $5d^{10}$ states of the Au atom observed in this work. The energies of all levels are taken from the present measurement (see table 4) except that for the $7p_{\frac{3}{2}}$ level (taken from George *et al* 1988) and $6g_{\frac{9}{2}}$ levels (extrapolated from the values reported in table 4). The Ritz wavenumbers ν and air wavelengths λ are calculated using these energy values.

Transition i–k	Lower level (cm^{-1})	Upper level (cm^{-1})	ν (cm^{-1})	λ (nm)	S_{ik} (au)	f_{ik}	A_{ki} (s^{-1})
$6g_{\frac{9}{2}}$–$8f_{\frac{7}{2}}$	71 355.890	72 155.539	799.649	12502.1	9.78×10^{1}	2.38×10^{-2}	1.27×10^{4}
$6g_{\frac{7}{2}}$–$8f_{\frac{7}{2}}$	71 355.845	72 155.539	799.694	12501.4	2.79	8.48×10^{-4}	3.62×10^{2}
$6g_{\frac{7}{2}}$–$8f_{\frac{5}{2}}$	71 355.845	72 158.019	802.174	12462.7	7.22×10^{1}	2.20×10^{-2}	1.26×10^{4}
$6g_{\frac{9}{2}}$–$7h_{\frac{11}{2}}$	71 355.890	72 168.489	812.599	12302.8	5.91×10^{3}	1.46	5.36×10^{5}
$6g_{\frac{9}{2}}$–$7h_{\frac{9}{2}}$	71 355.890	72 168.489	812.599	12302.8	1.10×10^{2}	2.70×10^{-2}	1.19×10^{4}
$6g_{\frac{7}{2}}$–$7h_{\frac{9}{2}}$	71 355.845	72 168.489	812.644	12302.2	4.82×10^{3}	1.49	5.24×10^{5}
$9s_{\frac{1}{2}}$–$9p_{\frac{1}{2}}$	68 680.631	69 648.344	967.713	10330.8	4.48×10^{2}	6.58×10^{-1}	4.11×10^{5}
$8p_{\frac{3}{2}}$–$9s_{\frac{1}{2}}$	67 487.264	68 680.631	1193.367	8377.37	5.23×10^{2}	4.74×10^{-1}	9.00×10^{5}
$9s_{\frac{1}{2}}$–$9p_{\frac{3}{2}}$	68 680.631	69 969.927	1289.296	7754.06	6.64×10^{2}	1.30	7.21×10^{5}
$5g_{\frac{9}{2}}$–$7f_{\frac{7}{2}}$	70 011.968	71 339.538	1327.570	7530.51	2.20×10^{1}	8.89×10^{-3}	1.31×10^{4}
$5g_{\frac{7}{2}}$–$7f_{\frac{7}{2}}$	70 011.96	71 339.538	1327.578	7530.46	6.30×10^{-1}	3.17×10^{-4}	3.73×10^{2}
$5g_{\frac{7}{2}}$–$7f_{\frac{5}{2}}$	70 011.96	71 341.709	1329.749	7518.17	1.66×10^{1}	8.38×10^{-3}	1.32×10^{4}
$8d_{\frac{5}{2}}$–$7f_{\frac{7}{2}}$	70 007.956	71 339.538	1331.582	7507.82	2.17×10^{3}	1.47	1.30×10^{6}
$8d_{\frac{5}{2}}$–$7f_{\frac{5}{2}}$	70 007.956	71 341.709	1333.753	7495.60	1.08×10^{2}	7.30×10^{-2}	8.66×10^{4}
$5g_{\frac{9}{2}}$–$6h_{\frac{11}{2}}$	70 011.968	71 359.307	1347.339	7420.01	4.02×10^{3}	1.65	1.66×10^{6}
$5g_{\frac{9}{2}}$–$6h_{\frac{9}{2}}$	70 011.968	71 359.307	1347.339	7420.01	7.45×10^{1}	3.05×10^{-2}	3.69×10^{4}
$5g_{\frac{7}{2}}$–$6h_{\frac{9}{2}}$	70 011.96	71 359.307	1347.347	7419.97	3.28×10^{3}	1.68	1.62×10^{6}
$8d_{\frac{3}{2}}$–$7f_{\frac{5}{2}}$	69 971.407	71 341.709	1370.302	7295.67	1.41×10^{3}	1.47	1.22×10^{6}
$8p_{\frac{1}{2}}$–$9s_{\frac{1}{2}}$	66 935.902	68 680.631	1744.729	5729.99	1.70×10^{2}	4.51×10^{-1}	9.16×10^{5}
$7p_{\frac{1}{2}}$–$6d_{\frac{3}{2}}$	60 033.076	61 951.885	1918.809	5210.15	1.65×10^{2}	4.81×10^{-1}	5.90×10^{5}
$5g_{\frac{9}{2}}$–$8f_{\frac{7}{2}}$	70 011.968	72 155.539	2143.571	4663.84	2.15	1.40×10^{-3}	5.36×10^{3}
$5g_{\frac{7}{2}}$–$8f_{\frac{7}{2}}$	70 011.96	72 155.539	2143.579	4663.82	6.14×10^{-2}	5.00×10^{-5}	1.53×10^{2}
$5g_{\frac{7}{2}}$–$8f_{\frac{5}{2}}$	70 011.96	72 158.019	2146.059	4658.43	1.60	1.30×10^{-3}	5.33×10^{3}
$8d_{\frac{5}{2}}$–$8f_{\frac{7}{2}}$	70 007.956	72 155.539	2147.583	4655.13	2.51×10^{2}	2.73×10^{-1}	6.29×10^{5}
$8d_{\frac{5}{2}}$–$8f_{\frac{5}{2}}$	70 007.956	72 158.019	2150.063	4649.76	1.26×10^{1}	1.37×10^{-2}	4.22×10^{4}
$5g_{\frac{9}{2}}$–$7h_{\frac{11}{2}}$	70 011.968	72 168.489	2156.521	4635.83	3.05×10^{2}	2.00×10^{-1}	5.16×10^{5}
$5g_{\frac{9}{2}}$–$7h_{\frac{9}{2}}$	70 011.968	72 168.489	2156.521	4635.83	5.64	3.70×10^{-3}	1.15×10^{4}
$5g_{\frac{7}{2}}$–$7h_{\frac{9}{2}}$	70 011.96	72 168.489	2156.529	4635.82	2.48×10^{2}	2.03×10^{-1}	5.05×10^{5}
$7d_{\frac{3}{2}}$–$9p_{\frac{1}{2}}$	67 469.675	69 648.344	2178.669	4588.71	1.47×10^{2}	2.43×10^{-1}	1.54×10^{6}
$8d_{\frac{3}{2}}$–$8f_{\frac{5}{2}}$	69 971.407	72 158.019	2186.612	4572.04	1.76×10^{2}	2.93×10^{-1}	6.23×10^{5}
$8s_{\frac{1}{2}}$–$8p_{\frac{1}{2}}$	64 742.879	66 935.902	2193.023	4558.67	1.58×10^{2}	5.26×10^{-1}	1.69×10^{6}
$7d_{\frac{5}{2}}$–$9p_{\frac{3}{2}}$	67 510.6	69 969.927	2459.327	4065.04	1.09×10^{2}	1.35×10^{-1}	8.19×10^{5}
$7d_{\frac{5}{2}}$–$6f_{\frac{5}{2}}$	67 510.6	69 981.893	2471.293	4045.36	6.12×10^{1}	7.66×10^{-2}	3.12×10^{5}
$7d_{\frac{5}{2}}$–$6f_{\frac{7}{2}}$	67 510.6	69 985.563	2474.963	4039.36	1.22×10^{3}	1.53	4.69×10^{6}
$5f_{\frac{5}{2}}$–$8d_{\frac{3}{2}}$	67 489.277	69 971.407	2482.130	4027.70	9.06×10^{-1}	1.14×10^{-3}	7.02×10^{3}
$8p_{\frac{3}{2}}$–$8d_{\frac{3}{2}}$	67 487.264	69 971.407	2484.143	4024.44	1.14×10^{1}	2.15×10^{-2}	8.83×10^{4}
$7d_{\frac{3}{2}}$–$9p_{\frac{3}{2}}$	67 469.675	69 969.927	2500.252	3998.51	1.10×10^{1}	2.09×10^{-2}	8.70×10^{4}
$7d_{\frac{3}{2}}$–$6f_{\frac{5}{2}}$	67 469.675	69 981.893	2512.218	3979.46	8.31×10^{2}	1.58	4.45×10^{6}
$5f_{\frac{7}{2}}$–$8d_{\frac{5}{2}}$	67 493.483	70 007.956	2514.473	3975.89	7.48×10^{-1}	7.14×10^{-4}	4.01×10^{3}
$5f_{\frac{7}{2}}$–$5g_{\frac{7}{2}}$	67 493.483	70 011.96	2518.477	3969.57	3.90×10^{1}	3.73×10^{-2}	1.58×10^{5}
$5f_{\frac{7}{2}}$–$5g_{\frac{9}{2}}$	67 493.483	70 011.968	2518.485	3969.56	1.37×10^{3}	1.31	4.42×10^{6}
$5f_{\frac{5}{2}}$–$8d_{\frac{5}{2}}$	67 489.277	70 007.956	2518.679	3969.25	3.60×10^{-2}	4.59×10^{-5}	1.94×10^{2}
$8p_{\frac{3}{2}}$–$8d_{\frac{5}{2}}$	67 487.264	70 007.956	2520.692	3966.08	8.80×10^{1}	1.68×10^{-1}	4.76×10^{5}
$5f_{\frac{5}{2}}$–$5g_{\frac{7}{2}}$	67 489.277	70 011.96	2522.683	3962.95	1.05×10^{3}	1.34	4.28×10^{6}
$8s_{\frac{1}{2}}$–$8p_{\frac{3}{2}}$	64 742.879	67 487.264	2744.385	3642.81	2.47×10^{2}	1.03	2.58×10^{6}
$8p_{\frac{1}{2}}$–$8d_{\frac{3}{2}}$	66 935.902	69 971.407	3035.505	3293.45	1.18×10^{1}	5.42×10^{-2}	1.67×10^{5}
$7d_{\frac{5}{2}}$–$7f_{\frac{7}{2}}$	67 510.6	71 339.538	3828.938	2610.98	1.14×10^{2}	2.21×10^{-1}	1.62×10^{6}
$7d_{\frac{5}{2}}$–$7f_{\frac{5}{2}}$	67 510.6	71 341.709	3831.109	2609.50	5.73	1.11×10^{-2}	1.09×10^{5}
$5f_{\frac{7}{2}}$–$6g_{\frac{7}{2}}$	67 493.483	71 355.845	3862.362	2588.38	3.56	5.21×10^{-3}	5.19×10^{4}
$5f_{\frac{7}{2}}$–$6g_{\frac{9}{2}}$	67 493.483	71 355.890	3862.407	2588.35	1.24×10^{2}	1.82×10^{-1}	1.45×10^{6}

Table 3. (Continued)

Transition i–k	Lower level (cm^{-1})	Upper level (cm^{-1})	ν (cm^{-1})	λ (nm)	S_{ik} (au)	f_{ik}	A_{ki} (s^{-1})
$5f_{\frac{5}{2}}$–$6g_{\frac{7}{2}}$	67 489.277	71 355.845	3866.568	2585.57	9.62×10^{1}	1.88×10^{-1}	1.41×10^{6}
$7d_{\frac{3}{2}}$–$7f_{\frac{5}{2}}$	67 469.675	71 341.709	3872.034	2581.92	8.16×10^{1}	2.40×10^{-1}	1.60×10^{6}
$5f_{\frac{7}{2}}$–$7g_{\frac{9}{2}}$	67 493.483	72 166.209	4672.726	2139.49	3.33×10^{1}	5.91×10^{-2}	6.88×10^{5}
$5f_{\frac{7}{2}}$–$7g_{\frac{7}{2}}$	67 493.483	72 166.221	4672.738	2139.49	9.51×10^{-1}	1.69×10^{-3}	2.46×10^{4}
$5f_{\frac{5}{2}}$–$7g_{\frac{7}{2}}$	67 489.277	72 166.221	4676.944	2137.56	2.58×10^{1}	6.10×10^{-2}	6.68×10^{5}
$7p_{\frac{1}{2}}$–$8s_{\frac{1}{2}}$	60 033.076	64 742.879	4709.803	2122.65	4.03×10^{1}	2.88×10^{-1}	4.26×10^{6}
$8s_{\frac{1}{2}}$–$9p_{\frac{1}{2}}$	64 742.879	69 648.344	4905.465	2037.99	1.54	1.15×10^{-2}	1.84×10^{5}
$6d_{\frac{3}{2}}$–$8p_{\frac{1}{2}}$	61 951.885	66 935.902	4984.017	2005.87	3.95×10^{1}	1.49×10^{-1}	4.95×10^{6}
$8s_{\frac{1}{2}}$–$9p_{\frac{3}{2}}$	64 742.879	69 969.927	5227.048	1912.60	1.02×10^{1}	8.08×10^{-2}	7.36×10^{5}
$6d_{\frac{5}{2}}$–$8p_{\frac{3}{2}}$	62 034.361	67 487.264	54 52.903	1833.38	3.22×10^{1}	8.90×10^{-2}	2.65×10^{6}
$6d_{\frac{5}{2}}$–$5f_{\frac{5}{2}}$	62 034.361	67 489.277	5454.916	1832.71	2.76×10^{1}	7.62×10^{-2}	1.51×10^{6}
$6d_{\frac{5}{2}}$–$5f_{\frac{7}{2}}$	62 034.361	67 493.483	5459.122	1831.30	5.52×10^{2}	1.52	2.27×10^{7}
$6d_{\frac{3}{2}}$–$8p_{\frac{3}{2}}$	61 951.885	67 487.264	5535.379	1806.07	3.30	1.39×10^{-2}	2.84×10^{5}
$6d_{\frac{3}{2}}$–$5f_{\frac{5}{2}}$	61 951.885	67 489.277	5537.392	1805.41	3.80×10^{2}	1.60	2.18×10^{7}
$7s_{\frac{1}{2}}$–$7p_{\frac{1}{2}}$	54 485.235	60 033.076	5547.841	1802.01	4.26×10^{1}	3.59×10^{-1}	7.37×10^{6}
$7p_{\frac{1}{2}}$–$7d_{\frac{3}{2}}$	60 033.076	67 469.675	7436.599	1344.33	1.29	1.46×10^{-2}	2.69×10^{5}

Here the sum runs through all components of the multiplet; p_i, w_i and A_i are the positions, FWHMs and intensities of the multiplet components; Δ represents uncertainties. For each component these quantities were obtained by a Gaussian fitting; an example of such a fitting of hyperfine components together with the resulting averaged lines is given in figure 3. Equations (1) have a clear physical meaning: A is determined as the area under the spectral line, $\bar{p}$ is the 'centre of gravity' of the multiplet, and w can be considered to be proportional to the root mean square deviation.

The line identification in this work essentially uses the dipole matrix elements (line strengths) for the transition between the $(N\mathrm{d}^{10})nl_j$ states of Cu ($N = 3$), Ag ($N = 4$) and Au ($N = 5$). We report here the results of the dipole transition moment calculation for gold only since the corresponding tables for silver and copper have already been published in our previous papers (Civiš *et al* 2010b) and (Civiš *et al* 2011) correspondingly. The Fues model potential method (FMP) for these calculations was outlined in the previous paper (Civiš *et al* 2010b); the choice of the radial quantum number n_r (which is equal to the number of nodes of the radial wavefunction) for all the atoms under study is given in table 1.

The procedure for extracting the energy values for the levels involved in the observed transitions is briefly described in our previous paper (Civiš *et al* 2010b). Since it implies a least-squares fitting, it is obvious that adding new transitions to this procedure can slightly change (and, generally speaking, improve) the output results for the energy levels. Indeed, as a rule, they demonstrate slight differences (within the specified error range) from those reported in our previous studies (Civiš *et al* 2010a, 2010b, 2011) based on fewer sets of observed transitions. In some cases (e.g. for Au) the discrepancies are not small and they are caused by the new classification of some transitions given in this paper, having taken into account the whole set of the observed lines. We consider these values (shown in tables 4, 7 and 9) as recommended. All the uncertainties in the tables below are given in round brackets after the corresponding values and should be treated as their rightmost significant digits, e.g. 123.4(5.6) means 123.4 ± 5.6.

3. Results and discussion

3.1. Au

Our measurements of Au FTIR spectra were performed in three spectral regions (1200–1600, 1900–3600, 5200–7500 cm^{-1}) and this has resulted in some corrections to our previous identification (Civiš *et al* 2010a) of Au I levels which were based on the 1900–3600 cm^{-1} range only. The measured emission lines are presented in table 2.

The strongest lines measured in the 5200–7500 cm^{-1} region are the 5459.12 and 5537.4 cm^{-1} lines. Together with the weaker 5454.9 cm^{-1} line, they are easily classified as due to the 6d–5f transition triplet. This yields the fine-structure splitting of about 4 cm^{-1} between the $5f_{\frac{5}{2}}$ and $5f_{\frac{7}{2}}$ states. The latter value, in turn, suggests that the two strongest lines (2522.69 and 2518.49 cm^{-1}) in the 1900–3600 cm^{-1} region are due to the 5f–5g transitions. Following the first (and the only) report on the IR spectrum of gold (George *et al* 1988), in our previous paper (Civiš *et al* 2010a) we gave another classification for these lines based on measurements in the 1800–4000 cm^{-1} range only. The present classification is essentially based on the 5g states discovered from measurements in the 5200–7500 cm^{-1} range. The correctness of the present assignment is supported by the calculations of the dipole transition matrix elements presented in table 3. Indeed, according to this table, the most intense lines in the 1900–3600 cm^{-1} region should correspond to the $5f_{\frac{7}{2}}$–$5g_{\frac{9}{2}}$ and $5f_{\frac{5}{2}}$–$5g_{\frac{7}{2}}$ transitions. The third component of this triplet, the $5f_{\frac{7}{2}}$–$5g_{\frac{7}{2}}$ line, has significantly low intensity and is blended by the strong 2518.49 cm^{-1} line, due to small (about 0.01 cm^{-1}, see table 4) fine-structure splitting between the 5g levels.

Table 4. Revised values of some levels of Au I.

Term	Energy (cm^{-1})	Other sources
$5d^{10}7h$	72 168.489(37)	This work
$5d^{10}7g_{\frac{9}{2}}$	72 166.211(47)	This work
$5d^{10}7g_{\frac{7}{2}}$	72 166.188(45)	This work
$5d^{10}6h$	71 359.307(35)	This work
$5d^{10}6g_{\frac{7}{2}}$	71 355.845(43)	This work
$5d^{10}7f_{\frac{5}{2}}$	71 341.709(40)	This work
$5d^{10}7f_{\frac{7}{2}}$	71 339.538(34)	71 339.569[a]
$5d^{10}5g_{\frac{9}{2}}$	70 011.968(35)	This work
$5d^{10}5g_{\frac{7}{2}}$	70 011.960(47)	This work
$5d^{10}8d_{\frac{5}{2}}$	70 007.956(33)	70 007.6[b] , 70 007.975[c]
$5d^{10}6f_{\frac{7}{2}}$	69 985.561(45)	69 985.559[a]
$5d^{10}6f_{\frac{5}{2}}$	69 981.893(43)	69 988.172[a]
$5d^{10}8d_{\frac{3}{2}}$	69 971.407(40)	69 971.3[b] , 69 971.418[c]
$5d^{10}9p_{\frac{3}{2}}$	69 969.926(94)	69 969.89[d] , 69 967.489[a]
$5d^{10}9p_{\frac{1}{2}}$	69 648.345(75)	69 648.28[d] , 69 950.681[a]
$5d^{10}9s_{\frac{1}{2}}$	68 680.631(50)	68 680.5[b] , 68 680.628[c]
$5d^{10}7d_{\frac{5}{2}}$	67 510.600(45)	67 510.7[b] , 67 510.605[c]
$5d^{10}5f_{\frac{5}{2}}$	67 489.277(47)	67 490.0[b] , 67 489.276[f] , 67 491.487[a]
$5d^{10}5f_{\frac{7}{2}}$	67 493.483(35)	67 485.3[b] , 67 485.292[a]
$5d^{10}7d_{\frac{3}{2}}$	67 469.675(44)	67 469.4[b] , 67 469.683[c]
$5d^{10}8p_{\frac{3}{2}}$	67 487.264(29)	67 487.11[d] , 67 487.291[a]
$5d^{10}8p_{\frac{1}{2}}$	66 935.902(29)	66 935.76[d] , 66 935.941[a]
$5d^{10}8s_{\frac{1}{2}}$	64 742.879(29)	64 742.4[b] , 64 742.896[c] , 64 742.911[a]
$\left[\left(5d^9_{\frac{3}{2}}6s\right)_2 6p_{\frac{3}{2}}\right]_{\frac{3}{2}}$	63 005.873(38)	63 005.1[b] (20° state), 63 005.7[e] (J series, $n = 6$), 63 005.883[f]
$\left[\left(5d^9_{\frac{3}{2}}6s\right)_2 6p_{\frac{3}{2}}\right]_{\frac{1}{2}}$	62 568.757(131)	62 568.7[e] (I series, $n = 6$)
$5d^{10}6d_{\frac{5}{2}}$	62 034.361(35)	62 033.7[b] , 62034.363[c]
$5d^{10}6d_{\frac{3}{2}}$	61 951.885(48)	61 951.6[b] , 61 951.886[c]
$\left[\left(5d^9_{\frac{3}{2}}6s\right)_1 6p_{\frac{3}{2}}\right]_{\frac{3}{2}}$	61 563.839(20)	61 563.840[f] , 61 563.7[e] (E series, $n = 6$), 61 563.3[b] (19° state)
$5d^{10}7p_{\frac{1}{2}}$	60 033.076(20)	60 033.0[b] , 60 032.85[d] , 60 033.076[f]
$\left[\left(5d^9_{\frac{3}{2}}6s\right)_2 6p_{\frac{1}{2}}\right]_{\frac{3}{2}}$	58 846.546(19)	58 845.1[b] (16° state), 58 845.414[c] (16° state), 58 846.4[e] (H series, $n = 6$), 58 846.546[f]
$5d^{10}7s_{\frac{1}{2}}$	54 485.235(50)	54 484.9[b] , 54 485.235[c]

[a] Civiš *et al* (2010a).
[b] Platt and Sawyer (1941).
[c] Ehrhardt and Davis (1971).
[d] Brown and Ginter (1978).
[e] Jannitti *et al* (1979).
[f] George *et al* (1988).

The presence of only one very prominent line, 1347.34 cm^{-1}, in the 1200–1600 cm^{-1} range can easily be explained by assigning it as due to the 5g–6h transition. The triplet of possible lines is not resolved because of the small fine-structure splitting of the 5g and 6h levels. This classification is also supported by table 3 which lists the 5g–6h transition as the most probable in the 1200–1600 cm^{-1} range (if we take into account the sum of the intensities of the three $5g_{\frac{7}{2}}$–$6h_{\frac{9}{2}}$, $5g_{\frac{9}{2}}$–$6h_{\frac{9}{2}}$ and $5g_{\frac{9}{2}}$–$6h_{\frac{11}{2}}$ lines with almost equal wavenumbers).

Table 5. A summary of corrections to the previous results (Civiš *et al* 2010a) for the classification of Au lines in the 1900–3600 range.

Wavenumber (cm^{-1})	Previous	Present
2156.48	$8d_{\frac{5}{2}}$–$8f_{\frac{7}{2}}$	5g–7h
2428.36	$9p_{\frac{3}{2}}$–$12s_{\frac{1}{2}}$	Not observed
2512.22	$9p_{\frac{1}{2}}$–$10d_{\frac{3}{2}}$	$7d_{\frac{3}{2}}$–$6f_{\frac{5}{2}}$
2518.49	$5f_{\frac{7}{2}}$–$8d_{\frac{5}{2}}$[a], $7d_{\frac{3}{2}}$–$6f_{\frac{5}{2}}$	$5f_{\frac{7}{2}}$–$5g_{\frac{9}{2}}$
2522.69	$5f_{\frac{7}{2}}$–$8d_{\frac{5}{2}}$	$5f_{\frac{5}{2}}$–$5g_{\frac{7}{2}}$
2743.37	Not classified	Not observed
2747.57	$9p_{\frac{1}{2}}$–$12s_{\frac{1}{2}}$	Not observed
2749.6	$9d_{\frac{3}{2}}$–23p	Not observed

[a] George *et al* (1988).

Given the energy levels of the 5f, 5g and 6h states, one can easily predict the energies of the nf, ng and nh levels by the extrapolation of the Rydberg formula assuming the quantum defects to be independent of n. Some levels (with $n = 6, 7$) of such a series are involved into the observed transitions, and their energies can then be determined from the measured wavenumbers. The discovery of the ng and nh levels allows us now to make some corrections to our previous classification (Civiš *et al* 2010a) based on emission measurements in the 1800–4000 cm^{-1} range only. The summary of corrections to the previous results are given in table 5 and we consider the present classification as the recommended one. Some weak lines reported in the previous work were not observed in the present measurements; this could be due to different plasma conditions in two experiments. Note that there are also some differences between the line sets observed in our measurements and in the paper by George *et al* (1988): we observed no lines with wavenumbers greater than 6000 cm^{-1} from those listed by George *et al* (1988). In turn, in the 2100–3100 cm^{-1} range, their list lacks all lines observed in this work except the 2518.49 cm^{-1} line. This is probably caused by the different excitation mechanisms in the hollow cathode discharge (George *et al* 1988) and laser ablation experiments.

Table 4 contains the revised energy values of the Au levels obtained from the present measurement in three spectral ranges. The majority of the energies are close to the previously reported values. The most significant discrepancy (about 8 cm^{-1}) is found for the $5f_{\frac{5}{2}}$ term whose energy value was reported 70 years ago (Platt and Sawyer 1941). Together with the incorrect classification of the 2518.49 cm^{-1} line, this old-reported energy value has caused some problems with discrepancies between the measured and calculated wavenumbers in the paper by George *et al* (1988, bottom of p 1501). With our new classification involving the g- and h-states, the observed set of lines and levels seems to be self-consistent and we consider the energy values of the levels presented in table 4 to be the recommended ones.

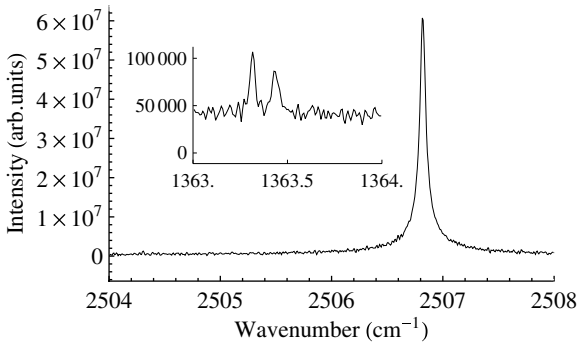

Figure 2. The 4f–5g (2506.82 cm^{-1}) line with a non-resolved fine-splitting structure and $5f_{\frac{7}{2}}$–$6g_{\frac{9}{2}}$ and $5f_{\frac{5}{2}}$–$6g_{\frac{7}{2}}$ doublet (1362 cm^{-1}) in Ag I. The arbitrary units for intensity have different scales on vertical axes in the inset and in the main graph.

3.2. Ag

The emission spectra of Ag were recorded in the three ranges, 1200–1600 cm^{-1}, 4100–5000 cm^{-1} and 5200–7500 cm^{-1}. Only for the latter range have we found an earlier (but century-old) study (Randall 1911) of Ag lines which reported four lines: 5438.6, 5460.7, 5740.0 and 5943.9 cm^{-1}. Our results (six lines in table 6) display some differences but obviously have a much higher accuracy, which made it possible for us to resolve the fine structure of the 4f states.

Indeed, our previous measurement (Civiš *et al* 2010b) has shown that the fine splitting of the f-states in Ag is quite small (0.122 cm^{-1} and 0.245 cm^{-1} for the 5f and 7f states correspondingly) and that it is considerably low as compared to the fine-structure splitting of the f-states in Au and Cu. The fine structure of the 4f state in Ag remained unresolved. We noted (Civiš *et al* 2010b) that, to obtain reliable values of the fine-splitting component of the 4f levels, one should consider the transitions from these states to *n*d states, since the latter have larger fine-structure splitting. Such transitions (with $n = 5$) have been observed in this work in the 5200–7500 cm^{-1} range and this allowed us to resolve the fine structure for the 4f state. We have also resolved this for the 6g state, using the 5f–6g doublet measured at 1363 cm^{-1}. Unfortunately, our data are still not sufficient to resolve the fine structure of the 5g state from the most prominent 2506 cm^{-1} line since, due to its high intensity and comparatively large width, it cannot be reliably fitted by a two-peak curve. We show this line together with the less intensive 1363 cm^{-1} doublet in figure 2.

The present measurements in the 1200–1600 cm^{-1} range also help us to resolve some problems with line identification in the previous measurement (Civiš *et al* 2010b) using a low-sensitive MCT detector resulting in a high noise level. We are able to observe the 7d–6f doublet at 1336.6 and 1342.15 cm^{-1} while the most prominent 1345.6 cm^{-1} line (incorrectly classified as due to the $7d_{\frac{3}{2}}$–$6f_{\frac{5}{2}}$ transition (Civiš *et al* 2010b)) corresponds to the 5g–5h transition, similar to the case of Au.

Table 7 presents the energies of the Ag levels involved in the observed transitions. Their uncertainties are lower than those for Au and Cu (see table 9), since for the Ag levels we used the high-accuracy reference values published by Pickering and Zilio (2001). Most of the values do not differ much from the previous measurement (Civiš *et al* 2010b) and from other sources. The exception is the $6f_{\frac{5}{2}}$ level whose value was extracted using an incorrect identification of the 1345.6 cm^{-1} line (Civiš *et al* 2010b). In this table we did not include some levels for which we have obtained exactly the same values as reported in the previous work (Civiš *et al* 2010b).

Table 6. Ag I lines and their identification. Each of the three spectral ranges, 1200–1600 cm^{-1}, 4100–5000 cm^{-1} and 5200–7500 cm^{-1}, has its own scale of arbitrary units for the emission intensity.

Wavenumber (cm^{-1})	Intensity (arbitrary units)	SNR	FWHM (cm^{-1})	Identification
1336.596(3)	1.91×10^{3}	9.85	0.032(9)	$7d_{\frac{5}{2}}$–$6f_{\frac{7}{2}}$
1342.154(4)	1.53×10^{3}	7.42	0.032(10)	$7d_{\frac{3}{2}}$–$6f_{\frac{5}{2}}$
1345.5757(4)	1.81×10^{4}	54.9	0.033(1)	5g–6h
1363.315(2)	3.06×10^{3}	12.7	0.029(5)	$5f_{\frac{7}{2}}$–$6g_{\frac{9}{2}}$
1363.435(3)	3.14×10^{3}	8.63	0.042(8)	$5f_{\frac{5}{2}}$–$6g_{\frac{7}{2}}$
1392.791(7)	6.51×10^{3}	7.94	0.061(30)	$8p_{\frac{3}{2}}$–$8d_{\frac{5}{2}}$
1460.111(1)	1.73×10^{3}	19.3	0.018(3)	$7p_{\frac{3}{2}}$–$8s_{\frac{1}{2}}$
4241.535(8)	1.63×10^{4}	8.56	0.071(28)	$5p_{\frac{3}{2}}$–$4d^{9}5s^{2}(^{2}D_{\frac{3}{2}})$
4356.957(17)	1.72×10^{4}	5.07	0.093(52)	$7p_{\frac{3}{2}}$–$10s_{\frac{1}{2}}$
4659.898(6)	2.15×10^{5}	20.9	0.122(9)	4f–7g
4743.434(11)	3.67×10^{4}	6.42	0.092(35)	$7p_{\frac{3}{2}}$–$9d_{\frac{5}{2}}$
4773.611(4)	1.05×10^{5}	27.1	0.101(13)	$7s_{\frac{1}{2}}$–$8p_{\frac{3}{2}}$
5440.5263(4)	1.68×10^{6}	41.5	0.041(1)	$5d_{\frac{5}{2}}$–$4f_{\frac{7}{2}}$
5460.7604(4)	9.06×10^{5}	76.5	0.041(1)	$5d_{\frac{3}{2}}$–$4f_{\frac{5}{2}}$
5712.7521(6)	4.73×10^{5}	55.2	0.038(2)	$6p_{\frac{3}{2}}$–$6d_{\frac{5}{2}}$
5741.2630(7)	6.70×10^{5}	45.3	0.041(2)	$6s_{\frac{1}{2}}$–$6p_{\frac{1}{2}}$
5905.714(1)	2.02×10^{5}	27.6	0.037(3)	$6p_{\frac{1}{2}}$–$6d_{\frac{3}{2}}$
5944.6650(5)	9.83×10^{5}	55.5	0.039(1)	$6s_{\frac{1}{2}}$–$6p_{\frac{3}{2}}$

3.3. Cu

To our knowledge, the only study of the Cu spectrum in the 5200–7500 cm^{-1} range was reported about 60 years ago (Shenstone 1948) where four (5484.1, 5496.6, 6003.2 and 6245.0 cm^{-1}) lines were mentioned. Our measurement yielded eight lines (see table 8) which can easily be classified as consisting of two triplets (4d–4f and 5p–5d) and the 5s–5p doublet. The latter consists of two very close lines which are due to the small (about 0.3 cm^{-1}) fine-structure splitting of the 5p term of Cu I. This doublet is shown in figure 3; the hyperfine structure is clearly seen. The reported (table 8) parameters of such multiplets are averaged over the hyperfine structure according to equations (1).

Similar to Au and Ag, the most prominent line (1344 cm^{-1}) of Cu in the 1200–1600 cm^{-1} range is due to the 5g–6h transition. The 1277 and 1302 cm^{-1} lines are easily identified using energy values taken from the literature. The remaining four lines are identified as being due to the two most prominent pairs of the 5f–6g and 6d–6f triplets; this identification is based on a comparison of the corresponding line strengths calculated using the FMP method. The information about the 6h term extracted from

Table 7. Revised values of some levels of Ag I.

Term	Energy (cm^{-1})	Other sources
$4d^{10}7g$	58 864.644(7)	This work
$4d^{10}9d_{\frac{5}{2}}$	58 864.603(16)	58 864.614 (Pickering and Zilio 2001)
$4d^{10}10s_{\frac{1}{2}}$	58 478.051(30)	58 478.047 (Pickering and Zilio 2001)
$4d^{10}6h$	58 057.140(4)	This work
$4d^{10}6g_{\frac{9}{2}}$	58 054.713(3)	58 054.723 (Civiš *et al* 2010b)
$4d^{10}6g_{\frac{7}{2}}$	58 054.711(4)	58 054.723 (Civiš *et al* 2010b)
$4d^{10}8d_{\frac{5}{2}}$	58 053.388(8)	58 053.404 (Pickering and Zilio 2001)
$4d^{10}6f_{\frac{5}{2}}$	58 041.987(5)	58 045.481 (Civiš *et al* 2010b)
$4d^{10}6f_{\frac{7}{2}}$	58 042.063(4)	This work
$4d^{10}5g$	56 711.565(3)	56 711.1 (Shenstone 1940)
$4d^{10}7d_{\frac{5}{2}}$	56 705.467(2)	56 705.498 (Pickering and Zilio 2001), 56 705.435 (Civiš *et al* 2010b)
$4d^{10}7d_{\frac{3}{2}}$	56 699.832(3)	56 699.768 (Pickering and Zilio 2001), 56 699.911 (Civiš *et al* 2010b)
$4d^{10}5f_{\frac{7}{2}}$	56 691.397(2)	56 691.4 (Shenstone 1940), 56 691.397 (Civiš *et al* 2010b)
$4d^{10}5f_{\frac{5}{2}}$	56 691.275(2)	56 691.4 (Shenstone 1940), 56 691.275 (Civiš *et al* 2010b)
$4d^{10}8p_{\frac{3}{2}}$	56 660.597(3)	56 660.559 (Pickering and Zilio 2001), 56 660.556 (Civiš *et al* 2010b)
$4d^{10}4f_{\frac{7}{2}}$	54 204.745(3)	54 204.73 (Shenstone 1940)
$4d^{10}4f_{\frac{5}{2}}$	54 204.729(2)	54 204.73 (Shenstone 1940)
$4d^{10}7p_{\frac{3}{2}}$	54 121.108(1)	54 121.129 (Pickering and Zilio 2001), 54 121.059 (Civiš *et al* 2010b)
$4d^{10}7p_{\frac{1}{2}}$	54 041.037(2)	54 040.99 (Brown and Ginter 1977), 54 041.087 (Civiš *et al* 2010b)
$4d^{10}7s_{\frac{1}{2}}$	51 886.965(1)	51 886.971 (Pickering and Zilio 2001), 51 886.954 (Civiš *et al* 2010b)
$4d^{10}6p_{\frac{3}{2}}$	48 500.810(1)	48 500.805 (Pickering and Zilio 2001), 48 500.804 (Civiš *et al* 2010b)
$4d^{10}6p_{\frac{1}{2}}$	48 297.406(1)	48 297.402 (Pickering and Zilio 2001, Civiš *et al* 2010b)
$4d^{10}6s_{\frac{1}{2}}$	42 556.147(1)	42 556.152 (Pickering and Zilio 2001)

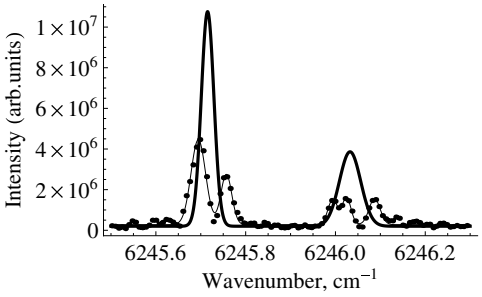

Figure 3. The $5s_{\frac{1}{2}}$–$5p_{\frac{1}{2},\frac{3}{2}}$ doublet lines of Cu I. The hyperfine components are fitted to Gaussian shape (thin curve), and the parameters of the averaged lines (thick curves) are calculated using equations (1).

Table 8. Cu I lines and their identification. Each of the four spectral ranges, 1200–1600, 1900–3600 cm^{-1} (only 2153 cm^{-1} line), 4100–5000 and 5200–7500 cm^{-1}, has its own scale of arbitrary units for the emission intensity.

Wavenumber (cm^{-1})	Intensity (arbitrary units)	SNR	FWHM (cm^{-1})	Identification
1277.179(5)	6.48×10^3	13.6	0.047(22)	$7s_{\frac{1}{2}}$–$7p_{\frac{3}{2}}$
1301.977(8)	6.09×10^3	9.69	0.073(28)	$7p_{\frac{3}{2}}$–$7d_{\frac{5}{2}}$
1344.291(3)	1.18×10^5	37.1	0.088(09)	5g –6h
1354.361(5)	2.76×10^4	12.2	0.087(15)	$5f_{\frac{7}{2}}$–$6g_{\frac{9}{2}}$
1361.593(5)	1.93×10^4	11.4	0.089(16)	$5f_{\frac{5}{2}}$–$6g_{\frac{7}{2}}$
1364.339(6)	1.46×10^4	11.6	0.083(18)	$6d_{\frac{5}{2}}$–$6f_{\frac{7}{2}}$
1366.874(6)	8.57×10^3	10.3	0.065(22)	$6d_{\frac{3}{2}}$–$6f_{\frac{5}{2}}$
2153.234(9)	6.20×10^4	8.51	0.099(29)	5g –7h
4221.555(6)	4.81×10^4	10.4	0.090(22)	$6p_{\frac{1}{2}}$–$7d_{\frac{3}{2}}$
4466.497(5)	8.69×10^4	9.44	0.108(18)	$6p_{\frac{3}{2}}$–$7d_{\frac{5}{2}}$
4646.928(5)	1.20×10^4	14.5	0.109(16)	$4f_{\frac{5}{2}}$–$7g_{\frac{7}{2}}$
4649.903(4)	1.15×10^5	16.9	0.122(12)	$4f_{\frac{7}{2}}$–$7g_{\frac{9}{2}}$
4680.179(3)	1.06×10^5	27.2	0.110(10)	$5d_{\frac{5}{2}}$–$7f_{\frac{7}{2}}$
4683.967(5)	6.93×10^4	17.8	0.105(14)	$5d_{\frac{3}{2}}$–$7f_{\frac{5}{2}}$
4842.019(8)	2.60×10^4	10.5	0.112(24)	$4d_{\frac{5}{2}}$–$6p_{\frac{3}{2}}$
4848.850(11)	6.13×10^3	3.59	0.054(51)	$4d_{\frac{3}{2}}$–$6p_{\frac{3}{2}}$
5484.3040(2)	1.06×10^7	267.	0.0349(5)	$4d_{\frac{5}{2}}$–$4f_{\frac{7}{2}}$
5487.269(2)	4.95×10^5	15.7	0.029(5)	$4d_{\frac{5}{2}}$–$4f_{\frac{5}{2}}$
5494.1249(2)	7.44×10^5	181.	0.0354(5)	$4d_{\frac{3}{2}}$–$4f_{\frac{5}{2}}$
6004.403(2)	1.31×10^5	25.8	0.047(7)	$5p_{\frac{1}{2}}$–$5d_{\frac{3}{2}}$
6004.721(3)	1.97×10^4	8.52	0.019(7)	$5p_{\frac{3}{2}}$–$5d_{\frac{3}{2}}$
6008.3527(6)	2.68×10^5	67.1	0.038(2)	$5p_{\frac{3}{2}}$–$5d_{\frac{5}{2}}$
6245.715(1)	3.71×10^5	18.1	0.033(4)	$5s_{\frac{1}{2}}$–$5p_{\frac{1}{2}}$
6246.033(2)	2.17×10^5	6.94	0.056(21)	$5s_{\frac{1}{2}}$–$5p_{\frac{3}{2}}$

the measurements in the 1200–1600 cm^{-1} region makes it possible for us to identify the 2153 cm^{-1} line (not reported in the previous work (Civiš *et al* 2011)) as due to the 5g–7h transition.

The revised Cu I level energies using the present measurements are given in table 9. For the majority of levels, the difference between the results reported in this and in other works is of the same order of magnitude as the uncertainty specified. Nevertheless, the present values of the $6g_{\frac{7}{2},\frac{9}{2}}$ levels differ by almost 0.6 cm^{-1} as compared to our previous work (Civiš *et al* 2011). We consider the present values to be preferable since these are extracted here from stronger lines (1354 and 1361 cm^{-1}) while the previous work used the less prominent 3837 and 3840 cm^{-1} lines which lie at the boundary of the detector's sensitivity. The present values of $7g_{\frac{7}{2},\frac{9}{2}}$ also differ from the values reported previously (Civiš *et al* 2011): by 0.475 and 1.237 cm^{-1} respectively. We consider the present values to be the recommended ones, since in their extraction far more intensive (4646.928 and 4649.903 cm^{-1}) lines were

Table 9. Revised values of some levels of Cu I.

Term	Energy (cm^{-1})	Other sources
$3d^{10}7g_{\frac{7}{2}}$	60 076.634(25)	60 076.159 (Civiš *et al* 2011)
$3d^{10}7g_{\frac{9}{2}}$	60 076.217(19)	60 074.980 (Civiš *et al* 2011)
$3d^{10}7f_{\frac{5}{2}}$	60 071.634(11)	This work
$3d^{10}7f_{\frac{7}{2}}$	60 071.199(9)	60 071.510 (Civiš *et al* 2011)
$3d^{10}6h$	59 268.422(20)	This work
$3d^{10}6g_{\frac{7}{2}}$	59 266.776(10)	59 267.202 (Civiš *et al* 2011)
$3d^{10}6g_{\frac{9}{2}}$	59 266.026(10)	59 266.676 (Civiš *et al* 2011)
$3d^{10}6f_{\frac{7}{2}}$	59 259.436(30)	This work
$3d^{10}6f_{\frac{5}{2}}$	59 259.916(28)	This work
$3d^{10}7d_{\frac{5}{2}}$	59 250.565(27)	59 250.72 (Shenstone 1948)
$3d^{10}7d_{\frac{3}{2}}$	59 249.303(26)	59 249.46 (Shenstone 1948)
$3d^{10}7p_{\frac{3}{2}}$	57 948.572(11)	57 948.57 (Ralchenko *et al* 2008), 57 948.71 (Shenstone 1948)
$3d^{10}5g_{\frac{7}{2}}$	57 924.549(26)	57 924.610 (Civiš *et al* 2011)
$3d^{10}5g_{\frac{9}{2}}$	57 924.132(20)	57 924.075 (Civiš *et al* 2011)
$3d^{10}5f_{\frac{7}{2}}$	57 911.591(10)	57 908.7 (Shenstone 1948), 57 911.090 (Civiš *et al* 2011)
$3d^{10}5f_{\frac{5}{2}}$	57 905.120(10)	57 905.2 (Shenstone 1948), 57 905.23 (Longmire *et al* 1980), 57 905.041 (Civiš *et al* 2011)
$3d^{10}6d_{\frac{5}{2}}$	57 895.097(29)	57 895.1 (Shenstone 1948), 57 895.084 (Civiš *et al* 2011)
$3d^{10}6d_{\frac{3}{2}}$	57 893.042(27)	57 893.05 (Shenstone 1948), 57 893.028 (Civiš *et al* 2011)
$3d^{10}7s_{\frac{1}{2}}$	56 671.387(10)	56 671.387 (Shenstone 1948)
$3d^{10}4f_{\frac{5}{2}}$	55 429.739(26)	55 429.8 (Shenstone 1948)
$3d^{10}4f_{\frac{7}{2}}$	55 426.357(20)	55 426.3 (Shenstone 1948)
$3d^{10}5d_{\frac{5}{2}}$	55 391.004(9)	55 391.292 (Shenstone 1948), 55 390.569 (Civiš *et al* 2011)
$3d^{10}5d_{\frac{3}{2}}$	55 387.667(10)	55 387.668 (Shenstone 1948), 55 387.621 (Civiš *et al* 2011)
$3d^{10}6p_{\frac{1}{2}}$	55 027.748(26)	55 027.74 (Shenstone 1948), 55 027.713 (Longmire *et al* 1980), 55 027.763 (Civiš *et al* 2011)
$3d^{10}6p_{\frac{3}{2}}$	54 784.074(35)	54 784.06 (Shenstone 1948), 54 784.073 (Longmire *et al* 1980), 54 784.081 (Civiš *et al* 2011)
$3d^{10}6s_{\frac{1}{2}}$	52 848.735(9)	52 848.749 (Shenstone 1948), 52 848.752 (Civiš *et al* 2011)
$3d^{10}4d_{\frac{5}{2}}$	49 942.057(20)	49 942.057 (Shenstone 1948)
$3d^{10}4d_{\frac{3}{2}}$	49 935.614(26)	49 935.2 (Shenstone 1948)
$3d^{10}5p_{\frac{1}{2}}$	49 383.168(19)	49 383.26 (Shenstone 1948)
$3d^{10}5p_{\frac{1}{2}}$	49 382.818(10)	49 382.95 (Shenstone 1948)
$3d^{10}5s_{\frac{1}{2}}$	43 147.22(1)	43 137.209 (Shenstone 1948)

involved as compared to the weak (2163.89 and 2171.118) lines used for extracting $7g_{\frac{7}{2},\frac{9}{2}}$ in the previous work (Civiš *et al* 2011). The present values display fine-structure splitting of about 0.4 cm^{-1} which is more realistic than the 1.18 cm^{-1} splitting resulting from the previous data (Civiš *et al* 2011).

4. Conclusion

This paper continues our studies of the IR emission spectra of metals in laser-induced plasma using Fourier-transform spectroscopy. Our measurements of Au, Ag and Cu spectra in four ranges (1200–1600, 1900–3600, 4100–5000 and 5200–7500 cm^{-1}) result in 64 lines (32 for Au, 12 for Ag and 20 for Cu) being reported which have not been previously and in the refinement of 19 lines which have already been published (9 for Au, 6 for Ag and 4 for Cu). We also provide a new classification for four Au lines and one Ag line.

The majority of the lines are due to transitions between the $Nd^{10}nl_j$ states with closed core ($N = 3, 4, 5$ for Cu, Ag and Au, correspondingly) and $n = 4, \ldots, 10$. The line classification is performed using relative line strengths expressed in terms of transition dipole matrix elements calculated with the help of the Fues model potential. We show the results for the transition probabilities and oscillator strengths for transitions between the reported $5d^{10}nl_j$ states of Au I (the previous papers contained such results for Ag (Civiš *et al* 2010b) and Cu (Civiš *et al* 2011)).

For the classification of the observed IR lines, an important role is played by the f-, g- and h-states including those discovered in the present measurements. For all three elements considered, the most intensive emission line in 1200–1600 cm^{-1} corresponds to the 5g–6h transition (for an example, see the transition probability table 3 for Au). Indeed, due to small quantum defects (of the order of 10^{-2} and 10^{-3} for the g- and h-states, respectively) this transition yields emission lines with close wavenumbers (1345–1347 cm^{-1}) for Au, Ag and Cu (see figure 1).

The most prominent lines in the 1900–3600 cm^{-1} range are the pairs $nf_{\frac{5}{2}}$–$5g_{\frac{7}{2}}$ and $nf_{\frac{7}{2}}$–$5g_{\frac{9}{2}}$ where n is the principal quantum number of the first valence f-state, $n = 5$ for Au and $n = 4$ for Ag and Cu. For Au and Cu, this nf–5g doublet occurs at 2517–2522 cm^{-1} (see table 2 and the previous paper (Civiš *et al* 2011)). Due to very small fine splitting of the 4f state ($E\left(4f_{\frac{7}{2}}\right) - E\left(4f_{\frac{7}{2}}\right) = 0.016$ cm^{-1} in Ag (see table 7)) we saw only one Ag 4f–5g line (Civiš *et al* 2010b) at 2506 cm^{-1}.

In the 4100–5000 cm^{-1} range, the most prominent emission takes place from the 7g-state to the first valence *n*f-state. The strongest lines in the 5200–7500 cm^{-1} are due to the n'd–*n*f transitions from first valence *n*f-states (with *n* values given above) and the first valence n'd-states ($n' = 6, 5, 4$ for Au, Ag and Cu correspondingly).

From the recorded spectra we extract revised values for the energies of 70 known levels (23 for Au, 20 for Ag and 27 for Cu) and of 15 previously unreported f-, g- and h-levels (8 for Au, 3 for Ag and 4 for Cu).

Acknowledgments

This work was financially supported by the Grant Agency of the Academy of Sciences of the Czech Republic (grant no IAA400400705).

References

Brown C M and Ginter M L 1977 *J. Opt. Soc. Am.* **67** 1323–7
Brown C M and Ginter M L 1978 *J. Opt. Soc. Am.* **68** 243–6
Civiš S, Matulková I, Cihelka J, Kawaguchi K, Chernov V E and Buslov E Y 2010a *Phys. Rev.* A **81** 012510
Civiš S, Matulková I, Cihelka J, Kubelík P, Kawaguchi K and Chernov V E 2010b *Phys. Rev.* A **82** 022502
Civiš S, Matulková I, Cihelka J, Kubelík P, Kawaguchi K and Chernov V E 2011 *J. Phys. B: At. Mol. Opt. Phys.* **44** 025002
Ehrhardt J C and Davis S P 1971 *J. Opt. Soc. Am.* **61** 1342–9
Fano U 1974 *J. Phys. B: At. Mol. Phys.* **7** L401–4
George S, Grays A and Engleman R Jr 1988 *J. Opt. Soc. Am.* B **5** 1500–2
Hanni M E, Keele J A, Lundeen S R and Sturrus W G 2008 *Phys. Rev.* A **78** 062510
Jannitti E, Cantù A M, Grisendi T, Pettini M and Tozzi G P 1979 *Phys. Scr.* **20** 156–62
Kawaguchi K, Sanechika N, Nishimura Y, Fujimori R, Oka T N, Hirahara Y, Jaman A and Civiš S 2008 *Chem. Phys. Lett.* **463** 38–41
Keele J A, Woods S L, Hanni M E, Lundeen S R and Sturrus W G 2010 *Phys. Rev.* A **81** 022506
Longmire M S, Brown C M and Ginter M L 1980 *J. Opt. Soc. Am.* **70** 423–9
Lundeen S R 2005 *Advances in Atomic, Molecular, and Optical Physics* vol 52, ed P R Berman and C C Lin (New York: Academic) pp 161–208
MacAdam K B, Dyubko S F, Efremov V A, Gerasimov V G and Kutsenko A S 2009 *J. Phys. B: At. Mol. Opt. Phys.* **42** 165009
Napier S A, Cvejanović D, Williams J F and Pravica L 2008 *Phys. Rev.* A **78** 032706
Pickering J C and Zilio V 2001 *Eur. Phys. J.* D **13** 181–5
Platt J R and Sawyer R A 1941 *Phys. Rev.* **60** 866–76
Ralchenko Y, Kramida A and Reader J and NIST ASD Team 2008 NIST Atomic Spectra Database version 3.1.5
Randall H M 1911 *Astrophys. J.* **34** 1–20
Shenstone A G 1940 *Phys. Rev.* **57** 894–8
Shenstone A G 1948 *Phil. Trans. R. Soc.* A **241** 297–322
Themelis S I 2010 *Phys. Rev.* A **81** 064504

J. Phys. B: At. Mol. Opt. Phys. **44** (2011) 225006 (4pp) doi:10.1088/0953-4075/44/22/225006

Atomic cesium 6h states observed by time-resolved FTIR spectroscopy

S Civiš[1,3], P Kubelík[1], P Jelínek[1], V E Chernov[1,2] and M Yu Knyazev[2]

[1] J Heyrovský Institute of Physical Chemistry, Academy of Sciences of the Czech Republic, Dolejškova 3, 18223 Prague 8, Czech Republic
[2] Voronezh State University, 394693 Voronezh, Russia

E-mail: civis@jh-inst.cas.cz

Received 14 September 2011, in final form 16 October 2011
Published 8 November 2011
Online at stacks.iop.org/JPhysB/44/225006

Abstract
The infrared emission spectra of Cs resulting from the laser ablation of CsI tablets in a vacuum were recorded using time-resolved Fourier-transform spectroscopy in the 1200–1600 cm^{-1} range with a resolution of 0.017 cm^{-1}. The 6h level of Cs was observed. The probabilities of transitions between the observed levels are calculated.

1. Introduction

Atomic cesium has been involved in a number of modern atomic physics experiments, such as the cooling and trapping of atoms, ultracold atom collisions and the formation of cold molecules, and evidence for effects of quantum electrodynamics and parity non-conservation, not to mention the atomic Cs frequency standard. Due to such wide applications, the atomic spectrum of neutral Cs has become one of the most important and well-studied spectra (Sansonetti 2009).

Although the list of Cs levels includes the states with orbital momentum $l \leqslant 4$, it lacks the levels with higher momenta. At the same time, the atomic states with high angular momentum are of interest for various problems of atomic and molecular physics (Clark and Greene 1999), such as the excitation and decay of autoionizing states (Napier *et al* 2008, Themelis 2010) or the extraction of multipole moments and/or polarizabilities of ions from the high-l Rydberg electron spectra of corresponding neutral atoms (Lundeen 2005) obtained using precise microwave (Hanni *et al* 2008) or optical (Keele *et al* 2010) measurements of high-l states.

Unlike the high-excited Rydberg levels, the low-excited high-l states (for example, the nh series begins with the principal quantum number $n = 6$) can be observed only in the infrared (IR) range. Indeed, nh states are linked by dipole transitions to n'g states, and the transition energy for the minimal $n = 6$, $n' = 5$ is about 1330 cm^{-1}. This estimate is given according to the Rydberg formula with zero quantum defects (and they are really low for the high-l states). The transitions between higher n, n' lie below 1000 cm^{-1}.

A good technique for the observation of the transitions in the above spectral range is laser-induced breakdown spectroscopy (LIBS) which consists of analysing the light spectrum emitted from a plasma created on the sample surface by laser pulses (laser ablation). Being a versatile and sensitive probe for the detection and identification of trace substances, laser ablation has many practical advantages over the conventional methods of chemical analysis of elements and is consequently being considered for a growing number of applications (Lee *et al* 2004, Babánková *et al* 2006, Gomes *et al* 2004, Barthélemy *et al* 2005, Aragon and Aguilera 2008).

Here we use LIBS together with time-resolved Fourier-transform infrared (FTIR) spectroscopy to extract the energy and width of the 6h level of Cs from the IR emission spectra in the 1300–1600 cm^{-1} range. Note that the measurements in this spectral range are quite difficult due to the low sensitivity of the MCT detector and high background (blackbody) radiation level. To our knowledge, there are no laboratory measured spectra of metals below 1800 cm^{-1} except our previous work (Civiš *et al* 2011a).

2. Methods

The vapours of excited Cs atoms are produced during the ablation of the salt (CsI) targets by a high-repetition rate (1.0 kHz) pulsed nanosecond ArF laser (ExciStar S-Industrial V2.0 1000, pulse length 12 ns, $\lambda = 193$ nm, output energy of 15 mJ, fluence about 2–20 J cm^{-2}) inside a vacuum chamber (average pressure 10^{-2} torr).

The time-resolution FTIR spectra were measured using the Bruker IFS 120 HR spectrometer (modified for the time-

[3] Author to whom any correspondence should be addressed.

0953-4075/11/225006+04$33.00

© 2011 IOP Publishing Ltd Printed in the UK & the USA

resolution scan of emission data) in a spectral range of 1200–1600 cm^{-1} using a CaF_2 beam splitter and a mercury–cadmium–telluride (MCT) detector. The infrared emission (axial distance from the target about 10 mm) was focused into the spectrometer using a CaF_2 lens.

For data sampling, we used the so-called 1/3-sampling (Civiš *et al* 2010), where the scanner velocity was set to produce a 3 kHz He–Ne laser interference signal, and the ArF laser oscillation was triggered at one-third of the He–Ne frequency. Measurements were carried out with a resolution of 0.017 cm^{-1} and three scans were needed to complete the interferogram. The resolution of 0.017 allows us to collect all together 64 time-shifted interferograms. At higher resolution, the number of interferograms has to be reduced to 30. A higher spectral resolution requires longer scanning time, an increasing number of the laser pulses (the lifetime of the ArF excimer laser is limited by the total number of pulses) and reduction of entrance aperture of the spectrometer (less photons on the detector).

From 3 to 30 scans were usually coadded to obtain a reasonable signal-to-noise ratio. The acquired spectrograms were post-zero filled by a factor of 2 and analysed using a commercial software routine (Bruker OPUS Ver.3.1) (OPU 2010). Subsequently, the spectra were corrected by subtracting the blackbody background spectrum. For more details of the experimental setup, see our previous papers (Kawaguchi *et al* 2008, Civiš *et al* 2010, Civiš *et al* 2011b).

The identification of the transitions was made assuming that for an optically thin plasma at local thermal equilibrium (LTE), the emission transition from an upper state k to a lower state i has the intensity I_{ki} proportional to the transition probability A_{ki} and to the transition wavenumber ν_{ki}:

$$I_{ki} \sim g_k A_{ki} \nu_{ki} \exp\left(-\frac{E_k}{k_B T}\right), \qquad (1)$$

where k_B is the Boltzmann constant, T is the temperature, and E_k and g_k being the energy and the degeneracy factor of the upper state, respectively.

Since at the low pressures used in our experiment the atom concentration is low, we can consider our plasma to be optically thin. However, in the same conditions some deviations from LTE conditions can occur (Giacomo *et al* 2001) but the Boltzmann distribution of the atomic populations remains valid (Qi *et al* 2007), although with different temperatures of electrons and atoms (Giacomo *et al* 2001). This means that even if the observed line intensities display some deviations from the proportionality to the A-values, they should describe the qualitative picture of the relative line intensities adequately enough to assign the lines. The Boltzmann plot made according to (1) is presented in figure 1; the linear fitting gives the plasma temperature $T = 940 \pm 140$ K. The uncertainty of T is low enough to consider the A_{ik} values to be calculated with reasonable accuracy.

The dipole matrix elements required for knowledge of A_{ki} were calculated using single-channel quantum defect theory (QDT) (Chernov *et al* 2000, 2005, Kornev *et al* 2009).

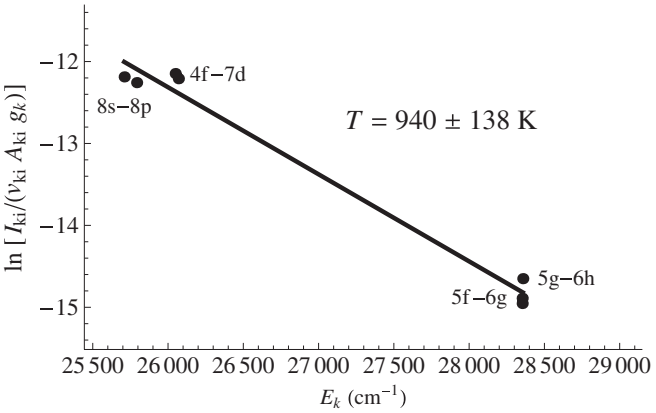

Figure 1. Boltzmann plot of the ablation plasma.

3. Results and discussion

The infrared emission was observed in the 1300–1600 cm^{-1} (with MID IR interference filter) spectral region. The recorded Cs emission spectrum is shown in figure 2. No line emissions from iodine atoms were encountered in our spectrum. The list of the observed lines with their parameters and identification is presented in table 1.

The use of the time-resolved scheme is essential, since the emission intensities of the spectra lines are dependent on the time delay after the ArF laser pulse shot. The time profiles of the emission lines have maxima at different delay times $\tau \simeq 10 \ldots 20$ μs after a laser shot. Some examples of time profiles of the observed lines are presented in figure 3. Such a non-monotonic decay of the emission intensity could be due to a complex combination of the collisional cascade repopulation of the atomic Cs states (Civiš *et al* 2010) and the transfer processes in ablation products (Khalil and Sreenivasan 2005, Kawaguchi *et al* 2008).

We have also calculated the probabilities of the transitions between the observed Cs levels. The results are presented in table 2. The accuracy of the QDT calculations was tested by comparison with NIST values (Ralchenko *et al* 2010) for 6s–np transitions in Cs up to $n = 14$. These NIST values are taken from the weighted mean lifetimes of the laser-excited experiments of Rafac *et al* (1999) with an uncertainty of only 0.2...0.3% for $n = 6$, from direct absorption measurements (Vasilyev *et al* 2002) with 0.8% accuracy for $n = 7$ and also from the critical compilation by Morton (2000) for $n = 8 \ldots 14$ who averaged some earlier absolute absorption measurements with accuracy of 0.03–0.11 dex (7–29%). We also used the oscillator strengths measured by Shabanova *et al* (1979) by Rozhdestvensky's hook method (accuracy 5–10%). The maximal discrepancy between our results and the values from the above-mentioned sources was about 25% for $n = 6$; for higher n, the discrepancy is considerably lower. Among the transitions presented in table 2, only for the 8s–8p doublet can we compare our results with the Dirac–Hartree–Fock calculations of Sieradzan *et al* (2004). Normalization of the dipole matrix elements given by Sieradzan *et al* (2004)

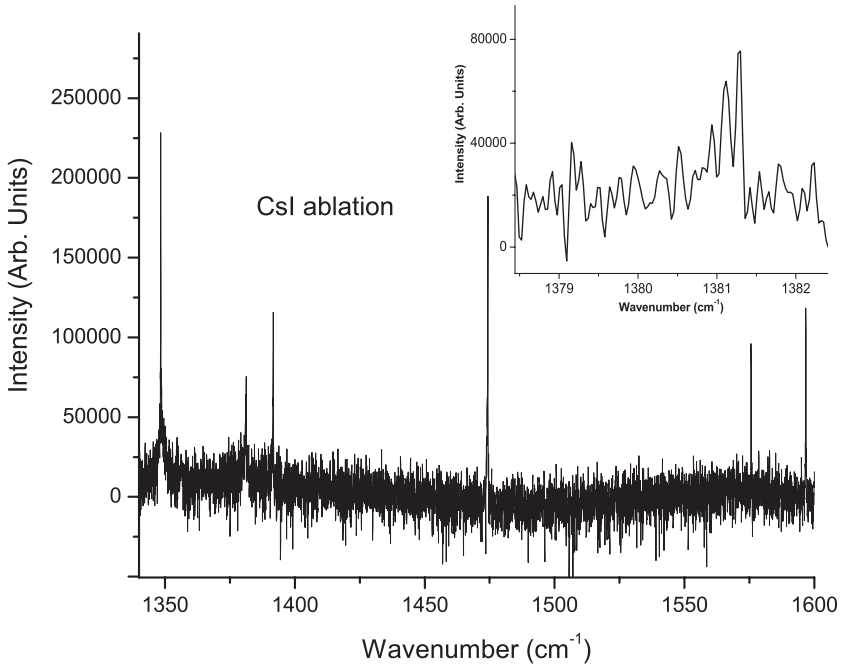

Figure 2. The recorded Cs emission spectrum. The fine structure of the 5f–6g line (1381 cm^{-1}) is clearly seen in the inset.

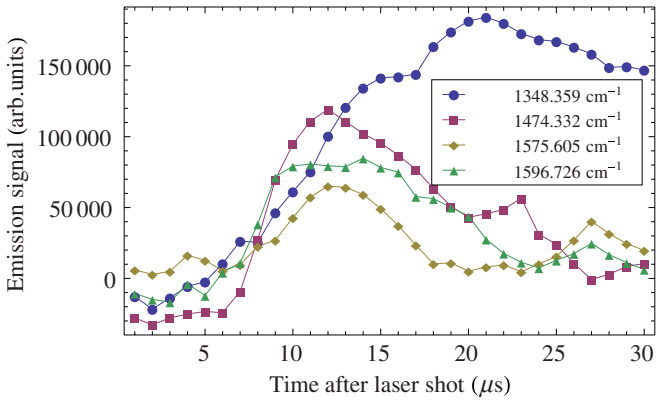

Figure 3. Time profiles of some Cs emission lines.
(This figure is in colour only in the electronic version)

Table 1. Cs IR line wavenumbers ν_{ki}, intensities I_{ki}, signal-to-noise ratios (SNR) and full-widths at half-maxima (FWHM).

ν_{ki} (cm^{-1})	I_{ki} (arb. units)	SNR	FWHM (cm^{-1})	Identification
1348.359(2)	6.21×10^3	8.85	0.043(7)	5g–6h
1381.126(3)	5.12×10^2	3.35	0.041(12)	$5f_{\frac{5}{2}}$–$6g_{\frac{7}{2}}$
1381.277(8)	1.52×10^3	2.38	0.038(32)	$5f_{\frac{7}{2}}$–$6g_{\frac{9}{2}}$
1391.662(8)	4.80×10^3	4.29	0.089(26)	$8s_{\frac{1}{2}}$–$8p_{\frac{1}{2}}$
1474.332(6)	9.68×10^3	6.91	0.105(19)	$8s_{\frac{1}{2}}$–$8p_{\frac{3}{2}}$
1575.605(8)	3.28×10^3	5.58	0.067(25)	$4f_{\frac{5}{2}}$–$7d_{\frac{3}{2}}$
1596.726(7)	4.29×10^3	5.90	0.062(15)	$4f_{\frac{7}{2}}$–$7d_{\frac{5}{2}}$

to the transition probabilities yields $A(8s_{\frac{1}{2}} - 8p_{\frac{1}{2}}) = 8.46 \times 10^5$ s^{-1} and $A(8s_{\frac{1}{2}} - 8p_{\frac{3}{2}}) = 9.71 \times 10^5$ s^{-1} which is very close to our results (see table 2).

After the identification of the observed lines, the energies E_k of the levels involved in the corresponding transitions can be extracted from the measured ν_{ki} values. To this end, we applied

Table 2. The QDT-calculated transition probabilities A_{ki} between the observed states of the Cs atom. The Ritz wavenumbers ν_{ki} and air wavelengths λ_{ki} are calculated using the energy level values from Ralchenko *et al* (2010), except those for the 6h levels taken from the present measurement (see table 3).

Transition	ν_{ki} (cm^{-1})	λ_{ki} (nm)	A_{ki} (s^{-1})
$7d_{\frac{5}{2}}$–$5f_{\frac{7}{2}}$	902.380	11 078.8	5.07×10^5
$7d_{\frac{5}{2}}$–$5f_{\frac{5}{2}}$	902.530	11 076.9	3.38×10^4
$7d_{\frac{3}{2}}$–$5f_{\frac{5}{2}}$	923.469	10 825.8	5.02×10^5
$5g_{\frac{9}{2}}$–$6h_{\frac{11}{2}}$	1348.369	7414.35	1.67×10^6
$5g_{\frac{9}{2}}$–$6h_{\frac{9}{2}}$	1348.369	7414.35	3.71×10^4
$5g_{\frac{7}{2}}$–$6h_{\frac{9}{2}}$	1348.372	7414.33	1.63×10^6
$5f_{\frac{5}{2}}$–$6g_{\frac{7}{2}}$	1381.141	7238.41	1.08×10^6
$5f_{\frac{7}{2}}$–$6g_{\frac{7}{2}}$	1381.291	7237.63	3.99×10^4
$8s_{\frac{1}{2}}$–$8p_{\frac{1}{2}}$	1391.705	7183.47	8.46×10^5
$8s_{\frac{1}{2}}$–$8p_{\frac{3}{2}}$	1474.359	6780.76	9.60×10^5
$4f_{\frac{5}{2}}$–$7d_{\frac{3}{2}}$	1575.607	6345.03	3.35×10^5
$4f_{\frac{5}{2}}$–$7d_{\frac{5}{2}}$	1596.546	6261.81	1.60×10^4
$4f_{\frac{7}{2}}$–$7d_{\frac{5}{2}}$	1596.728	6261.10	3.20×10^5
$4f_{\frac{5}{2}}$–$5g_{\frac{7}{2}}$	2535.827	3942.41	4.29×10^6
$4f_{\frac{7}{2}}$–$5g_{\frac{7}{2}}$	2536.009	3942.13	1.59×10^5
$4f_{\frac{5}{2}}$–$6g_{\frac{7}{2}}$	3880.217	2576.47	1.45×10^6
$4f_{\frac{7}{2}}$–$6g_{\frac{7}{2}}$	3880.399	2576.35	5.36×10^4

the same procedure as that used in our previous works (Civiš *et al* 2010, 2011a, 2011b). Briefly, to obtain the best estimates for the level energy values E_k, we performed a minimization of the sum of deviations not only between $E_i - E_j$ and the measured wavenumbers ν_{ij} but including also the deviations between some E_i and the 'reference' values L_i for these levels taken from NIST (Sansonetti 2009). Then the level energy values E_k are found by solving a linear system with a matrix dependent on ν_{ij} and L_i. This matrix also determines the

Table 3. Energy values E_k of the Cs I levels involved in the observed transitions.

Term	E_k (cm^{-1})	NIST values
6h	28 356.426(60)	This work
$6g_{\frac{9}{2}}$	28 352.444(3)	28 352.4460(6)
$6g_{\frac{7}{2}}$	28 352.443(7)	28 352.4444(5)
$5f_{\frac{5}{2}}$	26 971.316(9)	26 971.3030(30)
$5f_{\frac{7}{2}}$	26 971.162(9)	26 971.1535(30)
$7d_{\frac{5}{2}}$	26 068.777(23)	26 068.7730(5)
$7d_{\frac{3}{2}}$	26 047.847(38)	26 047.8342(5)
$8p_{\frac{3}{2}}$	25 791.480(12)	25 791.508(30)
$8p_{\frac{1}{2}}$	25 708.813(13)	25 708.85473(3)
$4f_{\frac{5}{2}}$	24 472.242(53)	24 472.2269(20)
$4f_{\frac{7}{2}}$	24 472.053(29)	24 472.0455(20)

dependence of the uncertainties δL_k of the energy levels on the uncertainties of the measured wavenumbers $\delta \nu_{ij}$ (given in table 1) and the uncertainties of the reference energies δL_i (Sansonetti 2009).

The results are presented in table 3. All the E_k values coincide within the specified uncertainties with the level values taken from NIST (Sansonetti 2009). The latter have far higher precision apart from the $8p_{\frac{3}{2}}$ level, for which we report a value with a slightly lower uncertainty. Our spectral resolution does not allow us to resolve the fine structure of the 6h level. Indeed, the fine-structure separation of *h* levels should be less than that of *g* levels. The latter is quite low as can be seen from table 3, while the 5f level has a fine separation of about 0.15 cm^{-1} and it is clearly seen in our spectra (see the inset in figure 2).

4. Conclusion

This work reports the IR spectrum of atomic cesium in 1200–1600 cm^{-1} recorded using Fourier-transform infrared (FTIR) spectroscopy of a plasma formed by ablation of a CsI target by a pulsed nanosecond ArF laser in a vacuum. The IR spectra of metals in this range were not reported previously. The recorded spectra allowed us to extract the excitation energy and width of the $5p^6$ 6h state of Cs which has not been known before. The other Cs levels extracted from the observed lines are in good agreement with NIST Atomic Spectra Database. We also calculate the probabilities of transitions between the observed lines.

Acknowledgment

This work was financially supported by the Grant Agency of the Academy of Sciences of the Czech Republic (Grant No. IAA400400705).

References

Aragon C and Aguilera J A 2008 *Spectrochim. Acta* B **63** 893–916
Babánková D, Civiš S and Juha L 2006 *Prog. Quantum Electron.* **30** 75–88
Barthélemy O, Margot J, Chaker M, Sabsabi M, Vidal F, Johnston T W, Laville S and Drogoff B L 2005 *3rd Int. Conf. on Laser Induced Plasma Spectroscopy and Applications (LIBS04) (Torremolinos, Spain, 28 September–01 October 2004) Spectrochim. Acta* B **60** 905–14
Chernov V E, Dorofeev D L, Kretinin I Y and Zon B A 2005 *Phys. Rev.* A **71** 022505
Chernov V, Manakov N and Starace A 2000 *Eur. Phys. J.* D **8** 347–59
Civiš S, Matulková I, Cihelka J, Kawaguchi K, Chernov V E and Buslov E Y 2010 *Phys. Rev.* A **81** 012510
Civiš S, Matulková I, Cihelka J, Kubelík P, Kawaguchi K and Chernov V E 2010 *Phys. Rev.* A **82** 022502
Civiš S, Matulková I, Cihelka J, Kubelík P, Kawaguchi K and Chernov V E 2011a *J. Phys. B: At. Mol. Opt. Phys.* **44** 105002
Civiš S, Matulková I, Cihelka J, Kubelík P, Kawaguchi K and Chernov V E 2011b *J. Phys. B: At. Mol. Opt. Phys.* **44** 025002
Clark W and Greene C H 1999 *Rev. Mod. Phys.* **71** 821–33
Giacomo A D, Shakhatov V and Pascale O D 2001 *1st Int. Conf. on Laser Induced Plasma Spectroscopy and Applications (LIBS 2000) (Tirrenia, Italy, 08–12 October 2000) Spectrochim. Acta B* **56** 753–76
Gomes A, Aubreton A, Gonzalez J J and Vacquié S 2004 *J. Phys. D: Appl. Phys.* **37** 689
Hanni M E, Keele J A, Lundeen S R and Sturrus W G 2008 *Phys. Rev.* A **78** 062510
Kawaguchi K, Sanechika N, Nishimura Y, Fujimori R, Oka T N, Hirahara Y, Jaman A and Civiš S 2008 *Chem. Phys. Lett.* **463** 38–41
Keele J A, Woods S L, Hanni M E, Lundeen S R and Sturrus W G 2010 *Phys. Rev.* A **81** 022506
Khalil A and Sreenivasan N 2005 *Laser Phys. Lett.* **2** 445–51
Kornev A S, Kretinin I Y and Zon B A 2009 *Laser Phys.* **19** 231–3
Lee W B, Wu J Y, Lee Y I and Sneddon J 2004 *Appl. Spectrosc. Rev.* **39** 27–97
Lundeen S R 2005 *Advances in Atomic, Molecular, and Optical Physics (Advances In Atomic, Molecular, and Optical Physics* vol 52*)* ed P R Berman and C C Lin (San Diego, CA: Academic) pp 161–208
Morton D C 2000 *Astrophys. J., Suppl. Ser.* **130** 403
Napier S A, Cvejanović D, Williams J F and Pravica L 2008 *Phys. Rev.* A **78** 032706
OPU 2010 Opus spectroscopy software http://www.brukeroptics.com/opus.html
Qi H, Sun Y, Liu X, Hou X and Li Y 2007 *Laser Phys. Lett.* **4** 212–7
Rafac R J, Tanner C E, Livingston A E and Berry H G 1999 *Phys. Rev.* A **60** 3648–62
Ralchenko Y, Kramida A and Reader J 2010 (NIST ASD Team) NIST Atomic Spectra Database (version 4.0), http://physics.nist.gov/asd
Sansonetti J E 2009 *J. Phys. Chem. Ref. Data* **38** 761–923
Shabanova L N, Monakov Y N and Khlyustalov A N 1979 *Opt. Spectrosk.* **47** 3–7
Shabanova L N, Monakov Y N and Khlyustalov A N 1979 *Opt. Spectrosc.* **47** 1 (Engl. Transl.)
Sieradzan A, Havey M D and Safronova M S 2004 *Phys. Rev.* A **69** 022502
Themelis S I 2010 *Phys. Rev.* A **81** 064504
Vasilyev A A, Savukov I M, Safronova M S and Berry H G 2002 *Phys. Rev.* A **66** 020101

Astronomy & Astrophysics manuscript no. Na07
May 3, 2012
© ESO 2012

Na I spectra in the 1.4–14 micron range: transitions and oscillator strengths involving f-, g- and h-states

S. Civiš[1]⋆, M. Ferus[1], P. Kubelík[1], P. Jelinek[1], V. E. Chernov[1,2], and E. M. Zanozina[3,1]

[1] J. Heyrovský Institute of Physical Chemistry, Academy of Sciences of the Czech Republic, Dolejškova 3, 18223 Prague 8, Czech Republic e-mail: civis@jh-inst.cas.cz
[2] Voronezh State University, 394693 Voronezh, Russia
[3] State Research Center of Russian Federation Troitsk Institute of Innovation and Fusion Research, 142190 Troitsk, Moscow Region, Russia

ABSTRACT

Context. Compared with the visible and ultraviolet ranges, fewer atomic and ionic lines are available in the infrared spectral region. Atlases of stellar spectra often provide only a short list of identified lines, and modern laboratory-based spectral features for wavelengths longer than 1 micron are not available for most elements. For the efficient use of the growing capabilities of IR astronomy, detailed spectroscopical information on atomic line features in the infrared (IR) region is needed.
Aims. Parts of the infrared stellar (*e.g.*, solar) spectra in the 1200–1800 cm^{-1} (5.6–8 μm) range have never been observed from the ground because of heavy contamination of the spectrum by telluric absorption lines. Such an infrared spectrum represents a great challenge for laboratory observations of new, unknown infrared atomic transitions involving the atomic levels with high orbital momentum and their comparison with the available spectra.
Methods. The vapors of excited Na atoms are produced during the ablation of the salt (sodium iodide, NaI) targets by a high-repetition rate (1.0 kHz) pulsed nanosecond ArF laser ExciStar S-Industrial V2.0 1000, pulse length 12 ns, λ = 193 nm, output energy of 15 mJ, fluence about 2–20 J/cm^2 inside a vacuum chamber (average pressure 10^{-2} Torr). The time-resolved emission spectrum of the neutral atomic potassium (Na I) was recorded in the 700–7000 cm^{-1} region using the Fourier transform infrared spectroscopy technique with a resolution of 0.02 cm^{-1}. The f-values calculated in the quantum-defect theory approximation are presented for the transitions involving the reported Na I levels.
Results. This study reports precision laboratory measurements for 26 Na I lines in the range of 700–7000 cm^{-1} (14–1.4 μm), including 20 lines not measured previously in the laboratory. This results in newly observed 7*h*, 6*h*, and 6*g* levels, and improved energy determination for ten previously known levels. The doublet structure of the 4f level has been observed for the first time. For transitions between the observed levels, we report calculated f-values that agree reasonably well with experiment.
Conclusions. The recorded Na I line features agree with the data from the available solar spectrum atlases. The energy values of Na I *4s*, *4p*, *5p*, *6p*, *4f*, *5f*, and *5g* levels extracted from our spectra have lower uncertainties as compared to the values reported several decades ago, but the latter values slightly differ from ours.

Key words. Time-resolved Fourier transform infrared spectroscopy, Sodium, oscillator strengths

1. Introduction

There are several reasons why the spectra of neutral sodium are of astrophysical importance. For instance, in studying the galactic fountain process (gas flows from the disk of galaxies produced by multiple supernova explosions which play an important role in formation of high, and intermediate velocity clouds, see Spitoni et al. (2008)), Na I is a good tracer for a neutral gas because of its low first ionization potential (5.1 eV). Na I absorption is expected to be observed in the inflow (the later) stage of the galactic fountain process when the gas is mostly neutral, and nearly absent during the outflow (the earlier) stage when the gas is believed to be almost fully ionized. The sodium enrichment of supergiant atmospheres is one of the long-standing problems in observational stellar astrophysics (Andrievsky et al. 2002). The overabundance of Na in the atmospheres of F, G, K supergiants is in a correlation with the stellar mass. The high probability of emissions of Na I at visible wavelengths makes its detection easy to use in studies of the exospheres (the outermost atmospheric layers) of some solar system bodies, *e.g.*, Mercury (Mouawad et al. 2011), the Moon (Matta et al. 2009; Lee et al. 2011) and Io (Grava et al. 2010). Na I has also been identified in exoplanetary atmospheres (Jensen et al. 2011) through space-based, from onboard the Hubble Space Telescope (Charbonneau et al. 2002) and ground-based, the Hobby–Eberly Telescope (Redfield et al. 2008), observations.

The detection of neutral sodium in the aforementioned examples was performed at optical wavelengths. The sodium enrichment of the atmospheres of 48 supergiants and bright giants and its connection with stellar gravity was studied using two Na I lines, 6154 and 6160 Å (Andrievsky et al. 2002). The observations of time-variable Na I absorption features near the resonance doublet (D lines at 589 nm) in circumstellar matter are used for the investigation of evolution models of type Ia supernova progenitors (Sternberg et al. 2011). The Na I emission at the resonance doublet recorded by MESSENGER's Mercury Atmospheric and Surface Composition Spectrometer (MASCS) was used to constrain models of Mercury's sodium exosphere (Mouawad et al. 2011). The measured Na I absorption near the resonance doublet in the transmission spectrum of an extrasolar planet (Charbonneau et al. 2002) showed large dis-

⋆ Corresponding author

Article published by EDP Sciences, to be cited as http://dx.doi.org/10.1051/0004-6361/201219215

crepancies with models that used a solar abundance of atomic sodium in planetary atmosphere. The amount of absorption of Na I for other planets differs significantly (Redfield et al. 2008), which indicates that the two exoplanets may have significantly different atmospheric properties, in particular the temperature profiles of their atmospheres. A direct measurement of the effective temperature of the planetary atmospheres and confirmation of a thermal inversion therein could be provided by exploiting the enhanced contrast between stars and their planets in the infrared wavelengths (O'Donovan et al. 2010).

The infrared (IR) range is becoming more and more important in astronomical research. Recent research topics include studies of dust-obscured objects and interstellar clouds, cool objects such as dwarfs, disks or planets, and the extended atmospheres of evolved stars, including objects at cosmological distances from the Earth (Kerber et al. 2009). The great advantages of Fourier transform infrared spectroscopy (FTIR), such as its constant high resolution and energy throughput, have made the IR spectral region more accessible for laboratory spectral measurements (Nilsson 2009).

However, compared with the visible and ultraviolet ranges, fewer atomic and ionic lines are available in the IR spectral region (Ryde 2010). Atlases of stellar spectra often provide only a short list of identified lines (Lobel 2011), and modern laboratory based spectral features for wavelengths longer than 1 micron are not available for most elements (Wahlgren 2011). The powerful capabilities of IR astronomy cannot be fully utilized without detailed spectroscopical information on atomic line features in the IR region, in particular, wavelengths and oscillator strengths (Biémont 1994; Grevesse & Noels 1994; Pickering 1999; Jorissen 2004; Johansson 2005; Pickering et al. 2011).

New laboratory spectra may identify spectral lines in the IR that could result in the discovery of new excited atomic levels that are difficult to compute accurately and must be determined solely from IR lines (Wahlgren 2011). Including additional energy levels, atomic transition lines and oscillator strengths will increase the reliability of astrophysical calculations such as stellar or planetary atmosphere models.

Na I at 7880 cm^{-1} (1.269 μm) first appears in early G spectral type stars and grows in strength toward later types (Wallace et al. 2000). The near-infrared line list (with oscillator strengths computed or obtained by fitting the solar spectrum) for Na I includes the 10182–12679 and 16374–16389 cm^{-1} (0.98186–0.78849 and 0.61056–0.60999 μm) ranges (Meléndez & Barbuy 1999). Some Na I lines are identified in the solar spectrum in Atmospheric Chemistry Experiment with a space-borne Fourier transform spectrometer (ACE-FTS) which has been performed onboard a SCISAT-1 satellite (Hase et al. 2010). The ACE solar atlas covers the 700–4430 cm^{-1} (14.3–2.26) range at a resolution of 0.02 cm^{-1}. The measurements performed with FTS at the McMath-Pierce solar telescope (National Solar Observatory, Kitt Peak) cover the range 460–13600 cm^{-1} (22–0.74 μm), performed with some corrections to account for telluric absorption (Wallace et al. 1996). Parts of the IR range in 1200–1800 cm^{-1} (8–5.6 μm) have never been observed from the ground due to heavy contamination of the spectrum by telluric absorption lines. Such an infrared spectrum represents a great challenge for laboratory observations of new, unknown infrared atomic transitions involving the atomic levels with high orbital momentum (Civiš et al. 2011a) and their comparison with the available stellar (*e.g.*, solar) spectra. An attempt to fill this gap for Na I is made in the present paper.

Since the middle of the past century, when the measurements of the Na I spectrum were performed by Risberg (1956) in the range of 0.737-1.14 μm (13559–8767 cm^{-1}) and by Johansson (1961) in the range of 1.2–3.0 μm (7885–4276 cm^{-1}), only one neutral sodium IR line (*4f–5g* transition at 2472.622 cm^{-1} *i.e.* 4.04319 μm) has been reported (Litzen 1970). In this hollow-cathode measurement no lines with longer wavelengths were recorded, and no emissions from *ng* (with $n > 5$) nor *nh*-levels were observed. The energies of the *ng* and *nh* levels of Na I for $6 \leq n \leq 13$ available in the NIST database (Ralchenko et al. 2010) or critical compilations (Sansonetti 2008) are calculated by extrapolation from the higher *nh* and *ng* levels with $n \geq 13$ (Dyubko et al. 1997). They have never been measured experimentally. The f-values for the Na I transitions listed in the NIST database and critical compilations (Kelleher & Podobedova 2008) are taken from the very old measurements by Filippov & Prokofjew (1929) (taken before the rise of quantum mechanics) or from multi-configuration Dirac–Hartree–Fock calculations using the code by Froese Fischer (2002).

Here we report the results of an FTIR spectroscopy study of Na I transitions in four IR ranges: 1.4–2.5, 2.7–5.0, 5.9–9.1 and 11.1–14.3 μm. From the recorded spectra, we extracted the excitation energies of the *7h*, *6h*, and *6g* states of Na I for which only theoretical predictions were previously avaible. In addition, we also calculated f-values for all transitions involving the observed Na I levels using quantum-defect theory (QDT) approximation. Comparisons with measured transition probabilities and oscillator strengths (Miculis & Meyer 2005; Nawaz et al. 1992) indicate that the QDT is a suitable approximation.

2. Methods

Transitions in the four IR spectra ranges defined previously can be observed using laser-induced breakdown spectroscopy (LIBS), which analyzes the light spectrum emitted from plasma created on the sample surface by laser pulses (laser ablation). Laser ablation is a versatile and sensitive probe for the detection and identification of trace substances. As such, this technique has many practical advantages over the conventional chemical analysis methods (Aragon & Aguilera 2008; Lednev & Pershin 2008) and is being used in a growing number of applications (Lee et al. 2004; Babánková et al. 2006; Gomes et al. 2004; Barthélemy et al. 2005; Aragon & Aguilera 2008). In this study, we combined LIBS with time-resolved Fourier-transform infrared (FTIR) spectroscopy to record IR emission spectra in seven spectral ranges: 800–1000, 1000–1300, 1200–1600, 1600–2000, 2000–3500, 4100–5000, and 5000–7700 cm^{-1} (12.5–10, 10–7.7, 8.33–6.25, 6.25–5.0, 5.0–2.85, 2.34–2.0, 2.0–1.3 μm). Note that measurements in the range below 1800 cm^{-1} ($\lambda > 5.55$ μm) are quite difficult because of the low sensitivity of the mercury-cadmium-telluride (MCT) detector and the high background (blackbody) radiation level. To our knowledge, there are no laboratory-measured spectra of alkali metals below 1800 cm^{-1}. All the wavenumbers listed in the NIST database (Ralchenko et al. 2010) for the alkali metal atomic lines below 1800 cm^{-1} are Ritz wavenumbers (*i.e.*, obtained by subtracting of known energy level values, not from laboratory-measured spectra). Below we briefly describe the experimental setup used in the present work. For more details see our previous papers (Kawaguchi et al. 2008; Civiš et al. 2010; Civiš et al. 2011b).

The vapors of excited Na atoms are produced during the ablation of the salt (NaI) targets by a high-repetition rate (1.0 kHz) pulsed nanosecond ArF laser (ExciStar S-Industrial V2.0 1000, pulse length 12 ns, $\lambda = 193$ nm, output energy of 15 mJ, fluence about 2–20 J/cm^2) inside a vacuum chamber (average pres-

sure 10^{-2} Torr). The time resolution FTIR spectra were measured using the Bruker IFS 120 HR spectrometer. For the 2000–7700 cm^{-1} (1.3–5.0 μm) range we used a CaF_2 beam splitter and an InSb detector, while for the 700–2000 cm^{-1} range, a KBr beam splitter and an HgCdTe (MCT) detector were used. The infrared emission (axial distance from the target approximately 10 mm) was focused into the spectrometer using a CaF_2 or ZnSe lens (for 2000–7700 cm^{-1} (1.3–5.0 μm) or 700–2000 cm^{-1} (14.3–5.0 μm) respectively). The wavenumbers, line widths and their intensities (as well as the uncertainties for these quantities) are presented in Table 1.

For data sampling, we used the so-called 1/3-sampling (Civiš et al. 2010), where the scanner velocity was set to produce a 3 kHz He–Ne laser interference signal, and the ArF laser oscillation was triggered at one third of the He-Ne frequency. Measurements were performed with a resolution of 0.017 cm^{-1}, and three scans were needed to complete the interferogram. The resolution of 0.017 cm^{-1} allows us to collect 64 time-shifted interferograms. At higher resolutions, the number of interferograms was reduced to 30. Higher spectral resolution requires a longer scanning time, an increase in the number of laser pulses (the lifetime of the ArF excimer laser is limited by the total number of pulses) and a reduction of the entrance aperture of the spectrometer (fewer photons on the detector).

Usually, 3 to 30 scans were coadded to obtain a reasonable signal-noise ratio. The acquired spectrograms were post-zero filled by a factor of 2 and analyzed using a commercial software routine (Bruker OPUS Ver.3.1) (OPUS 2010). Finally, the spectra were corrected by subtracting the blackbody background spectrum.

Using a time-resolved scheme is essential, because the emission intensities of the spectra lines are dependent on the time delay after the ArF laser pulse shot. The time profiles of the emission lines have maxima at different delay times $\tau \simeq 10..20$ μs after a laser shot. This non-monotonic decay of the emission intensity could be due to a complex combination of the repopulation of the atomic Na states by collisional cascade (Civiš et al. 2010) and the transfer processes in ablation products (Khalil & Sreenivasan 2005; Kawaguchi et al. 2008).

For an optically thin plasma at local thermal equilibrium (LTE), the emission transition from an upper state k to a lower state i has the intensity I_{ki} proportional to the transition probability A_{ki} and to the transition wavenumber ν_{ki}:

$$I_{ki} \sim g_k A_{ki} \nu_{ki} \exp\left(-\frac{E_k}{k_B T}\right), \quad (1)$$

where k_B is the Boltzmann constant, T is the excitation temperature, E_k and g_k being the energy and the degeneracy factor of the upper state, respectively. Since at the low pressures, used in our experiment the atom concentration is low, we can consider our plasma to be optically thin. However, in the same conditions some deviations from LTE conditions can occur, see Giacomo et al. (2001), but the Boltzmann distribution of the atomic populations remains valid according to Qi et al. (2007), although with different temperatures of electrons and atoms, see Giacomo et al. (2001). This means that even if the observed line intensities slightly deviate from the proportionality to the A-values, they should describe the qualitative picture of the relative line intensities well enough to assign the lines. The dipole matrix elements required to determine A_{ki} were calculated using the single-channel quantum defect theory (QDT) (Chernov et al. 2000, 2005a).

3. Results and discussion

A list of the observed lines with their parameters and identification is presented in Table 1. The measurements were performed in the seven spectral ranges mentioned in the Section 2. Only lines within the same spectral range have intensities with the same scale. Eighteen lines in Table 1 have not previously been measured in laboratories. Also, note that we have resolved the fine structure of the 3d–4f transition, see Figure 1.

Table 1 also contains the wavenumbers of some Na I lines as measured in laboratories (Litzen 1970; Johansson 1961), by a ground-based (McMath-Pierce solar telescope at Kitt Peak (Wallace et al. 1996)) and space-based (ACE (Hase et al. 2010)) Fourier transform spectrometers. The uncertainty of ACE peak picking is 0.001 cm^{-1}, which is less than our technique. The accuracy of the National Solar Observatory wavenumbers (Wallace et al. 1996) can be evaluated from the resolving power $R = 300000$; the uncertainty $\Delta\nu = 0.008$–0.015 cm^{-1} for $\nu = 2400$–4500 cm^{-1} (4.16–2.22 μm) is somewhat greater than uncertainties given in Table 1. However, for several lines our uncertainties are better than previous laboratory measurements, 0.005 cm^{-1} in (Johansson 1961) and 0.01 cm^{-1} in (Litzen 1970). Our wavenumbers agree with these laboratory measurements within the uncertainties, but the measurements do not always coincide with the wavenumbers listed in the ACE and NSO atlases.

The ACE-FTS spectral data are represented as three data lists. The second data list (according to Hase et al. 2010) contains the set of wavenumbers and transitions specified in the graphic ACE atlas pages. A simple analysis shows that the Na I line wavenumbers encountered in data list 2 are simply the Ritz wavenumbers obtained from the Na I level energies stored in the NIST database (Ralchenko et al. 2010). The first data list is presented in two variants: (a) the list of observed lines and (b) the corrected (by an empirical calibration factor of 1.00000294) version of the observed data; the correction was made to achieve closer agreement with the line positions specified in the second data list. We consider the ACE data list 1 (uncorrected) to be the most relevant to compare with our results since the above correction (by a calibration factor of 1.00000294) was performed in the ACE atlas (Hase et al. 2010) to aid the assignment of the spectral signatures in the ACE solar spectrum with the line positions given in current spectroscopic line-lists.

The largest discrepancies occur for the lines corresponding to transitions from high-l levels (5g, 6g, 6h, 7h). These discrepancies could be explained by the Stark shift of solar lines due to high (up to 1000 Vcm^{-1}) electric fields in the Sun's atmosphere. For instance, Mg I solar lines in the range of 7–12 μm (corresponding to transitions from nl levels with $n, l \geq 6$) can differ from laboratory measurements by -0.01 to $+0.03$ cm^{-1} (Chang & Schoenfeld 1991). The quadratic Stark effect is determined by the polarizability. Even in its ground state, the polarizability of Na I is twice as high as that of Mg in its first excited state (Chernov et al. 2005a,b). Therefore, the wavenumbers of the high-l Na solar lines can differ from their laboratory values by more than 0.03 cm^{-1}, explaining the discrepancies in Table 1. Improved atomic spectra measurements of transitions from the high-l levels, below 2000 cm^{-1} ($\lambda > 5$ μm), may yield more precise solar electric field strengths.

New laboratory spectroscopic measurements are important for a proper interpretation of current and future astrophysical spectra in the IR domain. Measured spectra and ACE-FTS solar spectra in the vicinity of the most prominent lines are shown in Figure 2.

Table 1. Observed Na lines and their identification. Each of the seven spectral ranges has its own scale of arbitrary units for the emission intensity, I, which are given logarithmically. The uncertainties of the other measurements are 0.001 cm^{-1} (ACE) and 0.008–0.015 cm^{-1} (NSO)

Present work						Other measurements		
Wavenumber (cm^{-1})	Air wavelengths (μm)	log(I)	SNR	HWHM (cm^{-1})	Identification	NIST (Sansonetti 2008)	ACE (Hase et al. 2010)	NSO (Wallace et al. 1996)
808.786 ± 0.004	12.3608	4.60	3.6	0.070 ± 0.009	$6g$–$7h$			
925.012 ± 0.011	10.8077	4.33	5.5	0.064 ± 0.037	$6s_{\frac{1}{2}}$–$6p_{\frac{3}{2}}$			
1094.097 ± 0.006	9.137466	3.73	9.5	0.048 ± 0.021	$3d_{\frac{3}{2}}$–$4p_{\frac{1}{2}}$		1094.102	
1099.744 ± 0.003	9.090547	4.11	27.	0.063 ± 0.008	$3d_{\frac{5}{2}}$–$4p_{\frac{3}{2}}$		1099.746	
1329.751 ± 0.008	7.518155	3.28	6.3	0.061 ± 0.029	$5p_{\frac{3}{2}}$–$6s_{\frac{1}{2}}$		1329.765	
1332.218 ± 0.013	7.504233	3.48	3.1	0.090 ± 0.045	$5p_{\frac{1}{2}}$–$6s_{\frac{1}{2}}$		1332.240	
1341.651 ± 0.003	7.451472	3.94	15.	0.091 ± 0.009	$5g$–$6h$		1341.677	
1343.194 ± 0.009	7.442912	3.55	7.4	0.095 ± 0.027	$5f$–$6g$		1343.246	
1839.707 ± 0.003	5.434166	6.23	22.	0.097 ± 0.010	$5s_{\frac{1}{2}}$–$5p_{\frac{1}{2}}$		1839.707	
1842.185 ± 0.002	5.426857	6.51	32.	0.105 ± 0.008	$5s_{\frac{1}{2}}$–$5p_{\frac{3}{2}}$		1842.183	
1993.867 ± 0.007	5.014012	6.25	9.4	0.162 ± 0.021	$5p_{\frac{3}{2}}$–$5d_{\frac{5}{2}}$		1993.856	
1996.353 ± 0.010	5.007769	5.93	7.9	0.133 ± 0.031	$5p_{\frac{1}{2}}$–$5d_{\frac{3}{2}}$		1996.369	
2150.197 ± 0.009	4.649469	1.86	3.9	0.047 ± 0.052	$5g$–$7h$		2150.336	
2472.603 ± 0.002	4.043218	3.75	40.	0.119 ± 0.006	$4f$–$5g$	2472.620 ± 0.010	2472.612	2472.62
2508.928 ± 0.003	3.984679	3.34	26.	0.127 ± 0.008	$4d_{\frac{5}{2}}$–$5f_{\frac{7}{2}}$		2508.927	2508.94
2928.083 ± 0.003	3.414272	3.07	27.	0.111 ± 0.009	$4p_{\frac{3}{2}}$–$5s_{\frac{1}{2}}$		2928.086	
2933.671 ± 0.004	3.407769	2.72	18.	0.096 ± 0.014	$4p_{\frac{1}{2}}$–$5s_{\frac{1}{2}}$		2933.682	
2969.160 ± 0.013	3.367038	2.74	4.5	0.104 ± 0.043	$5p_{\frac{3}{2}}$–$7s_{\frac{1}{2}}$		2969.179	
3344.378 ± 0.005	2.989277	3.49	13.	0.109 ± 0.016	$5p_{\frac{3}{2}}$–$6d_{\frac{5}{2}}$		3344.365	
3346.866 ± 0.006	2.987055	3.20	11.	0.112 ± 0.019	$5p_{\frac{1}{2}}$–$6d_{\frac{3}{2}}$		3346.820	
4276.126 ± 0.003	2.337927	5.76	5.1	0.178 ± 0.012	$4p_{\frac{3}{2}}$–$4d_{\frac{5}{2}}$	4276.150 ± 0.005	4276.132	4276.151
4281.759 ± 0.004	2.334851	5.24	11.	0.106 ± 0.011	$4p_{\frac{1}{2}}$–$4d_{\frac{3}{2}}$	4281.784 ± 0.006	4281.756	4281.776
4526.968 ± 0.002	2.208381	6.11	13.	0.160 ± 0.006	$4s_{\frac{1}{2}}$–$4p_{\frac{1}{2}}$	4526.999 ± 0.006		4526.999
4532.568 ± 0.001	2.205653	6.35	25.	0.152 ± 0.004	$4s_{\frac{1}{2}}$–$4p_{\frac{3}{2}}$	4532.594 ± 0.006		4532.589
5414.005 ± 0.003	1.846557	5.22	1.3	0.089 ± 0.020	$3d_{\frac{3}{2}}$–$4f_{\frac{5}{2}}$	5414.058 ± 0.009		
5414.063 ± 0.002	1.846537	5.35	1.8	0.096 ± 0.015	$3d_{\frac{5}{2}}$–$4f_{\frac{7}{2}}$	5414.058 ± 0.009		

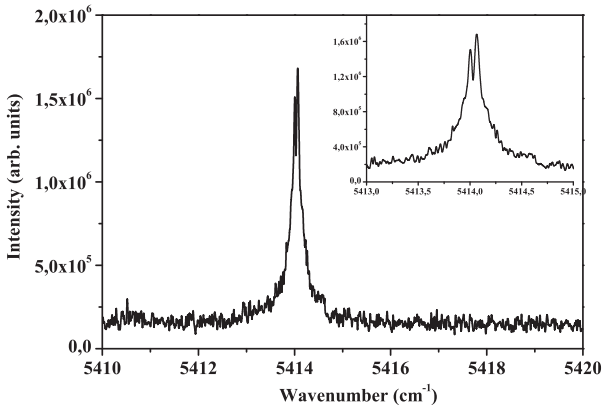

Fig. 1. Resolved fine structure of the $3d$–$4f$ transition.

The energies, E_k, of the levels involved in the corresponding transitions can be extracted from the measured ν_{ki} values. For this refinement we used a least-squares fitting algorithm that is similar to the one proposed by Radziemski et al. (1972). To obtain the best estimates for the level energy values E_k, we performed a minimization of a sum of deviations not only between $E_k - E_j$ and the measured wavenumbers, but also included the deviations between some E_k and the "reference" values for these levels taken from Ralchenko et al. (2010) and Litzen (1970). The weights in the sum of squared deviations were proportional to the inverse uncertainties of the corresponding wavenumbers or "reference" energies. These revised values, together with the new h-level energies, are presented in Table 2.

For most of the observed levels, the extracted E_k agrees with the calculated uncertainties using the level values given by the NIST database and compilation tables (Ralchenko et al. 2010; Sansonetti 2008). The exceptions are the $5d$ and $7s$ levels. The slight disagreement with previous works (Martin & Zalubas 1981; Juncar et al. 1981) can be caused by uncertainties in the wavenumbers of the lines involving these levels (as compared to other lines listed in Table 1). Our energies for the nd levels (with $n = 3, 4, 6$) and ns levels (with $n = 5, 6$) agree with the higher precision values measured in previous works (Martin & Zalubas 1981; Juncar et al. 1981). For the $4s$, $4p$, $5p$, $6p$, $4f$, $5f$ and $5g$ levels, we report more accurate energies than previous measurements (Risberg 1956; Johansson 1961; Litzen 1970; Arqueros 1988).

The energies of the $7h$, $6h$, and $6g$ levels, given in square brackets in Table 2, have not been measured before. However, theoretical predictions based on extrapolation from the higher nh and ng levels with $n \geq 13$ (Dyubko et al. 1997) were avail-

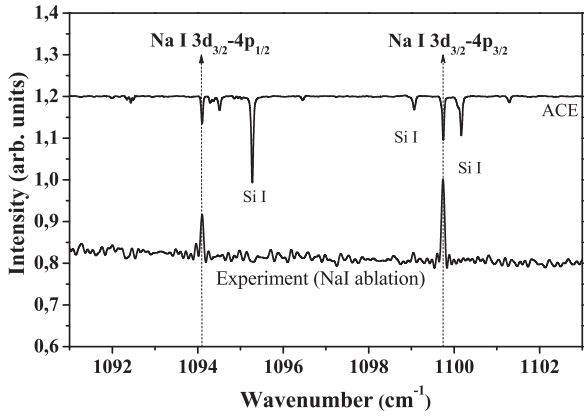

Fig. 2. Emission spectra from NaI ablation plasma and the ACE (Hase et al. 2010) solar spectra.

able. Our spectral resolution does not allow us to resolve the fine structure of the *h* and *g* levels. The fine splitting of these levels should be less than the *nf*-levels, which generally decreases with n and is resolved here only for $n = 4$. This fine splitting ($\sim$ 0.06 cm^{-1}) is clearly observed in our spectra (see inset in Figure 1).

To check the adequacy of the QDT calculations, we compared the dipole matrix elements calculated using QDT with other experimental and calculated values. Although all these dipole matrix elements (f- or A-values) can be easily expressed through each other, we kept the original data of the sources being compared (A-values for 3*p*–*ns*, *nd* transitions and f-values for *3s*–*np* transitions).

Table 3 compares the probabilities (A-values) for the $3p_{\frac{3}{2}}$–$ns_{\frac{1}{2}}$, $nd_{\frac{3}{2}}$ transitions with model potential calculations (modified Coulomb approximation) (Miculis & Meyer 2005) and NIST data (obtained from Dirac–Hartree–Fock (Froese Fischer 2002) or the R-matrix (Taylor 1995) theory). The Dirac–Hartree–Fock calculations differ from our QDT results by not more than 6%. The NIST A-values for $n < 8$ are closer to our values. For higher n, the QDT approximation should give more adequate results than the Dirac–Hartree–Fock calculations.

For some 3*s*–*np* transitions only the multiplet f-values (*i.e*, summed over the fine structure components) were measured using laser-based Faraday rotation spectroscopy (Nawaz et al. 1992). We compare the multiplet f-values with the NIST database and our calculations in Table 4. For $n < 17$ our calculations agree well (1–5%) with the laser-based Faraday rotation spectroscopy measurements (Nawaz et al. 1992) while for

Table 3. Comparison of probabilities (A-values) for several $3p_{\frac{3}{2}}$–$ns_{\frac{1}{2}}$, $nd_{\frac{3}{2}}$ transitions in Na I with the NIST database values (Ralchenko et al. 2010). The latter are taken from Miculis & Meyer (2005) if not otherwise stated.

Transition	Present work	Calculation [1]	NIST
$3p_{\frac{3}{2}}$–$4s_{\frac{1}{2}}$	1.68E+7	1.78E+7	1.76E+7 [2]
$3p_{\frac{3}{2}}$–$3d_{\frac{3}{2}}$	8.31E+6	8.58E+6	8.57E+6 [2]
$3p_{\frac{3}{2}}$–$5s_{\frac{1}{2}}$	4.79E+6	5.07E+6	4.98E+6 [2]
$3p_{\frac{3}{2}}$–$4d_{\frac{3}{2}}$	1.98E+6	2.02E+6	2.02E+6 [2]
$3p_{\frac{3}{2}}$–$6s_{\frac{1}{2}}$	2.18E+6	2.31E+6	2.27E+6 [2]
$3p_{\frac{3}{2}}$–$5d_{\frac{3}{2}}$	7.99E+5	8.15E+5	
$3p_{\frac{3}{2}}$–$7s_{\frac{1}{2}}$	1.19E+6	1.26E+6	1.23E+6 [2]
$3p_{\frac{3}{2}}$–$6d_{\frac{3}{2}}$	4.08E+5	4.16E+5	4.14E+5 [2]
$3p_{\frac{3}{2}}$–$8s_{\frac{1}{2}}$	7.21E+5	7.66E+5	7.50E+5 [2]
$3p_{\frac{3}{2}}$–$7d_{\frac{3}{2}}$	2.39E+5	2.43E+5	2.44E+5 [2]
$3p_{\frac{3}{2}}$–$9s_{\frac{1}{2}}$	4.70E+5	5.00E+5	5.61E+5 [2]
$3p_{\frac{3}{2}}$–$8d_{\frac{3}{2}}$	1.52E+5	1.55E+5	1.95E+5 [2]
$3p_{\frac{3}{2}}$–$10s_{\frac{1}{2}}$	3.24E+5	3.44E+5	6.50E+5 [2]
$3p_{\frac{3}{2}}$–$9d_{\frac{3}{2}}$	1.03E+5	1.14E+5	
$3p_{\frac{3}{2}}$–$11s_{\frac{1}{2}}$	2.33E+5	2.47E+5	
$3p_{\frac{3}{2}}$–$10d_{\frac{3}{2}}$	7.38E+4	7.50E+4	7.80E+4 [3]
$3p_{\frac{3}{2}}$–$12s_{\frac{1}{2}}$	1.73E+5	1.84E+5	
$3p_{\frac{3}{2}}$–$11d_{\frac{3}{2}}$	5.44E+4	5.54E+4	
$3p_{\frac{3}{2}}$–$13s_{\frac{1}{2}}$	1.32E+5	1.40E+5	
$3p_{\frac{3}{2}}$–$12d_{\frac{3}{2}}$	4.13E+4	4.20E+4	
$3p_{\frac{3}{2}}$–$14s_{\frac{1}{2}}$	1.03E+5	1.09E+5	
$3p_{\frac{3}{2}}$–$13d_{\frac{3}{2}}$	3.22E+4	3.26E+4	
$3p_{\frac{3}{2}}$–$15s_{\frac{1}{2}}$	8.17E+4	8.70E+4	
$3p_{\frac{3}{2}}$–$14d_{\frac{3}{2}}$	2.56E+4	2.59E+4	
$3p_{\frac{3}{2}}$–$16s_{\frac{1}{2}}$	6.60E+4	7.03E+4	
$3p_{\frac{3}{2}}$–$15d_{\frac{3}{2}}$	2.07E+4	2.09E+4	
$3p_{\frac{3}{2}}$–$17s_{\frac{1}{2}}$	5.41E+4	5.76E+4	
$3p_{\frac{3}{2}}$–$16d_{\frac{3}{2}}$	1.69E+4	1.71E+4	
$3p_{\frac{3}{2}}$–$18s_{\frac{1}{2}}$	4.49E+4	4.78E+4	
$3p_{\frac{3}{2}}$–$17d_{\frac{3}{2}}$	1.41E+4	1.42E+4	
$3p_{\frac{3}{2}}$–$19s_{\frac{1}{2}}$	3.77E+4	4.01E+4	
$3p_{\frac{3}{2}}$–$18d_{\frac{3}{2}}$	1.18E+4	1.19E+4	
$3p_{\frac{3}{2}}$–$20s_{\frac{1}{2}}$	3.19E+4	3.40E+4	
$3p_{\frac{3}{2}}$–$19d_{\frac{3}{2}}$	1.00E+4	1.01E+4	
$3p_{\frac{3}{2}}$–$20d_{\frac{3}{2}}$	8.55E+3	8.62E+3	

References. [1] Model potential (modified Coulomb approximation (Miculis & Meyer 2005); [2] Dirac–Hartree–Fock calculations (Froese Fischer 2002); [3] close-coupled calculations by R-matrix method (Taylor 1995)

$n = 18$ the difference is about 19%. The NIST values are taken from quite old measurement by Filippov & Prokofjew (1929). Their results disagree more strongly with our calculations and the measurements by Nawaz et al. (1992).

While the theoretical publications report f-values, most experimental studies measured the radiative lifetimes. However, f-values can be extracted from the reported lifetimes in a way similar to that used in our previous work (Civiš et al. 2010). In our comparison, we used QDT to calculate the ratios between f-values. These ratios are used to determine the absolute f-values from previously published experimental or theoretical lifetimes of the $3p_{\frac{1}{2},\frac{3}{2}}$, $4p_{\frac{1}{2},\frac{3}{2}}$ and $4d_{\frac{3}{2}}$ levels. Table 5 compares several QDT calculated f-values with f-values extracted from

Table 2. Improved energy measurements (cm^{-1}) of several Na I levels

Level	Present work	Other sources
$7h$	39209.670 ± 0.015	[39209.887 ± 0.002] (Dyubko et al. 1997)
$6h$	38401.144 ± 0.012	[38401.147 ± 0.002] (Dyubko et al. 1997)
$6g$	38400.865 ± 0.015	[38400.904 ± 0.002] (Dyubko et al. 1997)
$6d_{\frac{3}{2}}$	38387.266 ± 0.002	38387.268 ± 0.002 (Martin & Zalubas 1981; Juncar et al. 1981)
$6d_{\frac{5}{2}}$	38387.252 ± 0.002	38387.255 ± 0.002 (Martin & Zalubas 1981; Juncar et al. 1981)
$7s_{\frac{1}{2}}$	38012.022 ± 0.016	38012.042 ± 0.002 (Martin & Zalubas 1981; Juncar et al. 1981)
$6p_{\frac{3}{2}}$	37297.622 ± 0.021	37297.61 ± 0.02 (Risberg 1956)
$5g$	37059.497 ± 0.011	37059.54 ± 0.07 (Litzen 1970)
$5f_{\frac{7}{2}}$	37057.658 ± 0.007	37057.65 ± 0.02 (Risberg 1956)
$5d_{\frac{3}{2}}$	37036.740 ± 0.013	37036.772 ± 0.002 (Martin & Zalubas 1981; Juncar et al. 1981)
$5d_{\frac{5}{2}}$	37036.729 ± 0.010	37036.752 ± 0.002 (Martin & Zalubas 1981; Juncar et al. 1981)
$6s_{\frac{1}{2}}$	36372.610 ± 0.013	36372.618 ± 0.002 (Martin & Zalubas 1981; Juncar et al. 1981)
$5p_{\frac{3}{2}}$	35042.862 ± 0.006	35042.85 ± 0.02 (Risberg 1956)
$5p_{\frac{1}{2}}$	35040.387 ± 0.006	35040.38 ± 0.02 (Risberg 1956)
$4f_{\frac{7}{2}}$	34586.897 ± 0.007	34586.92 ± 0.02 (Johansson 1961)
$4f_{\frac{5}{2}}$	34586.893 ± 0.005	34586.92 ± 0.02 (Johansson 1961)
$4d_{\frac{3}{2}}$	34548.761 ± 0.002	34548.764 ± 0.002 (Martin & Zalubas 1981; Juncar et al. 1981)
$4d_{\frac{5}{2}}$	34548.726 ± 0.003	34548.729 ± 0.002 (Martin & Zalubas 1981; Juncar et al. 1981)
$5s_{\frac{1}{2}}$	33200.673 ± 0.003	33200.673 ± 0.002 (Martin & Zalubas 1981; Juncar et al. 1981)
$4p_{\frac{3}{2}}$	30272.586 ± 0.002	30272.58 ± 0.02 (Risberg 1956)
$4p_{\frac{1}{2}}$	30266.991 ± 0.003	30266.99 ± 0.02 (Risberg 1956)
$3d_{\frac{3}{2}}$	29172.888 ± 0.002	29172.887 ± 0.002 (Martin & Zalubas 1981; Juncar et al. 1981)
$3d_{\frac{5}{2}}$	29172.837 ± 0.003	29172.837 ± 0.002 (Martin & Zalubas 1981; Juncar et al. 1981)
$4s_{\frac{1}{2}}$	25740.013 ± 0.002	25739.999 ± 0.003 (Arqueros 1988)

Table 4. Multiplet f-values of Na I.

Transition	Present work	Experiment [1]	NIST
3s–9p	8.246E-5	8.110E-5	8.98E-5 [2],[3]
3s–10p	5.210E-5	5.322E-5	5.28E-5 [2]
3s–11p	3.563E-5	3.614E-5	5.35E-5 [2],[4]
3s–12p	2.449E-5	2.545E-5	3.93E-5 [2],[4]
3s–13p	1.946E-5	1.867E-5	3.04E-5 [2],[4]
3s–14p	1.427E-5	1.421E-5	2.27E-5 [2],[4]
3s–15p	1.143E-5	1.102E-5	1.81E-5 [2],[4]
3s–16p	9.385E-6	8.940E-6	15.5E-6 [2],[4]
3s–17p	8.588E-6	7.330E-6	12.39E-6 [2],[4]
3s–18p	7.503E-6	6.040E-6	10.32E-6 [2],[4]
3s–19p	5.637E-6	5.090E-6	

References. [1] Laser-based Faraday rotation spectroscopy (Nawaz et al. 1992); [2] Rozhdestvensky's hook method (Filippov & Prokofjew 1929); [3] Dirac–Hartree–Fock calculations (Froese Fischer 2002); [4] Coulomb approximation (Anderson & Zilitis 1964);

experimental and theoretical lifetimes. The overall agreement of our QDT calculation with the experimental values is not worse than that of other theoretical values given in the last column of Table 5.

Tables 3, 4, and 5 show that the QDT calculations agree well with other methods. Table 6 presents the oscillator strength and the transition probability for each transition between the observed Na I states. Except where noted, the Ritz wavenumbers ν and air wavelengths λ given in Table 6 were calculated using the energy levels given in Table 2. In some instances, the energy was taken from more accurate sources (Martin & Zalubas 1981; Juncar et al. 1981). Therefore, some wavenumbers presented in Tables 6 and 1 may be slightly different. To our knowledge, no dipole matrix elements have been reported for most of the Na I transitions listed in Table 6.

4. Conclusion

We report the results of an FTIR spectroscopy study of Na I transitions in the range of 700–7000 cm^{-1} (1.4–14 μm). Few spectra of Na I have been measured in this spectral range (Johansson 1961; Litzen 1970) and no laboratory measurements of metal spectra are known below 1800 cm^{-1} (λ >5.5 μm). Although the recorded wavenumbers agree with previous laboratory measurements within the corresponding uncertainties, they only partially agree with the data from the ACE solar spectrum (Hase et al. 2010) and infrared spectral atlases of the Sun from NOAO (Wallace et al. 1996). Therefore, new laboratory spectroscopic measurements are needed for the proper interpretation of current and future astrophysical spectra in the infrared domain.

The recorded spectra allowed us to extract the excitation energies of the *7h*, *6h*, and *6g* states of Na I for which only theoretical predictions were available. These predictions were calculated by extrapolation from the higher *nh* and *ng* levels with $n \geq 13$ (Dyubko et al. 1997)). The present study yielded more accurate energies for the *4s*, *4p*, *5p*, *6p*, *4f*, *5f*, and *5g* levels of Na I (Risberg 1956; Johansson 1961; Litzen 1970; Arqueros 1988). For instance, the NIST energies of $4f_{\frac{5}{2},\frac{7}{2}}$ levels were reported a half century ago (Johansson 1961) without fine-structure resolution.

The f-values calculated using the quantum-defect theory approximation were presented for all transitions involving the observed Na I levels. The approximation technique compares well with transition probabilities and oscillator strengths measured in other works (Miculis & Meyer 2005; Nawaz et al. 1992).

Table 5. Comparison of Na I oscillator strengths ($f \times 100$) with strengths obtained from previously published experimental or calculated lifetimes

		Other sources	
Transition	Present work	Experiment	Theory
$3s\,^2S_{\frac{1}{2}}$–$3p\,^2P^o_{\frac{3}{2}}$	62.2	64.07 ± 0.09 [2]	64.4 [1]
		64.13 ± 0.14 [3]	63.1 [5]
		64.16 ± 0.06 [4]	64.7 [7]
$3s\,^2S_{\frac{1}{2}}$–$3p\,^2P^o_{\frac{1}{2}}$	31.1	32.01 ± 0.04 [2]	32.2 [1]
		31.99 ± 0.12 [6]	32.3 [7]
		31.81 ± 0.06 [8]	31.91 ± 0.12 [9]
$3s\,^2S_{\frac{1}{2}}$–$4p\,^2P^o_{\frac{3}{2}}$	0.883	0.962 ± 0.03 [10]	0.875 [1]
			0.926 [5]
			0.886 [7]
			0.881 ± 0.033 [11]
$3s\,^2S_{\frac{1}{2}}$–$4p\,^2P^o_{\frac{1}{2}}$	0.434	0.467 ± 0.014 [10]	0.431 [1]
			0.436 [7]
			0.437 ± 0.016 [11]
$4s\,^2S_{\frac{1}{2}}$–$4p\,^2P^o_{\frac{3}{2}}$	95.1	103 ± 3 [10]	94.3 [1]
			99.7 [5]
			95.4 [7]
			94.9 ± 3.5 [11]
$4s\,^2S_{\frac{1}{2}}$–$4p\,^2P^o_{\frac{1}{2}}$	47.5	51.1 ± 1.5 [10]	47.1 [1]
			47.7 [7]
			47.7 ± 1.8 [11]
$3d\,^2D^o_{\frac{3}{2}}$–$4p\,^2P^o_{\frac{3}{2}}$	1.96	2.13 ± 0.07 [10]	1.94 [1]
			2.05 [5]
			1.96 [7]
			1.95 ± 0.07 [11]
$3d\,^2D^o_{\frac{5}{2}}$–$4p\,^2P^o_{\frac{3}{2}}$	11.7	12.8 ± 0.4 [10]	11.6 [1]
			12.3 [5]
			11.8 [7]
			11.7 ± 0.4 [11]
$3d\,^2D^o_{\frac{3}{2}}$–$4p\,^2P^o_{\frac{1}{2}}$	9.75	10.5 ± 0.03 [10]	9.67 [1]
			9.78 [7]
			9.80 ± 0.37 [11]
$3p\,^2P^o_{\frac{1}{2}}$–$4d\,^2D_{\frac{3}{2}}$	9.64	10.1 ± 0.1 [12]	9.76 [1]
		9.82 ± 0.06 [13]	9.76 [5]
		9.56 ± 0.05 [14]	9.77 [7]
$3p\,^2P^o_{\frac{3}{2}}$–$4d\,^2D_{\frac{3}{2}}$	0.962	1.01 ± 0.01 [12]	0.974 [1]
		0.980 ± 0.006 [13]	0.974 [5]
		0.954 ± 0.005 [14]	0.975 [7]
$4p\,^2P^o_{\frac{1}{2}}$–$4d\,^2D_{\frac{3}{2}}$	94.4	98.7 ± 1 [12]	95.5 [1]
		96.1 ± 0.6 [13]	95.5 [5]
		93.6 ± 0.5 [14]	95.6 [7]
$4p\,^2P^o_{\frac{3}{2}}$–$4d\,^2D_{\frac{3}{2}}$	9.45	9.89 ± 0.1 [12]	9.57 [1]
		9.63 ± 0.06 [13]	9.57 [5]
		9.37 ± 0.05 [14]	9.58 [7]

References. [1] Calculations by model potential method (Miculis & Meyer 2005); [2] beam-gas-laser spectroscopy (Volz et al. 1996); [3] precision spectroscopy on an optically prepared sample of ultracold, two-level atoms (Oates et al. 1996); [4] molecular spectroscopy of the Na_2 purely long-range O_g^- state (Jones et al. 1996); [5] numerical Coulomb approximation (Lindgård & Nielsen 1977); [6] measurements by molecular beam method (Tiemann et al. 1996); [7] realistic calculations including the core polarization, spin-orbit interaction, and blackbody radiation (Theodosiou 1984); [8] observing the decay in flight of laser-excited atoms in a fast atomic beam (Gaupp et al. 1982); [9] multiconfiguration Hartree–Fock calculations (Carlsson et al. 1992); [10] detecting the time-resolved fluorescence from the directly populated levels by the delayed-coincidence technique (Marek 1977); [11] multiconfiguration Hartree–Fock calculations (Jönsson et al. 1996); [12] measurements by stepwise excitation of a fast ion beam (Kandela 1984); [13] direct oscillography of the time dependence of light emitted from Na atoms, excited by short pulses of electrons (Karstensen & Schramm 1966); [14] time resolved observations of the fluorescence radiation after stepwise excitation by two pulsed dye lasers (Kaiser 1975)

Acknowledgements. This work was financially supported by the Grant Agency of the Academy of Sciences of the Czech Republic (grant No. IAA400400705), by the Ministry of Finance of the Czech Republic (Project ECPF:049/4V) and the Ministry of Education, Youth, and Sports of the Czech Republic (grant No. LM2010014).

References

Anderson, E. M. & Zilitis, V. A. 1964, Opt. Spectrosk., 16, 177, opt. Spectrosc. **16** (2), 99 (1964)
Andrievsky, S. M., Egorova, I. A., Korotin, S. A., & Burnage, R. 2002, Astron. Astrophys., 389, 519
Aragon, C. & Aguilera, J. A. 2008, Spectrochim. Acta, Part B, 63, 893
Arqueros, F. 1988, Opt. Commun., 67, 341
Babánková, D., Civiš, S., & Juha, L. 2006, Prog. Quantum Electron., 30, 75
Barthélemy, O., Margot, J., Chaker, M., et al. 2005, Spectrochim. Acta, Part B, 60, 905, 3rd International Conference on Laser Induced Plasma Spectroscopy and Applications (LIBS04), Torremolinos, Spain, Sep. 28–Oct.01, 2004
Biémont, E. 1994, in IAU Symposia, Vol. 154, Infrared Solar Physics, ed. D. M. Rabin, J. T. Jefferies, & C. Lindsey, Int. Astron. Union (PO Box 17, 3300 AA Dordrecht, Netherlands: Kluwer Academic Publ.), 501–510, 154th Symposium of the International-Astronomical-Union - 1st International Meeting devoted to Infrared Physics, Tucson, AZ, Mar. 02–06, 1992
Carlsson, J., Jönsson, P., Sturesson, L., & Fischer, C. F. 1992, Phys. Scr., 46, 394
Chang, E. S. & Schoenfeld, W. G. 1991, Astrophys. J., 383, 450
Charbonneau, D., Brown, T. M., Noyes, R. W., & Gilliland, R. L. 2002, Astrophys. J., 568, 377
Chernov, V., Manakov, N., & Starace, A. 2000, Eur. Phys. J. D, 8, 347
Chernov, V. E., Dorofeev, D. L., Kretinin, I. Y., & Zon, B. A. 2005a, Phys. Rev. A, 71, 022505
Chernov, V. E., Dorofeev, D. L., Kretinin, I. Y., & Zon, B. A. 2005b, J. Phys. B, 38, 2289
Civiš, S., Matulková, I., Cihelka, J., et al. 2010, Phys. Rev. A, 81, 012510
Civiš, S., Matulková, I., Cihelka, J., et al. 2010, Phys. Rev. A, 82, 022502
Civiš, S., Matulková, I., Cihelka, J., et al. 2011a, J. Phys. B, 44, 105002
Civiš, S., Matulková, I., Cihelka, J., et al. 2011b, J. Phys. B, 44, 025002
Dyubko, S., Efremov, V., Podnos, S., Sun, X., & MacAdam, K. B. 1997, J. Phys. B, 30, 2345
Filippov, A. & Prokofjew, W. 1929, Z. Phys., 56, 458
Froese Fischer, C. 2002, The MCHF/MCDHF Collection (non-orthogonal B-spline CI caclulations), http://atoms.vuse.vanderbilt.edu
Gaupp, A., Kuske, P., & Andrä, H. J. 1982, Phys. Rev. A, 26, 3351
Giacomo, A. D., Shakhatov, V., & Pascale, O. D. 2001, Spectrochimica Acta Part B: Atomic Spectroscopy, 56, 753, 1st International Conference on Laser-Induced Plasma Spectroscopy and Applications (LIBS 2000), Tirrenia, Italy, Oct. 08-12, 2000
Gomes, A., Aubreton, A., Gonzalez, J. J., & Vacqui, S. 2004, J. Phys. D, 37, 689
Grava, C., Schneider, N. M., & Barbieri, C. 2010, in IAU Symposium Proceedings Series, Vol. 269, Galileo's Medicean Moons: Their Impact on 400 Years of Discovery, ed. Barbieri, C. and Chakrabarti, S. and Coradini, M. and Lazzarin, M., Int. Astronom Union; European Space Agency (The Pitt Building, Trumpington St, Cambridge CB2 1RP, Cambs, England: Cambridge Univ. Press), 224–228, 269th Symposium of the International Astronomical Union, Padova, Italy, Jan 06-09, 2010
Grevesse, N. & Noels, A. 1994, Phys. Scr., T51, 47, 25th Conference of the European-Group-for-Atomic-Spectroscopy (EGAS), Caen, France, Jul. 13–16, 1993
Hase, F., Wallace, L., McLeod, S. D., Harrison, J. J., & Bernath, P. F. 2010, J. Quant. Spectrosc. Radiat. Transfer, 111, 521
Jensen, A. G., Redfield, S., Endl, M., et al. 2011, Astrophys. J., 743, 203
Johansson, I. 1961, Ark. Fys. (Stockholm), 20, 135
Johansson, S. 2005, in High Resolution Infrared Spectroscopy In Astronomy, Proceedings, ed. Kaufl, H. U. and Siebenmorgen, R. and Moorwood, A., ESO Astrophysics Symposia, ESO (Heidelberger Platz 3, D-14197 Berlin, Germany: Springer–Verlag Berlin), 62–67, ESO Workshop on High Resolution Infrared Spectroscopy in Astronomy, Garching, Germany, Nov. 18–21, 2003
Jones, K. M., Julienne, P. S., Lett, P. D., et al. 1996, Europhys. Lett., 35, 85
Jönsson, P., Ynnerman, A., Froese Fischer, C., Godefroid, M. R., & Olsen, J. 1996, Phys. Rev. A, 53, 4021
Jorissen, A. 2004, Phys. Scr., T112, 73
Juncar, P., Pinard, J., Hamon, J., & Chartier, A. 1981, Metrologia, 17, 77
Kaiser, D. 1975, Phys. Lett. A, 51, 375
Kandela, S. A. 1984, Appl. Opt., 23, 2152
Karstensen, F. & Schramm, J. 1966, Z. Phys., 195, 370
Kawaguchi, K., Sanechika, N., Nishimura, Y., et al. 2008, Chem. Phys. Lett., 463, 38

Kelleher, D. E. & Podobedova, L. I. 2008, J. Phys. Chem. Ref. Data, 37, 267
Kerber, F., Nave, G., Sansonetti, C. J., & Bristow, P. 2009, Phys. Scr., T134, 014007
Khalil, A. & Sreenivasan, N. 2005, Laser Phys. Lett., 2, 445
Lednev, V. N. & Pershin, S. M. 2008, Laser Phys., 18, 850
Lee, D.-W., Kim, S. J., Lee, D.-H., Jin, H., & Kim, K.-S. 2011, J. Geophys. Res., 116, 7213
Lee, W.-B., Wu, J.-Y., Lee, Y.-I., & Sneddon, J. 2004, Appl. Spectrosc. Rev., 39, 27
Lindgård, A. & Nielsen, S. E. 1977, At. Data Nucl. Data Tables, 19, 533
Litzen, U. 1970, Phys. Scr., 1, 253
Lobel, A. 2011, Can. J. Phys., 89, 395, special Issue on the 10th International Colloquium on Atomic Spectra and Oscillator Strengths for Astrophysical and Laboratory Plasmas
Marek, J. 1977, J. Phys. B, 10, L325
Martin, W. C. & Zalubas, R. 1981, J. Phys. Chem. Ref. Data, 10, 153
Matta, M., Smith, S., Baumgardner, J., et al. 2009, Icarus, 204, 409
Meléndez, J. & Barbuy, B. 1999, Astrophys. J., Suppl. Ser., 124, 527
Miculis, K. & Meyer, W. 2005, J. Phys. B, 38, 2097
Mouawad, N., Burger, M. H., Killen, R. M., et al. 2011, Icarus, 211, 21
Nawaz, M., Farooq, W. A., & Connerade, J.-P. 1992, J. Phys. B, 25, 5327
Nilsson, H. 2009, Phys. Scr., T134, 014009, 9th International Conference on Atomic Spectroscopy and Oscillator Strengths for Astrophysical and Laboratory Plasma, Lund, Sweden, Aug. 07–10, 2007
Oates, C. W., Vogel, K. R., & Hall, J. L. 1996, Phys. Rev. Lett., 76, 2866
O'Donovan, F. T., Charbonneau, D., Harrington, J., et al. 2010, Astrophys. J., 710, 1551
OPUS. 2010, Opus Spectroscopy Software, http://www.brukeroptics.com/opus.html
Pickering, J., Blackwell-Whitehead, R., Thorne, A., Ruffoni, M., & Holmes, C. 2011, Can. J. Phys., 89, 387, special Issue on the 10th International Colloquium on Atomic Spectra and Oscillator Strengths for Astrophysical and Laboratory Plasmas.
Pickering, J. C. 1999, Phys. Scr., T83, 27, 6th International Colloquium on Atomic Spect and Oscillator Strengths (ASOS 6), Victoria, Canada, Aug. 09–13, 1998
Qi, H., Sun, Y., Liu, X., Hou, X., & Li, Y. 2007, Laser Phys. Lett., 4, 212
Radziemski, L. J., Fisher, K. J., Steinhaus, D. W., & Goldman, A. S. 1972, Comput. Phys. Commun., 3, 9
Ralchenko, Y., Kramida, A., Reader, J., & NIST ASD Team. 2010, NIST Atomic Spectra Database (version 4.0)
Redfield, S., Endl, M., Cochran, W. D., & Koesterke, L. 2008, Astrophys. J., Lett., 673, L87
Risberg, P. 1956, Ark. Fys. (Stockholm), 10, 583
Ryde, N. 2010, Astron. Nachr., 331, 433
Sansonetti, J. E. 2008, J. Phys. Chem. Ref. Data, 37, 1659
Spitoni, E., Recchi, S., & Matteucci, F. 2008, Astron. Astrophys., 484, 743
Sternberg, A., Gal-Yam, A., Simon, J. D., et al. 2011, Science, 333, 856
Taylor, K. T. 1995, TOPBASE (Opacity Project), http://cdsweb.u-strasbg.fr/topbase/topbase.html
Theodosiou, C. E. 1984, Phys. Rev. A, 30, 2881
Tiemann, E., Knöckel, H., & Richling, H. 1996, Z. Phys. D, 37, 323
Volz, U., Majerus, M., Liebel, H., Schmitt, A., & Schmoranzer, H. 1996, Phys. Rev. Lett., 76, 2862
Wahlgren, G. M. 2011, Can. J. Phys., 89, 345, special Issue on the 10th International Colloquium on Atomic Spectra and Oscillator Strengths for Astrophysical and Laboratory Plasmas.
Wallace, L., Livingston, W., Hinkle, K., & Bernath, P. 1996, Astrophys. J., Suppl. Ser., 106, 165
Wallace, L., Meyer, M. R., Hinkle, K., & Edwards, S. 2000, Astrophys. J., 535, 325

Table 6. QDT-calculated transition dipole moments for the observed transitions between Na I levels. The energy levels are taken from Table 2 except for those with an asterisk, which are taken from Martin & Zalubas (1981); Juncar et al. (1981). The air wavelengths are specified.

Transition i–k	Lower level (cm^{-1})	Upper level (cm^{-1})	ν (cm^{-1})	λ (nm)	$\log(g_i f_{ik})$	f_{ik}	A_{ki} (s^{-1})
$5d\,^2\!/_2$–$6p\,^2\!/_2$	37036.772*	37297.622	260.85	38325.8	−1.50	5.59×10^{-2}	2.54×10^{3}
$5d\,^2\!/_2$–$6p\,^1\!/_2$	37036.772*	37297.622	260.85	38325.8	+0.110	2.79×10^{-1}	2.54×10^{4}
$5d\,^5\!/_2$–$6p\,^3\!/_2$	37036.752*	37297.622	260.87	38322.8	+0.698	3.35×10^{-1}	2.28×10^{4}
$4d\,^3\!/_2$–$5p\,^1\!/_2$	34548.764*	35040.387	491.623	20335.2	−0.269	1.91×10^{-1}	6.14×10^{4}
$4d\,^3\!/_2$–$5p\,^3\!/_2$	34548.764*	35042.862	494.098	20233.4	−1.88	3.83×10^{-2}	6.23×10^{3}
$4d\,^5\!/_2$–$5p\,^3\!/_2$	34548.729*	35042.862	494.133	20232.0	+0.322	2.30×10^{-1}	5.61×10^{4}
$6p\,^3\!/_2$–$7s\,^1\!/_2$	37297.622	38012.042*	714.42	13993.6	+0.860	5.91×10^{-1}	4.02×10^{5}
$6p\,^1\!/_2$–$7s\,^1\!/_2$	37297.622	38012.042*	714.42	13993.6	+0.167	5.91×10^{-1}	2.01×10^{5}
$6g\,^9\!/_2$–$7h\,^9\!/_2$	38400.865	39209.681	808.786	12361.2	−1.28	2.78×10^{-2}	1.21×10^{4}
$6g\,^9\!/_2$–$7h\,^{11}\!/_2$	38400.865	39209.681	808.786	12361.2	+2.71	1.50	5.46×10^{5}
$6g\,^7\!/_2$–$7h\,^9\!/_2$	38400.865	39209.681	808.786	12361.2	+2.50	1.53	5.34×10^{5}
$6s\,^1\!/_2$–$6p\,^3\!/_2$	36372.618*	37297.622	925.012	10807.7	+1.12	1.53	4.38×10^{5}
$6s\,^1\!/_2$–$6p\,^1\!/_2$	36372.618*	37297.622	925.012	10807.7	+0.428	7.67×10^{-1}	4.38×10^{5}
$6p\,^3\!/_2$–$6d\,^5\!/_2$	37297.622	38387.255*	1089.633	9174.90	+1.44	1.05	5.55×10^{5}
$6p\,^3\!/_2$–$6d\,^3\!/_2$	37297.622	38387.268*	1089.646	9174.79	−0.759	1.17×10^{-1}	9.25×10^{4}
$6p\,^1\!/_2$–$6d\,^3\!/_2$	37297.622	38387.268*	1089.646	9174.79	+0.850	1.17	4.63×10^{5}
$3d\,^3\!/_2$–$4p\,^1\!/_2$	29172.887*	30266.991	1094.097	9137.46	−0.942	9.75×10^{-2}	1.56×10^{5}
$3d\,^3\!/_2$–$4p\,^3\!/_2$	29172.887*	30272.586	1099.699	9090.92	−2.55	1.96×10^{-2}	1.58×10^{4}
$3d\,^5\!/_2$–$4p\,^3\!/_2$	29172.837*	30272.586	1099.744	9090.55	−0.354	1.17×10^{-1}	1.42×10^{5}
$5f\,^7\!/_2$–$6d\,^5\!/_2$	37057.658	38387.255*	1329.597	7519.03	−1.53	2.70×10^{-2}	4.25×10^{4}
$5f\,^5\!/_2$–$6d\,^5\!/_2$	37057.658	38387.255*	1329.597	7519.03	−4.53	1.80×10^{-3}	2.13×10^{3}
$5f\,^5\!/_2$–$6d\,^3\!/_2$	37057.658	38387.268*	1329.61	7518.95	−1.89	2.52×10^{-2}	4.46×10^{4}
$5p\,^3\!/_2$–$6s\,^1\!/_2$	35042.862	36372.618*	1329.751	7518.16	+0.592	4.52×10^{-1}	1.07×10^{6}
$5p\,^1\!/_2$–$6s\,^1\!/_2$	35040.387	36372.618*	1332.218	7504.23	−0.103	4.51×10^{-1}	5.34×10^{5}
$5g\,^9\!/_2$–$6h\,^9\!/_2$	37059.497	38401.148	1341.651	7451.47	−1.17	3.11×10^{-2}	3.74×10^{4}
$5g\,^9\!/_2$–$6h\,^{11}\!/_2$	37059.497	38401.148	1341.651	7451.47	+2.82	1.68	1.68×10^{6}
$5g\,^7\!/_2$–$6h\,^9\!/_2$	37059.497	38401.148	1341.651	7451.47	+2.62	1.71	1.65×10^{6}
$5f\,^7\!/_2$–$6g\,^9\!/_2$	37057.658	38400.865	1343.194	7442.91	+2.22	1.15	1.11×10^{6}
$5f\,^7\!/_2$–$6g\,^7\!/_2$	37057.658	38400.865	1343.194	7442.91	−1.33	3.29×10^{-2}	3.95×10^{4}
$5f\,^5\!/_2$–$6g\,^7\!/_2$	37057.658	38400.865	1343.194	7442.91	+1.96	1.18	1.07×10^{6}
$5s\,^1\!/_2$–$5p\,^1\!/_2$	33200.673*	35040.387	1839.707	5434.17	+0.222	6.24×10^{-1}	1.41×10^{6}
$5s\,^1\!/_2$–$5p\,^3\!/_2$	33200.673*	35042.862	1842.185	5426.86	+0.916	1.25	1.41×10^{6}
$5p\,^3\!/_2$–$5d\,^5\!/_2$	35042.862	37036.752*	1993.867	5014.01	+1.34	9.50×10^{-1}	1.68×10^{6}
$5p\,^3\!/_2$–$5d\,^3\!/_2$	35042.862	37036.772*	1993.91	5013.90	−0.858	1.06×10^{-1}	2.80×10^{5}
$5p\,^1\!/_2$–$5d\,^3\!/_2$	35040.387	37036.772*	1996.353	5007.77	+0.742	1.05	1.40×10^{6}
$5g\,^9\!/_2$–$7h\,^9\!/_2$	37059.497	39209.681	2150.197	4649.47	−3.15	4.30×10^{-3}	1.32×10^{4}
$5g\,^9\!/_2$–$7h\,^{11}\!/_2$	37059.497	39209.681	2150.197	4649.47	+0.842	2.32×10^{-1}	5.96×10^{5}
$5g\,^7\!/_2$–$7h\,^9\!/_2$	37059.497	39209.681	2150.197	4649.47	+0.636	2.36×10^{-1}	5.83×10^{5}
$4f\,^7\!/_2$–$5d\,^5\!/_2$	34586.897	37036.752*	2449.855	4080.76	−2.49	1.04×10^{-2}	5.56×10^{4}
$4f\,^5\!/_2$–$5d\,^5\!/_2$	34586.893	37036.752*	2449.859	4080.75	−5.48	6.94×10^{-4}	2.78×10^{3}
$4f\,^5\!/_2$–$5d\,^3\!/_2$	34586.893	37036.772*	2449.879	4080.72	−2.84	9.72×10^{-3}	5.84×10^{4}
$4f\,^7\!/_2$–$5g\,^9\!/_2$	34586.897	37059.497	2472.603	4043.22	+2.35	1.31	4.27×10^{6}
$4f\,^7\!/_2$–$5g\,^7\!/_2$	34586.897	37059.497	2472.603	4043.22	−1.21	3.74×10^{-2}	1.52×10^{5}
$4f\,^5\!/_2$–$5g\,^7\!/_2$	34586.893	37059.497	2472.603	4043.22	+2.09	1.35	4.12×10^{6}
$4d\,^3\!/_2$–$5f\,^5\!/_2$	34548.764*	37057.658	2508.894	3984.73	+1.24	8.62×10^{-1}	2.41×10^{6}
$4d\,^5\!/_2$–$5f\,^7\!/_2$	34548.729*	37057.658	2508.928	3984.68	+1.59	8.21×10^{-1}	2.59×10^{6}
$4d\,^5\!/_2$–$5f\,^5\!/_2$	34548.729*	37057.658	2508.928	3984.68	−1.40	4.11×10^{-2}	1.72×10^{5}
$4p\,^3\!/_2$–$5s\,^1\!/_2$	30272.586	33200.673*	2928.083	3414.27	+0.215	3.10×10^{-1}	3.55×10^{6}
$4p\,^1\!/_2$–$5s\,^1\!/_2$	30266.991	33200.673*	2933.671	3407.77	−0.478	3.10×10^{-1}	1.78×10^{6}

Table 6. continued.

Transition i–k	Lower level (cm^{-1})	Upper level (cm^{-1})	ν (cm^{-1})	λ (nm)	$\log(g_i f_{ik})$	f_{ik}	A_{ki} (s^{-1})
$5p\,^2P_{3/2}$–$7s\,^2S_{1/2}$	35042.862	38012.042*	2969.160	3367.04	−2.07	3.17×10^{-2}	3.73×10^{5}
$5p\,^2P_{1/2}$–$7s\,^2S_{1/2}$	35040.387	38012.042*	2971.655	3364.21	−2.76	3.18×10^{-2}	1.87×10^{5}
$5p\,^2P_{3/2}$–$6d\,^2D_{5/2}$	35042.862	38387.255*	3344.378	2989.28	−0.478	1.55×10^{-1}	7.72×10^{5}
$5p\,^2P_{3/2}$–$6d\,^2D_{3/2}$	35042.862	38387.268*	3344.406	2989.25	−2.68	1.72×10^{-2}	1.29×10^{5}
$5p\,^2P_{1/2}$–$6d\,^2D_{3/2}$	35040.387	38387.268*	3346.866	2987.06	−1.07	1.72×10^{-1}	6.44×10^{5}
$4f\,^2F_{7/2}$–$6d\,^2D_{5/2}$	34586.897	38387.255*	3800.358	2630.61	−4.21	1.85×10^{-3}	2.38×10^{4}
$4f\,^2F_{5/2}$–$6d\,^2D_{5/2}$	34586.893	38387.255*	3800.362	2630.61	−7.20	1.24×10^{-4}	1.19×10^{3}
$4f\,^2F_{5/2}$–$6d\,^2D_{3/2}$	34586.893	38387.268*	3800.375	2630.60	−4.57	1.73×10^{-3}	2.50×10^{4}
$4f\,^2F_{7/2}$–$6g\,^2G_{9/2}$	34586.897	38400.865	3813.968	2621.23	+0.353	1.78×10^{-1}	1.38×10^{6}
$4f\,^2F_{7/2}$–$6g\,^2G_{7/2}$	34586.897	38400.865	3813.968	2621.23	−3.20	5.08×10^{-3}	4.93×10^{4}
$4f\,^2F_{5/2}$–$6g\,^2G_{7/2}$	34586.893	38400.865	3813.972	2621.22	+0.0935	1.83×10^{-1}	1.33×10^{6}
$5s\,^2S_{1/2}$–$6p\,^2P_{3/2}$	33200.673*	37297.622	4096.949	2440.17	−2.50	4.12×10^{-2}	2.31×10^{5}
$5s\,^2S_{1/2}$–$6p\,^2P_{1/2}$	33200.673*	37297.622	4096.949	2440.17	−3.19	2.06×10^{-2}	2.31×10^{5}
$4p\,^2P_{3/2}$–$4d\,^2D_{5/2}$	30272.586	34548.729*	4276.126	2337.93	+1.22	8.51×10^{-1}	6.92×10^{6}
$4p\,^2P_{3/2}$–$4d\,^2D_{3/2}$	30272.586	34548.764*	4276.178	2337.90	−0.973	9.45×10^{-2}	1.15×10^{6}
$4p\,^2P_{1/2}$–$4d\,^2D_{3/2}$	30266.991	34548.764*	4281.759	2334.85	+0.636	9.44×10^{-1}	5.77×10^{6}
$4s\,^2S_{1/2}$–$4p\,^2P_{1/2}$	25740.013	30266.991	4526.968	2208.38	−0.0513	4.75×10^{-1}	6.49×10^{6}
$4s\,^2S_{1/2}$–$4p\,^2P_{3/2}$	25740.013	30272.586	4532.568	2205.65	+0.643	9.51×10^{-1}	6.51×10^{6}
$3d\,^2D_{3/2}$–$4f\,^2F_{5/2}$	29172.887*	34586.893	5414.005	1846.56	+1.40	1.01	1.31×10^{7}
$3d\,^2D_{5/2}$–$4f\,^2F_{5/2}$	29172.837*	34586.893	5414.06	1846.54	−1.25	4.79×10^{-2}	9.37×10^{5}
$3d\,^2D_{5/2}$–$4f\,^2F_{7/2}$	29172.837*	34586.897	5414.063	1846.54	+1.75	9.59×10^{-1}	1.41×10^{7}
$3d\,^2D_{3/2}$–$5p\,^2P_{1/2}$	29172.887*	35040.387	5867.5	1703.84	−7.47	1.42×10^{-4}	6.52×10^{3}
$3d\,^2D_{3/2}$–$5p\,^2P_{3/2}$	29172.887*	35042.862	5869.975	1703.12	−9.15	2.65×10^{-5}	6.10×10^{2}
$3d\,^2D_{5/2}$–$5p\,^2P_{3/2}$	29172.837*	35042.862	5870.025	1703.11	−6.95	1.59×10^{-4}	5.48×10^{3}
$4p\,^2P_{3/2}$–$6s\,^2S_{1/2}$	30272.586	36372.618*	6100.032	1638.89	−2.38	2.31×10^{-2}	1.15×10^{6}
$4p\,^2P_{1/2}$–$6s\,^2S_{1/2}$	30266.991	36372.618*	6105.627	1637.39	−3.07	2.32×10^{-2}	5.76×10^{5}
$4p\,^2P_{3/2}$–$5d\,^2D_{5/2}$	30272.586	37036.752*	6764.166	1477.97	−0.677	1.27×10^{-1}	2.59×10^{6}
$4p\,^2P_{3/2}$–$5d\,^2D_{3/2}$	30272.586	37036.772*	6764.186	1477.97	−2.88	1.41×10^{-2}	4.31×10^{5}
$4p\,^2P_{1/2}$–$5d\,^2D_{3/2}$	30266.991	37036.772*	6769.781	1476.75	−1.27	1.41×10^{-1}	2.16×10^{6}
$4p\,^2P_{3/2}$–$7s\,^2S_{1/2}$	30272.586	38012.042*	7739.456	1291.73	−3.54	7.28×10^{-3}	5.82×10^{5}
$4p\,^2P_{1/2}$–$7s\,^2S_{1/2}$	30266.991	38012.042*	7745.051	1290.79	−4.23	7.30×10^{-3}	2.92×10^{5}
$3d\,^2D_{3/2}$–$5f\,^2F_{5/2}$	29172.887*	37057.658	7884.771	1267.92	−0.453	1.59×10^{-1}	4.41×10^{6}
$3d\,^2D_{5/2}$–$5f\,^2F_{7/2}$	29172.837*	37057.658	7884.821	1267.91	−0.0921	1.52×10^{-1}	4.72×10^{6}
$3d\,^2D_{5/2}$–$5f\,^2F_{5/2}$	29172.837*	37057.658	7884.821	1267.91	−3.09	7.59×10^{-3}	3.15×10^{5}
$4p\,^2P_{3/2}$–$6d\,^2D_{5/2}$	30272.586	38387.255*	8114.669	1232.00	−1.74	4.40×10^{-2}	1.29×10^{6}
$4p\,^2P_{3/2}$–$6d\,^2D_{3/2}$	30272.586	38387.268*	8114.682	1232.00	−3.94	4.88×10^{-3}	2.15×10^{5}
$4p\,^2P_{1/2}$–$6d\,^2D_{3/2}$	30266.991	38387.268*	8120.277	1231.15	−2.32	4.89×10^{-2}	1.08×10^{6}
$3d\,^2D_{3/2}$–$6p\,^2P_{3/2}$	29172.887*	37297.622	8124.735	1230.47	−10.8	4.86×10^{-6}	2.14×10^{2}
$3d\,^2D_{3/2}$–$6p\,^2P_{1/2}$	29172.887*	37297.622	8124.735	1230.47	−9.24	2.43×10^{-5}	2.14×10^{3}
$3d\,^2D_{5/2}$–$6p\,^2P_{3/2}$	29172.837*	37297.622	8124.785	1230.47	−8.65	2.91×10^{-5}	1.93×10^{3}
$4s\,^2S_{1/2}$–$5p\,^2P_{1/2}$	25740.013	35040.387	9300.374	1074.93	−3.69	1.25×10^{-2}	7.22×10^{5}
$4s\,^2S_{1/2}$–$5p\,^2P_{3/2}$	25740.013	35042.862	9302.849	1074.65	−2.98	2.53×10^{-2}	7.30×10^{5}
$4s\,^2S_{1/2}$–$6p\,^2P_{3/2}$	25740.013	37297.622	11557.609	864.993	−4.59	5.07×10^{-3}	2.26×10^{5}
$4s\,^2S_{1/2}$–$6p\,^2P_{1/2}$	25740.013	37297.622	11557.609	864.993	−5.28	2.54×10^{-3}	2.26×10^{5}

A&A 541, A125 (2012)
DOI: 10.1051/0004-6361/201218867
© ESO 2012

Astronomy & Astrophysics

Potassium spectra in the 700–7000 cm^{-1} domain: Transitions involving f-, g-, and h-states

S. Civiš[1], M. Ferus[1], P. Kubelík[1], P. Jelinek[1], and V. E. Chernov[1,2]

[1] J. Heyrovský Institute of Physical Chemistry, Academy of Sciences of the Czech Republic, Dolejškova 3, 18223 Prague 8, Czech Republic
e-mail: civis@jh-inst.cas.cz
[2] Voronezh State University, 394693 Voronezh, Russia

Received 23 January 2012 / Accepted 28 February 2012

ABSTRACT

Context. The infrared (IR) range is becoming increasingly important to astronomical studies of cool or dust-obscured objects, such as dwarfs, disks, or planets, and in the extended atmospheres of evolved stars. A general drawback of the IR spectral region is the much lower number of atomic lines available (relative to the visible and ultraviolet ranges).
Aims. We attempt to obtain new laboratory spectra to help us identify spectral lines in the IR. This may result in the discovery of new excited atomic levels that are difficult to compute theoretically with high accuracy, hence can be determined solely from IR lines.
Methods. The K vapor was formed through the ablation of the KI (potassium iodide) target by a high-repetition-rate (1.0 kHz) pulsed nanosecond ArF laser (λ = 193 nm, output energy of 15 mJ) in a vacuum (10^{-2} Torr). The time-resolved emission spectrum of the neutral atomic potassium (K) was recorded in the 700–7000 cm^{-1} region using the Fourier transform infrared spectroscopy technique with a resolution of 0.02 cm^{-1}. The f-values calculated in the quantum-defect theory approximation are presented for the transitions involving the reported K levels.
Results. Precision laboratory measurements are presented for 38 K lines in the infrared (including 25 lines not measured previously in the laboratory) range using time-resolved Fourier transform infrared spectroscopy. The 6g, 6h, and 7h levels of K are observed for the first time, in addition to updated energy values of the other 23 K levels and the f-values for the transitions involving these levels.
Conclusions. The recorded wave numbers are in good agreement with the data from the available solar spectrum atlases. Nevertheless, we correct their identification for three lines (1343.699, 1548.559, and 1556.986 cm^{-1}).

Key words. atomic data – line: identification – methods: laboratory – infrared: general – techniques: spectroscopic

1. Introduction

Understanding the chemical evolution of our Galaxy requires the determination of the element abundances in stars of different metallicities. Potassium is an odd-Z element that is mainly produced in massive stars by explosive oxygen burning (see Zhang et al. 2006b, and references therein).

An analysis of K abundances of 58 metal-poor stars (Zhang et al. 2006b) found that the dependence of [K/Fe] versus [Fe/H] agrees with the theoretical predictions of the chemical evolution models of the Galaxy. The spectroscopic determination of potassium abundances in metal-poor stars is difficult to obtain only because the resonance doublet (K at 7665 Å and 7699 Å) lines are available in this analysis; moreover, these K lines are often blended with very strong telluric O_2 lines.

Since it is one of the most important references in astronomy, the solar spectrum forms the basis of the description of the chemical evolution of our Galaxy. An analysis of the absorption lines found in the solar spectrum provides detailed information about the isotopic and elemental abundance distribution of a very large number of elements found in the solar system (Lodders 2003).

One of the most important problems of atmospheric line formation, is the assumption of local thermodynamic equilibrium (LTE), which is usually applied to the computation of atomic populations and radiative transfer (Gehren et al. 2001). Non-local thermal equilibrium (NLTE) occurs under high temperatures and low pressures, when the photon absorption rate exceeds the atom-electron collision rate. These conditions occur, for example, in metal-poor stars where electron collisions have lower rates because the free electron density is correlated with metal abundance (Gehren et al. 2001).

The level populations of the atoms with low ionization potentials are particularly sensitive to deviations from LTE. As for other atoms with one electron in the outermost shell, K has one of the lowest ionization energies (4.34 eV) in the periodic system. Neutral sodium constitutes approximately 0.7% of the sodium atoms under the conditions of the solar photosphere, whereas neutral potassium represents only 0.1%. The photospheric solar potassium abundance based on the theoretical NLTE model atmospheres is $\log \varepsilon_{\odot}(K) = 5.12 \pm 0.03$ (Zhang et al. 2006a); the Fe abundance is also calculated by accounting for NLTE (Gehren et al. 2001). There are several stellar atmosphere models that predict different photospheric/coronal abundance ratios as a function of ionization potential. Hence, K abundance can be used to test these models for different stars. For instance, CORONAS-F solar spacecraft measurements (Sylwester et al. 2010) yielded possible values of the coronal abundance of K with a peak at $\log \varepsilon_{\odot}(K) = 5.86$ and a half-peak range of 5.63–6.09. The latter measurements were based on the resonant line of the He-like K (K) ion in the X-ray range.

In addition to the optical, UV, and X-ray ranges, the infrared (IR) range is becoming increasingly important to astronomical research, for instance in studies of dust-obscured objects and interstellar clouds, cool objects such as dwarfs, disks, or planets and the extended atmospheres of evolved stars, including objects at cosmological distances from the Earth (Kerber et al. 2009).

The IR spectrum of the most studied object, the Sun, has been recorded from the ground (Wallace et al. 1996) and the stratosphere (Goldman et al. 1996), but, even in the atmospheric window regions, the recorded spectra contain many telluric atmosphere absorption lines. Pure solar IR spectra were recorded by the ATMOS (Atmospheric Trace Molecule Spectroscopy) Fourier transform spectrometer (FTS) during four Space Shuttle missions (Farmer et al. 1989) in the 600–4800 cm^{-1} range at a resolution of 0.01 cm^{-1} ($R = \lambda/\Delta\lambda \sim 6 \times 10^4$–$5 \times 10^5$). A more recent program, the Atmospheric Chemistry Experiment with a space-borne FTS (ACE-FTS), has been performed on board a SCISAT-1 satellite (Hase et al. 2010). The ACE solar atlas covers the 700–4430 cm^{-1} frequency range at a resolution of 0.02 cm^{-1} ($R \sim 2 \times 10^4$–2×10^5).

The current space-born spectrographs performing IR studies of objects other than the Sun, have lower spectral resolutions. The *Spitzer* Space Telescope has a resolution of $R \sim 600$ in the $\lambda = 10$–37 micron range (Houck et al. 2004); the AKARI satellite (Murakami et al. 2007) is equipped with a Far-Infrared Surveyor (FTS with resolution $\Delta\nu = 0.19$ cm^{-1}) and a near- and mid-IR camera with a resolution of up to $\Delta\lambda = 0.0097$ microns ($R \sim 100$–1000). Nevertheless, the forthcoming spatial and airborne telescopes are expected to have a much higher resolution. For instance, the airborne Stratospheric Observatory For Infrared Astronomy (SOFIA) (Gehrz et al. 2009) is planned to be complemented with the Echelon-cross-Echelle Spectrograph (EXES) with a resolution of $R \sim 10^5$ in the wavelength region of 4.5 to 28.3 microns (Richter et al. 2010). The future SPace Infrared telescope for Cosmology and Astrophysics (SPICA) (Goicoechea et al. 2011) will carry a mid-IR, high resolution spectrometer (MIRHES) operating in the 4–18 micron range with a spectral resolution of $R \sim 3 \times 10^4$.

The great advantages of Fourier transform infrared spectroscopy (FTIR), such as its constant high resolution and energy throughput, have made the IR spectral region more accessible for laboratory spectral measurements (Nilsson 2009). Nevertheless, the powerful capacities of IR astronomy, including the existing VLT with CRyogenic Infra-Red Echelle Spectrograph, (CRIRES) and the future ground-based (e.g., E-ELT) or satellite-borne (e.g., Gaia, 0.33–1.05 micron range) IR telescopes, cannot be fully utilized without detailed spectroscopic information on atomic line features (in particular, wavelengths and oscillator strengths) in the IR region (Biémont 1994; Grevesse & Noels 1994; Pickering 1999; Jorissen 2004; Johansson 2005; Pickering et al. 2011).

A general drawback of the IR spectral region is the much lower number of atomic and ionic lines available (relative to the visible and ultraviolet ranges) (Ryde 2010). Modern laboratory spectral features are lacking for most elements with wavelengths longer than 1 micron (Wahlgren 2011). On the other hand, atlases of stellar spectra often provide only a short list of identified lines (Lobel 2011). Even in the solar IR atlas (Hase et al. 2010), there are a number of lines with doubtful or missing identifications.

New laboratory spectra may help us to identify spectral lines in IR and potentially discover new excited atomic levels. These levels are difficult to compute with high accuracy theoretically, hence they can be determined solely from IR lines (Wahlgren 2011). The inclusion of additional atomic lines and higher energy levels will increase the reliability of astrophysical calculations such as stellar atmosphere models. For instance, modern analyses of solar chemical compositions (Asplund et al. 2009) measure substantially lower metallicities than determined two decades ago. The use of high-resolution solar spectra (Hase et al. 2010) for the computation of the Sun's irradiance spectrum is still in its initial stage of development (Kurucz 2011).

The above-mentioned development of IR astronomy, together with the lack of high-resolution laboratory data for atomic spectral features, illustrates the importance of reporting new IR atomic lines, highly-excited levels, and oscillator strengths. For instance, the identification of IR atomic lines may be used for reliable temperature, gravity, and abundance analyses for a wide range of ultra-cool dwarfs, from M dwarf stars to brown dwarfs as well as extra-solar giant planets (Lyubchik et al. 2004). A comparison of these atomic lines with computed profiles can be used as key diagnostics of ultra-cool dwarf atmospheres (Lyubchik et al. 2007). Laboratory-measured manganese IR line features were used to determine the Mn abundance in the atmospheres of the Sun, Arcturus, and a dwarf (Blackwell-Whitehead et al. 2011). Together with the molecular IR bands, atomic (including K) IR lines provide good diagnostics for a self-consistent pure-infrared spectral classification scheme in most cases for both L and T dwarfs (McLean et al. 2003). The investigation of the gravity-sensitive features of atomic (including K) IR line features was used as a way to distinguish between young and old brown dwarfs (McGovern et al. 2004). Even without a direct application to the stellar atmosphere and abundance models, information on atomic spectral features is in constant demand from the astrophysical community (Raassen et al. 1998; Blackwell-Whitehead et al. 2005; Wallace & Hinkle 2007; Brown et al. 2009; Wallace & Hinkle 2009; Deb & Hibbert 2010; Thorne et al. 2011).

Parts of the spectra in the 800–1800 cm^{-1} (12.5–5.6 microns) range are difficult to observe from the ground owing to the heavy contamination of the spectrum by telluric absorption lines. This infrared spectrum represents a great challenge for laboratory observations of new, unknown infrared atomic transitions involving atomic levels with a high orbital momentum (Civiš et al. 2011b) and their comparison with the available stellar (e.g., solar) spectra. An attempt to fill this gap for K is made in the present paper.

After K spectrum measurements were made by Risberg (1956) in the 0.3101–1.1772 μm range a half of century ago, potassium IR lines were reported by Johansson & Svendenius (1972) who extended the measurements up to 3.735 μm and by Litzen (1970) who reported the 5g-levels of K from his measurement of 4.0169 μm line. In these hollow-cathode measurements, no lines with longer wavelengths were recorded, nor was emission from ng (with $n > 5$) or nh-levels observed. Here, we report the results of a FTIR spectroscopy study of K transitions in the following IR ranges: 1.4–2.5, 2.7–5.0, 5.9–9.1 and 11.1–14.3 microns.

2. Method

Time-resolved FTIR spectroscopy was applied to observing the emission arising after the irradiation of a potassium iodine (KI) target with a pulsed nanosecond ArF ($\lambda = 193$ nm) laser. A high-repetition-rate ArF laser ExciStar S-Industrial V2.0 1000 (193 nm, laser pulse width 12 ns, frequency 1 kHz) with 15 mJ pulse energy was focused on a rotating and linearly traversing target (CsI tablet) with a vacuum chamber (average pressure 10^{-1} Torr). The IR emission of the laser plume was measured

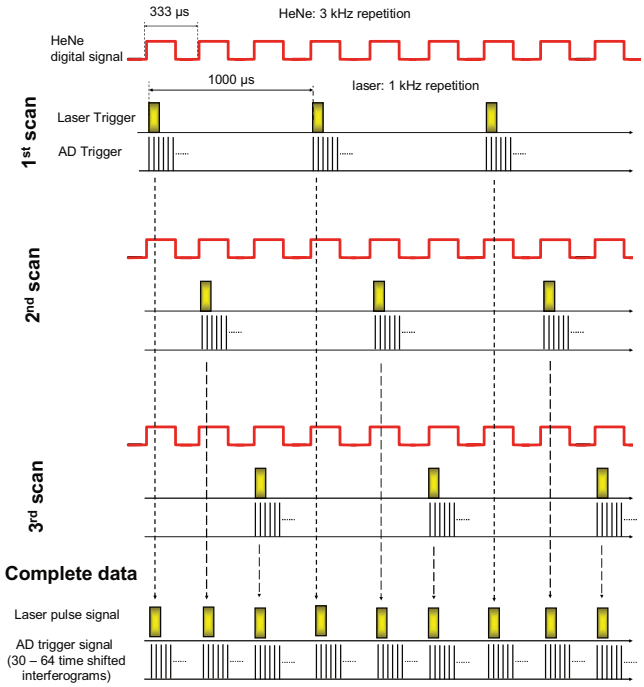

Fig. 1. Timing diagram for the interleaved sampling. During the scan, the laser pulse and the AD trigger sampling are induced with a rate of $1/n$ times of the He–Ne laser fringe frequency. The complete interferograms are obtained after n scans ($n = 3$ here).

in the probed area at an axial distance of $L = 9$ mm from the target. The emission from this area was focused into the spectrometer by CaF_2 (100 mm) or ZnSe (127 mm) lenses (for the 1600–7700 cm^{-1} or 800–1600 cm^{-1} spectral ranges, respectively). Two different detectors (MCT and InSb) and two beamsplitters (KBr and CaF_2) were used to cover the measured spectral range. The measurements were performed with a resolution of 0.017 cm^{-1}.

The continuous scanning method was used to measure the time-resolved FTIR spectra. After each ArF laser trigger point, several data points were sampled during the continual movement of the interferometer mirror. The synchronization of the laser ablation, which is the source of the emission, with the signal acquisition requires a special technique. In the case of the common time-resolved FT measurement, the time-shifted signals from a detector are sampled at each zero-crossing point of the HeNe laser fringes. A complication is that the repetition rate lasers suitable for ablation experiments is lower then the frequency of the HeNe laser fringes produced by the interferometer. Therefore, the laser pulse is triggered only in the chosen (every second, third, or fourth etc.) zero-cross point of the HeNe laser fringes. As a result, $1/n$ of each time-resolved interferogram is obtained after each scan Kawaguchi et al. (2005). The timing diagram is shown in Fig. 1, where the time sequence corresponds to the case of $n = 3$; several measurements were performed with the divider $n = 4$. An assembly of the n parts of the interferogram sampled at the same time after the laser pulse provides the complete interferogram. The output of this process is a set of time-resolved interferograms (30–64).

Our system was designed using a field programable gate array (FPGA) processor. The main role of the FPGA processor in our experiment was to initiate a laser pulse and AD trigger signals (the signal for data collection from the detector) synchronously with the He–Ne laser fringe signals from the spectrometer. The FPGA processor also controls the data transmission from the digital input board to the PC. The width of the ablation laser pulse, as well as the offset value between the beginning of the laser pulse and the data acquisition, can be preset.

In the present experiments, we used a 60 μs offset followed by the 30 AD trigger acquisition signals covering a 30 μs interval. The matrix of data signals corresponding to the AD triggers was stored and Fourier-transformed. The acquired interferograms were post-zerofilled using the OPUS Bruker program OPUS (2010) and subsequently corrected by subtracting the blackbody background spectrum. The wavenumbers, line widths, and their intensities were then obtained using the OPUS peak picking procedure. For more details of the experimental setup, we refer to our previous papers (Civiš et al. 2010a; Kawaguchi et al. 2008).

The use of the time-resolved scheme is essential because the emission intensities of the spectral lines depend on the time delay after the ArF laser pulse shot. The maxima of time profiles of the emission lines arise at different delay times $\tau \simeq 3$–10 μs, hence one should examine a wide time-domain range (0–30 μs) to avoid missing a line in the resulting spectra. The intensities reported in Table 1 below were obtained as the emission values at the time profile maxima. This non-monotonic decay of the emission intensity could be due to the complex population kinetics of the atomic K states in the ablation plasma.

Such a complex system was not solely used to excite the spectrum of a neutral atom. Although inexpensive potassium hollow cathode lamps are commercially available, they are apparatuses of quite moderate power used mostly with visible range optics. Their usage in the IR requires substantial modifications (e.g., IR optics and windows). We note that previous hollow-cathode studies of the K spectrum did not report many of the IR lines that are listed in this work. In addition, our scheme was designed to perform measurements of the IR spectra of several targets, not solely potassium (see our previous results, Civiš et al. 2010a; Civiš et al. 2010b, 2011b).

In this paper we record FTIR spectra in the five spectral ranges of 700–900, 1100–1700, 2000–3700, 4100–5000 and 5000–7000 cm^{-1} (11–14, 5.9–9.1, 2.7–5.0, 2.0–2.4 and 1.4–2.0 μm, respectively). An InSb detector was used for all spectral domains except the 700–900 and 1100–1700 cm^{-1} domain, where an MCT detector was used. All of the observed emission lines were classified as to transitions between $3p^6\, nl_j$ K levels with $n = 3...7$ and $l = 0...4$. No halogen (Cl, Br, F or I) lines were observed in the recorded emission spectra. The spectral resolution was either 0.1 cm^{-1} (four scans, higher signal-to-noise ratio (S/N)) or 0.017 cm^{-1} (one scan, lower S/N). The acquired interferograms were post-zerofilled (zero filling 2, trapezoid apodization function, for details see, e.g., the book by Stuart 2004) using Bruker OPUS software and subsequently corrected by subtracting the blackbody background spectrum.

The results of the line measurement and assignment are presented in Table 1. The wavenumbers, line widths, and their intensities (as well as the uncertainties in these quantities) were obtained by fitting a Lorentzian line shape.

To identify the observed lines, we assumed that, under LTE conditions and negligible self-absorption (optically thin plasma), the intensity of a spectral line due to radiative transition from the upper state $|k\rangle$ to the lower state $|i\rangle$ is proportional to the line strength S_{ik}, which is related to the oscillator strength f_{ik} according to $S_{ik} = \dfrac{3\hbar e^2 g_i}{2m_e\omega_{ik}} f_{ik}$ (Larsson 1983), where ω_{ik} is 2π multiplied by the transition frequency, g_i is the degeneracy factor of the lower level, and m_e and e are the electron mass and

Table 1. K lines and their identification.

Present work					Other measurements[a]		
Wavenumber (cm^{-1})	Wavelength (μm)	Intensity (arb. units)	S/N	HWHM (cm^{-1})	Identification	Laborat.	ACE [3][b]
729.694(8)	13.7006	1.41×10^4	5.32	0.057(26)	$4d_{\frac{3}{2}}$–$4f_{\frac{5}{2}}$		
730.755(6)	13.6807	1.10×10^4	5.04	0.048(37)	$4d_{\frac{5}{2}}$–$4f_{\frac{7}{2}}$		
795.575(16)	12.5661	5.98×10^3	3.34	0.049(60)	$7s_{\frac{1}{2}}$–$7p_{\frac{1}{2}}$		
800.081(12)	12.4953	1.15×10^4	5.38	0.047(32)	$7s_{\frac{1}{2}}$–$7p_{\frac{3}{2}}$		
809.189(12)	12.3547	2.15×10^4	4.33	0.107(39)	6g –7h		
884.125(11)	11.3075	1.63×10^4	4.62	0.073(38)	$5d_{\frac{3}{2}}$–$7p_{\frac{1}{2}}$		
889.117(8)	11.2441	2.55×10^4	7.70	0.075(22)	$5d_{\frac{5}{2}}$–$7p_{\frac{3}{2}}$		
1177.545(3)	8.489930	1.86×10^5	35.5	0.083(9)	$6p_{\frac{3}{2}}$–$5d_{\frac{5}{2}}$		NA / NA /.55
1178.041(13)	8.486355	1.66×10^4	2.97	0.066(57)	$6p_{\frac{3}{2}}$–$5d_{\frac{3}{2}}$		
1186.478(2)	8.426009	1.00×10^5	34.9	0.071(9)	$6p_{\frac{1}{2}}$–$5d_{\frac{3}{2}}$		
1266.577(4)	7.893144	6.16×10^4	17.6	0.073(11)	$6p_{\frac{3}{2}}$–$7s_{\frac{1}{2}}$		
1275.007(3)	7.840956	3.30×10^4	14.2	0.061(15)	$6p_{\frac{1}{2}}$–$7s_{\frac{1}{2}}$		
1343.699(4)	7.440114	1.61×10^5	16.1	0.136(13)	5g –6h		.702/.698/.703 (Mg I 6g ^{3}G–8h ^{3}H)
1352.873(5)	7.389662	5.34×10^4	8.72	0.106(17)	5f –6g		
1548.559(5)	6.455856	1.17×10^5	5.10	0.097(17)	$6s_{\frac{1}{2}}$–$6p_{\frac{1}{2}}$		.566/.561/.564 (CO 12–11)
1556.986(4)	6.420915	2.10×10^5	15.0	0.096(11)	$6s_{\frac{1}{2}}$–$6p_{\frac{3}{2}}$		.99/.986/ NA (unassigned)
1601.103(3)	6.243992	9.40×10^4	16.6	0.091(11)	$4d_{\frac{3}{2}}$–$6p_{\frac{1}{2}}$		
1609.533(12)	6.211289	1.60×10^4	2.60	0.083(54)	$4d_{\frac{3}{2}}$–$6p_{\frac{3}{2}}$		
1610.601(3)	6.207170	1.72×10^5	30.5	0.093(10)	$4d_{\frac{5}{2}}$–$6p_{\frac{3}{2}}$		
2057.382(8)	4.859221	8.97×10^2	3.79	0.078(24)	$4f_{\frac{7}{2}}$–$5d_{\frac{5}{2}}$		
2057.898(15)	4.858003	7.69×10^2	2.68	0.086(54)	$4f_{\frac{5}{2}}$–$5d_{\frac{3}{2}}$		
2489.439(3)	4.015874	5.40×10^4	7.92	0.111(8)	4f –5g	.462 [1]	.446/.438/.46
2676.927(4)	3.734608	1.11×10^5	4.16	0.126(12)	$5p_{\frac{3}{2}}$–$4d_{\frac{5}{2}}$	.938 [2]	.936/.928/.938
2678.012(10)	3.733095	8.23×10^3	2.88	0.105(34)	$5p_{\frac{3}{2}}$–$4d_{\frac{3}{2}}$	.008 [2]	.011/.003/.008
2696.757(3)	3.707147	6.08×10^4	4.23	0.123(11)	$5p_{\frac{1}{2}}$–$4d_{\frac{3}{2}}$	.765 [2]	.767/.759/.765
2730.542(3)	3.661278	2.87×10^4	5.09	0.118(10)	$5p_{\frac{3}{2}}$–$6s_{\frac{1}{2}}$	.554 [2]	.556/.548/.571
2749.299(3)	3.636299	1.43×10^4	6.01	0.115(11)	$5p_{\frac{1}{2}}$–$6s_{\frac{1}{2}}$	.309 [2]	.283/.274/.328
3164.389(4)	3.159306	3.38×10^4	5.07	0.118(11)	$3d_{\frac{3}{2}}$–$5p_{\frac{1}{2}}$	.396 [2]	.401/.392/.394
3183.135(4)	3.140700	6.32×10^3	4.11	0.112(14)	$3d_{\frac{3}{2}}$–$5p_{\frac{3}{2}}$	.153 [2]	.154/.144/.151
3185.455(3)	3.138413	6.34×10^4	5.00	0.118(10)	$3d_{\frac{5}{2}}$–$5p_{\frac{3}{2}}$	.461 [2]	.467/.458/.459
3208.542(7)	3.115831	5.11×10^3	3.36	0.104(21)	$4d_{\frac{3}{2}}$–$5f_{\frac{5}{2}}$		NA / NA /.583
3209.628(4)	3.114776	9.90×10^3	5.68	0.120(14)	$4d_{\frac{5}{2}}$–$5f_{\frac{7}{2}}$		NA / NA /.653
3674.823(7)	2.720477	1.03×10^3	6.10	0.088(20)	$5s_{\frac{1}{2}}$–$5p_{\frac{1}{2}}$	.827 [2]	.825/.814/.831
3693.570(4)	2.706669	5.37×10^3	5.20	0.107(12)	$5s_{\frac{1}{2}}$–$5p_{\frac{3}{2}}$	.585 [2]	.58 /.569/.586
4555.000(8)	2.194791	2.94×10^4	2.99	0.058(36)	$4d_{\frac{3}{2}}$–$6f_{\frac{5}{2}}$		
4556.057(11)	2.194281	5.55×10^4	3.83	0.095(38)	$4d_{\frac{5}{2}}$–$6f_{\frac{7}{2}}$		
6590.857(10)	1.516839	1.87×10^5	6.51	0.069(16)	$3d_{\frac{3}{2}}$–$4f_{\frac{5}{2}}$		
6593.169(3)	1.516307	2.39×10^5	8.89	0.069(9)	$3d_{\frac{5}{2}}$–$4f_{\frac{7}{2}}$		

Notes. Each of the five spectral ranges (700–900, 1100–1700, 2000–3700, 4100–5000, and 5000–7000 cm^{-1}) has its own scale of arbitrary units for the emission intensity. [(a)] Only the fractional part of the wavenumbers in cm^{-1}. [(b)] Data format: line list 1 (corrected)/line list 1 (observed)/line list 2 (see Hase et al. 2010, Sect. 4). NA means that the line is not listed in the corresponding line list.

References. [1] Johansson & Svendenius (1972); [2] Litzen (1970); [3] Hase et al. (2010).

charge, respectively. When LTE is fulfilled and self-absorption is negligible (or properly taken into account), the f-values can be determined from the laser-ablation plasma spectra if the temperature of the atom energy distribution is known (Manrique et al. 2011).

Since the atom concentration is low at the low pressures used in our experiment, we can consider our plasma to be optically thin. However, under the same conditions, some deviations from LTE conditions can occur, but the Boltzmann distribution of the atomic populations remains valid (Giacomo et al. 2001), though with different temperatures for electrons and atoms. This means that even if the observed line intensities display some deviations from the proportionality to the S-values, they should describe the qualitative picture of the relative line intensities adequately enough to assign the lines. A typical example of a Boltzmann plot for the ablation plasma can be found in Civiš et al. (2011a). The uncertainty in the excitation temperature is small enough to consider the Boltzmann population distribution to be a satisfactory approximation for our experiment. The moderate deviation of the Boltzmann plot's points away from the straight line

Table 2. Comparison of the QDT-calculated (this work) K oscillator strengths with other works.

Transition	ν (cm^{-1})	λ (μ)m	$\log(g_i f_{ik})$	f_{ik}	
$4s_{\frac{1}{2}}$–$10p_{\frac{3}{2}}$	33 411.3986	0.299211788	−10.8	1.00×10^{-5}	8.46×10^{-6} [1]
$4s_{\frac{1}{2}}$–$10p_{\frac{1}{2}}$	33 410.2306	0.299222249	−12.	3.22×10^{-6}	2.91×10^{-6} [1]
$4s_{\frac{1}{2}}$–$9p_{\frac{3}{2}}$	32 941.9262	0.303476190	−10.1	1.99×10^{-5}	1.86×10^{-5} [1]
$4s_{\frac{1}{2}}$–$9p_{\frac{1}{2}}$	32 940.203	0.30349207	−11.2	6.78×10^{-6}	6.6×10^{-6} [1]
$4s_{\frac{1}{2}}$–$8p_{\frac{3}{2}}$	32 230.11	0.3101789	−9.29	4.62×10^{-5}	4.68×10^{-5} [1]
$4s_{\frac{1}{2}}$–$8p_{\frac{1}{2}}$	32 227.44	0.3102046	−10.3	1.69×10^{-5}	1.76×10^{-5} [1]
$4s_{\frac{1}{2}}$–$7p_{\frac{3}{2}}$	31 074.4	0.321715	−8.21	1.36×10^{-4}	1.54×10^{-4} [1]
$4s_{\frac{1}{2}}$–$7p_{\frac{1}{2}}$	31 069.9	0.321762	−9.14	5.37×10^{-5}	6.18×10^{-5} [1]
$4s_{\frac{1}{2}}$–$6p_{\frac{3}{2}}$	29 007.71	0.3446372	−6.74	5.91×10^{-4}	5.92×10^{-4} [1]
$4s_{\frac{1}{2}}$–$6p_{\frac{1}{2}}$	28 999.27	0.3447375	−7.6	2.51×10^{-4}	2.58×10^{-4} [1]
$4s_{\frac{1}{2}}$–$5p_{\frac{3}{2}}$	24 720.139	0.40441422	−4.53	5.40×10^{-3}	5.69×10^{-3} [1]
$4s_{\frac{1}{2}}$–$5p_{\frac{1}{2}}$	24 701.382	0.40472132	−5.31	2.48×10^{-3}	2.63×10^{-3} [1]
$4p_{\frac{1}{2}}$–$9d_{\frac{3}{2}}$	20 586.9392	0.485609209	−5.92	1.34×10^{-3}	1.3×10^{-3} [2]
$4p_{\frac{3}{2}}$–$9d_{\frac{3}{2}}$	20 529.2289	0.486974338	−7.49	1.39×10^{-4}	1.2×10^{-4} [2]
$4p_{\frac{3}{2}}$–$9d_{\frac{5}{2}}$	20 529.1632	0.486975896	−5.29	1.26×10^{-3}	1.1×10^{-3} [2]
$4p_{\frac{1}{2}}$–$10s_{\frac{1}{2}}$	20 229.041	0.49420087	−6.26	9.52×10^{-4}	7.8×10^{-4} [2]
$4p_{\frac{1}{2}}$–$8d_{\frac{3}{2}}$	20 193.0467	0.495081800	−5.63	1.79×10^{-3}	1.6×10^{-3} [2]
$4p_{\frac{3}{2}}$–$10s_{\frac{1}{2}}$	20 171.3307	0.495614801	−5.58	9.47×10^{-4}	7.83×10^{-4} [2]
$4p_{\frac{3}{2}}$–$8d_{\frac{3}{2}}$	20 135.3364	0.496500783	−7.2	1.86×10^{-4}	1.7×10^{-4} [2]
$4p_{\frac{3}{2}}$–$8d_{\frac{5}{2}}$	20 135.2379	0.496503212	−5.	1.68×10^{-3}	1.4×10^{-3} [2]
$4p_{\frac{1}{2}}$–$9s_{\frac{1}{2}}$	19 663.1654	0.508423398	−5.79	1.53×10^{-3}	1.36×10^{-3} [2]
$4p_{\frac{1}{2}}$–$7d_{\frac{3}{2}}$	19 613.258	0.50971714	−5.35	2.38×10^{-3}	2.3×10^{-3} [2]
$4p_{\frac{3}{2}}$–$9s_{\frac{1}{2}}$	19 605.4551	0.509920004	−5.1	1.52×10^{-3}	1.4×10^{-3} [2]
$4p_{\frac{3}{2}}$–$7d_{\frac{3}{2}}$	19 555.5477	0.511221379	−6.92	2.48×10^{-4}	2.2×10^{-4} [2]
$4p_{\frac{3}{2}}$–$7d_{\frac{5}{2}}$	19 555.3921	0.511225447	−4.71	2.24×10^{-3}	2.1×10^{-3} [2]
$4p_{\frac{1}{2}}$–$8s_{\frac{1}{2}}$	18 780.191	0.53232786	−5.22	2.71×10^{-3}	2.7×10^{-3} [2]
$4p_{\frac{3}{2}}$–$8s_{\frac{1}{2}}$	18 722.4807	0.533968732	−4.53	2.70×10^{-3}	2.69×10^{-3} [2]
$4p_{\frac{1}{2}}$–$6d_{\frac{3}{2}}$	18 710.9804	0.534296928	−5.13	2.96×10^{-3}	3.4×10^{-3} [2]
$4p_{\frac{3}{2}}$–$6d_{\frac{3}{2}}$	18 653.2701	0.535949978	−6.69	3.10×10^{-4}	3.3×10^{-4} [2]
$4p_{\frac{3}{2}}$–$6d_{\frac{5}{2}}$	18 653.0045	0.535957610	−4.49	2.81×10^{-3}	3.0×10^{-3} [2]
$4p_{\frac{1}{2}}$–$7s_{\frac{1}{2}}$	17 289.063	0.57823999	−4.47	5.71×10^{-3}	6.17×10^{-3} [2]
$4p_{\frac{3}{2}}$–$7s_{\frac{1}{2}}$	17 231.3527	0.580176621	−3.78	5.68×10^{-3}	6.21×10^{-3} [2]
$4p_{\frac{1}{2}}$–$5d_{\frac{3}{2}}$	17 200.5619	0.581215207	−5.29	2.52×10^{-3}	2.8×10^{-3} [2]
$4p_{\frac{3}{2}}$–$5d_{\frac{3}{2}}$	17 142.8516	0.583171849	−6.82	2.72×10^{-4}	2.8×10^{-4} [2]
$4p_{\frac{3}{2}}$–$5d_{\frac{5}{2}}$	17 142.3479	0.583188985	−4.62	2.47×10^{-3}	2.4×10^{-3} [2]
$4p_{\frac{1}{2}}$–$6s_{\frac{1}{2}}$	14 465.5247	0.691108150	−3.38	1.71×10^{-2}	1.95×10^{-2} [2]
$4p_{\frac{1}{2}}$–$4d_{\frac{3}{2}}$	14 412.961	0.69362862	−7.08	4.19×10^{-4}	3.8×10^{-4} [2]
$4p_{\frac{3}{2}}$–$4d_{\frac{3}{2}}$	14 355.251	0.69641712	−9.04	2.96×10^{-5}	3.7×10^{-5} [2]
$4p_{\frac{3}{2}}$–$4d_{\frac{5}{2}}$	14 354.181	0.69646903	−6.88	2.56×10^{-4}	3.4×10^{-4} [2]
$4s_{\frac{1}{2}}$–$4p_{\frac{3}{2}}$	13 042.896027	0.76648991044	+0.162	5.88×10^{-1}	6.7×10^{-1} [3]
$4s_{\frac{1}{2}}$–$4p_{\frac{1}{2}}$	12 985.185724	0.76989645407	−0.534	2.93×10^{-1}	3.33×10^{-1} [3]
$4p_{\frac{1}{2}}$–$3d_{\frac{3}{2}}$	8551.802	1.169024	+0.536	8.55×10^{-1}	9.02×10^{-1} [2]
$4p_{\frac{3}{2}}$–$3d_{\frac{3}{2}}$	8494.092	1.176967	−1.07	8.54×10^{-2}	9.02×10^{-2} [2]
$4p_{\frac{3}{2}}$–$3d_{\frac{5}{2}}$	8491.784	1.177287	+1.12	7.69×10^{-1}	8.08×10^{-1} [2]
$4p_{\frac{1}{2}}$–$5s_{\frac{1}{2}}$	8041.365	1.243230	−1.07	1.71×10^{-1}	1.8×10^{-1} [2]
$4p_{\frac{3}{2}}$–$5s_{\frac{1}{2}}$	7983.655	1.252217	−0.374	1.72×10^{-1}	1.83×10^{-1} [2]

References. [1]: Shabanova & Khlyustalov (1985a,b); [2]: Villars (1952); [3]: Wang et al. (1997).

can be considered as evidence that S_{ik} values are calculated with enough accuracy (at least to confirm our line identifications).

Using K atomic-level energy data (Ralchenko et al. 2011, and references therein), we checked all of the transitions in the 700–7000 cm^{-1} range allowed by the electric dipole rules. In the cases of transitions with close wavenumbers, we chose those with greater line strength. For the calculation of the oscillator strengths, we used single-channel quantum defect theory (QDT), which has proved its efficiency for the calculation of first- (Alcheev et al. 2002) and second- (Chernov et al. 2005; Akindinova et al. 2009) order matrix elements in atoms and molecules. We tested our QDT technique by comparing the QDT calculations with the experimental oscillator strengths available at NIST (Ralchenko et al. 2011). The results of this comparison

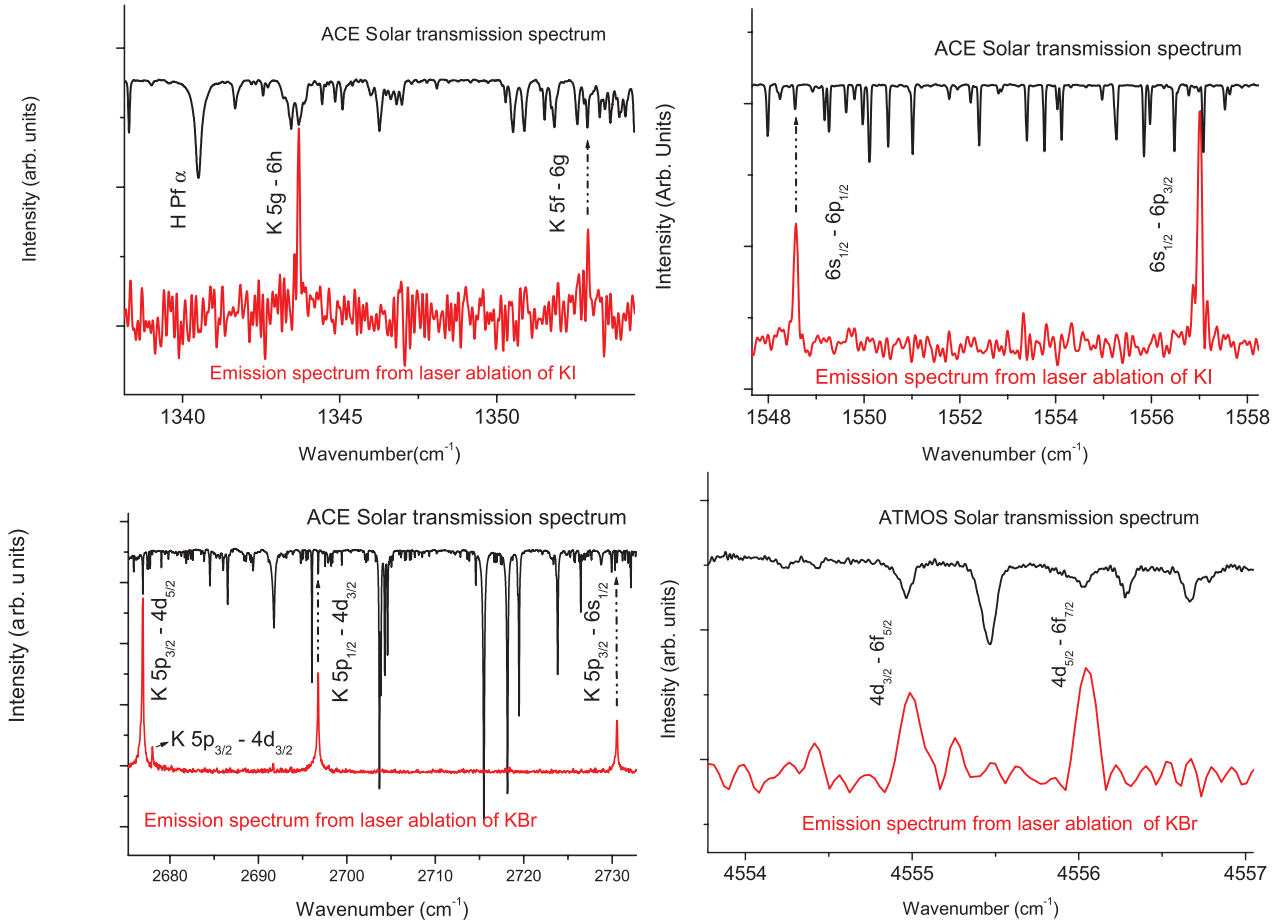

Fig. 2. K I emission spectra from the ablation plasma and the Solar spectra recorded from space-born spectrometers.

are presented in Table 2 with references to the original papers. For the majority of K transitions, the QDT calculations indicate that there is closer agreement with the experimental data of Ralchenko et al. (2011) than the Fues model potential used in our previous works (Civiš et al. 2010a; Civiš et al. 2010b, 2011c). There are a number of other (not listed in Table 2) transitions for which only theoretical f-values are available at NIST. These values were calculated (Anderson & Zilitis 1964) using the Coulomb approximation (CA), which is somewhat similar to the QDT and FMP techniques. Some of these CA f-values are closer to our FMP values than QDT calculations. We do not present these large data lists here, and give these CA values only for the transitions between the K levels observed in the present work, which are listed in Table 3. This table was used to classify the observed lines.

After classification, we refined the energy values for some levels involved in the assigned transitions. To this end, we applied a procedure similar to that used in our previous studies (Civiš et al. 2010b, 2011c,b). Table 4 presents some K revised energy values, E_i, and their uncertainties.

3. Results

The FTIR spectra of K were recorded in five spectral regions (700–900, 1100–1700, 2000–3700, 4100–5000, and 5000–7000 cm^{-1}). The measured emission lines are presented in Table 1 (with different intensity unit scales for different spectral regions). This table also contains the wavenumbers of some K lines in the above spectral regions measured both in the laboratories (Litzen 1970; Johansson & Svendenius 1972) and space (the ACE-FTS solar atlas described by Hase et al. 2010). The ACE-FTS spectral data actually represented as three data lists. The second data list (according to Hase et al. 2010) contains the set of wavenumbers and transitions specified in the graphic ACE atlas pages. A simple analysis shows that the K line wavenumbers encountered in the data list 2 are simply the Ritz wavenumbers obtained from the K level energies stored in the NIST database (Ralchenko et al. 2011). The first data list is presented in two variants: (a) the list of observed lines and (b) the corrected (by an empirical calibration factor of 1.00000294) version of the observed data; the correction was made to achieve closer agreement with the line positions specified in the second data list. All three variants (list 1 corrected, list 1 observed and list 2) are compared in Table 1 with the K lines observed in the present work.

We consider the ACE data list 1 (uncorrected) to be the most relevant to compare with our results since the above correction (by a calibration factor of 1.00000294) was performed in the ACE atlas (Hase et al. 2010) to aid the assignment of the spectral signatures in the ACE solar spectrum with the line positions given in current spectroscopic line-lists. The uncertainty in ACE peak picking is 0.001 cm^{-1}, which is better than those of our lines. At the same time, for a number of lines our uncertainties are better than those of the previous laboratory measurements, including the values of 0.005 cm^{-1} in Johansson & Svendenius (1972) and 0.01 cm^{-1} in Litzen (1970). Both of these previous laboratory measurements and our results coincide with ACE data within the corresponding uncertainties. However, our wavenumbers are generally closer to those of ACE compared to the wavenumbers from the previous measurements (Johansson & Svendenius 1972; Litzen 1970).

Some parts of the measured emission spectra in the vicinity of the most prominent lines are shown in Fig. 2 (upper red curve), together with the ACE-FTS or ATMOS solar transmission spectra (upper black curve) in the corresponding ranges. The majority of our emission peaks are lined up with the closest ACE features. As shown in Table 1, the majority of the line wavenumbers measured in the present work in the 2000–3700 cm^{-1} range are in good agreement (within 0.01 cm^{-1}) with the values from the non-corrected list 1 of ACE. The spectral regions (4100–5000 and 5000–7000 cm^{-1}) are not covered by the ACE atlas. In the 1100–1700 cm^{-1} range, the most prominent line observed in the present work is the 1343.699 cm^{-1} line. According to Table 3, this line should be the most prominent for all of the spectral ranges considered. The ACE data list 2 attributes its identification to the Mg I $6g^3G$–$8h^3H$ transition. This is probably incorrect since the ACE data list 2 identification is based only on a Ritz wavenumber obtained from the NIST database (Hase et al. 2010, Table 3). However, to our knowledge, there has been no report of a measured Mg I line near 1343.7 cm^{-1}. Moreover, our preliminary FTIR measurements in the laser ablation of magnesium salts do not show an Mg line at this position. Thus, we consider that the solar 1343.699 cm^{-1} line belongs to K I according to Table 1.

The revised energy values of the K I levels obtained from the present measurement are presented in Table 4. The majority of the energies coincide with the previously reported values within the uncertainty limits. Given the smaller (as compared to the previous measurements) uncertainty in our values for f-, g-, and 7p-level energies, the revised energy values can be considered as the recommended ones.

Table 3 presents the oscillator strengths for the transitions between the $3p^6$ states of K I observed in the present work. When possible, we also included in Table 3 the f-values from the NIST database (Ralchenko et al. 2011). All of these NIST f-values were calculated using a Coulomb approximation (Anderson & Zilitis 1964); thus, as one would expect, the majority of these f-values are in good (within 10% accuracy) agreement with our QDT calculations, which also use the wave functions with Coulomb asymptotics.

Some transitions listed in this table were not observed in our experiment, and we present them for completeness only. We note that the intensities that are measured are not strictly proportional to the line strengths because the coefficient of this proportionality depends on the upper state population, even for the equilibrium population distribution. For example, in the 1100–1700 cm^{-1} range, the largest line strength corresponds to the 1343.699 cm^{-1} line, while, in our laser-ablated plasma, the 1548.559, 1556.986, and 1610.601 cm^{-1} lines appear to be much more prominent. However, in the solar ACE spectra (Hase et al. 2010), the 1548.559 and 1556.986 cm^{-1} lines are very weak compared to the 1343.699 cm^{-1} line (and the 1610.601 cm^{-1} line does not appear at all in the ACE spectra). Obviously the f-values are insufficient for an accurate determination of the intensities of solar lines, which are also determined by the populations of the atomic and ionic states in the line-forming regions of the solar photosphere.

4. Conclusion

While current and future satellite-based spectrometers are and will be capable of recording the IR spectra of various objects in almost the full IR range, there are great difficulties in analyzing laboratory IR spectroscopy for wavelengths longer than 5 microns. To our knowledge, there are no laboratory measured spectra of metals above 5.5 microns. In the present work, we have reported the results of an FTIR spectroscopy study of K I transitions in the IR wavelength ranges, 1.4–2.5, 2.7–5.0, 5.9–9.1, and 11.1–14.3 microns. We list 38 IR lines of K I (at a resolution of 0.017 cm^{-1}), 25 of which had not been previously experimentally observed in a laboratory. The recorded wave numbers are in good agreement with the data from the ACE solar spectrum. We corrected the ACE identification of three lines (1343.699, 1548.559, and 1556.986 cm^{-1}). From the 809.189, 1352.873, and 1343.698 cm^{-1} lines, we report the energy values of the 7h, 6g, and 6h levels, which had not been observed for K I. We also update the energies of another 23 K I levels, most of which had been reported some decades ago. The f-values calculated assuming the quantum-defect theory approximation are presented for the transitions involving the reported K I levels. Some of these f-values have not been previously calculated, while the others are in good agreement with the f-values available from the NIST database.

Table 4. Revised energy values (cm^{-1}) of some levels of K I.

Level	Present work	Other sources
7h	32768.775(27)	
6h	31961.001(10)	
6g	31959.583(20)	
$6f_{\frac{7}{2}}$	31953.141(11)	31953.17(6) (Risberg 1956)
$6f_{\frac{5}{2}}$	31953.154(9)	31953.17(6) (Risberg 1956)
$8s_{\frac{1}{2}}$	31765.377(3)	31765.3767(30) (Thompson et al. 1983)
$7p_{\frac{3}{2}}$	31074.378(14)	31074.40(6) (Risberg 1956)
$7p_{\frac{1}{2}}$	31069.865(19)	31069.90(6) (Risberg 1956)
5g	30617.306(8)	30617.31(1) (Litzen 1970)
$5f_{\frac{7}{2}}$	30606.710(8)	30606.73(6) (Risberg 1956)
$5f_{\frac{5}{2}}$	30606.700(9)	30606.73(6) (Risberg 1956)
$7s_{\frac{1}{2}}$	30274.252(3)	30274.2487(30) (Thompson et al. 1983)
$5d_{\frac{3}{2}}$	30185.748(3)	30185.7476(30) (Thompson et al. 1983)
$5d_{\frac{5}{2}}$	30185.244(3)	30185.244(3) (Thompson et al. 1983)
$6p_{\frac{3}{2}}$	29007.685(3)	29007.71(5) (Risberg 1956)
$6p_{\frac{1}{2}}$	28999.262(4)	28999.27(5) (Risberg 1956)
$4f_{\frac{7}{2}}$	28127.855(4)	28127.85(5) (Risberg 1956)
$4f_{\frac{5}{2}}$	28127.865(4)	28127.85(5) (Risberg 1956)
$6s_{\frac{1}{2}}$	27450.701(2)	27450.7104(30) (Thompson et al. 1983)
$4d_{\frac{3}{2}}$	27398.152(4)	27398.147(5) (Johansson & Svendenius 1972)
$4d_{\frac{5}{2}}$	27397.079(3)	27397.077(5) (Johansson & Svendenius 1972)
$5p_{\frac{3}{2}}$	24720.142(3)	24720.139(5) (Johansson & Svendenius 1972)
$5p_{\frac{1}{2}}$	24701.390(3)	24701.382(5) (Johansson & Svendenius 1972)
$3d_{\frac{3}{2}}$	21536.997(4)	21536.988(5) (Johansson & Svendenius 1972)
$3d_{\frac{5}{2}}$	21534.683(4)	21534.680(5) (Johansson & Svendenius 1972)
$5s_{\frac{1}{2}}$	21026.560(4)	21026.551(5) (Johansson & Svendenius 1972)

Acknowledgements. This work was financially supported by the Grant Agency of the Academy of Sciences of the Czech Republic (grant No. IAA400400705), by the Ministry of Finance of the Czech Republic (Project ECPF:049/4V) and the Ministry of Education, Youth, and Sports of the Czech Republic (grant No. LM2010014).

References

Akindinova, E. V., Chernov, V. E., Kretinin, I. Y., & Zon, B. A. 2009, Phys. Rev. A, 79, 032506
Alcheev, P. G., Chernov, V. E., & Zon, B. A. 2002, J. Mol. Spectrosc., 211, 71
Anderson, E. M., & Zilitis, V. A. 1964, Opt. Spectrosk., 16, 177
Asplund, M., Grevesse, N., Sauval, A. J., & Scott, P. 2009, ARA&A, 47, 481

Biémont, E. 1994, in Infrared Solar Physics, ed. D. M. Rabin, J. T. Jefferies, & C. Lindsey, Int. Astron. Union (Dordrecht, The Netherlands: Kluwer Academic Publ.), 501, 154th Symposium of the International-Astronomical-Union, 1st International Meeting devoted to Infrared Physics, Tucson, AZ, Mar. 02–06, 1992, IAU Symp., 154,
Blackwell-Whitehead, R. J., Pickering, J. C., Pearse, O., & Nave, G. 2005, ApJS, 157, 402
Blackwell-Whitehead, R., Pavlenko, Y. V., Nave, G., et al. 2011, A&A, 525, A44
Brown, M. S., Federman, S. R., Irving, R. E., Cheng, S., & Curtis, L. J. 2009, ApJ, 702, 880
Chernov, V. E., Dorofeev, D. L., Kretinin, I. Y., & Zon, B. A. 2005, Phys. Rev. A, 71, 022505
Civiš, S., Matulková, I., Cihelka, J., et al. 2010a, Phys. Rev. A, 81, 012510
Civiš, S., Matulková, I., Cihelka, J., et al. 2010b, Phys. Rev. A, 82, 022502
Civiš, S., Kubelík, P., Jelínek, P., Chernov, V. E., & Knyazev, M. Y. 2011a, J. Phys. B, 44, 225006
Civiš, S., Matulková, I., Cihelka, J., et al. 2011b, J. Phys. B, 44, 105002
Civiš, S., Matulková, I., Cihelka, J., et al. 2011c, J. Phys. B, 44, 025002
Deb, N. C., & Hibbert, A. 2010, ApJ, 711, L104
Farmer, C. B., Norton, R. H., & Geller, M. 1989, NASA Reference Publication, 1224
Gehren, T., Butler, K., Mashonkina, L., Reetz, J., & Shi, J. 2001, A&A, 366, 981
Gehrz, R., Becklin, E., de Pater, I., et al. 2009, Adv. Space Res., 44, 413
Giacomo, A. D., Shakhatov, V., & Pascale, O. D. 2001, Spectrochimica Acta Part B: Atomic Spectroscopy, 56, 753, 1st International Conference on Laser-Induced Plasma Spectroscopy and Applications (LIBS 2000), Tirrenia, Italy, Oct. 08–12, 2000
Goicoechea, J. R., Nakagawa, T., & on behalf of the SAFARI/SPICA teams 2011, in Conditions and impact of star formation: New results with Herschel and beyond, The 5th Zermatt ISM Symposium (EDP Sciences)
Goldman, A., Blatherwick, R. D., Murcray, F. J., & Murcray, D. G. 1996, Appl. Opt., 35, 2821
Grevesse, N., & Noels, A. 1994, Phys. Scr., T51, 47
Hase, F., Wallace, L., McLeod, S. D., Harrison, J. J., & Bernath, P. F. 2010, J. Quant. Spec. Radiat. Transf., 111, 521
Houck, J. R., Roellig, T. L., van Cleve, J., et al. 2004, ApJS, 154, 18
Johansson, S. 2005, in High Resolution Infrared Spectroscopy In Astronomy, Proceedings, ed. H. U. Kaufl, R. Siebenmorgen, & A. Moorwood, ESO Astrophysics Symposia, ESO (Heidelberger Berlin, Germany: Springer–Verlag Berlin), 62, ESO Workshop on High Resolution Infrared Spectroscopy in Astronomy, Garching, Germany, Nov. 18–21, 2003
Johansson, I., & Svendenius, N. 1972, Phys. Scr., 5, 129
Jorissen, A. 2004, Phys. Scr., T112, 73
Kawaguchi, K., Hama, Y., & Nishida, S. 2005, J. Mol. Spectrosc., 232, 1
Kawaguchi, K., Sanechika, N., Nishimura, Y., et al. 2008, Chem. Phys. Lett., 463, 38
Kerber, F., Nave, G., Sansonetti, C. J., & Bristow, P. 2009, Phys. Scr., T134, 014007
Kurucz, R. L. 2011, Can. J. Phys., 89, 417
Larsson, M. 1983, A&A, 128, 291
Litzen, U. 1970, Phys. Scr., 1, 253
Lobel, A. 2011, Can. J. Phys., 89, 395
Lodders, K. 2003, ApJ, 591, 1220
Lyubchik, Y., Jones, H., Pavlenko, Y., et al. 2004, A&A, 416, 655
Lyubchik, Y., Jones, H. R. A., Pavlenko, Y. V., et al. 2007, A&A, 473, 257
Manrique, J., Aguilera, J., & Aragón, C. 2011, J. Quant. Spec. Radiat. Transf., 112, 85
McGovern, M. R., Kirkpatrick, J. D., McLean, I. S., et al. 2004, ApJ, 600, 1020
McLean, I., McGovern, M., Burgasser, A., et al. 2003, ApJ, 596, 561
Murakami, H., Baba, H., Barthel, P., et al. 2007, PASJ, 59, S369
Nilsson, H. 2009, Phys. Scr., T134, 014009
OPUS 2010, Opus Spectroscopy Software, http://www.brukeroptics.com/opus.html
Pickering, J. C. 1999, Phys. Scr., T83, 27
Pickering, J., Blackwell-Whitehead, R., Thorne, A., Ruffoni, M., & Holmes, C. 2011, Can. J. Phys., 89, 387
Raassen, A. J. J., Pickering, J. C., & Uylings, P. H. M. 1998, A&AS, 130, 541
Ralchenko, Y., Kramida, A., Reader, J., & NIST ASD Team 2011, NIST Atomic Spectra Database (version 4.1.0)
Richter, M. J., Ennico, K. A., McKelvey, M. E., & Seifahrt, A. 2010, Proc. SPIE, 7735, 77356Q
Risberg, P. 1956, Ark. Fys. (Stockholm), 10, 583
Ryde, N. 2010, Astron. Nachr., 331, 433
Shabanova, L. N., & Khlyustalov, A. N. 1985a, Opt. Spectrosk., 59, 207,
Shabanova, L. N., & Khlyustalov, A. N. 1985b, Opt. Spectrosc., 59, 123
Stuart, B. H. 2004, Infrared Spectroscopy: Fundamentals and Applications (Analytical Techniques in the Sciences (AnTs), 1st edn. (Wiley)
Sylwester, J., Sylwester, B., Phillips, K. J. H., & Kuznetsov, V. D. 2010, ApJ, 710, 804
Thompson, D. C., O'Sullivan, M. S., Stoicheff, B. P., & Xu, G. X. 1983, Can. J. Phys., 61, 949
Thorne, A. P., Pickering, J. C., & Semeniuk, J. 2011, ApJS, 192, 11
Villars, D. S. 1952, J. Opt. Soc. Am., 42, 552
Wahlgren, G. M. 2011, Can. J. Phys., 89, 345
Wallace, L., & Hinkle, K. 2007, ApJS, 169, 159
Wallace, L., & Hinkle, K. 2009, ApJ, 700, 720
Wallace, L., Livingston, W., Hinkle, K., & Bernath, P. 1996, ApJS, 106, 165
Wang, H., Li, J., Wang, X. T., et al. 1997, Phys. Rev. A, 55, R1569
Zhang, H. W., Butler, K., Gehren, T., Shi, J. R., & Zhao, G. 2006a, A&A, 453, 723
Zhang, H. W., Gehren, T., Butler, K., Shi, J. R., & Zhao, G. 2006b, A&A, 457, 645

Table 3. Calculated oscillator strengths, f_{ik}, for the transitions between the $3p^6$ states of K observed in the present work.

Transition	ν (cm^{-1})	λ (μ)m	$\log(g_i f_{ik})$ (QDT)	f_{ik}	
				QDT	NIST
$3d_{\frac{5}{2}}$–$6f_{\frac{5}{2}}$	10 418.47	959.571	−3.86	3.52×10^{-3}	3.3×10^{-3}
$3d_{\frac{5}{2}}$–$6f_{\frac{7}{2}}$	10 418.456	959.572	−0.863	7.03×10^{-2}	6.4×10^{-2}
$3d_{\frac{3}{2}}$–$6f_{\frac{5}{2}}$	10 416.157	959.784	−1.22	7.38×10^{-2}	6.8×10^{-2}
$5s_{\frac{1}{2}}$–$7p_{\frac{3}{2}}$	10 047.818	994.968	−4.94	3.57×10^{-3}	4.2×10^{-3}
$5s_{\frac{1}{2}}$–$7p_{\frac{1}{2}}$	10 043.305	995.415	−5.71	1.66×10^{-3}	2.1×10^{-3}
$3d_{\frac{5}{2}}$–$7p_{\frac{3}{2}}$	9539.695	1047.96	−4.26	2.35×10^{-3}	1.9×10^{-3}
$3d_{\frac{3}{2}}$–$7p_{\frac{3}{2}}$	9537.381	1048.22	−6.46	3.92×10^{-4}	3.1×10^{-4}
$3d_{\frac{3}{2}}$–$7p_{\frac{1}{2}}$	9532.868	1048.71	−4.86	1.93×10^{-3}	1.6×10^{-3}
$3d_{\frac{5}{2}}$–$5f_{\frac{7}{2}}$	9072.024	1101.99	+0.0545	1.76×10^{-1}	1.6×10^{-1}
$3d_{\frac{5}{2}}$–$5f_{\frac{5}{2}}$	9072.013	1101.99	−2.94	8.78×10^{-3}	8.0×10^{-3}
$3d_{\frac{3}{2}}$–$5f_{\frac{5}{2}}$	9069.7	1102.27	−0.307	1.84×10^{-1}	1.7×10^{-1}
$5s_{\frac{1}{2}}$–$6p_{\frac{3}{2}}$	7981.119	1252.61	−3.23	1.98×10^{-2}	2.1×10^{-2}
$5s_{\frac{1}{2}}$–$6p_{\frac{1}{2}}$	7972.695	1253.94	−3.97	9.42×10^{-3}	1.1×10^{-2}
$3d_{\frac{5}{2}}$–$6p_{\frac{3}{2}}$	7473.001	1337.78	−3.05	7.88×10^{-3}	6.6×10^{-3}
$3d_{\frac{3}{2}}$–$6p_{\frac{3}{2}}$	7470.688	1338.2	−5.25	1.31×10^{-3}	1.1×10^{-3}
$3d_{\frac{3}{2}}$–$6p_{\frac{1}{2}}$	7462.264	1339.71	−3.65	6.48×10^{-3}	5.5×10^{-3}
$5p_{\frac{1}{2}}$–$8s_{\frac{1}{2}}$	7063.987	1415.24	−4.04	8.84×10^{-3}	8.7×10^{-3}
$5p_{\frac{3}{2}}$–$8s_{\frac{1}{2}}$	7045.235	1419.01	−3.35	8.77×10^{-3}	8.8×10^{-3}
$3d_{\frac{5}{2}}$–$4f_{\frac{5}{2}}$	6593.18	1516.3	−1.45	3.92×10^{-2}	3.4×10^{-2}
$3d_{\frac{5}{2}}$–$4f_{\frac{7}{2}}$	6593.17	1516.31	+1.55	7.85×10^{-1}	6.9×10^{-1}
$3d_{\frac{3}{2}}$–$4f_{\frac{5}{2}}$	6590.867	1516.84	+1.19	8.24×10^{-1}	7.8×10^{-1}
$5p_{\frac{1}{2}}$–$7s_{\frac{1}{2}}$	5572.862	1793.92	−2.92	2.71×10^{-2}	2.7×10^{-2}
$5p_{\frac{3}{2}}$–$7s_{\frac{1}{2}}$	5554.11	1799.98	−2.23	2.70×10^{-2}	2.7×10^{-2}
$5p_{\frac{1}{2}}$–$5d_{\frac{3}{2}}$	5484.357	1822.87	−4.2	7.49×10^{-3}	7.8×10^{-3}
$5p_{\frac{3}{2}}$–$5d_{\frac{3}{2}}$	5465.605	1829.12	−5.9	6.83×10^{-4}	8.0×10^{-4}
$5p_{\frac{3}{2}}$–$5d_{\frac{5}{2}}$	5465.101	1829.29	−3.71	6.10×10^{-3}	7.1×10^{-3}
$4d_{\frac{5}{2}}$–$6f_{\frac{5}{2}}$	4556.075	2194.27	−3.22	6.65×10^{-3}	6.7×10^{-3}
$4d_{\frac{5}{2}}$–$6f_{\frac{7}{2}}$	4556.061	2194.28	−0.226	1.33×10^{-1}	1.3×10^{-1}
$4d_{\frac{3}{2}}$–$6f_{\frac{5}{2}}$	4555.001	2194.79	−0.58	1.40×10^{-1}	1.4×10^{-1}
$4f_{\frac{7}{2}}$–$6g_{\frac{9}{2}}$	3831.728	2609.08	+0.365	1.80×10^{-1}	
$4f_{\frac{7}{2}}$–$6g_{\frac{7}{2}}$	3831.728	2609.08	−3.19	5.15×10^{-3}	
$4f_{\frac{5}{2}}$–$6g_{\frac{7}{2}}$	3831.718	2609.08	+0.104	1.85×10^{-1}	
$5s_{\frac{1}{2}}$–$5p_{\frac{3}{2}}$	3693.577	2706.66	+0.669	9.76×10^{-1}	1.0
$4d_{\frac{5}{2}}$–$7p_{\frac{3}{2}}$	3677.299	2718.65	−2.09	2.06×10^{-2}	1.8×10^{-2}
$4d_{\frac{3}{2}}$–$7p_{\frac{3}{2}}$	3676.226	2719.44	−4.29	3.44×10^{-3}	3.1×10^{-3}
$5s_{\frac{1}{2}}$–$5p_{\frac{1}{2}}$	3674.825	2720.48	−0.0263	4.87×10^{-1}	5.0×10^{-1}
$4d_{\frac{3}{2}}$–$7p_{\frac{1}{2}}$	3671.713	2722.78	−2.69	1.70×10^{-2}	1.6×10^{-2}
$6s_{\frac{1}{2}}$–$7p_{\frac{3}{2}}$	3623.677	2758.88	−2.72	3.31×10^{-2}	
$6s_{\frac{1}{2}}$–$7p_{\frac{1}{2}}$	3619.164	2762.32	−3.45	1.59×10^{-2}	
$4d_{\frac{5}{2}}$–$5f_{\frac{7}{2}}$	3209.629	3114.78	+0.858	3.93×10^{-1}	3.9×10^{-1}
$4d_{\frac{5}{2}}$–$5f_{\frac{5}{2}}$	3209.618	3114.79	−2.14	1.97×10^{-2}	1.9×10^{-2}
$4d_{\frac{3}{2}}$–$5f_{\frac{5}{2}}$	3208.544	3115.83	+0.502	4.13×10^{-1}	4.2×10^{-1}
$3d_{\frac{5}{2}}$–$5p_{\frac{3}{2}}$	3185.459	3138.41	−0.0661	1.56×10^{-1}	1.4×10^{-1}
$3d_{\frac{3}{2}}$–$5p_{\frac{3}{2}}$	3183.146	3140.69	−2.26	2.61×10^{-2}	2.2×10^{-2}
$3d_{\frac{3}{2}}$–$5p_{\frac{1}{2}}$	3164.394	3159.3	−0.646	1.31×10^{-1}	1.1×10^{-1}
$6p_{\frac{1}{2}}$–$8s_{\frac{1}{2}}$	2766.115	3614.19	−2.62	3.65×10^{-2}	
$6p_{\frac{3}{2}}$–$8s_{\frac{1}{2}}$	2757.692	3625.23	−1.93	3.62×10^{-2}	
$5p_{\frac{1}{2}}$–$6s_{\frac{1}{2}}$	2749.309	3636.29	−0.462	3.15×10^{-1}	3.2×10^{-1}
$5p_{\frac{3}{2}}$–$6s_{\frac{1}{2}}$	2730.557	3661.26	+0.237	3.17×10^{-1}	3.2×10^{-1}
$5p_{\frac{1}{2}}$–$4d_{\frac{3}{2}}$	2696.762	3707.14	+0.892	1.22	1.2
$5p_{\frac{3}{2}}$–$4d_{\frac{3}{2}}$	2678.01	3733.1	−0.717	1.22×10^{-1}	1.2×10^{-1}
$5p_{\frac{3}{2}}$–$4d_{\frac{5}{2}}$	2676.936	3734.6	+1.47	1.09	1.1
$4f_{\frac{7}{2}}$–$5g_{\frac{7}{2}}$	2489.451	4015.85	−1.21	3.73×10^{-2}	
$4f_{\frac{7}{2}}$–$5g_{\frac{9}{2}}$	2489.451	4015.85	+2.34	1.30	

Table 3. continued.

Transition	ν (cm^{-1})	λ (μm)	$\log(g_i f_{ik})$ (QDT)	f_{ik}	
				QDT	NIST
$4f_{\frac{5}{2}}$–$5g_{\frac{7}{2}}$	2489.441	4015.87	+2.08	1.34	
$5g_{\frac{9}{2}}$–$7h_{\frac{9}{2}}$	2151.469	4646.72	−3.3	3.69×10^{-3}	
$5g_{\frac{9}{2}}$–$7h_{\frac{11}{2}}$	2151.469	4646.72	+0.688	1.99×10^{-1}	
$5g_{\frac{7}{2}}$–$7h_{\frac{9}{2}}$	2151.469	4646.72	+0.485	2.03×10^{-1}	
$4f_{\frac{5}{2}}$–$5d_{\frac{3}{2}}$	2057.884	4858.04	−1.07	5.69×10^{-2}	
$4f_{\frac{7}{2}}$–$5d_{\frac{5}{2}}$	2057.39	4859.2	−0.717	6.10×10^{-2}	
$4f_{\frac{5}{2}}$–$5d_{\frac{5}{2}}$	2057.38	4859.23	−3.71	4.07×10^{-3}	
$5d_{\frac{5}{2}}$–$6f_{\frac{5}{2}}$	1767.91	5654.85	−2.66	1.16×10^{-2}	
$5d_{\frac{5}{2}}$–$6f_{\frac{7}{2}}$	1767.896	5654.9	+0.331	2.32×10^{-1}	
$5d_{\frac{3}{2}}$–$6f_{\frac{5}{2}}$	1767.406	5656.47	−0.0243	2.44×10^{-1}	
$4d_{\frac{5}{2}}$–$6p_{\frac{3}{2}}$	1610.606	6207.15	+0.627	3.12×10^{-1}	3.0×10^{-1}
$4d_{\frac{3}{2}}$–$6p_{\frac{3}{2}}$	1609.532	6211.29	−1.57	5.21×10^{-2}	5.0×10^{-2}
$4d_{\frac{3}{2}}$–$6p_{\frac{1}{2}}$	1601.108	6243.97	+0.0431	2.61×10^{-1}	2.4×10^{-1}
$6s_{\frac{1}{2}}$–$6p_{\frac{3}{2}}$	1556.985	6420.92	+0.94	1.28	
$6s_{\frac{1}{2}}$–$6p_{\frac{1}{2}}$	1548.561	6455.85	+0.248	6.41×10^{-1}	
$5f_{\frac{5}{2}}$–$6g_{\frac{7}{2}}$	1352.883	7389.61	+1.95	1.17	
$5f_{\frac{7}{2}}$–$6g_{\frac{9}{2}}$	1352.873	7389.66	+2.21	1.14	
$5f_{\frac{7}{2}}$–$6g_{\frac{7}{2}}$	1352.873	7389.66	−1.35	3.25×10^{-2}	
$5g_{\frac{7}{2}}$–$6h_{\frac{9}{2}}$	1343.698	7440.12	+2.6	1.68	
$5g_{\frac{9}{2}}$–$6h_{\frac{11}{2}}$	1343.698	7440.12	+2.8	1.65	
$5g_{\frac{9}{2}}$–$6h_{\frac{9}{2}}$	1343.698	7440.12	−1.19	3.05×10^{-2}	
$5g_{\frac{7}{2}}$–$6f_{\frac{5}{2}}$	1335.849	7483.84	−2.77	7.85×10^{-3}	
$5g_{\frac{7}{2}}$–$6f_{\frac{7}{2}}$	1335.835	7483.91	−6.06	2.91×10^{-4}	
$5g_{\frac{9}{2}}$–$6f_{\frac{7}{2}}$	1335.835	7483.91	−2.51	8.14×10^{-3}	
$6p_{\frac{1}{2}}$–$7s_{\frac{1}{2}}$	1274.99	7841.06	−0.0965	4.54×10^{-1}	
$6p_{\frac{3}{2}}$–$7s_{\frac{1}{2}}$	1266.567	7893.21	+0.601	4.56×10^{-1}	
$6p_{\frac{1}{2}}$–$5d_{\frac{3}{2}}$	1186.487	8425.95	+1.12	1.53	
$6p_{\frac{3}{2}}$–$5d_{\frac{3}{2}}$	1178.063	8486.2	−0.491	1.53×10^{-1}	
$6p_{\frac{3}{2}}$–$5d_{\frac{5}{2}}$	1177.559	8489.83	+1.71	1.38	
$5d_{\frac{5}{2}}$–$7p_{\frac{3}{2}}$	889.134	11 243.8	+1.02	4.64×10^{-1}	
$5d_{\frac{3}{2}}$–$7p_{\frac{3}{2}}$	888.63	11 250.2	−1.17	7.74×10^{-2}	
$5d_{\frac{3}{2}}$–$7p_{\frac{1}{2}}$	884.117	11 307.6	+0.44	3.88×10^{-1}	
$6g_{\frac{9}{2}}$–$7h_{\frac{9}{2}}$	809.192	12 354.6	−1.3	2.72×10^{-2}	
$6g_{\frac{9}{2}}$–$7h_{\frac{11}{2}}$	809.192	12 354.6	+2.69	1.47	
$6g_{\frac{7}{2}}$–$7h_{\frac{9}{2}}$	809.192	12 354.6	+2.48	1.50	
$7s_{\frac{1}{2}}$–$7p_{\frac{3}{2}}$	800.126	12 494.6	+1.14	1.57	
$7s_{\frac{1}{2}}$–$7p_{\frac{1}{2}}$	795.613	12 565.5	+0.454	7.87×10^{-1}	
$4d_{\frac{5}{2}}$–$4f_{\frac{5}{2}}$	730.785	13 680.2	−2.25	1.76×10^{-2}	1.7×10^{-2}
$4d_{\frac{5}{2}}$–$4f_{\frac{7}{2}}$	730.775	13 680.4	+0.75	3.53×10^{-1}	3.3×10^{-1}
$4d_{\frac{3}{2}}$–$4f_{\frac{5}{2}}$	729.711	13 700.3	+0.392	3.70×10^{-1}	3.5×10^{-1}
$7p_{\frac{1}{2}}$–$8s_{\frac{1}{2}}$	695.512	14 374.0	+0.167	5.91×10^{-1}	
$7p_{\frac{3}{2}}$–$8s_{\frac{1}{2}}$	690.999	14 467.9	+0.864	5.93×10^{-1}	
$5d_{\frac{5}{2}}$–$5f_{\frac{7}{2}}$	421.464	23 720.4	+1.42	6.87×10^{-1}	
$5d_{\frac{5}{2}}$–$5f_{\frac{5}{2}}$	421.453	23 721.	−1.58	3.43×10^{-2}	
$5d_{\frac{3}{2}}$–$5f_{\frac{5}{2}}$	420.949	23 749.4	+1.06	7.20×10^{-1}	

Notes. The Ritz wavenumbers, ν, and air wavelengths, λ, are calculated using the energy values taken from the present measurement (see Table 4). The NIST f-values (last column) were calculated using a Coulomb approximation (Anderson & Zilitis 1964).

Laser ablation of CsI: time-resolved Fourier-transform infrared spectra of atomic cesium in the 800–8000 cm^{-1} range

Svatopluk Civiš,[1,*] Martin Ferus,[1] Petr Kubelík,[1] Petr Jelínek,[1] Vladislav E. Chernov,[1,2] and Mikhail Yu. Knyazev[2]

[1]*J. Heyrovský Institute of Physical Chemistry, Academy of Sciences of the Czech Republic, Dolejškova 3, 18223 Prague 8, Czech Republic*
[2]*Voronezh State University, 394693 Voronezh, Russia*
**Corresponding author: civis@jh-inst.cas.cz*

Received December 8, 2011; revised January 31, 2012; accepted February 8, 2012; posted February 8, 2012 (Doc. ID 159481); published April 30, 2012

Fourier-transform time-resolved spectroscopy of laser-induced breakdown of Cs vapor in a vacuum has been used for the measurement of atomic Cs emission spectra in the 800–8000 cm^{-1} range with a resolution of 0.02 cm^{-1}. The 6*h* and 7*h* levels of Cs are observed. The dipole transition matrix elements (transition probabilities, oscillator, and line strengths) between the observed levels are calculated using quantum defect theory. © 2012 Optical Society of America

OCIS codes: 300.6210, 300.6300, 300.6340, 020.4900.

1. INTRODUCTION

The spectrum of neutral Cs atom has become one of the most important and well studied [1] due to a number of modern atomic physics experiments involving atomic cesium, such as the cooling and trapping of atoms, ultracold atom collisions and the formation of cold molecules, and evidence for effects of quantum electrodynamics and parity nonconservation, not to mention the atomic Cs frequency standard.

The most complete compilation of Cs levels available in the literature [1] includes the states with orbital angular momentum $l \le 4$, but it lacks the levels with higher angular momenta. Such high-l states are of interest for various problems of atomic and molecular physics [2], such as the excitation and decay of autoionizing states [3,4] or the extraction of multipole moments and/or polarizabilities of ions from the high-l Rydberg electron spectra of corresponding neutral atoms [5] obtained using precise microwave [6] or optical [7] measurements of high-l states.

Unlike the high-excited Rydberg levels, the low-excited high-l states (for example, the nh series begins with the principal quantum number $n = 6$) can be observed only in the infrared (IR) spectral range. Indeed, nh states are linked by dipole transitions to $n'g$ states, and the transition energy for the minimal $n' = 5$ is about 1330 cm^{-1} ($n = 6$) and 810 cm^{-1} ($n = 7$). This estimate is given according to the Rydberg formula with zero quantum defects (the outer electron's interaction with the atomic core is weak in high-l states, so these states have small quantum defects decreasing with l [5]). The transitions between higher n, n' lie below 600 cm^{-1}.

The transitions in the spectral ranges mentioned above can be observed by analyzing the light spectrum emitted from a plasma created on the sample surface by laser radiation. The corresponding technique, laser-induced breakdown spectroscopy (LIBS), is a versatile and sensitive probe for the detection and identification of trace substances. LIBS has many practical advantages over the conventional methods of chemical analysis of elements and is consequently being considered for a growing number of applications [8–12].

In this work LIBS is used together with time-resolved Fourier-transform infrared (FTIR) spectroscopy for recording Cs emission spectra in the 800–8000 cm^{-1} range. From these spectra one can extract the energies of some Cs levels involved in the observed transitions. Although most of these energies are available in literature with very good accuracy, our energy values for $7p_{\frac{3}{2}}$ and $8p_{\frac{3}{2}}$ levels have smaller uncertainties.

A part of the above mentioned spectral region (the 1200–1600 cm^{-1} range) has been measured for Cs in our recent work [13] reporting the 6*h* Cs level energy that was previously unknown. In this paper we have extended the measured range to cover the 800–1200 cm^{-1} spectral region and determine the 7*h* Cs level energy. No experimental measurement of Cs IR lines the 800–2500 cm^{-1} range is reported in literature or NIST database [14]. To our knowledge, no alkali atom lines have been experimentally measured in the 800–1600 cm^{-1} range previously due to several problems. First, the HgCdTe (MCT) detectors used in this range are not always characterized by sensitivity and/or sufficient signal-to-noise ratio (SNR). Second, the background blackbody radiation inside the spectrometer chamber (at laboratory temperature) decreases readability of the spectra recorded in this domain. Third, as mentioned above, the spectral lines in this spectral region are due to transition from high-excited states and their complex population dynamics requires using the time-resolution technique for reliable recording of the emission spectra (see our earlier works [15–17]). This work attempts to fill this gap. In addition to our recent work [13] (where we have observed seven Cs lines not reported previously), we report here 15 new Cs lines in the 800–1200 and 1600–2500 cm^{-1} ranges. We also present the dipole transition matrix elements (transition

0740-3224/12/051112-07$15.00/0 © 2012 Optical Society of America

probabilities, oscillator and line strengths) between the observed levels calculated using quantum defect theory (QDT).

2. METHODS

A. Experimental

The sketch of the experimental setup is presented in Fig. 1. Time-resolved FTIR spectroscopy was applied for observation of the emission arising after the irradiation of a CsI target with a pulsed nanosecond ArF ($\lambda = 193$ nm) laser. A high repetition rate ArF laser ExciStar *S*-Industrial V2.0 1000 (193 nm, laser pulse width 12 ns, frequency 1 kHz) with 15 mJ pulse energy was focused on a rotating and linearly traversing target (CsI tablet) inside a vacuum chamber (average pressure 10^{-1} Torr). The IR emission of the laser plume was measured in the probed area at axial distance L ranging from 1 to 9 mm from the target. The emission from this area was focused into the spectrometer by CaF_2 (100 mm) or ZnSe (127 mm) lenses (for 1600–7700 cm^{-1} or 800–1600 cm^{-1} spectral range, respectively). Two different detectors (MCT and InSb) and two beamsplitters (KBr and CaF_2) were used to cover the whole measured spectral range. The measurements were carried out with a resolution of 0.02 cm^{-1} for five values of the distance L: 1, 3, 5, 7, and 9 mm. The emission was observed in seven spectral ranges: 800–1000, 1000–1300, 1200–1600, 1600–2000, 2000–3500, 4100–5000, and 5000–7700 cm^{-1}.

The continuous scanning method was used for the measurement of the time-resolved FTIR spectra. After each ArF laser trigger point, several data points were sampled during the continual movement of the interferometer mirror. The synchronization of the laser ablation, which is the source of the emission, with the signal acquisition requires a special technique. In the case of the common time-resolved FT measurement, the time shifted signals from a detector are sampled at each zero-crossing point of HeNe laser fringes. A complication comes from the fact that the repetition rate of the lasers suitable for ablation experiments is lower then the frequency of the HeNe laser fringes produced by the interferometer. Therefore the laser pulse is triggered only in the chosen (every second, third, or fourth, etc.) zero-cross point of the HeNe laser fringes. As a result $1/n$ of each time-resolved interferogram is obtained after each scan [18]. The timing diagram is shown in Fig. 2, where the time sequence corresponds to the case of $n = 3$; several measurements were carried out with the divider $n = 4$. An assembly of the n parts of the interferogram sampled at the same time after the laser pulse provides the complete interferogram. The output of this process is a set of time-resolved interferograms (30–64).

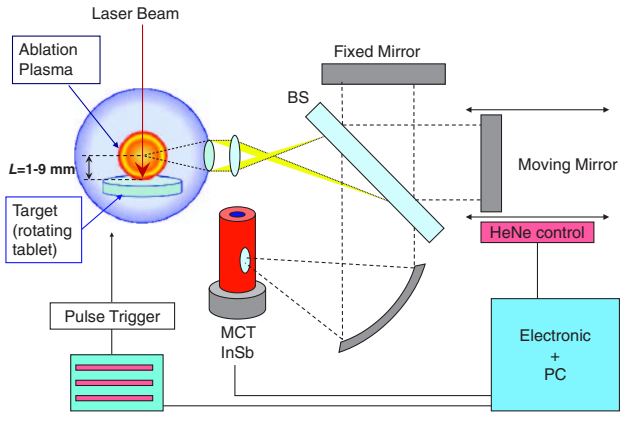

Fig. 1. (Color online) Experimental setup for LIBS.

Our system was designed using a field programmable gate array (FPGA) processor. The main role of the FPGA processor in our experiment was to initiate a laser pulse and analog-digital (AD) trigger signals (the signal for data collection from the detector) synchronously with the HeNe laser fringe signals from the spectrometer. The FPGA processor also controls the data transmission from the digital input board to the PC. The width of the ablation laser pulse can be preset, as well as the offset value between the beginning of the laser pulse and the data acquisition.

In the present experiments we used a 60 μs offset followed by the 30 AD trigger acquisition signals covering a 30 μs interval. The matrix of data signals corresponding to the AD triggers is stored and Fourier-transformed. The acquired interferograms were postzero filled using the OPUS Bruker program [19] and subsequently corrected by subtracting the blackbody background spectrum. The wavenumbers, line widths, and their intensities were then obtained using the OPUS peak picking procedure.

B. Line Identification and Dipole Transition Matrix Elements

To record Cs spectra we studied the plasma formed by a laser ablation of the cesium iodide CsI. To ensure that our plasma spectra contained only Cs lines, we made a control measurement with a cesium bromide (CsBr) target, which did not result in appearing or disappearing of the spectral lines as compared to the case of CsI. However, the SNR achieved for the CsI target was better, so we report only the results of CsI ablation. We do not expect any emissions from the halogen atoms for the following reason. The Cs levels from which the emission was registered have excitation energies not higher than ~30000 cm^{-1}, while the lowest excited levels (those from which dipole radiative transitions are possible) of the halogen atoms have much higher energies [14]: ~64000 cm^{-1} ($4s^2 4p^4 (^3P_2) 5s$ (^2P) levels of Br) and ~56000 cm^{-1} ($5s^2 5p^4 (^3P_2) 6s$ (^{2}[2]) levels of I). So these halogen atoms' levels should be much less populated as compared to the Cs levels so that no emission lines of I or Br are expected in our ablation plasma spectra.

All the lines observed are classified as belonging to transitions between the neutral Cs $(5p^6) nl_j$ atom states. The transition between the states with the orbital angular momentum $l < 5$ is easily identified using the available Cs level list [1,14]. However, since the $(5p^6) 6h$ ($l = 5$) level has not been observed previously, at first approximation we assumed it to have very small quantum defect $\mu \simeq 0.01$ and used the Rydberg formula:

$$E(nl_j) = V_{\text{ion}} - \frac{Z^2 \mathcal{R}_{\text{Cs}}}{n^{*2}} = V_{\text{ion}} - \frac{Z^2 \mathcal{R}_{\text{Cs}}}{(n - \mu_{lj})^2}, \qquad (1)$$

where $V_{\text{ion}} = 31406.46766$ cm^{-1} [1] stands for the ionization potential of the Cs atom whose $(5p^6)$ core's charge is $Z = 1$; $\mathcal{R}_{\text{Cs}} = 109736.86254$ cm^{-1} [1] is the mass-corrected Rydberg constant for Cs.

However, this first approximation can have an error of order of tens of cm^{-1}. The only transition possible from the $6h$ level can be to the $5g$ level, and the only line appearing in the corresponding spectral region is the 1348.359 cm^{-1} line.

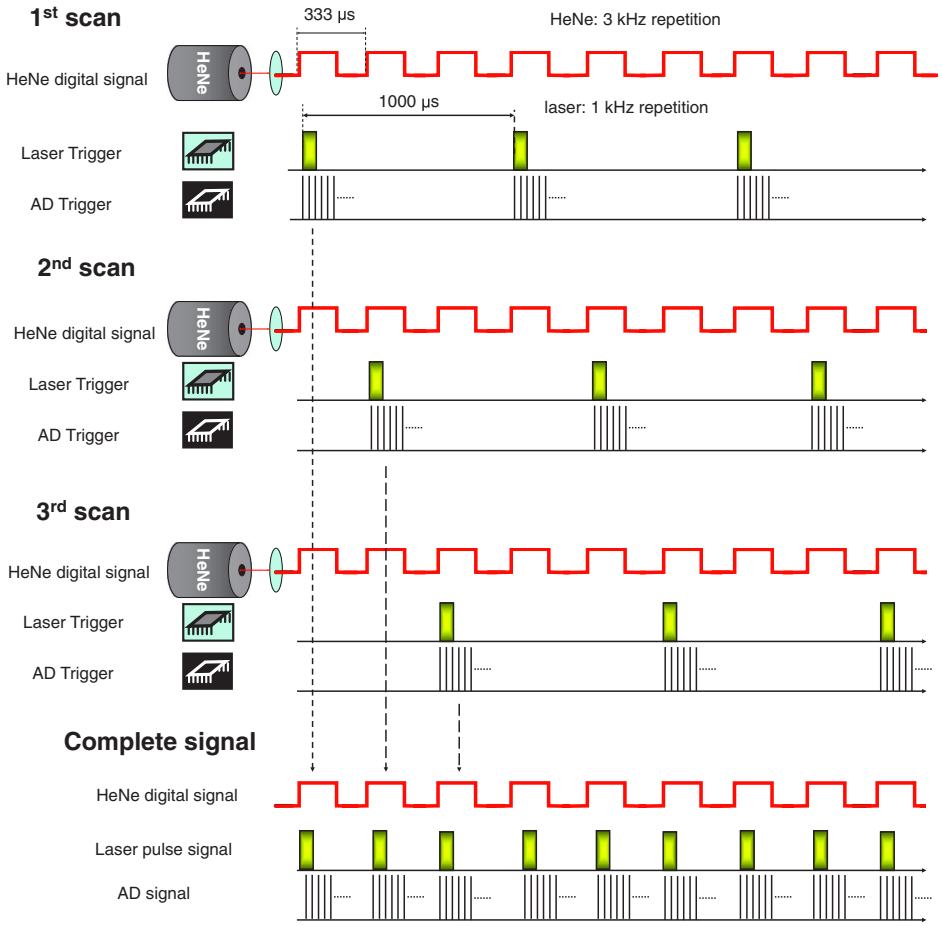

Fig. 2. (Color online) Timing diagram for the interleaved sampling. During the scan, the laser pulse and the analog-digital (AD) trigger sampling are induced with a rate of $1/n$ times of the HeNe laser fringe frequency. The complete interferograms are obtained after n scans ($n = 3$ here).

To ensure this line is indeed due to the $5g$ – $6h$ transition, we estimate its relative intensity. The same considerations apply to the $6g$–$7h$ transition.

For an optically thin plasma at local thermal equilibrium (LTE), the emission transition from an upper state k to a lower state i has the intensity I_{ki} proportional to the transition probability A_{ki} and to the transition wavenumber ν_{ki}:

$$I_{ki} \sim g_k A_{ki} \nu_{ki} \exp\left(-\frac{E_k}{k_B T}\right), \tag{2}$$

where k_B is the Boltzmann constant, T is the excitation temperature, and E_k and g_k are the energy and the degeneracy factor of the upper state, respectively.

Since at the low pressures used in our experiment, the atom concentration is low, we can consider our plasma to be optically thin. However, in the same conditions, some deviations from LTE conditions can occur [20], but the Boltzmann distribution of the atomic populations remains valid [21], although with different temperatures of electrons and atoms [20]. This means that even if the observed line intensities display some deviations from the proportionality to the A-values, they should describe the qualitative picture of the relative line intensities well enough to assign the lines.

The Boltzmann plot made according to Eq. (2) is presented in Fig. 3, displaying a typical example of calculating the excitation temperature from tour data (e.g., for the 2000–3500 cm^{-1} range). The linear fitting gives the plasma temperature $T = 2250 \pm 560$ K. The uncertainty of T is small enough to consider the Boltzmann population distribution [Eq. (2)] to be valid for our experiment. The moderate distortion of the Boltzmann plot from the straight line can be considered as an evidence that A_{ik} values are calculated with enough accuracy (at least to confirm our line identifications).

The investigation of atomic emission in our LIBS experiment is complicated by nonequilibrium and nonstationary conditions of the plasma for the excited states [12]. In particular, the emission intensities of the spectral lines show a

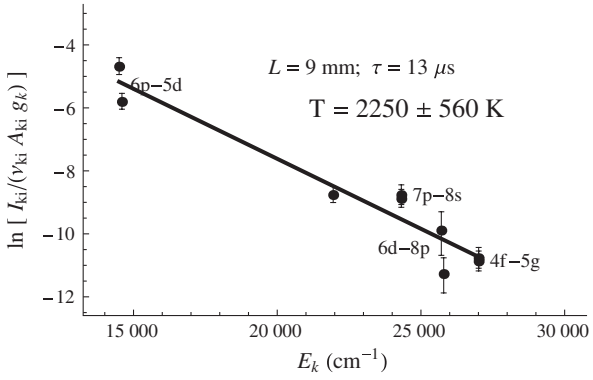

Fig. 3. Boltzmann plot of the ablation plasma.

complex dependence on the time delay τ after the ArF laser pulse shot (see Fig. 5 below). So the use of the time-resolved scheme is essential in our experiment. For analyzing the excitation temperature, there is no good substitute for calculating T separately for each distance L between the probed area and the target surface and delay time τ after the laser shot. We cannot identify any dependence that could simplify such an analysis. There are hints in the data at some rich dynamics in the plasma that cause T to evolve in some complex way as a function of time and location, but the uncertainties in T as measured (300…600 K) are too great to explore those dynamics in detail.

The dipole matrix elements required for knowledge of A_{ki} were calculated using single-channel QDT [22–24]. This technique is quite similar to the Fues model potential (FMP) method used in our previous papers (see, e.g., [16]) with the radial wavefunction of nl_j state given in terms of Whittaker functions by

$$R_{nlj}(r) = \frac{Z^{1/2}}{r\,n^*}\left[\frac{\Xi_l(E(nl_j))}{\Pi_l(n^*)}\right]^{1/2} W_{n^*,l+1/2}\left(\frac{2Zr}{n^*}\right) \times \left[\Gamma(l+1+n^*)\Gamma(n^*-l)\left(1+\frac{\partial\mu_{lj}(n^*)}{\partial n^*}\right)\right]^{-1/2}, \quad (3)$$

where the effective principal quantum number n^* is connected to the energy level $E(nl_j)$ and quantum defect μ_{lj} via the Rydberg formula [Eq. (1)]. The functions $\Xi_l(E(nl_j))$ and $\Pi_l(n^*)$ in Eq. (3) are connected with an interpolation of the quantum defect function $\mu_{lj}(n^*)$ [24]. The core polarization effects were taken into account according to [25].

The adequacy of the QDT approximation was tested by comparison the dipole matrix elements for 6*s*–*np* transitions with the values from the NIST database [14] and with *ab initio* Dirac–Hartree–Fock calculations [26]. The results are presented in Table 1, where the line strengths (*S*-values) are listed; these *S*-values are the squared reduced dipole matrix elements given in [26]. The maximal discrepancy between our and NIST values was about 25% for 6*s*–6*p* transitions; for transitions involving higher principal quantum numbers, the discrepancy is considerably lower. This comparison shows the QDT technique to be adequate for the calculation of matrix elements of the transition between the levels observed in the present experiment

3. RESULTS AND DISCUSSION

A part of the recorded Cs emission spectrum is shown in Fig. 4 without subtraction of the background blackbody radiation signal component. The list of the observed lines with their parameters and identification is presented in Table 2. Since the measurements were done in seven spectral ranges, 800–1000, 1000–1300, 1200–1600, 1600–2000, 2000–3500, 4100–5000, and 5000–7700 cm^{-1}, intensity values have the same scale only for lines within the same range of wavenumbers. All the uncertainties in the tables below are given in round brackets after the corresponding values and should be treated as their rightmost significant digits; e.g., 123.4(56) means 123.4 ± 5.6.

As mentioned above, the intensities of the emission lines display a complex nonmonotonic behavior as functions of the time delay τ after the ArF laser pulse shot. These dependencies, or the time profiles of the emission lines, have

Table 1. Comparison of QDT-Calculated *S*-Values of Cs (this work) with the Experimental and *ab initio* Dirac–Hartree–Fock (DHF) Calculation Results Listed In [26] and the NIST Database [14] (for the 6*s* – *np* and 6*p* – 5*d* transitions)

np_j level	$6s_{\frac{1}{2}} - np_j$			$8s_{\frac{1}{2}} - np_j$	
	This work	DHF [26]	NIST [14]	This work	DHF [26]
$6p_{\frac{1}{2}}$	1.655×10^{1}	2.015×10^{1}	2.023×10^{1}	9.711×10^{-1}	1.055×10^{0}
$6p_{\frac{3}{2}}$	3.301×10^{1}	3.999×10^{1}	4.009×10^{1}	1.963×10^{0}	2.137×10^{0}
$7p_{\frac{1}{2}}$	6.829×10^{-2}	7.618×10^{-2}	7.59×10^{-2}	8.375×10^{1}	8.558×10^{1}
$7p_{\frac{3}{2}}$	2.981×10^{-1}	3.434×10^{-1}	3.44×10^{-1}	1.911×10^{2}	1.96×10^{2}
$8p_{\frac{1}{2}}$	5.467×10^{-3}	6.561×10^{-3}	5.22×10^{-3}	3.098×10^{2}	3.136×10^{2}
$8p_{\frac{3}{2}}$	4.271×10^{-2}	4.752×10^{-2}	4.44×10^{-2}	5.915×10^{2}	5.983×10^{2}
$9p_{\frac{1}{2}}$	9.662×10^{-4}	1.849×10^{-3}	1.04×10^{-3}	3.002×10^{0}	3.038×10^{0}
$9p_{\frac{3}{2}}$	1.284×10^{-2}	1.613×10^{-2}	1.33×10^{-2}	8.693×10^{0}	8.815×10^{0}
$10p_{\frac{1}{2}}$	2.522×10^{-4}	2.209×10^{-3}	2.64×10^{-4}	4.465×10^{-1}	4.02×10^{-1}
$10p_{\frac{3}{2}}$	5.455×10^{-3}	1.3×10^{-2}	5.21×10^{-3}	1.513×10^{0}	1.341×10^{0}
$11p_{\frac{1}{2}}$	8.352×10^{-5}	1.156×10^{-3}	9.16×10^{-5}	1.388×10^{-1}	1.211×10^{-1}
$11p_{\frac{3}{2}}$	2.825×10^{-3}	7.225×10^{-3}	2.8×10^{-3}	5.166×10^{-1}	4.449×10^{-1}
$12p_{\frac{1}{2}}$	3.254×10^{-5}	6.76×10^{-4}	3.93×10^{-5}	6.065×10^{-2}	5.198×10^{-2}
$12p_{\frac{3}{2}}$	1.66×10^{-3}	4.489×10^{-3}	1.59×10^{-3}	2.404×10^{-1}	2.034×10^{-1}
$13p_{\frac{1}{2}}$	1.429×10^{-5}	4.41×10^{-4}	1.79×10^{-5}	3.212×10^{-2}	2.723×10^{-2}
$13p_{\frac{3}{2}}$	1.063×10^{-3}	3.025×10^{-3}	1.04×10^{-3}	1.331×10^{-1}	1.116×10^{-1}
$14p_{\frac{1}{2}}$	6.881×10^{-6}	2.89×10^{-4}	8.86×10^{-6}	1.923×10^{-2}	1.613×10^{-2}
$14p_{\frac{3}{2}}$	7.256×10^{-4}	2.116×10^{-3}	6.28×10^{-4}	8.239×10^{-2}	6.864×10^{-2}
$15p_{\frac{1}{2}}$	3.564×10^{-6}	2.25×10^{-4}	3.4×10^{-6}	1.252×10^{-2}	1.04×10^{-2}
$15p_{\frac{3}{2}}$	5.185×10^{-4}	1.521×10^{-3}	3.9×10^{-4}	5.498×10^{-2}	4.537×10^{-2}

$6p_j$ level	$6p_j - 5d_{\frac{3}{2}}$		$6p_j - 5d_{\frac{5}{2}}$	
	This work	NIST [14]	This work	NIST [14]
$6p_{\frac{1}{2}}$	4.88×10^{1}	4.92×10^{1}		
$6p_{\frac{3}{2}}$	1.00×10^{1}	9.97	9.21×10^{1}	9.84×10^{1}

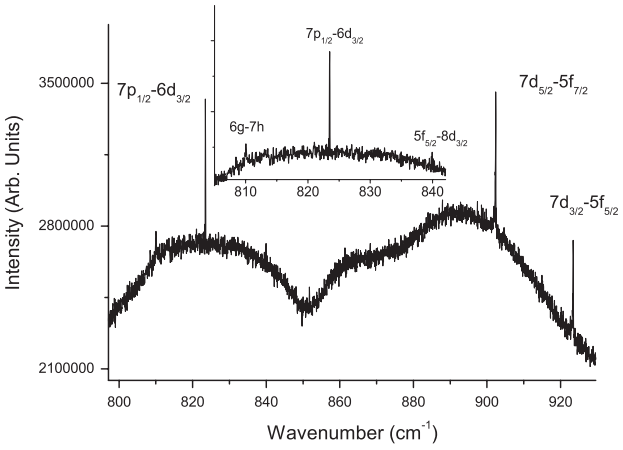

Fig. 4. A part of the recorded Cs emission spectrum (without subtraction of the background blackbody radiation signal component).

maxima at different delay times τ ranging from about 10 to 20 μs. Some examples of time profiles of the observed lines are presented in Fig. 5. The dependence of the time profiles on the distance L between the probed area at the target surface is shown in Fig. 6. Note that for the closest distance $L = 1$ mm, we observed quite high noise in the measured spectra. This is probably due to thermal radiation from the target heated by the laser pulses.

A nonmonotonic decay of the emission intensity shown in Figs. 5 and 6 could be due to the complex population kinetics of the atomic Cs states in the ablation plasma and the transfer processes in ablation products [27,28]. While complete understanding of the time profiles is not necessary for the main results of this work, it seems possible that the profiles may vary with τ and L in a way that might be useful if one wished to investigate in detail the dynamics of the plasma [29].

Table 2. Cs IR Line Wavenumbers ν_{ki}, Intensities I_{ki}, SNRs, FWHMs, and Oscillator Strengths f_{ik} for the Observed Lines[a]

ν_{ki}(cm^{-1}), this work	ν_{ki}(cm^{-1}), NIST [1]	I_{ki} (arb. u.)	SNR	FWHM (cm^{-1})	Identification	f_{ki}
642.439(10)		2.29×10^4	2.88	0.099(37)	$7p_{\frac{3}{2}} - 6d_{\frac{3}{2}}$	3.13×10^{-2}
685.289(8)		2.31×10^4	5.26	0.056(21)	$7p_{\frac{3}{2}} - 6d_{\frac{5}{2}}$	3.03×10^{-1}
810.050(16)		2.99×10^4	4.24	0.105(43)	$6g - 7h$	2.91
823.478(5)		9.23×10^4	6.95	0.072(16)	$7p_{\frac{1}{2}} - 6d_{\frac{3}{2}}$	3.98×10^{-1}
839.938(10)		2.14×10^4	6.47	0.066(25)	$5f_{\frac{5}{2}} - 8d_{\frac{3}{2}}$	2.87×10^{-1}
851.739(10)		8.82×10^3	3.81	0.051(17)	$5f_{\frac{7}{2}} - 8d_{\frac{5}{2}}$	3.02×10^{-1}
902.367(16)		1.41×10^5	1.42	0.014(7)	$7d_{\frac{5}{2}} - 5f_{\frac{7}{2}}$	1.25
923.437(11)		9.51×10^4	1.55	0.030(16)	$7d_{\frac{3}{2}} - 5f_{\frac{5}{2}}$	1.33
1119.152(2)		1.12×10^4	3.52	0.081(18)	$8p_{\frac{3}{2}} - 9s_{\frac{1}{2}}$	4.87×10^{-1}
1201.816(8)		6.84×10^3	5.35	0.083(20)	$8p_{\frac{1}{2}} - 9s_{\frac{1}{2}}$	4.63×10^{-1}
1348.359(2)		6.21×10^3	8.85	0.043(7)	$5g - 6h$	3.04
1381.126(3)		5.12×10^2	3.35	0.041(12)	$5f_{\frac{5}{2}} - 6g_{\frac{7}{2}}$	1.13
1381.277(8)		1.52×10^3	2.38	0.038(32)	$5f_{\frac{7}{2}} - 6g_{\frac{9}{2}}$	1.30
1391.662(8)		4.80×10^3	4.29	0.089(26)	$8s_{\frac{1}{2}} - 8p_{\frac{1}{2}}$	6.55×10^{-1}
1474.332(6)		9.68×10^3	6.91	0.105(19)	$8s_{\frac{1}{2}} - 8p_{\frac{3}{2}}$	1.32
1575.605(8)		3.28×10^3	5.58	0.067(25)	$4f_{\frac{5}{2}} - 7d_{\frac{3}{2}}$	1.34×10^{-1}
1596.726(7)		4.29×10^3	5.90	0.062(15)	$4f_{\frac{7}{2}} - 7d_{\frac{5}{2}}$	1.40×10^{-1}
1840.348(5)		1.26×10^6	4.60	0.110(18)	$6d_{\frac{5}{2}} - 4f_{\frac{7}{2}}$	8.23×10^{-1}
1883.397(3)		6.63×10^6	24.6	0.114(8)	$6d_{\frac{3}{2}} - 4f_{\frac{5}{2}}$	8.79×10^{-1}
2031.380(14)		7.08×10^4	3.71	0.105(47)	$8p_{\frac{3}{2}} - 8d_{\frac{5}{2}}$	2.82×10^{-1}
2102.423(12)		6.15×10^4	6.12	0.099(37)	$8p_{\frac{1}{2}} - 8d_{\frac{3}{2}}$	2.63×10^{-1}
2370.750(5)		6.58×10^3	10.5	0.037(19)	$7p_{\frac{3}{2}} - 8s_{\frac{1}{2}}$	3.44×10^{-1}
2535.825(5)	.8272(160)	5.99×10^3	3.71	0.046(8)	$4f_{\frac{5}{2}} - 5g_{\frac{7}{2}}$	1.32
2536.011(2)	.0113(160)	8.05×10^3	5.06	0.051(5)	$4f_{\frac{7}{2}} - 5g_{\frac{9}{2}}$	1.29
2551.800(6)	.8036(30)	3.35×10^3	8.75	0.066(33)	$7p_{\frac{1}{2}} - 8s_{\frac{1}{2}}$	3.25×10^{-1}
2766.948(4)	.9518(240)	1.00×10^5	12.9	0.063(2)	$6p_{\frac{3}{2}} - 5d_{\frac{3}{2}}$	2.11×10^{-2}
2864.529(1)	.5377(300)	3.52×10^5	4.29	0.092(3)	$6p_{\frac{3}{2}} - 5d_{\frac{5}{2}}$	2.00×10^{-1}
3229.818(7)	.818(30)	2.77×10^4	5.12	0.064(10)	$7s_{\frac{1}{2}} - 7p_{\frac{1}{2}}$	4.97×10^{-1}
3320.984(1)	.992(30)	2.96×10^5	9.71	0.107(4)	$6p_{\frac{1}{2}} - 5d_{\frac{3}{2}}$	2.46×10^{-1}
3410.862(4)	.868(30)	5.27×10^4	5.62	0.059(5)	$7s_{\frac{1}{2}} - 7p_{\frac{3}{2}}$	1.01
4122.382(5)	.3801(60)	7.56×10^4	9.68	0.055(28)	$7p_{\frac{3}{2}} - 7d_{\frac{5}{2}}$	2.80×10^{-1}
4282.499(4)	.5017(90)	3.02×10^5	4.29	0.084(8)	$7p_{\frac{1}{2}} - 7d_{\frac{3}{2}}$	2.68×10^{-1}
4339.464(10)	.4733(50)	5.07×10^4	3.93	0.038(23)	$6d_{\frac{5}{2}} - 5f_{\frac{7}{2}}$	5.12×10^{-2}
4382.478(12)	.4894(50)	1.71×10^4	3.70	0.097(40)	$6d_{\frac{3}{2}} - 5f_{\frac{5}{2}}$	4.73×10^{-2}
4964.280(12)	.2659(50)	1.48×10^4	5.26	0.082(36)	$7p_{\frac{3}{2}} - 9s_{\frac{1}{2}}$	2.76×10^{-2}
6803.221(5)	.2186(21)	1.52×10^6	5.37	0.081(4)	$6p_{\frac{3}{2}} - 7s_{\frac{1}{2}}$	1.93×10^{-1}
7173.343(14)	.3044(22)	2.93×10^4	4.01	0.068(42)	$7s_{\frac{1}{2}} - 8p_{\frac{1}{2}}$	9.11×10^{-3}
7266.091(14)	.0848(30)	4.58×10^4	3.65	0.123(54)	$5d_{\frac{3}{2}} - 7p_{\frac{1}{2}}$	2.15×10^{-2}
7349.552(6)	.5497(30)	4.56×10^4	2.80	0.056(25)	$5d_{\frac{5}{2}} - 7p_{\frac{3}{2}}$	2.12×10^{-2}
7357.260(6)	.2644(30)	6.77×10^5	3.15	0.085(12)	$6p_{\frac{1}{2}} - 7s_{\frac{1}{2}}$	1.79×10^{-1}

[a]Each of the seven spectral ranges, 800–1000, 1000–1300, 1200–1600, 1600–2000, 2000–3500, 4100–5000, and 5000–7700 cm^{-1}, has its own scale of arbitrary units for the emission intensity I_{ki}. Only the fractional parts are given for the NIST wavenumber values. The oscillator strengths f_{ki} are calculated using the QDT technique [Eq. (3)]

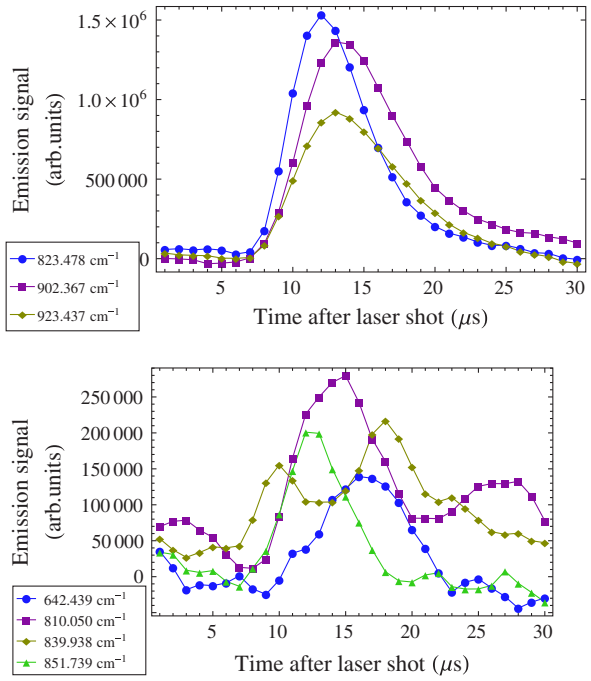

Fig. 5. (Color online) Time profiles of several Cs emission lines for $L = 9$ mm.

Table 3. Energy Values E_k of the Cs I Levels Involved in the Observed Transitions

Term	E_k(cm^{-1})	NIST values
7h	29162.472(43)	
6h	28356.426(45)	
$8p_{\frac{3}{2}}$	25791.480(12)	.508(30)
$7p_{\frac{3}{2}}$	21946.395(14)	.397(26)

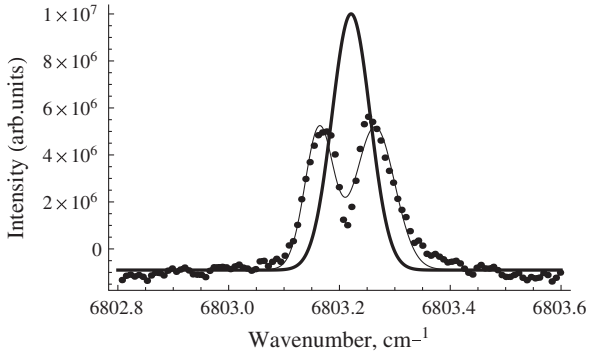

Fig. 7. The $6p_{\frac{3}{2}}$–$7s_{\frac{1}{2}}$ doublet lines of Cs. The hyperfine components are fitted to Gaussian shape (normal curve), and the parameters of the averaged line (bold curves) are calculated according to the authors' previous work [30].

The energies E_k of the levels involved in the corresponding transitions can be extracted from the measured ν_{ki} values. The procedure for extracting the energy values for the levels involved in the observed transitions is briefly described in our previous paper [16]. The extracted E_k values coincide within the calculated uncertainties with the level values taken from NIST [1,14]. The latter have far higher precision apart from the $7p_{\frac{3}{2}}$ and $8p_{\frac{3}{2}}$ levels, for which we report values with a slightly lower uncertainty. These values, together with the newly reported h-level energies, are presented in Table 3. Our spectral resolution does not allow us to resolve the fine structure of the $6h$ level. Indeed, the fine-structure separation of h levels should be less than that of g levels. The latter is quite low, while the $5f$ level has fine separation of about 0.15 cm^{-1} [1], and it is clearly seen from the our measured wavenumbers (see Table 2).

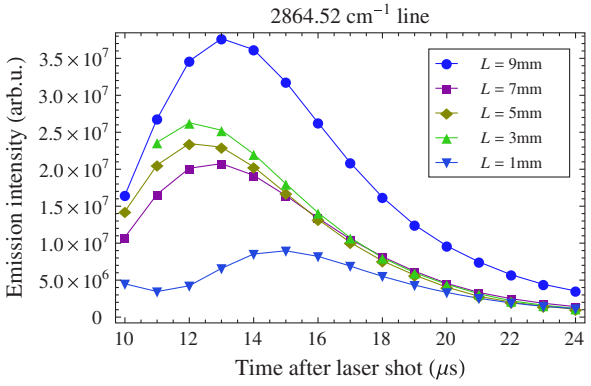

Fig. 6. (Color online) The dependence of the time profile of the 2864.52 cm^{-1} on the distance L between the probed area at the target surface.

Some of the measured lines (for instance, 6803.221 and 7357.26 cm^{-1}) display a hyperfine structure like that shown in the Fig. 7. Note that no hyperfine structure has been mentioned previously in the Cs IR line list [1] where these lines' wavenumbers are reported with a comparatively high precision (of about 0.002–0.01 cm^{-1}).

Since, to the authors' knowledge, the dipole transition matrix elements are available only for the transitions listed in Table 1, in this work we make QDT-calculations of these matrix elements (oscillator strengths f_{ik}) for the observed transitions in Table 2.

4. CONCLUSION

Using FTIR spectroscopy of a plasma formed by ablation of a CsI target by a pulsed nanosecond ArF laser in a vacuum, we report the IR spectrum of atomic cesium in the 800–8000 cm^{-1} region. We have substantially extended the spectral range (as compared to the 1200–1600 cm range measured in our recent work [13]). No spectra of alkali metals were measured previously in the 800–1200 cm^{-1} domain. The recorded spectra allowed us to extract the excitation energy of $5p^6\,7h$ state of Cs (in addition to the $5p^6\,6h$ level reported in our recent paper [13]), which has not been measured before. The other Cs levels extracted from the observed lines are in good agreement with NIST Atomic Spectra Database. We also calculate the probabilities of transitions for the observed lines. We show an asymmetric and multiple-peak behavior of the emission intensity as a function of the time delay after the ablating laser shot and of the distance between the probed area and the target surface. While complete understanding of the time profiles is not necessary for the main results of this work, it seems possible that the profiles may vary with time and location in a way that might be useful if one wished to investigate in detail the dynamics of the plasma.

ACKNOWLEDGMENTS

This work was financially supported by the Grant Agency of the Academy of Sciences of the Czech Republic (Grant No. IAA400400705) and Project ECPF:049/4V of the Ministry of Finance of the Czech Republic.

REFERENCES

1. J. E. Sansonetti, "Wavelengths, transition probabilities, and energy levels for the spectra of cesium (Cs I–Cs LV)," J. Phys. Chem. Ref. Data **38**, 761–923 (2009).
2. W. Clark and C. H. Greene, "Adventures of a Rydberg electron in an anisotropic world," Rev. Mod. Phys. **71**, 821–833 (1999).
3. S. A. Napier, D. Cvejanović, J. F. Williams, and L. Pravica, "Effect of electron correlations on the excitation of neutral states of zinc in the autoionizing region: a photon emission study," Phys. Rev. A **78**, 032706 (2008).
4. S. I. Themelis, "Partial widths with interchannel coupling for the P-3(0) Wannier-ridge states of H^-," Phys. Rev. A **81**, 064504 (2010).
5. S. R. Lundeen, "Fine structure in high-L Rydberg states: a path to properties of positive ions," in *Advances In Atomic, Molecular, and Optical Physics*, Vol. **52**, P. R. Berman and C. C. Lin, eds. (Academic Press, 2005), pp. 161–208.
6. M. E. Hanni, J. A. Keele, S. R. Lundeen, and W. G. Sturrus, "Microwave spectroscopy of high-L $n = 10$ Rydberg states of argon," Phys. Rev. A **78**, 062510 (2008).
7. J. A. Keele, S. L. Woods, M. E. Hanni, S. R. Lundeen, and W. G. Sturrus, "Optical spectroscopy of high-l Rydberg states of nickel," Phys. Rev. A **81**, 022506 (2010).
8. W.-B. Lee, J.-Y. Wu, Y.-I. Lee, and J. Sneddon, "Recent applications of laser-induced breakdown spectrometry: a review of material approaches," Appl. Spectrosc. Rev. **39**, 27–97 (2004).
9. D. Babánková, S. Civiš, and L. Juha, "Chemical consequences of laser-induced breakdown in molecular gases," Prog. Quantum Electron. **30**, 75–88 (2006).
10. A. Gomes, A. Aubreton, J. J. Gonzalez, and S. Vacquie, "Experimental and theoretical study of the expansion of a metallic vapour plasma produced by laser," J. Phys. D **37**, 689 (2004).
11. O. Barthelemy, J. Margot, M. Chaker, M. Sabsabi, F. Vidal, T. W. Johnston, S. Laville, and B. L. Drogoff, "Influence of the laser parameters on the space and time characteristics of an aluminum laser-induced plasma," Spectrochim. Acta, Part B **60**, 905–914 (2005).
12. C. Aragon and J. A. Aguilera, "Characterization of laser induced plasmas by optical emission spectroscopy: a review of experiments and methods," Spectrochim. Acta, Part B **63**, 893–916 (2008).
13. S. Civiš, P. Kubelík, P. Jelínek, V. E. Chernov, and M. Y. Knyazev, "Atomic cesium 6h states observed by time-resolved FTIR spectroscopy," J. Phys. B **44**, 225006 (2011).
14. Y. Ralchenko, A. Kramida, and J. Reader, and NIST ASD Team, "NIST Atomic Spectra Database (version 4.1.0)" (2011).
15. S. Civiš, I. Matulková, J. Cihelka, K. Kawaguchi, V. E. Chernov, and E. Y. Buslov, "Time-resolved Fourier-transform infrared emission spectroscopy of Au in the 1800–4000 $-cm^{-1}$ region: Rydberg transitions," Phys. Rev. A **81**, 012510 (2010).
16. S. Civiš, I. Matulková, J. Cihelka, P. Kubelík, K. Kawaguchi,, and V. E. Chernov, "Time-resolved Fourier-transform infrared emission spectroscopy of Ag in the (1300 – 3600) $-$ cm^{-1} region: transitions involving f and g states and oscillator strengths," Phys. Rev. A **82**, 022502 (2010).
17. S. Civiš, I. Matulková, J. Cihelka, P. Kubelík, K. Kawaguchi, and V. E. Chernov, "Time-resolved FTIR emission spectroscopy of Cu in the 1800 – 3800 cm^{-1} region: transitions involving f and g states and oscillator strengths," J. Phys. B **44**, 025002 (2011).
18. K. Kawaguchi, Y. Hama, and S. Nishida, "Time-resolved Fourier transform infrared spectroscopy: application to pulsed discharges," J. Mol. Spectrosc. **232**, 1–13 (2005).
19. "Opus spectroscopy software," http://www.brukeroptics.com/opus.html (2010).
20. A. D. Giacomo, V. Shakhatov, and O. D. Pascale, "Optical emission spectroscopy and modeling of plasma produced by laser ablation of titanium oxides," Spectrochim. Acta, Part B **56**, 753–776 (2001).
21. H. Qi, Y. Sun, X. Liu, X. Hou, and Y. Li, "Spatial spectroscopic diagnose of the plasma produced from laser ablation of a KTA crystal," Laser Phys. Lett. **4**, 212–217 (2007).
22. C. H. Greene, A. R. P. Rau, and U. Fano, "General form of the quantum-defect theory. II," Phys. Rev. A **26**, 2441–2459 (1982).
23. V. Chernov, N. Manakov, and A. Starace, "Exact analytic relation between quantum defects and scattering phases with applications to Green's functions in quantum defect theory," Eur. Phys. J. D **8**, 347–359 (2000).
24. V. E. Chernov, D. L. Dorofeev, I. Y. Kretinin, and B. A. Zon, "Method of the reduced-added Green function in the calculation of atomic polarizabilities," Phys. Rev. A **71**, 022505 (2005).
25. B. N. Chichkov and V. P. Shevelko, "Dipole transitions in atoms and ions with one valence electron," Phys. Scr. **23**, 1055–1065 (1981).
26. A. Sieradzan, M. D. Havey, and M. S. Safronova, "Combined experimental and theoretical study of the $6p^2P_j \rightarrow 8s^2S_{1/2}$ relative transition matrix elements in atomic Cs," Phys. Rev. A **69**, 022502 (2004).
27. A. Khalil and N. Sreenivasan, "Study of experimental and numerical simulation of laser ablation in stainless steel," Laser Phys. Lett. **2**, 445–451 (2005).
28. K. Kawaguchi, N. Sanechika, Y. Nishimura, R. Fujimori, T. N. Oka, Y. Hirahara, A. Jaman, and S. Civiš, "Time-resolved Fourier transform infrared emission spectroscopy of laser ablation products," Chem. Phys. Lett. **463**, 38–41 (2008).
29. M. Rossa, C. A. Rinaldi, and J. C. Ferrero, "Internal state populations and velocity distributions of monatomic species ejected after the 1064 nm laser irradiation of barium," J. Appl. Phys. **105**, 063306 (2009).
30. S. Civiš, I. Matulková, J. Cihelka, P. Kubelík, K. Kawaguchi, and V. E. Chernov, "Low-excited f-, g- and h-states in Au, Ag and Cu observed by Fourier-transform infrared spectroscopy in the 1000–7500 cm^{-1} region," J. Phys. B **44**, 105002 (2011).

Reference

[1] Benedikt, J., Letourneur, K. G. Y., Wisse, M., Schram, D. C., and van deSanden, M. C. M. (2002) *Diamond and Related Materials* **11(3-6)**, 989 – 993.

[2] Benedikt, J., Woen, R. V., vanMensfoort, S. L. M., Perina, V., Hong, J., and van deSanden, M. C. M. (2003) *Diamond and Related Materials* **12(2)**, 90 – 97 Proceedings of the 4th Specialist Meeting on Amorphous Carbon.

[3] Bogaerts, A., De Bie, C., Eckert, M., Georgieva, V., Martens, T., Neyts, E., and Tinck, S. (2010) *Pure and Applied Chemistry* **82(6)**, 1283–1299 19th International Symposium on Plasma Chemistry (ISPC-19), Bochum, GERMANY, JUL 26-31, 2009.

[4] Dorai, R. and Kushner, M. (2001) *Journal of Physics D: Applied Physics* **34**, 574.

[5] Franz, D., Hollenstein, M., and Hollenstein, C. (2000) *Thin Solid Films* **379(1-2)**, 37 – 44.

[6] Gogolides, E., Vauvert, P., Rhallabi, A., and Turban, G. (1998) *Microelectronic Engineering* **41-42**, 391 – 394 International Conference on Micro- and Nanofabrication.

[7] Graves, D. B. and Humbird, D. (2002) *Applied Surface Science* **192(1-4)**, 72 – 87.

[8] Herron, J. T. and Green, D. S. (2001) *Plasma Chemistry and Plasma Processing* **21**, 459–481 10.1023/A:1011082611822.

[9] Kim, M. T. (2003) *Applied Surface Science* **211(1-4)**, 285 – 292.

[10] Laimer, J., Misslinger, G., and Störi, H. (2003) *Surface and Coatings Technology* **174-175**, 938 – 942 Proceedings of the Eight International Conference on Plasma Surface Engineering.

[11] Lee, D. H., Kim, K.-T., Cha, M. S., and Song, Y.-H. (2010) *International Journal of Hydrogen Energy* **35(20)**, 10967 – 10976 Hyceltec 2009 Conference.

[12] Lowke, J. and Morrow, R. (1994) *Pure and Applied Chemistry* **66(6)**, 1287–1294.

[13] Meeks, E. and Ho, P. (2000) *Thin Solid Films* **365(2)**, 334 – 347.

[14] Misslinger, G., Laimer, J., and Störi, H. (2001) *Vacuum* **61(2-4)**, 413 – 417.

[15] Mollah, M. Y. A., Schennach, R., Patscheider, J., Promreuk, S., and Cocke, D. L. (2000) *Journal of Hazardous Materials* **79(3)**, 301 – 320.

[16] Paul, A. K., Dimri, A. K., and Bajpai, R. P. (2002) *Vacuum* **68(2)**, 191 – 196.

[17] Perrin, J., Leroy, O., and Bordage, M. C. (1996) *Contributions to Plasma Physics* **36(1)**, 3–49.

[18] Rusanov, A. and Fridman, A. (1994) *Pure & Appl. Chemistry* **66**, 1267–1274.

[19] van deSanden, M. C. M., vanHest, M. F. A. M., deGraaf, A., Smets, A. H. M., Letourneur, K. G. Y., Boogaarts, M. G. H., and Schram, D. C. (1999) *Diamond and Related Materials* **8(2-5)**, 677 – 681.

[20] Sieck, L. W., Heron, J. T., and Green, D. S. (2000) *Plasma Chemistry and Plasma Processing* **20**, 235–258 10.1023/A:1007021207704.

[21] Tae, M. and Kim (2003) *Applied Surface Science* **211(1–4)**, 285 – 292.

[22] Dalgarno, A. (1995) *International Journal of Mass Spectrometry and Ion Processes* **149–150(0)**, 429 – 437 Honour Biography David Smith.

[23] Smith, D. (1993) *International Journal of Mass Spectrometry and Ion Processes* **129(0)**, 1 – 15.

[24] Gerlich, D., Herbst, E., and Roueff, E. (2002) *Planetary and Space Science* **50(12–13)**, 1275 – 1285 Special issue on Deuterium in the Universe.

[25] Fray, N., Bénilan, Y., Cottin, H., Gazeau, M.-C., and Crovisier, J. (2005) *Planetary and Space Science* **53(12)**, 1243 – 1262.

[26] Smith, G. D. and Palmer, R. A. Handbook of Vibrational Spectroscopy (5 Volume Set) pp. 625 – 640 Wiley 1 edition (2002).

[27] Rödig, C. and Siebert, F. Handbook of Vibrational Spectroscopy (5 Volume Set) pp. 641 – 654 Wiley 1 edition (2002).

[28] Matsutani, K. Handbook of Vibrational Spectroscopy (5 Volume Set) pp. 655 – 665 Wiley 1 edition (2002).

[29] Griffiths, P. R., Hirsche, B. L., and Manning, C. J. (1999) *Vibrational Spectroscopy* **19(1)**, 165 – 176.

[30] Kawaguchi, K., Hama, Y., and Nishida, S. (2005) *Journal of Molecular Spectroscopy* **232(1)**, 1 – 13.

[31] Civiš, S., Šedivcová Uhlíková, T., Kubelík, P., and Kawaguchi, K. (2008) *Journal of Molecular Spectroscopy* **250(1)**, 20 – 26.

[32] van Dishoeck, E. F. and Black, J. H. (1989) *The Astrophysical Journal* **340**, 273–297.

[33] Federman, S. R., Danks, A. C., and Lambert, D. L. (1984) *The Astrophysical Journal* **287**, 219–227.

[34] Turner, B. E. and Thaddeus, P. (1977) *The Astrophysical Journal* **211**, 755–771.

[35] Allen, M. and Knapp, G. R. (1978) *The Astrophysical Journal* **225**, 843–856.

[36] Turner, B. E. and Gammon, R. H. (1975) *The Astrophysical Journal* **198**, 71–89.

[37] Civiš, S., Walters, A., Tretyakov, M., Bailleux, S., and Bogey, M. (1998) *The Journal of chemical physics* **108**, 8369.

[38] Gupta, H., Brünken, S., Tamassia, F., Gottlieb, C. A., McCarthy, M. C., and Thaddeus, P. (2007) *The Astrophysical Journal Letters* **655(1)**, L57.

[39] McCarthy, M. C., Gottlieb, C. A., Gupta, H., and Thaddeus, P. (2006) *The Astrophysical Journal Letters* **652(2)**, L141.

[40] Horká, V., Civiš, S., Špirko, V., and Kawaguchi, K. (2004) *Collection of Czechoslovak chemical communications* **69(1)**, 73–89.

[41] Gottlieb, C., Brünken, S., McCarthy, M., and Thaddeus, P. (2007) *The Journal of chemical physics* **126**, 191101.

[42] Agúndez, M., Cernicharo, J., Guélin, M., Kahane, C., Roueff, E., Klos, J., Aoiz, F. J., Lique, F., Marcelino, N., Goicoechea, J. R., González García, M., Gottlieb, C. A., McCarthy, M. C., and Thaddeus, P. (2010) *Astronomy and Astrophysics* **517**, L2.

[43] Ferus, M., Kubelík, P., Kawaguchi, K., Dryahina, K., Španěl, P., and Civiš, S. (2011) *The Journal of Physical Chemistry A* **115(10)**, 1885–1899.

[44] Civiš, S., Ferus, M., Kubelík, P., Jelínek, P., Chernov, V. E., and Knyazev, M. Y. (2012) *Journal of the Optical Society of America B* **29(5)**, 1112–1118.

[45] Civiš, S., Ferus, M., Kubelík, P., Jelínek, P., and Chernov, V. E. (2012) *Astronomy and Astrophysics* **541**, A125.

[46] Ferus, M. Charakterizace výboje v atmosféře methanu a helia pomocí časově rozlišené spektrometrie s fourierovou transformací Master's thesis Charles University in Prague (2008).

[47] Ralchenko, Y., Kramida, A. E., Reader, J., and NIST A.S.D. Team Nist atomic spectra database `http://physics.nist.gov/asd` (2011).

[48] Kawaguchi, K., Sanechika, N., Nishimura, Y., Fujimori, R., Oka, T. N., Hirahara, Y., Jaman, A., and Civiš, S. (2008) *Chemical Physics Letters* **463(1–3)**, 38–41.

[49] George, S., Grays, A., and Engleman, Jr., R. (1988) *Journal of the Optical Society of America B* **5(7)**, 1500–1502.

[50] Civiš, S., Matulková, I., Cihelka, J., Kubelík, P., Kawaguchi, K., and Chernov, V. E. (2010) *Physical Review A* **82**, 022502.

[51] Civiš, S., Matulková, I., Cihelka, J., Kubelík, P., Kawaguchi, K., and Chernov, V. E. (2011) *Journal of Physics B: Atomic, Molecular and Optical Physics* **44(2)**, 025002.

[52] Civiš, S., Matulková, I., Cihelka, J., Kubelík, P., Kawaguchi, K., and Chernov, V. E. (2011) *Journal of Physics B: Atomic, Molecular and Optical Physics* **44(10)**, 105002.

[53] Ross, J. E. and Aller, L. H. (1972) *Solar Physics* **25**, 30–43 10.1007/BF00155742.

[54] Merrill, P. W. (1947) *The Astrophysical Journal* **105**, 360.

[55] Cowley, C. R., Ryabchikova, T., Kupka, F., Bord, D. J., Mathys, G., and Bidelman, W. P. (2000) *Monthly Notices of the Royal Astronomical Society* **317(2)**, 299–309.

[56] Johnson, J. A. and Bolte, M. (2002) *The Astrophysical Journal* **579(2)**, 616.

[57] Cowan, J. J., Sneden, C., Burles, S., Ivans, I. I., Beers, T. C., Truran, J. W., Lawler, J. E., Primas, F., Fuller, G. M., Pfeiffer, B., and Kratz, K.-L. (2002) *The Astrophysical Journal* **572(2)**, 861.

[58] S. Civiš, M. Ferus, P. Kubelík, P. Jelínek, V. E. Chernov, and E. M. Zanozina (2012) *Astronomy and Astrophysics.*

[59] Civiš, S., Kubelík, P., Jelínek, P., Chernov, V. E., and Knyazev, M. Y. (2011) *Journal of Physics B: Atomic, Molecular and Optical Physics* **44(22)**, 225006.

[60] Abdallah, J., Palmer, N., Gekelman, W., Maggs, J., and Clark, R. (1999) *Journal of Physics-London-B Atomic Molecular and Optical Physics* **32**, 1001–1008.

[61] Babushok, V., Jr., F. D., Dagdigian, P., Gottfried, J., Munson, C., Nusca, M., and Miziolek, A. (2007) *Spectrochimica Acta Part B: Atomic Spectroscopy* **62(12)**, 1321 – 1328 A Collection of Papers Presented at the 4th International Conference on Laser Induced Plasma Spectroscopy and Applications (LIBS 2006).

[62] Battaile, C. C. (2008) *Computer Methods in Applied Mechanics and Engineering* **197(41-42)**, 3386 – 3398 Recent Advances in Computational Study of Nanostructures.

[63] Behnke, J., Golubovsky, Y. B., Nisimov, S. U., and Porokhova, I. A. (1996) *Contributions to Plasma Physics* **36(1)**, 75–91.

[64] Bel'kov, S. A., Gasparian, P. D., Dolgolyova, G. V., and Kochubey, Y. K. (1997) *Journal of Quantitative Spectroscopy and Radiative Transfer* **58(4-6)**, 471 – 489 Radiative Properties of Hot Dense Matter III.

[65] Bhattacharjee, B., Schwer, D. A., Barton, P. I., and Green, W. H. (2003) *Combustion and Flame* **135(3)**, 191 – 208.

[66] Boeuf, J., Pitchford, L., Fiala, A., and Belenguer, P. (1993) *Surface and Coatings Technology* **59(1-3)**, 32 – 40.

[67] Bogaerts, A., Bleecker, K. D., Kolev, I., and Madani, M. (2005) *Surface and Coatings Technology* **200(1-4)**, 62 – 67 PSE 2004.

[68] Bogaerts, A. and Gijbels, R. (2002) *Vacuum* **69(1-3)**, 37 – 52.

[69] Bogaerts, A. and Gijbels, R. (2000) *Journal of Analytical Atomic Spectrometry* **15**, 1191–1201.

[70] Bogaerts, A., Gijbels, R., Gamez, G., and Hieftje, G. M. (2004) *Spectrochimica Acta Part B: Atomic Spectroscopy* **59(4)**, 449 – 460 Colloquium Spectroscopicum Internationale XXXIII.

[71] Bogaerts, A., Gijbels, R., and Goedheer, W. (1995) *Journal of applied physics* **78(4)**, 2233–2241.

[72] Bogaerts, A., Gijbels, R., and Jackson, G. P. (2003) *Journal of Analytical Atomic Spectrometry* **18**, 533–548.

[73] Bogaerts, A., Gijbels, R., and Vlcek, J. (1998) *Spectrochimica Acta Part B: Atomic Spectroscopy* **53(11)**, 1517 – 1526.

[74] Bogaerts, A., vanStraaten, M., and Gijbels, R. (1995) *Spectrochimica Acta Part B: Atomic Spectroscopy* **50(2)**, 179 – 196.

[75] Bogaerts, A., Wilken, L., Hoffmann, V., Gijbels, R., and Wetzig, K. (2002) *Spectrochimica Acta Part B: Atomic Spectroscopy* **57(1)**, 109 – 119.

[76] Bruno, D., Capitelli, M., and Longo, S. (2004) *Contributions to Plasma Physics* **44(5-6)**, 485–491.

[77] Busquet, M. (1997) *Journal of Quantitative Spectroscopy and Radiative Transfer* **58(4-6)**, 519 – 530 Radiative Properties of Hot Dense Matter III.

[78] Chiu, Y.-M., Hung, C.-T., Hwang, F.-N., Chiang, M.-H., Wu, J.-S., and Chen, S.-H. (2011) *Computer Physics Communications* **182(1)**, 167 –

169 Computer Physics Communications Special Edition for Conference on Computational Physics Kaohsiung, Taiwan, Dec 15-19, 2009.

[79] Fichthorn, K. and Weinberg, W. (1991) *Journal of Chemical Physics* **95(2)**, 1090–1096.

[80] Hrach, R. and Entlicher, M. (1999) *Computer Physics Communications* **121-122**, 661 – 661 Proceedings of the Europhysics Conference on Computational Physics CCP 1998.

[81] Hrach, R., Horváth, M., Hrachová, V., and Entlicher, M. (1997) *Vacuum* **48(6)**, 561 – 564.

[82] Jemmer, P. (1999) *Mathematical and Computer Modelling* **30(11-12)**, 61 – 76.

[83] Tago, K., Kazumi, H., and Kobayashi, K. (1998) *Journal of Alloys and Compounds* **279(1)**, 60 – 65.

[84] Vahedi, V. and Surendra, M. (1995) *Computer Physics Communications* **87(1-2)**, 179 – 198 Particle Simulation Methods.

[85] Voronov, M. and Ganeev, A. (2009) *Spectrochimica Acta Part B: Atomic Spectroscopy* **64(5)**, 416 – 426.

[86] Yanallah, K., Ziane, S. H., Belasri, A., and Meslem, Y. (2006) *Journal of Molecular Structure: THEOCHEM* **777(1–3)**, 125 – 129.

[87] Bogaerts, A. (2009) *Spectrochimica Acta Part B: Atomic Spectroscopy* **64(2)**, 126 – 140.

[88] Bogaerts, A. (2007) *Journal of Analytical Atomic Spectrometry* **22**, 13–40.

[89] Bogaerts, A. and Gijbels, R. (2002) *Spectrochimica Acta Part B: Atomic Spectroscopy* **57(6)**, 1071 – 1099.

[90] Bogaerts, A., Gijbels, R., and Goedheer, W. (1999) *Spectrochimica Acta Part B: Atomic Spectroscopy* **54(9)**, 1335 – 1350.

[91] Goodwin, D. (2003) *Chemical Vapor Deposition XVI and EUROCVD* **14(40)**, 2003–08.

[92] Cheskis, S., Derzy, I., Lozovsky, V., Kachanov, A., and Romanini, D. (1998) *Applied Physics B: Lasers and Optics* **66**, 377–381 10.1007/s003400050404.

[93] Sung, Y.-i. and Lim, H. B. (2003) *Journal of Analytical Atomic Spectrometry* **18**, 897–901.

[94] Morrison, N. A., William, C., and Milne, W. I. (2003) *Journal of Applied Physics* **94(11)**, 7031–7043.

[95] Winchester, M. R. and Payling, R. (2004) *Spectrochimica Acta Part B: Atomic Spectroscopy* **59(5)**, 607 – 666.

[96] Corbella, C., Polo, M., Oncins, G., Pascual, E., Andújar, J., and Bertran, E. (2005) *Thin Solid Films* **482(1–2)**, 172 – 176.

[97] vanRossum, G. and deBoer, J. (1991) *CWI Quarterly* **4(4)**, 283–303.

12

[12]Seznam uvádí pouze literaturu citovanou v úvodní části práce (kapitoly 1, 2, 3 a 4). Kompletní seznam použité literatury sestává z prací citovaných v jednotlivých předložených publikacích (viz. dodatek C).